3D PRINTING STRUCTURED NANOCELLULOSES AND THEIR COMPOSITES: PRINTABILITY, STRUCTURES, AND PROPERTIES

A Dissertation
Presented to
The Academic Faculty

By

Vincent Li

In Partial Fulfillment
Of the Requirements for the Degree
Doctor of Philosophy in the
School of Chemical and Biomolecular Engineering

Georgia Institute of Technology

May 2019

3D PRINTING STRUCTURED NANOCELLULOSES AND THEIR COMPOSITES: PRINTABILITY, STRUCTURES, AND PROPERTIES

Approved by:

Professor Yulin Deng, Advisor
School of Chemical & Biomolecular Engineering
Georgia Institute of Technology

Professor Jerry H. Qi, Advisor
School of Mechanical Engineering
Georgia Institute of Technology

Professor Carson J. Meredith
School of Chemical & Biomolecular Engineering
Georgia Institute of Technology

Professor Meisha L. Shofner
School of Material Science Engineering
Georgia Institute of Technology

Professor Christopher O. Luettgen
School of Chemical & Biomolecular Engineering
Georgia Institute of Technology

Professor Robert J. Moon
School of Material Science Engineering
Georgia Institute of Technology

Date Approved: November 28th, 2018

ACKNOWLEDGEMENTS

I give my sincerest gratitude to my research advisors, Professor Yulin Deng and Professor Jerry H. Qi, for their guidance and support during my PhD study. Their wisdom and leadership have kept my research intellectually stimulating and technologically relevant. I will always be grateful for your efforts in providing me ample opportunity to explore different innovative ideas and practice independent thinking. In addition, I like to give thanks to my thesis committee members, Professor Carson Meredith, Professor Christopher Luettgen, Professor Meisha Shofner, and Professor Robert Moon. I really appreciate your time in ensuring my research is scientifically sound, and providing me advice for both personal and professional growth.

I would also like to thank the director, professors, staff, and fellow students in the Renewable Bioproducts Institute (RBI) at Georgia Institute of Technology. Together, they created an encouraging environment for my PhD development. I am also grateful for the Paper Science and Engineering financial support from RBI, which allowed me to expand my intellectual horizon, pursue my passion for scientific discovery, and broaden my professional network.

I also express my thanks to all previous and current researchers in Professor Deng and Professor Qi's group. With their help and collaboration, I was able to refine and generate ideas for solving challenging questions throughout my PhD career. I further give special thanks to Conner Dunn, Devin Roach, Xiao Kuang, Xiaoming Mu, Craig Hamel, Arie Mulyadi, Xu Du, Wei Liu, Feifei Sun, Zhe Zhang, and Chinmay Satam. Their intellectual assistance and heartfelt friendship were paramount to my scientific contributions and successful accomplishments. Lastly, I also give special thanks to my family and friends for their continual emotional support. Without a doubt, they have made my PhD journey much more enriching, meaningful, and fulfilling.

TABLE OF CONTENTS

LIST OF TABLES

LIST OF FIGURES

LIST OF ABBREVIATIONS

2D	Two-Dimensional
3D	Three-Dimensional
4D	Four-Dimensional
ASTM	American Society for Testing and Materials
ATR-FTIR	Attenuated Total Reflectance-Fourier Transform Infrared Spectroscopy
C	Carbon Atom
CAD	Computer Aided Designs
CAH	Contact Angle Hysteresis
CNCs	Cellulose Nanocrystals
CNFs	Cellulose Nanofibers
CVD	Chemical Vapor Deposition
DiGlyDA	1,3-Diglycerolate Diacrylate
DIW	Direct-Ink-Write
DLP	Digital Light Processing
DMA	Dynamic Mechanical Analyzer
EDS	Energy Dispersive Spectroscopy
EG	Ethylene Glycol
Eq.	Equation
FDA	Food and Drug Administration
FDM	Fused Deposition Modeling
FE-SEM	Field Emission-Scanning Electron Microscopy

FQA	Fiber Quality Analyzer
G-codes	Geometric Codes
H	Hydrogen Atom
intra-/inter-	Intramolecular/Intermolecular
Irgacure 819	Phenylbis(2,4,6-trimethylbenzoyl)phosphine Oxide
Kymene	Polyamide-Epichlorohydrin
LED	Light Emitting Diode
LOM	Laminated Object Manufacturing
M^4	Multi-Materials-Multi-Methods
MFC	Microfibrillated Cellulose
Mn	Number Average Molecular Weight
MTS	Mechanical Testing System
N_2	Nitrogen Gas
NaBr	Sodium Bromide
NaClO	Sodium Hypochlorite
NaOH	Sodium Hydroxide
O	Oxygen Atom
P+P	Pick-and-Place
PCD	Particle Charge Detector
PEDOT:PSS	Poly(3,4-ethylenedioxythiophene)-Poly(styrenesulfonate)
PEG	Polyethylene Glycol
PEGDA	Polyethylene Glycol Diacrylate
PFOTS	1H,1H,2H,2H-Perfluorooctyl-Trichlorosilane

Polydadmac	Polydimethyl Diallyl Ammonium Chloride
PVSK	Polyvinyl Sulfuric Acid Potassium Salt
S2	Secondary Layer of Cell Wall
SLA	Stereolithography
SLS	Selective Laser Sintering
STL	Standard Tessellation Language
Sudan I	1-Phenylazo-2-Napthol
T-CNFs	High Pressure Homogenized and TEMPO Oxidized Cellulose Nanofibers
TEM	Transmission Electron Microscopy
TEMPO	2,2,6,6-Tetramethyl-1-Piperidinyloxy
T_g	Glass Transition Temperature
TGA	Thermal Gravimetric Analyzer
$T_{max\ degradation}$	Temperature at Maximum Rate of Thermal Degradation
T_{onset}	Thermal Degradation Onset Temperature
UV	Ultraviolet
UV-Vis	Ultraviolet-Visible
wt %	Weight Percent
β-D	Beta-Dextrorotatory
δ	Delta
ρ	Density
Φ	Porosity

SUMMARY

Cellulose remains to be one of the most renewable and abundant engineering materials used in current society, where one of its largest impacts is in the pulp and paper manufacturing sector. In the past decade, a new area of cellulosic materials in the nanoscale regime has emerged. These nanocellulosic materials, also known as nanocellulose, present a wide range of new functionality and enhanced properties that can be incorporated into many different commercially available products. Two of the most fundamental forms of nanocellulose are cellulose nanocrystals (CNCs) and cellulose nanofibers (CNFs), which are typically generated from cellulosic biomass degradation through a combination of mechanical, thermal, or chemical treatments.

Along with the advent of nanocellulose, 3D printing, or additive manufacturing, is also revolutionizing the field of manufacturing and processing. 3D printing allows complex structures to be efficiently produced based on user's customized digital designs, while also satisfying on-demand fabrication without needing complex molding parts or processing tools. While traditional 3D printing materials are petroleum-based, nanocellulose can be used as a new class of 3D processable material for producing customizable and complexly shaped structures that are of cellulosic nature. Thus, opening up a new paradigm for producing a next generation of high performance cellulosic 3D products that are green, sustainable, and even potentially recyclable.

Although it is desirable to fabricate nanocellulose-based structures and composites with 3D printing, it remains as a challenge to not only formulate compatibilized nanocellulosic resins and gels that are 3D printable, but also fabricate the 3D structure with high structural complexity, good shape quality, and tunable properties. Therefore, the main purpose of this thesis dissertation is to not only produce nanocellulose-based formulations with good 3D printability, but also take

advantage of nanocellulose's fundamental properties to produce shape customizable, print quality controllable, and functionality tunable nanocellulosic 3D products that are suitable for different engineering applications. Overall, this thesis dissertation is organized by targeting three main scientific objectives, and then they were systematically explored by investigating four specific research studies.

The three main objectives are preparing compatible CNC-photocurable polymer resins for fabricating composite structures, formulating water-based CNC and CNF gels for fabricating purely CNC and CNF aerogel structures, and using CNC gel as support material for fabricating structures with intricate features. These objectives are further examined in detail through four research studies, which include using digital light processing (DLP) 3D printing to fabricate CNC-polyethylene glycol-based composites with potential biomedical applications, using direct-ink-write (DIW) 3D printing to make CNC aerogels with potential tissue engineering applications, using DIW to fabricate CNF aerogels with potential oil-water separation or electrical applications, and using multi-materials-multi-methods (M^4) hybrid 3D printing to fabricate complexly shaped structures with potential prototyping applications.

From each research study, the main scientific contributions are also summarized as follow:

1) CNC compatibilization with polyethylene glycol diacrylate (PEGDA) was achieved with the addition of 1,3-diglycerolate diacrylate (DiGlyDA) to the polymer matrix. The dispersion of CNCs was improved, and the compatibilized CNC-polyethylene glycol-based photocurable resin was successfully processed by DLP into various complexly shaped 3D composite structures. The concentration of incorporated CNCs and the curing layer thickness during DLP can also be controlled to tune the composites' final properties. Overall, the DLP 3D printed

CNC composite structures also demonstrated the potential for biomedical related applications.

2) The rheological properties of different water-based CNC gels were studied in order to produce a CNC gel that can be reproducibly processed by DIW and freeze-drying into different shape customizable CNC aerogel 3D structures. Moreover, the print quality was found to improve with increasing CNC concentration and DIW printing resolution. Dual pore CNC aerogel scaffolds were also successfully printed, where the customizable 3D structure and inner pore architecture can potentially enable advance CNC scaffold designs suited for specific cell integration requirements during tissue engineering.
3) The DIW processability of water-based CNF gel was improved by performing 2,2,6,6-Tetramethyl-1-piperidinyloxy (TEMPO) oxidation and high pressure homogenization. The resultant homogenized and TEMPO oxidized cellulose nanofiber (T-CNFs) gel was reproducibly printed using DIW, and then freeze-dried into various shape customizable CNF aerogel 3D structures. The resultant aerogels also demonstrated high porosity, high specific strength, reversible deformability, and structural templating capability. Different chemistries were also templated to the T-CNF aerogels to impart hydrophobicity and electromechanical properties, where they demonstrated the potential for oil/water separation and electronic related applications.
4) Traditional petroleum-based support materials are un-sustainable, non-recyclable, and difficult to be completely removed from the target structures after 3D processing. Instead, CNC gel can serve as an interesting 3D printing support

material due to its sustainability, renewability, and potential recyclability. After fabricating different kinds of complexly shaped structures with M^4 hybrid 3D printing, water was used to easily remove the CNC support structure. Even in a highly confined environment, such as the inside of a balloon structure, CNC support material was still easily removed. Overall, the fabricated complexly shaped 3D structures demonstrated the potential for prototyping applications.

Lastly, this dissertation is outlined in eight chapters. Chapter I provides a brief introduction on nanocellulose, and then an overview of nanocellulose 3D printing's historical development is given. Chapter II not only describes the established fundamental background of nanocellulose and 3D printing, but some state-of-the-art reviews on nanocellulose 3D printing are also given. Chapter III illustrates the overall scientific objectives and targeted research studies of this dissertation. The significance of each research study, the various challenges within each study that need to be addressed, and the technical approaches for overcoming those challenges are also discussed. Chapter IV demonstrates the potential to use CNCs and DLP to construct composite 3D structures with tailorable properties. Chapter V describes the formulation of a CNC gel that can be processed by DIW and freeze-drying into shape customizable and inner pore architecture controllable aerogel 3D structures. Chapter VI describes the generation of a high pressure homogenized and TEMPO modified CNF gel that can be reproducibly processed by DIW and freeze-drying into aerogel 3D structures with highly deformable, shape recoverable, and functionalizable properties. Chapter VII demonstrates the possibility of using CNC gel as a sustainable support material for constructing complexly shaped structures during M^4 hybrid 3D printing. Finally, Chapter VIII provides the overall conclusions and possible future directions for this dissertation.

CHAPTER I: INTRODUCTION

For centuries, petroleum-based plastics, polymers, and chemicals have been used in many manufacturing and production processes. However, these materials are unsustainable and non-renewable. Given the extensive use of petrochemicals, there is a high incentive for using a more sustainable and greener alternative. Cellulose, a natural and abundant polymer that represents up to 1.5 tera-tons of the planet's annual biomass production, is highly sustainable, renewable, recyclable, biocompatible, and biodegradable.[1-3] From the biomass' hierarchical structure, cellulose in a variety of different forms can be obtained. Since each has its own unique functionality, cellulose has long since been used by mankind as an engineering material in many different applications: for example, lumber in construction, pulp in paper products, fibers in textile, fluff in absorbent products, microcrystalline additives in food, modifying agents in cosmetics, biofuel in energy production, dissolved derivatives in viscose or lyocell, and many others (Figure 1.1).

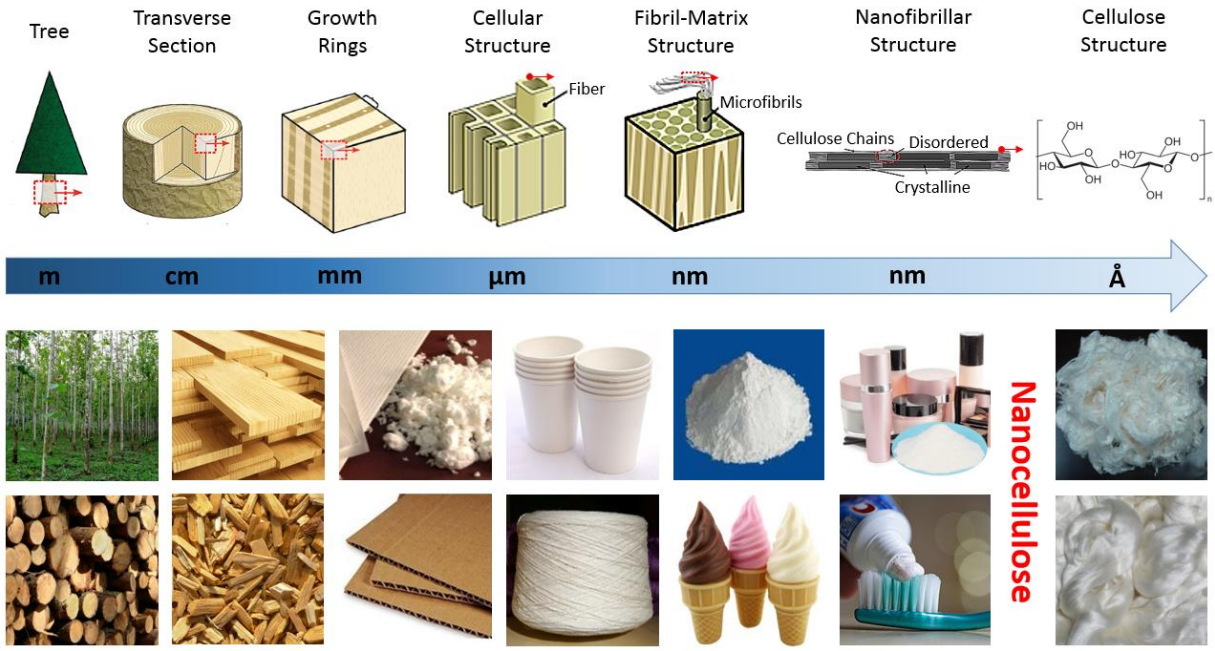

Figure 1.1: Hierarchical structure of trees, and different cellulose forms at different size scale are illustrated. Based on their dimensionality, various examples of their usage in different applications are also provided.[4]

In recent decades, a new class of cellulosic materials emerged from the nanoscale regime. These cellulose nanomaterials have been commonly termed as nanocellulose, which can include, algal cellulose, bacterial cellulose, tunicate cellulose, cellulose microfibers, cellulose microfibrils, microfibrillated cellulose (MFCs), cellulose nanofibers (CNFs), cellulose nanofibrils, nanofibrillated cellulose, cellulose nanocrystals (CNCs), nanocrystalline cellulose, cellulose nanowhiskers, cellulose nanoparticles, and many other similar names.[4] One of the first literature citation of cellulose fiber decomposition into highly reduced cellulose constituents was described by Thaysen et.al in 1926, which further sparked the idea of using bacteria and other methods to extract refined cellulose from different sources such as wood, plants, cotton, algae, and even tunicate.[5] After that, the study of biomass decomposition has been steadily gaining popularity.

In 1983, Turbak et.al. described an economical process to generate MFCs through high pressure homogenization, which was later patented by Rayonier Incorporated.[6-7] The patented

process was one of the first descriptions of producing nanocellulose at a scale that is industrially relevant, which enhanced the viability of using nanocellulose to improve commercial products. As more in depth exploration of nanocellulose production processes began to take place, more variety of different nanocellulosic materials also began to emerge. Ultimately, this led to a great increase in interest on nanocellulose within the scientific community, and the number of scientific publications involving nanocellulose has been accelerating since the 1900s (Figure 1.2A). Eventually, nanocellulose has also begun to find practical applications in areas of composite processing, structural templating, energy insulating foam/aerogel, tissue engineering, biomedical, pharmaceutical, flexible electronics, barrier films, rheology modification, specialty paper products, cement products, catalysis, food coatings, automotive parts, sensor engineering, additive manufacturing, and many others.

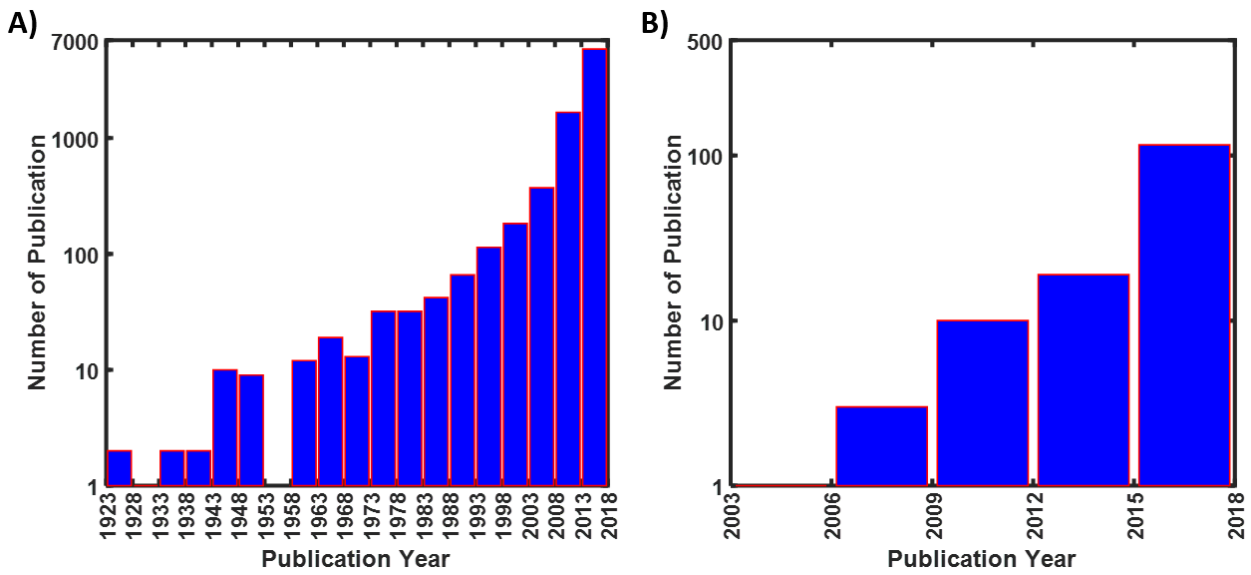

Figure 1.2: Utilizing SciFinder, the number of scientific literatures published within the field is plotted with their respective publication years. (A) As of September of 2018, publications that contained concepts of nanocellulose, algal cellulose, bacterial cellulose, tunicate cellulose, cellulose microfibers, cellulose microfibrils, microfibrillated cellulose, cellulose nanofibers, cellulose nanofibrils, nanofibrillated cellulose, cellulose nanocrystals, nanocrystalline cellulose, cellulose nanowhiskers, and cellulose nanoparticles, are illustrated. (B) As of September of 2018, publications that contained concepts of cellulose and 3D printing are illustrated. All left axes are represented in a log base 10 scale.

Currently, nanocellulose is not only a well-established field, but it is also studied worldwide. Nevertheless, even though it is highly desirable to enhance everyday products with nanocellulose, typical processing strategies still struggle to easily, reliably, and flexibly fabricate customizable nanocellulosic structures that are suited for different applications. 3D printing is a technology that is revolutionizing the field of manufacturing and processing, and it has shown great potential in directly fabricating complex parts from digital designs.[8-20] Overall, 3D printing has several advantages: novel structures can be constructed directly from digital designs, it is an agile and customizable manufacturing process, complex parts can be fabricated without complex tools, and it can satisfy on-demand fabrication.[19, 21-22] Initially, the concept of 3D printing first came into light around 1984, where Charles Hull invented an apparatus for creating plastic 3D objects with stereolithography.[23-24] The concept was to use a high energy beam to induce photo-polymerization of an acrylate-based resin, where the light exposed portion of the liquid photopolymer was solidified into layers with specified shapes. Between 2000 and 2010, the open source movement greatly accelerated the establishment of desktop 3D printers, which opened up the possibility to easily create complex parts based on user's instructions and digital designs.[23] Around the same time, 3D printing has also begun to impact the biomedical field, as bio-printing of implants and organs was accepted as a viable therapeutic medical treatment method. Currently, a variety of different 3D printers is available, and these 3D printers have found applications in both industrial settings and personal uses.

Among all 3D printing materials, petroleum-based polymers are the most commonly used and claim the largest portion of the 3D printing material market.[25-26] While other materials such as composites,[27] hydrogel,[28-29] glass,[30] metals,[31] ceramics,[32] sand,[33] and wax[34] are also used in 3D printing, these materials are unsustainable and non-renewable. On the other hand, nanocellulosic

materials are sustainable, renewable, biocompatible, and functionalizable, which make them an interesting and new class of material for 3D printing. Although the concept of using cellulose for 3D related application began during the early 2000s, literature publications on the actual 3D printing of nanocellulose were not prevalent until almost ten years later (Figure 1.2B). During the early 2010s, one of the first publications involving 3D printing nanocellulose was described by Markstedt et. al.[9] This work described the possibility of combining nanofibillated cellulose and alginate together to form a bio-ink that can be printed into 3D structures for the purpose of cartilage tissue engineering. They have demonstrated that it is possible to dispense the bio-ink into a customizable 3D structure, and then successfully cultured living cells onto these bio-scaffold structures. Currently, literature on nanocellulose 3D printing is experiencing a substantial growth in popularity and momentum. As a result, the number of scientific contributions involving nanocellulose 3D printing is expected to further increase, as there are still numerous opportunities to further enrich our fundamental understanding of processing nanocellulose with different 3D printing techniques.

CHAPTER II: ESTABLISHED LITERATURE BACKGROUND AND STATE OF THE ART REVIEW ON CELLULOSE 3D PRINTING

2.1 Established Background of Nanocellulose

Cellulose is a polysaccharide consisting of repeating units of two β-D-glucopyranose molecules, also known as cellobiose, that is linked together through β 1-4 glycosidic bonds (Figure 2.1).[4, 35-37] Each β-glucose molecule consists of a pyranose ring, where the C2, C3, and C6 carbon atoms contain hydroxyl groups. While the C6 carbon atom contains a primary hydroxyl group that favors esterification reactions, the C2 and C3 carbon atoms contain secondary hydroxyl groups that favor etherification reactions.[38] The ends of each cellulose chain are also capped by a β-glucose molecule with a reducing hydroxyl group on the C1 position, while the other end is capped by a non-reducing hydroxyl group on the C4 position. The number of repeating β-glucose units has been termed as the degree of polymerization, and it can have significant variations depending on the cellulose source and its processing conditions. Depending on the degree of polymerization, cellulose can also be used for different applications because its physical properties can be drastically different.

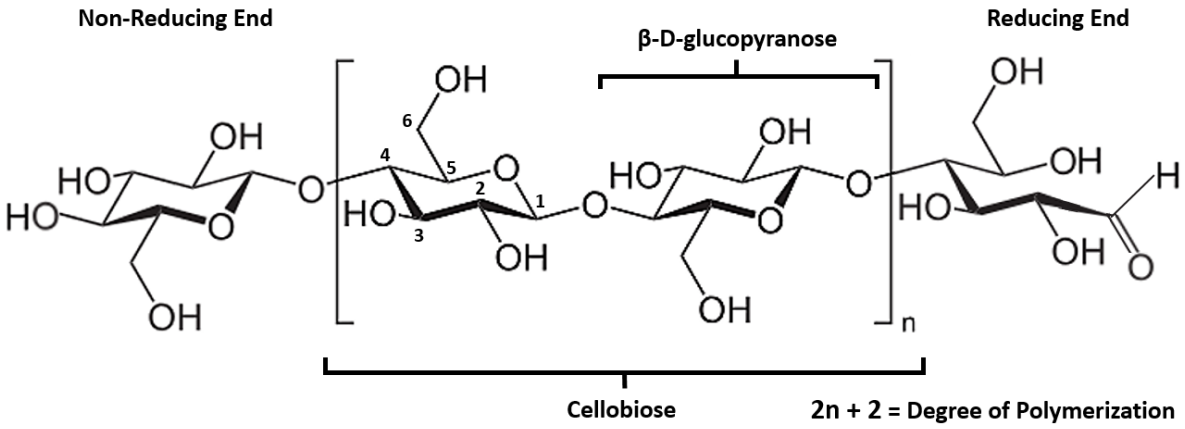

Figure 2.1: Chemical molecular structure of cellulose.

Currently, cellulose pulp extraction from trees or other biomass is commonly done through the Kraft cycle. This process involves using sodium hydroxide and sodium sulfide to remove hemicellulose, lignin, and extractives from the cellulosic structure, and allows the cellulose fibers that are mostly contained within the S2 layer of the cell wall to be liberated. From these cellulosic fibers, nanocellulose can be produced in either a bottom-up approach or a top-down approach.[4, 35, 39-40] Bottom-up generation of nanocellulose has been described using bacteria, algae, or fungi, where culturing mediums containing glucose or sucrose have been used.[4, 41] However, top-down strategies are more commonly favored by industries because of the ease of scalability. Typical top-down approaches involve breaking down cellulosic biomass with mechanical action, thermal treatment, chemical induced disintegration, acid hydrolysis dissolution, or even cellulose-based enzymatic degradation. Within the U.S. alone, it is estimated that nanocellulosic materials are produced at 6 million metric tons annually.[2, 42] This number is expected to further increase, as more and more pilot scale plants have progressed to industrial demonstration plants or even to full scale commercial production plants. As a result, nanocellulose is poised to become an integral part of the next disruptive technology because different nanocellulosic materials are becoming increasingly available.

Nanocellulose also exhibits exceptional properties, such as high crystallinity, low density, unique optical properties, alignment capability, low toxicity, low thermal expansion coefficient, high strength to weight ratio, high surface area to volume ratio, and reactive surface functional groups.[4, 43] While there have been many different forms of nanocellulose, the two most fundamental ones are CNCs and CNFs. CNCs are rod or rice like particles with high crystallinity, and they usually have length and diameter of around 100 to 1000 nm and 5 to 50 nm, respectively (Figure 2.2A). On the other hand, CNFs are string or spaghetti like materials with a length of up

to several microns, and width of around 10 to 100 nm (Figure 2.2B).[4, 39-40, 44-46] CNFs also contain both amorphous and crystalline regions, and their exceptionally high aspect ratios enable the capability for fibrillar network entanglement.

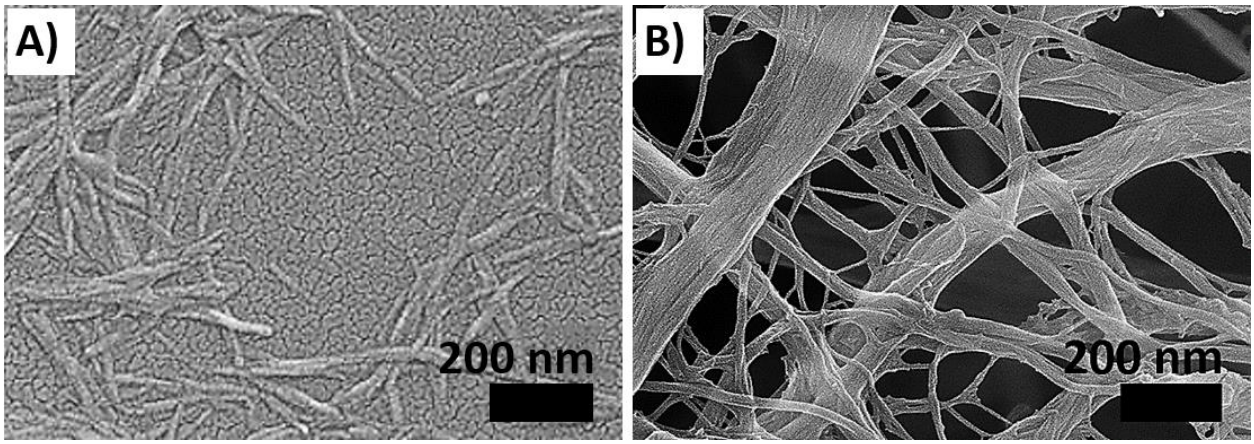

Figure 2.2: (A) CNCs and (B) CNFs that were used during this dissertation study.

CNCs and CNFs also have intricate van der Waals interactions and intra-/inter-cellulose chain hydrogen bondings that give rise to a high axial elastic modulus of 110 to 220 GPa for CNCs, and 15 to 150 GPa for CNFs.[4, 40, 47-52] In fact, studies have shown that CNCs and CNFs have Young's moduli that exceed that of glass fibers, Kevlar fibers, carbon fibers, and even some metals.[4, 47] Furthermore, their high surface area to volume ratios also provide an abundance of functionalizable hydroxyl groups for many different possible chemical modification schemes, which can include silylation with chlorosilanes, hydrolysis with sulfuric acid, esterification with carboxylic acid halides, esterification with acid anhydrides, etherification with epoxides, alcoholysis with isocyanates, oxidation with 2,2,6,6-Tetramethyl-1-piperidinyloxy (TEMPO), halogenation with chloroacetic acid, and many others (Figure 2.3).[4] As a result, it is possible to not only tailor the surface chemistries of nanocellulose to create formulations and gels that are suitable for different kinds of 3D printing techniques, but also produce mechanically enhanced and functionally tunable nanocellulosic products that are suited for different application requirements.

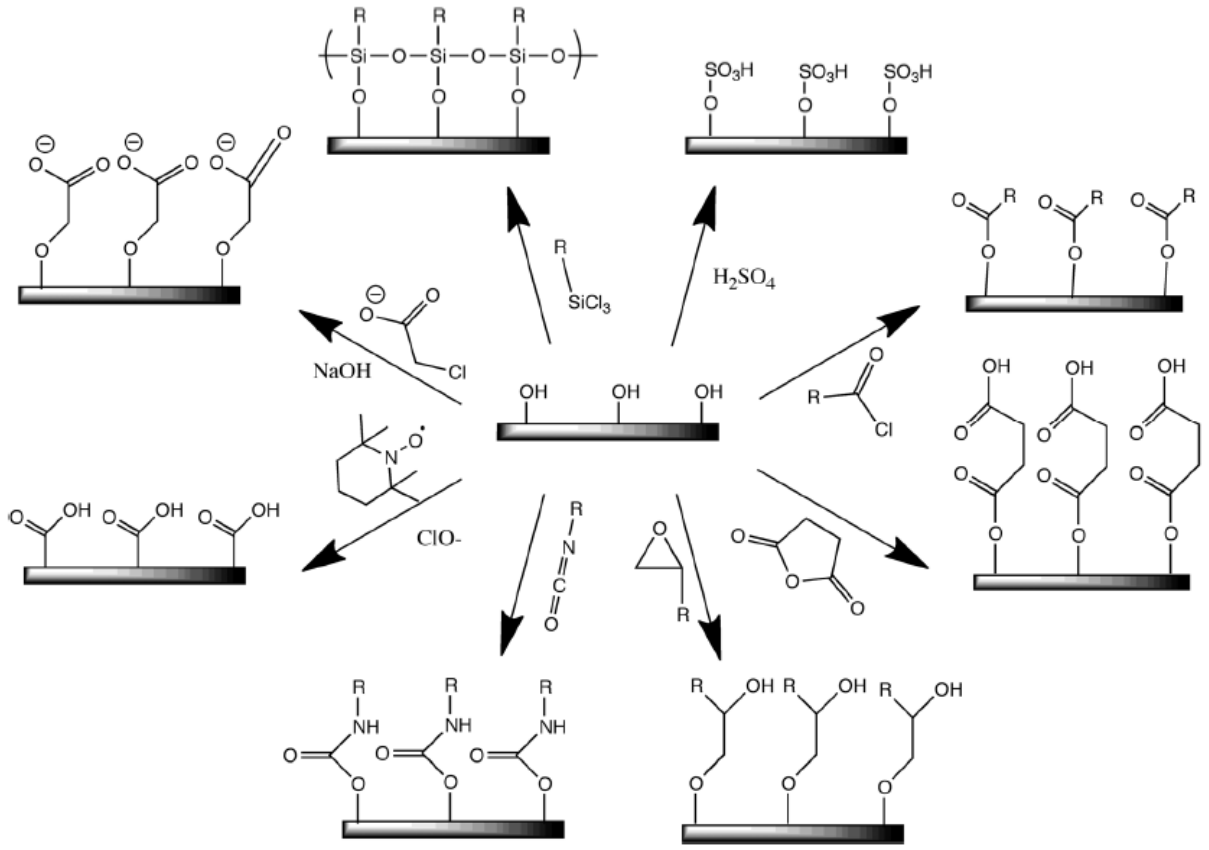

Figure 2.3: Different possible surface chemistry modification schemes between hydroxyl groups of nanocellulose and other functional molecular chemicals.[4]

2.2 Fundamentals of 3D Printing

According to American Society for Testing and Materials (ASTM) classification standards,[53] there are seven main types of 3D printing method, which include material extrusion, vat photo-polymerization, material jetting, reactive binder jetting, powder bed fusion, directed energy deposition, and stacked sheet lamination (Figure 2.4). In general, all 3D printing fabrication methods usually involve forming a layer of the print material into the desired shape, and then the 3D structure is created in a layer-by-layer manner. There are also sub-classes of 3D printing technique that fall under each main type of 3D printing method, which include direct-ink-write (DIW), fused deposition modeling (FDM), digital light processing (DLP), stereolithography (SLA), inkjet, selective laser sintering (SLS), and laminated object manufacturing (LOM). Each

technique has its own unique requirement of print material characteristics in order for it to be processable, and each technique's processing mechanism can also be different.

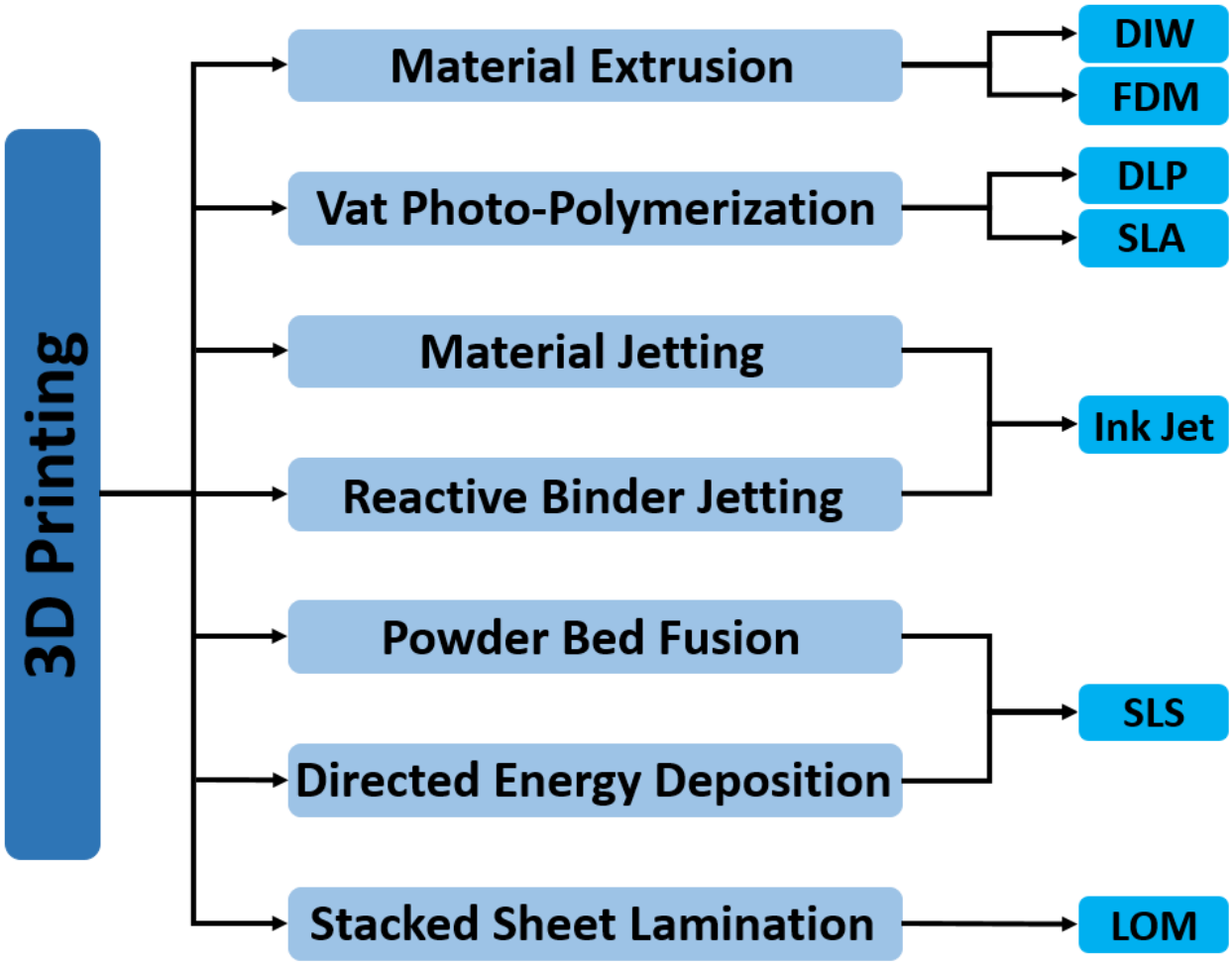

Figure 2.4: The seven main types of 3D printing method as described by ASTM classification standards. The sub-classes of 3D printing technique from each method include direct-ink-write (DIW), fused deposition modeling (FDM), digital light processing (DLP), stereolithography (SLA), inkjet, selective laser sintering (SLS), and laminated object manufacturing (LOM).

2.2.1 Direct-Ink-Write (DIW) and Fused Deposition Modeling (FDM)

Material extrusion 3D printing methods typically utilize pneumatic action or mechanical actuation to extrude the desired material out of a nozzle, and then the shape of the layer is controlled by the designated movement path of the nozzle. Material extrusion-based 3D printing techniques can include DIW and FDM, and they are among some of the most commonly used

techniques for printing cellulosic gels or cellulose-based plastic composites.[9, 26-28, 54-59] The premise of extrusion-based 3D printing requires the extruded material to hold its shape, so subsequent layers can be properly printed on top of the previously deposited layers. As a result, it either requires a high viscosity ink with appreciable shear thinning behavior for material deposition and shape holding during DIW processing, or it requires the material to undergo a phase transition between the liquid state and the solid state during FDM processing.

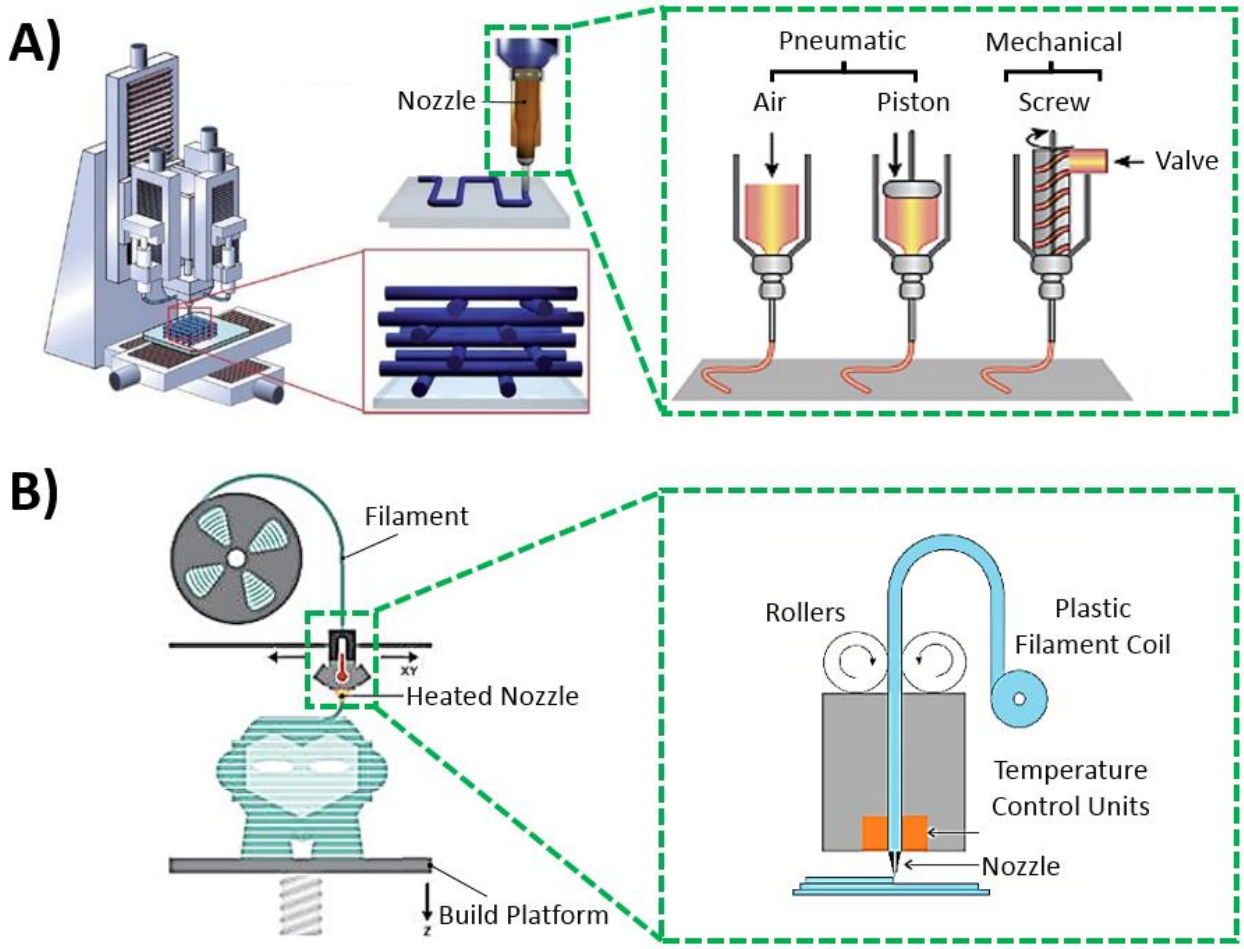

Figure 2.5: (A) Schematic of a DIW 3D printer, the material is usually extruded out of the nozzle through pneumatic or mechanical means.[60-61] (B) Schematic of a FDM 3D printer, the thermoplastic is usually liquefied into a flowable polymer by the heated nozzle in order to extrude the material out of the nozzle.[23]

During DIW 3D printing, high shear is induced within the printing nozzle so that shear thinning material can easily flow out of the nozzle. Afterwards, the material quickly regains its

high viscosity characteristics because there is no longer any shearing effect after the material is deposited onto the built stage (Figure 2.5A).[58, 62-64] On the other hand, a FDM print-head typically contains mechanical gears that feed a thermoplastic filament into a heated nozzle, and then the filament is liquefied into a flowable polymer in order for extrusion to take place. Afterwards, the deposited polymer quickly turns back into the solid phase through conductive or convective cooling (Figure 2.5B). As a result, even though DIW and FDM are both extrusion-based 3D printing techniques that rely on building a new layer on top of a previously printed layer with sufficient solidity, they are also different in that they have different processing and deposition mechanisms. For both DIW and FDM, complex structures can also be designed electronically in any commercially available 3D structure generating software, and then the line movement makeup for each 2D layer can be translated into geometric codes (G-codes). The G-code can be customized to control nozzle movement, speed, extrusion dimension, layer line density, etc.[8, 65] As a result, the syntax of the G-code can provide customizable control of both the processing parameters and the print quality during the extrusion process. This provides an economic and versatile approach to control shape fidelity and print quality without expensive fabrication of complex 3D molds or processing tools, which are required in traditional injection molding processes.[66]

2.2.2 Digital Light Processing (DLP) and Stereolithography (SLA)

Vat photo-polymerization involves placing a photosensitive liquid resin in a vat, and then light or laser illumination is used to induce the polymerization of the photosensitive liquid resin. Vat photo-polymerization-based 3D printing techniques can include DLP and SLA, and these can also be popular techniques for fabricating 3D cellulosic composite structures.[67-70] In both techniques, the concept is to use a light source to trigger the polymerization of the photosensitive

liquid resin into a specifically shaped solid layer, and then the build stage is translated to the next height position in order to cure the next layer. Within vat photo-polymerization, there is also a bottom-up and a top-down approach when building 3D structures. During bottom-up vat photo-polymerization, the printing structure is sequentially taken out of the resin bath as the stage is translated upwards in order to build the next layer. During top-down vat photo-polymerization, the printing structure is constantly submerged within the resin bath as the stage is translated downwards in order to build the next layer. Furthermore, DLP and SLA also have different processing mechanisms. DLP is a process that cures an entire layer at a time during the light exposure step, where the shape of each layer in the 3D object is controlled by the image projected by a light projector (Figure 2.6A). On the other hand, SLA involves using a focused energy source, such as a laser, to form a layer by writing lines (Figure 2.6B).

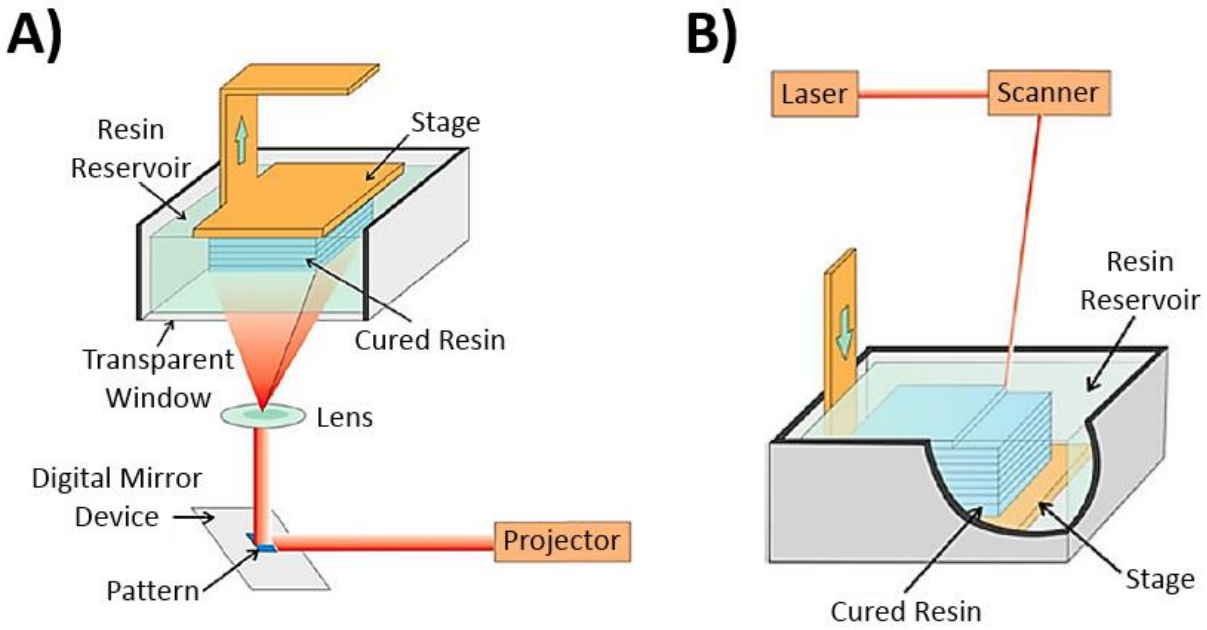

Figure 2.6: (A) Schematic of a bottom-up DLP 3D printer, where the photosensitive resin is polymerized into a layer during one light pattern exposure with the projector.[23] (B) Schematic of a top-down SLA 3D printer, where the photosensitive resin is polymerized into a layer by writing lines with a laser.[23]

The viscosity of the liquid resin is also usually relatively low, so uniform and efficient resin spreading throughout the stage can occur when it moves to the new height position. The curing kinetics, curing degree, and curing fidelity can be controlled by the photo-initiator and photo-absorber used in the photopolymer formulation. These vital components ensure an efficient curing process with controlled shape and structure, as only the part that is exposed to light is cured and the part that is not exposed to light is not cured. Photo-absorber also quickly attenuates the light intensity so that a sharp shape boundary can be produced, which allows very high structural accuracy and resolution to be obtained. The light intensity, wavelength, exposure duration, and curing layer thickness, can be adjusted to not only reduce the processing time required to complete the print, but also control the final printed part's properties.

2.2.3 Inkjet 3D Printing

Material jetting typically involves dispensing droplets of photosensitive liquid ink into the desired shape onto the build substrate, and then subsequently polymerizing the ink into a solid layer using UV light irradiation (Figure 2.7A). Reactive binder jetting is similar to material jetting, but a bonding agent is used instead of UV light in order to selectively bind the build material together into a solid layer. Since both methods require a print-head to deposit the target or bonding material, they can be categorized into the same technique of inkjet 3D printing.

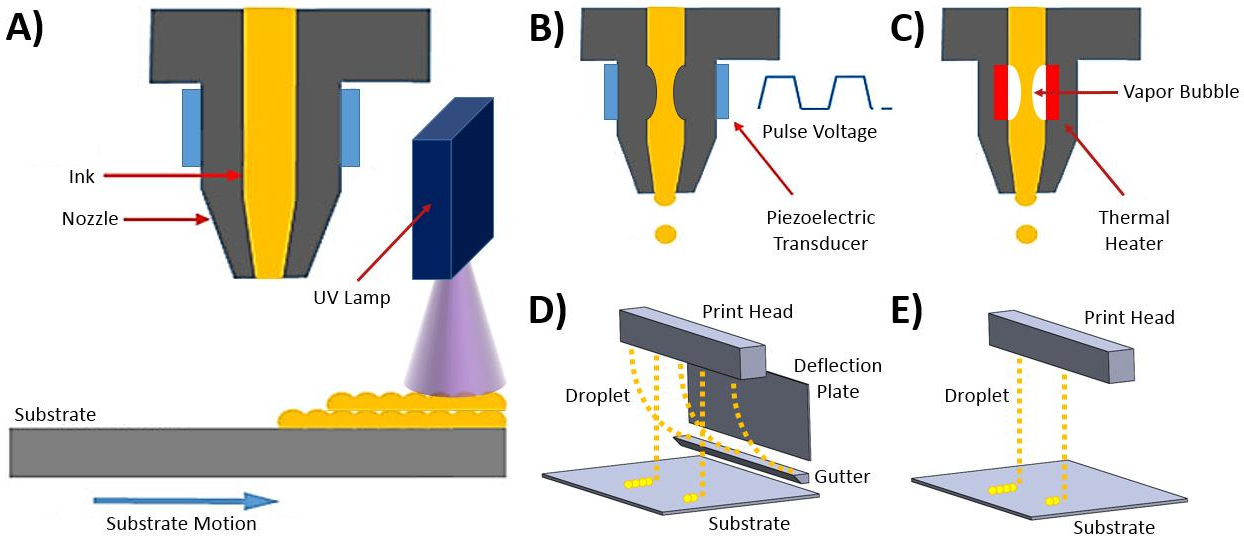

Figure 2.7: (A) Schematics of inkjet 3D printing, (B) piezoelectrically driven inkjet printing, (C) thermally driven inkjet printing, (D) continuous inkjet printing, (E) and drop-on-demand inkjet printing are illustrated.[71]

An inkjet print-head usually has two main deposition mechanisms, which are generating a pressure gradient within the nozzle through piezoelectrically induced fluctuation (Figure 2.7B) or thermally induced bubble vaporization (Figure 2.7C). There are also two forms of inkjet printing in order to control the shape of the deposited layer, which is classified into continuous inkjet printing and drop-on-demand inkjet printing. In continuous inkjet printing, streams of ink are deposited from all available nozzles on the print-head. However, an electrostatic field is used to electrically charge the ink streams, and then a deflection plate is used to selectively deflect certain streams to a gutter apparatus. The deflected ink can be recycled to the print-head for re-use, and the un-deflected ink can be deposited onto the substrate to form the desired pattern (Figure 2.7D). On the other hand, drop-on-demand inkjet printing relies on selectively inducing a pressure change within specified nozzles on the print-head. As a result, only certain nozzles will deposit ink onto the substrate in order to form the desired pattern (Figure 2.7E).[72]

Regardless of the deposition mechanism or the form of inkjet printing used, inkjet-based ink is usually a Newtonian fluid with low viscosity. Furthermore, special attention must also be

given to the density, viscosity, and surface tension of the ink. The ink must also have little to no contaminants, so print-head clogging is avoided. Degassing of the inkjet ink is also done prior to printing in order to remove air bubbles that are entrapped within the ink, so stable surface tension and meniscus pressure can be achieved during droplet formation. The nozzle diameter of the print-head can also have a significant impact on the printability of the ink. In fact, Derby et. al. had combined these inkjet printing considerations into a generalized printability parameter, where a range of printability parameter numbers is given as a guideline for stable droplet formation during inkjet deposition.[73-74] Overall, to achieve inkjet prints with good efficiency, reliability, and reproducibility, a careful selection of both the inkjet ink's fluid properties and the print-head parameters must be done to ensure they are compatible with one another.

2.2.4 Selective Laser Sintering (SLS)

Powder bed fusion utilizes an intense energy beam to selectively fuse a vat of powdered material together into a solid layer, and the shape of the layer is controlled by the scan path of the energy beam. Directed energy deposition combines the concept of material extrusion and powder bed fusion together, as powder feeders and focused energy beam are combined together into a single nozzle assembly. The powder feeders use sheath gas flow for powder deposition, and the depositing powder streams are controlled to converge into a single spot on the substrate. At the same time, an energy beam is focused on the converging powder streams, so the powder is melted and sintered together into a solid layer. The shape of the layer is once again controlled by the designated movement path of the nozzle assembly.[23, 75] Both powder bed fusion and directed energy deposition can also be classified under the same technique of SLS, as both require a focus energy beam to sinter powdered material together (Figure 2.8).

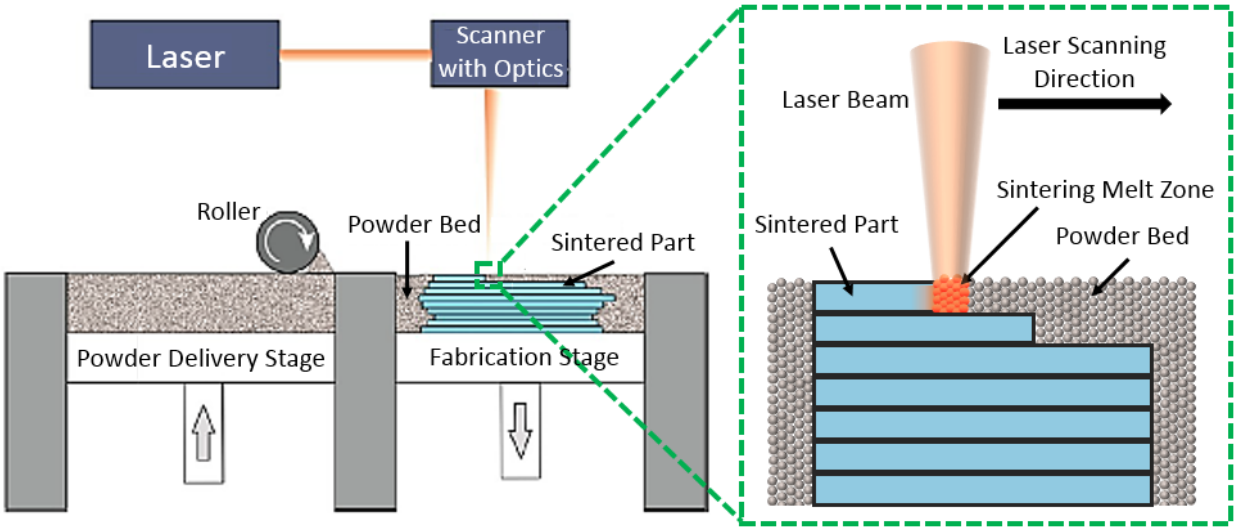

Figure 2.8: Schematic of a SLS 3D printer, where a laser is used to sinter the powder material together in order to form a solid layer.[23]

During SLS processing, a layer of powdered material is first distributed onto the fabrication stage, and then the powder is heated by the laser until the local temperature reaches the melting temperature of the powder. Once a layer of powder is sintered and fused with the building part, the stage is translated to a new height position before the process is repeated to build the next layer. The laser power, laser energy, laser scan speed, beam spot size, beam offset, layer thickness, bed temperature, exposure duration, and many other processing parameters can also affect the sintering process, which ultimately affects the final part's dimensional properties, accuracy, and resolution.[75] In general, optimization between the processing parameters and the sintering characteristic of the powder formulation is needed to achieve good quality prints.

2.2.5 Laminated Object Manufacturing (LOM)

Stack sheet lamination is a process where a 3D structure is constructed by cutting a sheet into a specifically shaped layer, stacking the layers, and then bonding the layers together. This 3D printing method has also been categorized under the LOM processing technique.[76] LOM begins

with using focused energy beam, wires electrical discharge machining, or water jet to cut a supply feed sheet into specifically shaped layers. Then, the layers are stacked together to form the 3D structure. A binding agent or an adhesive is also used to bond the stack of laminate layers together. Afterwards, the entire stack is lowered to the new height position, and the sheet supply roll feeds forward before the next layer is built in a similar manner. (Figure 2.9).

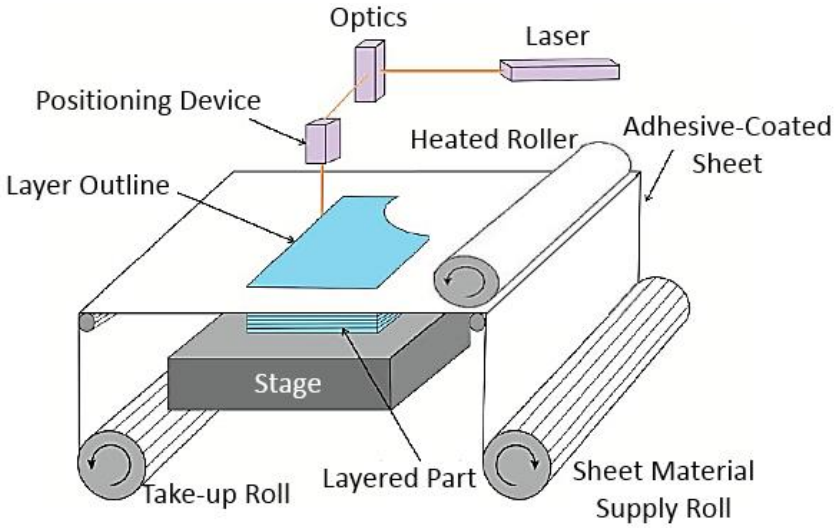

Figure 2.9: Schematic of a LOM 3D printer, where a 3D structure is constructed by cutting a supply sheet into specifically shaped layers, stacking the layers, and then bonding the layers together.[23]

During the cutting process of each layer, the penetration strength of the energy beam must be carefully controlled such that the cut layer can be separated from the supply sheet while also making sure the previously cut layers are not damaged. During the lamination process, heat is usually applied to ensure the layers are well bonded together. In this case, it is important to carefully control the temperature of the heated roller in order to avoid possible delamination issues. If the bonding temperature is too low, then there can be insufficient adhesion strength. Conversely, the printed part can also suffer from structural damage or defects if the bonding temperature is too high.

2.3 State of the Art Review on Cellulose 3D Printing

During the last decade, interests in processing cellulose with different 3D printing techniques have grown significantly.[26, 77-78] More specifically, processing nanocellulosic gels or inks with DIW related 3D printing has been favored because nanocellulosic suspension has shown the crucial shear thinning behavior.[79-86] For example, 3D printing of nanofibrillated cellulose-alginate bioink using a pneumatically driven micro-valve dispenser was demonstrated, as the bioink displayed shear thinning behavior within a viscosity range that spanned over five orders of magnitude. Although the shape fidelity still needed improvement despite calcium chloride-alginate crossing linking was preformed, the final structure demonstrated cell viability because the bioink contained human chondrocyte cells.[9, 54-55, 58, 87] This has greatly demonstrated the potential of using extrusion-based 3D printing technology to fabricate nanocellulosic structures with tissue engineering and regenerative medicine applications. Many other similar works were also observed, as they emphasized the benefit of how nanocellulose was able to enhance the printability of the ink due to increase in shear thinning effects.[56-59]

Meanwhile, FDM processing of purely cellulosic inks is rare because cellulose can undergo thermal decomposition during the FDM print-head's thermal heating. Instead, nanocellulose is incorporated into traditional thermoplastics in order to form a composite filament that is suitable for FDM processing. However, care must still be taken to ensure the integrity of nanocellulose is conserved during thermal heating. For this reason, either coupling agents are added to increase the nanocellulose's compatibility with the polymer matrix, or additives are added to increase the composite filament's melt flow rate such that there is limited heat exposure to the nanocellulose.[88-90] For example, silane coupling agents or hemicellulose/lignin bonding agents can help increase interfacial compatibility between micro/nanocellulose with polylactic acid, and polyethylene

glycol has also been used as an additive to improve the filament's plasticity and melt flow rate.[88, 91-92] Other binders used to improve compatibility include, inorganic particles, aerosolized water, gypsum, sodium silicate, cement, starch, urea formaldehyde, surfactants, and many others.[93-96] Instead of physical adsorption approaches, chemical modification of nanocellulose can also be performed to increase the interfacial compatibility and the thermal stability of the base matrix. Since sulfuric acid hydrolysis remains to be one of the most popular strategies for generating crystalline nanocellulose, sulfate ester functional groups are commonly left on the surfaces of the synthesized particles. These sulfate ester groups can be highly heat sensitive during heating, which has been attributed to the formation of thiols related species that favored the auto-catalytic degradation of cellulose. As a result, nanocellulose surface functionalization schemes, such as silylation, acetylation, esterification, polymer grafting, etc, have been studied by different research efforts.[97-104] In this case, the main goal is to replace sulfate ester groups with other functional groups that are also more compatible with the polymer matrix, while also increasing the thermal stability of the nanocellulose for FDM processing. Overall, there have been numerous reports of processing cellulose-based composite filaments into 3D structures with FDM, and literature works on this area are expected to see continual increase and improvement in the future.[93, 105-109]

In recent years, incorporation of nanocellulose into photocurable polymers and then subsequently processing the resin into 3D composite structures has been demonstrated. For example, lignin coated CNCs were added into methacrylate resin, and 3D printed CNC composites with improved mechanical properties and thermal stability were successfully fabricated by SLA.[67] The compatibilization between CNCs and methacrylate was improved by the hydrophobic lignin that was coated around the CNCs, which made them less polar and easier to disperse in the non-polar methacrylate matrix. CNCs have also been added to an oxetane and oligoacrylate-based

stereolithographic resin, and then SLA was used to fabricate 3D belt pulley and pump impeller structures with potential mechanical part replacement applications.[68] In this case, compatibilization with the polymer matrix was achieved by the etherification between hydroxyl groups on the CNCs and the epoxide functional groups in the polymer matrix. In another demonstration, SLA was used to fabricate complex architectures using CNCs and PEGDA.[69] CNC's compatibilization with the neat PEGDA matrix was achieved with the addition of water, but this also led to the loss of Young's modulus improvement despite CNCs were incorporated at different concentrations. Nevertheless, the resultant structures demonstrated great fidelity, and they could be useful for tissue engineering or biomedical related applications.

Since nanocellulosic materials tend to have strong self-interactions via hydrogen bonding, glycosidic bonds, and van der Waals attractions, they can easily form small scale agglomerates. As a result, uniformly dispersing nanocellulose within inkjet printing medium has been very difficult and challenging. In fact, suspending nanocellulosic particles within inkjet printing medium can also change the ink's meniscus formation capability, which could lead to irregular material jetting due to unstable droplet formations. Nevertheless, inkjet printing of cellulose related inks has also been demonstrated, but the usage of ionic liquids or complex solvent systems were needed to solubilize the cellulose into soluble constituents that can be mixed well with the inkjet printing medium.[76, 110] However, ionic liquids are usually expensive, and the utilization of cellulose solubilizing solvents, such as N,N-dimthylmorpholine/lithium chloride or N-methylmorpholine N-oxide, are not easily scalable without solvent recovery.[77, 111] In order to further lower the inkjet ink's viscosity for inkjet processing, other solvents, such as acetonitrile, ethanol, and dimethyl sulfoxide, can also be added to the inkjet formulation. While this provides better processing capability with inkjet printing, a careful selection of the print-head's working

material is still important because traditional plastic-based print-head can be damaged by organic solvents or other non-aqueous solvent systems.[112] After inkjet 3D printing, the resultant part is usually placed in water to regenerate the solubilized cellulose.[76, 113] However, layer solidification is typically done during the post processing step of cellulose regeneration, which meant additional layers cannot be easily built on top of the as-printed layer. This led to limitations in the final structure's height, as current demonstrations have only achieved final print height in the micrometer regime. As a result, actual inkjet printing of cellulose-based 3D structure in the macroscale regime still remains to be an active area of investigation.

While utilization of reactive binder jetting for constructing cellulosic 3D structures is not prevalent, there is a study that described binding wood chips together with jetting deposition of gypsum and cement.[94] Different simple 3D geometrical shapes, such as bars and truncated cones, in the macroscale regime were fabricated. Although more optimizations are needed before the 3D printed wood structure can be utilized in actual industrial or construction application, this work certainly demonstrated how bulk cellulosic materials can be processed into large scale 3D structures based on a reactive binder jetting strategy. Another work also describes using xantham gum and glucomannan as binders to induce recrystallization of amorphous cellulose powder.[114] The binders were inkjet printed onto a vat containing amorphous cellulose powder, where the final constructed structures were intended for food related applications. Similarly, even though the current structures suffered from resolution control and shape fidelity control, it is expected that further work on this area will expand due to excitement in 3D food printing applications.[115-119]

Due to possible thermal degradation of cellulose, processing cellulosic materials with powder bed fusion and directed energy deposition have been challenging because of the intense energy used during material fusion.[120] However, it is still possible to carefully select the cellulose

sources and processing conditions such that the thermal processing temperature lies between the cellulose's melting temperature and thermal degradation temperature. For example, processing starch cellulose and cellulose acetate powder with SLS techniques have been demonstrated.[121] In this case, careful control over the powder's properties, such as particle shape/size, energy absorption capacity, and melt flow behavior, was important. The laser operating conditions were also found to have a significant impact on whether or not the cellulose powders are bonded together or decomposed instead. Overall, this work demonstrated that it is possible to fabricate cellulose-based scaffold structures using a highly optimized SLS system.

The field of stack sheet lamination within rapid prototype processing has been established since the 1980s, [122-123] and now it is even utilized to process cellulosic materials. For example, a laminated nanocellulose-graphene oxide thin film structure was successfully fabricated, and it demonstrated the potential for rechargeable battery applications.[124] LOM processing of natural wood was also demonstrated, where a high performance plywood like structure was laminated from compressed wood layers.[125] These structures were strong yet lightweight, and they held great promise for low cost armor and ballistic energy absorption applications. Furthermore, these plywood like materials can also be used as floors, walls, or roofs in construction applications. In another instance, lamination of chemically treated wood layers into a transparent plywood composite structure was also described, and the resultant composite structure showcased load bearing properties.[126] Overall, laminating cellulosic materials into high performance functional structures have been expanding in recent years. Nevertheless, the fabricated structures were still relatively simplistic, and fabricating highly intricate cellulosic structures with LOM related techniques still remain to be seen in future investigations.

Overall, cellulose is becoming a common processing material in a variety of different 3D printing techniques. Especially with advancements in both nanocellulose and 3D printing development, there have been numerous innovative reports of 3D printing nanocellulose into functional structures with advanced applications. While there have been extensive demonstrations of 3D printing nanocellulose with excellent performance and properties, there is still significant room for further innovation and investigation in this area. Ultimately, this state of art review illustrated that nanocellulose 3D printing has only gained intense interest and momentum during recent decades, and it is expected that major breakthroughs and commercialization in this area will soon take place in the near future.

CHAPTER III: SCIENTIFIC OBJECTIVES, TARGETED RESEARCH STUDIES, SIGNIFICANCE, CHALLENGE ANALYSIS, AND TECHNICAL APPROACH

3.1 Organization of Scientific Objectives and Targeted Research Studies

As discussed in previous chapters, it is necessary to formulate 3D printable CNC and CNF-based resins and gels that are compatible with different 3D printing techniques. Also, it is desirable to fabricate nanocellulosic 3D structures with shape customizability, good print quality, and tunable properties. As a result, the three scientific objectives targeted in this dissertation include:

- Preparation of compatible CNC-photocurable polymer formulations, and then fabricate property-tunable 3D composite structures with potential biomedical applications
- Formulation of CNC and CNF gels that can be 3D processed into purely CNC and CNF aerogel structures with potential tissue engineering, oil-water separation, or electrical related applications
- Fundamental investigation of utilizing CNC gel as support material during hybrid 3D printing in order to process intricately shaped structures with potential prototyping applications

The objectives outlined in this dissertation are also systematically explored by targeting four specific areas of research study, which include fabricating CNC-polyethylene glycol-based composites with DLP, CNC aerogel structures with DIW-freeze-drying, CNF aerogel structures with DIW-freeze-drying, and complexly shaped structures with hybrid 3D printing while using CNC gel as supporting material (Figure 3.1).

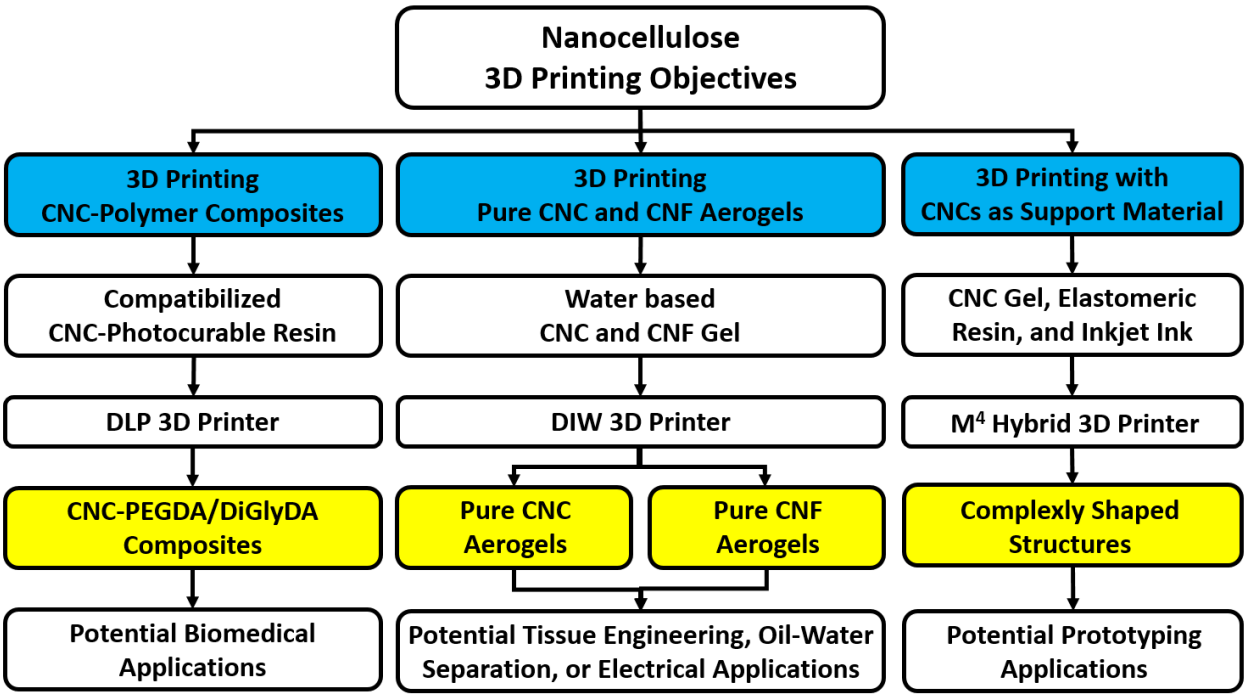

Figure 3.1: The overall scientific objectives of this dissertation are illustrated, and they are also broken down into various targeted areas of research study. The first row represents the three main scientific objectives that were targeted in this dissertation (labeled blue), the second row represents the various inks and gels that were formulated and used during the objective's exploration, the third row represents the 3D printing technique used to explore each objective, the fourth row represents the four areas of research study (labeled yellow), and the fifth row represents the potential applications from each research study.

3.2 Objective 1 - 3D Printing CNC-Polymer Composites

3.2.1 Investigate the compatibility between CNCs and polyethylene glycol diacrylate (PEGDA), and then fabricate shape customizable and property-tunable composite structures via DLP 3D printing

Since CNCs are a sustainable and abundant material with high specific Young's modulus and strength, they are ideal for reinforcing polymer matrices. In addition, polyethylene glycol (PEG)-based materials have also been approved by the FDA for clinical or biomedical applications. As a result, it is possible to fabricate high strength, structurally complex, and property-tunable cellulose-based 3D composites by combining CNCs, polyethylene glycol

diacrylate (PEGDA), and DLP 3D printing together. The main aim here is to verify the viability of using DLP to process different CNC composite structures, and then provide the relevant composite properties that are of importance to potential biomedical applications.

Nevertheless, it is difficult to evenly disperse CNCs within the polymer matrix, which usually results in the loss of mechanical improvement as stress cannot be efficiently transferred to the CNCs.[39, 127] Preforming CNC surface functionalization or grafting surfactants/polymers to and from CNCs' surface are typical strategies that have been employed by others to overcome this issue.[128-131] However, these strategies usually involve a complex reaction scheme, followed by generation of excess waste solvent during CNC purification.[127, 132-133] Instead, it is proposed to target the chemistry of the polymer matrix in order to improve compatibility. Since complex functionalization reactions and excess solvent for purification are not required, larger scale CNC-polymer processing is potentially made more feasible.

To improve CNCs' compatibility with the PEGDA polymer matrix, 1,3-diglycerolate diacrylate (DiGlyDA) can be blended with PEGDA to form a co-polymer matrix. The dispersibility of CNCs can be characterized by the Halpin-Tsai model and polarized light microscopy. Mechanical properties of DLP 3D printed CNC composites can be tested with the Dynamic Mechanical Analyzer (DMA). Furthermore, curing layer thickness during DLP 3D printing can also be potentially used to further tune the composites' mechanical and water swelling properties. The versatility of controlling composite's properties and structure using CNCs and DLP 3D printing can be potentially exploited to further advance biomedical related applications.

3.3 Objective 2 - 3D Printing Pure CNC and CNF Aerogels

3.3.1 Investigate the rheological properties of CNC gel, and then use DIW and freeze-drying to fabricate purely CNC-based aerogel structures with controlled shape, resolution, porosity, and inner pore architecture

Disease, trauma, and injury can sometimes lead to irreversible tissue damage, and cell regeneration is not possible without inserting a support scaffold into the traumatized area.[134] As a result, there is a need to fabricate biodegradable scaffold with controlled structural shape, porosity, and inner architectural features.[13, 135-137] DIW 3D printing provided a potential means to efficiently print water-based gel with high CNC concentration, while also providing control over structural complexity, resolution, porosity, and inner structural architecture. With structurally controllable and property-tunable CNC aerogel structures, they can have potential applications in biological tissue scaffold engineering. This study can lead to advancement in the field of regenerative medicine, and provide new therapeutic strategies for treating traumatized regions in the human body.

However, one limitation in traditional nanocellulose structural fabrication methods is the inability to flexibly fabricate 3D structures with different complicated shapes. In this regard, DIW 3D printing could provide a unique solution towards fabricating easily customizable CNC structures. In this case, the formulation of the CNC gel and the DIW processing parameters must be carefully controlled to not only achieve a printable mixture, but also produce a product with the desired structure, quality, porosity, and inner architectural features. During post processing, another common challenge is efficiently removing water from the 3D printed structure. Traditional evaporative techniques usually lead to structural shrinkage or damage, which has been attributed to capillary action during liquid water evaporation.

Overall, the viscosity of various CNC-water gel mixtures can be adjusted to achieve a DIW printable gel that yields 3D structures with controllable shape and resolution. The rheology of the gel can be studied through cone and plate viscometers. After DIW 3D printing, the gel structures can be subjected to freeze-drying in order to remove the water fraction from the formulation. In this case, capillary action from liquid water evaporation is avoided because the water is first frozen and then sublimated instead. As a result, it is expected that purely CNC-based aerogel structures that closely resembled their original computer aided designs (CAD) can be obtained. The print quality of DIW 3D printed CNC gel structures can be controlled by CNC concentrations and DIW printing parameters. 3D printing dual pore aerogel scaffold structures can also be attempted, where the customizable 3D structure and the inner architectural feature can potentially enable advance CNC scaffold designs suited for specific cell integration requirements.

3.3.2 Preform surface modification chemistry on CNFs with 2,2,6,6-Tetramethyl-1-piperidinyloxy (TEMPO) chemistry, and utilize DIW and freeze-drying to fabricate purely CNF-based aerogel structures with highly deformable, shape recoverable, and functionalizable properties

There is a high incentive to understand 3D printing parameters and ink formulation requirements for fabricating biocompatible 3D scaffold structures for biomedical implant, tissue scaffolding, or other applications. In most biomedical related applications, the structure should be soft and flexible so that the implant can easily deform depending on the patient's motor movement. While CNC aerogels are brittle and are not easily deformable without structural damage, CNFs' long and soft nanoscale properties should allow for the formation of deformable networks. After

DIW 3D printing and freeze-drying, the resultant CNF aerogels can also serve as templates for biological cell integration or facile addition of other functionality.

In terms of challenges, the two main ones are formulating a CNF-based gel that can be reproducibly processed by DIW 3D printing, and maintaining the 3D printed aerogel structures under a water environment. While it is desirable to process CNFs with DIW 3D printing, the non-uniformity of network entanglements within the CNF gel made them difficult to be processed by the DIW. Due to erratic deposition, the resultant DIW processed CNF gel structures usually have poor shape control. To enhance the homogeneity and printability of CNF-based gel, increasing the uniformity and dispersibility of CNFs in the gel should be beneficial for DIW printing. Another challenge in fabricating CNF-based aerogels is that they usually cannot retain their 3D structure after re-immersion into water. In this case, a cross-linking agent can be added to the gel formulation, so that aerogel cross-linking is possible.

To overcome these challenges, 2,2,6,6-Tetramethyl-1-piperidinyloxy (TEMPO) modification and high pressure homogenization can be performed to create a homogenized and TEMPO oxidized cellulose nanofiber (T-CNFs) gel that can be reproducibly processed by DIW 3D printing. A well-known cellulose cross-linking additive, known as polyamide-epichlorohydrin (Kymene), can also be added to the gel formulation so that aerogel cross-linking can occur. Once cross-linking is done, it may be possible to maintain the aerogel's structural integrity even under water and applied force. Additional functionalities can also be templated to the aerogel to impart secondary functionalities. As a result, it is possible that a highly deformable, reversibly compressible, shape recoverable, and functionality tunable CNF-based aerogel 3D structure can be obtained, which can greatly extend their potential use in many different types of applications.

3.4 Objective 3 - 3D Printing with CNCs as Support Material

3.4.1 Explore the concept of using CNC gel as a sustainable and potentially recyclable support material to fabricate complexly shaped structures using an integrated multi-materials-multi-methods hybrid 3D printer

With increasing needs and demands for more complex and intricate structures, it can be beneficial to combine different 3D printing techniques into a hybrid 3D printing platform. During hybrid 3D printing, multiple different materials can be concurrently processed by multiple different 3D print techniques into a single structure that is made of heterogeneous materials. In fact, it is also possible to control which part of the structure is made of which material, so different property or functionality can be targeted to different localized regions of the 3D structure. As a result, it greatly expands the level of complexity and potential functionality that a single 3D printed part can achieve. With this in mind, it is of interest to study if nanocellulosic materials can be utilized during hybrid 3D printing. Ultimately, the various potential impacts of nanocellulose within the field of hybrid 3D printing still remain to be discovered and investigated.

In terms of 3D printing complexly shaped objects, a sacrificial support material is usually a critical component during fabrication. However, traditional support materials are un-sustainable and non-recyclable because they are typically polymerized or solidified along with the target structure. During post processing, this not only makes it very difficult to efficiently remove the support material, but also generates a considerable amount of waste materials. To make 3D printing more green and sustainable, it is possible to replace traditional support material with CNC-based gel. This potentially also allows the CNC support material to be effectively removed with water during post processing. In regards to hybrid 3D printing, another challenge is to compatibilize the CNC support material with different 3D printing techniques like DIW and inkjet

printing. The interfacial resolution between surfaces of CNCs and other 3D printing materials is of great importance, as this dictates the level of resolution and complexity that can be obtained in the final 3D structure. The interfacial interaction between CNCs and other 3D printing materials is another critical aspect to consider, as it is important to showcase if water can actually remove all of the CNC supporting material even in highly confined spaces of 3D printed structures.

An in-house developed multi-materials-multi-methods hybrid 3D printer can be used to print different complexly shaped structures while using CNC gel as the support material. A custom made elastomeric resin and a commercially obtained inkjet ink can also be used to print different structures during the hybrid 3D printing process. The main concept here is CNC gel can be printed by DIW into supporting structures, while the elastomeric resin or inkjet ink can be respectively printed into the target structures by either DIW or inkjet 3D printing. While both the elastomeric resin and the inkjet ink are curable with UV irradiation, the water-based CNC gel is not. As a result, water can be used to quickly and efficiently remove the CNC support materials from the target structures after hybrid 3D processing. If needed, the resultant CNC suspension after water washing can potentially be re-processed back into a DIW printable gel. Furthermore, FTIR and FE-SEM analysis can be performed to assess the interfacial resolution and interfacial interaction between the CNC support and the other 3D printing materials. Overall, the feasibility of using CNCs as a sustainable support material to fabricate different complexly shaped structures during hybrid 3D printing will be verified.

CHAPTER IV: 3D PRINTED CELLULOSE NANOCRYSTAL COMPOSITIES THROUGH DIGITAL LIGHT PROCESSING

4.1 Introduction[1]

3D printing is a growing technology that is revolutionizing the field of manufacturing, and is already making an impact in industrial sectors such as aerospace, automotive, architecture, electronics, food production, and tissue engineering.[9, 94, 138-146] 3D printing also allows accurate fabrication of complicated structures based on digital designs,[14, 17-18] where complex tools or equipment are not needed.[19, 145] As 3D printing technologies are steadily gaining popularity in both personal and industrial use, the 3D printing industry is currently valued at approximately 6 billion dollars. The projected growth of the 3D printing industry within the next decade is predicted to be over 9 billion dollars, where at least 2 billion will be invested in biomedical applications.[25, 140, 147-148] As a result, there is a high incentive to fabricate customizable 3D structures for biomedical applications, such as replaceable organs and tissue scaffolding. Among all 3D printing materials, polymers are the most commonly used and claim the largest portion of the 3D printing material market.[25] Even though polymeric structures have reliable and robust mechanical integrity, they are typically reinforced by fillers such as carbon or glass fibers. However, these fillers are unsustainable and non-renewable. Instead, composites made with cellulosic material, such as cellulose nanocrystals (CNCs), can be of significant interest due to their renewability, strong mechanical properties, high crystallinity, low toxicity, and biocompatibility.[4, 40, 46, 144, 149]

[1] This chapter is modified from a submitted publication: **Li, V.**, Kuang, X., Mulyadi, A., Hamel, M. C., Deng, Y., Qi, H. J. (2018). 3D Printed Cellulose Nanocrystal Composites through Digital Light Processing. S*ubmitted to Cellulose.*

CNCs are highly crystalline cellulose nanoparticles with enhanced mechanical properties, which make them ideal for reinforcing traditional polymers.[1, 37, 46, 52, 127] However, CNCs are highly hydrophilic due to their large specific surface area of more than 300 m^2/g, where a large amount of hydroxyl groups reside on the surface and strong hydrogen bonding can form easily.[150] This leads to CNC agglomeration, and causes the loss of mechanical improvement.[136, 151-153] Therefore, CNC surface functionalization or surfactant/polymer grafting strategies are usually used. However, these strategies in general require complex reaction schemes. Also, grafting of hydrophobic chemicals is usually done in organic solvents, which generates excess waste solvent.[127, 132] Furthermore, traditional composite processing techniques usually have no overall shape control.[97, 128, 133, 154-156] This has especially limited composites' applicability within the biomedical fields due to the inability to fabricate complex shapes. With 3D printing revolutionizing current manufacturing processes, it is now possible to easily fabricate complex parts directly from computer aided designs (CAD). As a result, 3D printing techniques could provide a unique solution towards the fabrication of shape customizable composites.

Digital light processing (DLP) is a highly versatile 3D printing technique that is capable of printing objects at high resolution at a high speed. The process involves curing a photo-curable resin, where the shape of each layer in the 3D object can be controlled based on the image projected by a light source.[157] Since DLP method prints a layer at a time, it has much higher efficiency than other commonly used 3D printing approaches, such as direct-ink-write (DIW) and stereolithography (SLA), which form a layer by writing lines. Polyethylene glycol (PEG)-based photo-curable resins have been widely explored in DLP 3D printing. With FDA's approval on utilizing PEG-based materials for clinical applications, PEG-based composites have also been widely adopted for biomedical applications.[158-161] Furthermore, designing composite matrix with

enhanced mechanical strength and tunable properties is highly desirable for biomedical related applications, as the matrix needs to be able to withstand various loading stresses during delivery or usage.

Based on literature reviews, there are still limited studies on photo-curable cellulose-based 3D composites. Furthermore, recent works are stereolithography-based (SLA). Kumar et al. incorporated CNCs into a SLA resin, and printed pulley or impeller structures with enhanced mechanical properties.[68] Feng et al. incorporated lignin coated CNCs into a photosensitive methacrylate resin, and were also able to fabricate 3D structures through SLA.[67] Palaganas et al. successfully printed CNC 3D composite structures via SLA. CNC compatibilization with the neat PEGDA matrix was achieved through the addition of water, and Young's moduli of the composites were maintained around 28 MPa regardless of CNC concentrations. The complexly shaped composites demonstrated the potential for tissue engineering applications.[69] However, DLP 3D printing of CNC composites has not been reported yet.

In this study, CNCs were introduced to improve PEGDA's physical strength. Instead of preforming CNC surface modification, CNC's compatibility with neat PEGDA was improved by blending PEGDA with glycerol 1,3-diglycerolate diacrylate (DiGlyDA). This provided a more efficient, green, and scalable approach for generating CNC compatible polymer resin, which could enable larger scale use in future industrial applications. Highly complex 3D structures of CNCs, PEGDA, and DiGlyDA were printed via DLP 3D printing. In addition, the mechanical properties of 3D printed CNC composite structures were found to be tunable by varying CNC concentrations and layer curing thickness during DLP, making them suitable for a variety of applications.

4.2 Experimental Section

4.2.1 Materials

Freeze-dried CNCs derived from wood pulp were purchased from University of Maine Process Development Center (Orono, ME, USA), and used as received. Polyethylene glycol diacrylate (PEGDA) with number average molecular weight (Mn) of 700 and glycerol 1,3-diglycerolate diacrylate (DiGlyDA) with Mn of 348 were used as the monomeric components for the photocurable resin. Phenylbis(2,4,6-trimethylbenzoyl)phosphine oxide (Irgacure 819) was used as photo-initiator, and 1-phenylazo-2-napthol (Sudan I) was used as photo-absorber. All chemicals were purchased from Sigma-Aldrich (St. Louis, MO, USA) and used as received.

4.2.2 Ink Formulation and DLP Processing

PEGDA and DiGlyDA in a 1:1 mass ratio were mixed with Irgacure 819 (0.9 wt %) and Sudan I (0.05 wt %). The mixture was placed under magnetic stirring until it was well mixed. After that, freeze-dried CNCs were added to the resin. The mixture was homogenized by a high shear probe homogenizer (T18 basic, Ultra Turrax, IKA Works Inc., Wilmington, NC, USA) at 10,000 rpm, and then sonicated for 2 hours to ensure a homogeneous resin was obtained.

A bottom-up DLP 3D printer was used to fabricate CNC composite structures. In the DLP 3D printer, the resin was placed in a vat with a motorized stage, which can travel in the z-direction in a highly controlled manner (TDC001 DC Servo Motor Controller, ThorLabs Inc., Newton, NJ, USA). Due to the presence of acrylate functional groups, the acrylates can undergo free-radical polymerization given an appropriate light source and photo-initiators. A projector (model D912HD, Vivitek, Fremont, CA, USA) provided the light source for the photo-polymerization. SolidWorks 3D structures were first formatted as STL files, which were fed into the Creation

Workshop software to generate 2D layer make-ups of the 3D structures. Each layer served as a dynamic digital photo-mask, and it controlled the light projection to cure one layer. Then, the motorized stage was displaced by a distance of one layer thickness before the next layer was cured. Eventually, a 3D structure was constructed in a layer-by-layer manner. In this study, the projector intensity was approximately 18 mW/cm^2, and the exposure time of each layer was 4 seconds. Unless specified, the thickness of each cured layer (curing layer thickness) was set at 100 μm.

4.2.3 Transmission Electron Microscopy (TEM) Analysis of CNCs' Dimensionality and Aspect Ratio

A drop of diluted CNCs in water was deposited onto a carbon coated electron microscope grid (CF200-Cu, 200 Mesh, Electron Microscope Sciences, Hatfield, PA, USA) stained with uranyl acetate. TEM analysis was performed with a JEOL JEM-ARM200cF (JEOL, Ltd, Tokyo, Japan) TEM operating at 80 kV (Figure 4.1A). ImageJ software was used to measure the dimensions of CNCs, and the results are reported. The average length and diameter of the CNCs were estimated by ImageJ analysis software (particle count of 70) to be respectively 216 ± 40 nm and 9 ± 2 nm, which led to an average aspect ratio of 24 ± 2 (Figure 4.1B and 4.1C).

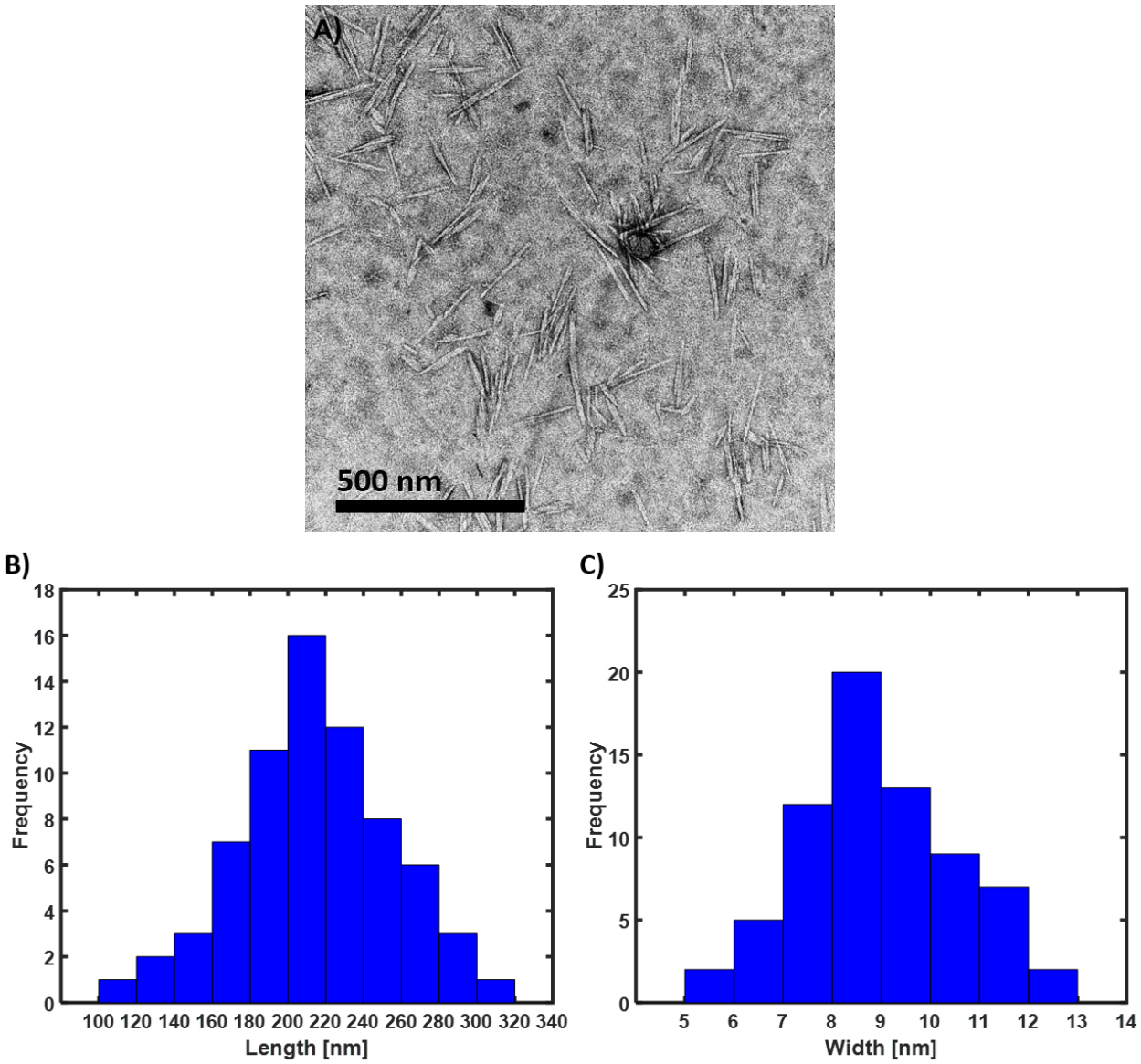

Figure 4.1: (A) TEM image of CNCs from mechanically refined wood pulp as obtained from the University of Maine. (B) From ImageJ analysis and a total particle count of 70, the CNCs' length distribution is plotted as a histogram with a bin size of 20 nm. (C) The corresponding CNCs' width distribution is also plotted as a histogram with a bin size of 1 nm.

4.2.4 Transparency and UV-Vis Transmittance Characterization of DLP Printed Composite Thin Films Made with Different CNC Concentrations

CNC composites were printed with DLP into thin films with a total thickness of 300 µm. The curing layer thickness was 100 µm. Then, UV-Vis transmittance analysis of the corresponding composite thin films was performed using a UV-Vis Spectrophotometer (8453 UV-VIS, Agilent,

CA, USA). The analysis was done under transmission mode, where the tested wavelength ranged from 200 to 800 nm.

4.2.5 Tensile Mechanical Properties of CNC Composites

Young's modulus, strain at break, and ultimate strength of CNC composites were obtained by using a dynamic mechanical analyzer (DMA) (Q800, TA Instruments, New Castle, DE, USA) under the uniaxial tensile mode. Polymer resins incorporated with different CNC concentrations were printed with DLP into dogbone-shaped structures (length, width, and thickness of approximately 30 by 5 by 0.3 mm, respectively). Four samples were tested for each formulation, and averages with standard deviations were reported. While maintaining the CNC concentration at 1 wt %, the dogbone-shaped structures were also printed with different curing layer thickness between 25 μm and 300 μm. Their tensile mechanical properties were obtained, and averages with standard deviations from four samples were similarly reported. All samples were tested at room temperature (~22 °C) under the controlled force mode of 1 MPa/min. The glassy storage modulus, rubbery storage modulus, and loss modulus of the CNC composites were also obtained through dynamic mechanical testing mode in the DMA, where the strain was oscillated at a frequency of 1 Hz with a peak amplitude of 0.1 %. The samples were first equilibrated at -20 °C for 10 mins, and then tested with a heating rate of 3 °C/min from -20 °C to 100 °C. From the ratio between the storage and loss modulus, the tan δ was determined. The temperature corresponding to the peak of the tan δ curve was set as the glass transition temperature (T_g).

4.2.6 The Halpin-Tsai Fitting Model

The Halpin-Tsai model is a micromechanical predictive model for reinforced composite incorporated with high aspect ratio fillers.[162] It assumes a homogeneous dispersion of reinforcing fillers within the polymer matrix, perfect interface between matrix and fillers, and no filler-filler interactions. It can be used to predict the filler's Young's modulus within the polymer matrix.[4, 35, 130] The Halpin Tsai model can be written as follows,

$$\frac{E_c}{E_m} = \frac{1+ \zeta\eta\varphi_f}{1-\eta\varphi_f} \tag{4.1}$$

$$\text{with } \eta = \frac{(\frac{E_f}{E_m}-1)}{(\frac{E_f}{E_m}+\zeta)} \tag{4.2}$$

$$\text{and } \zeta = (0.5s)^{1.8} \tag{4.3}$$

where E_c, E_f, and E_m are Young's moduli for the composite, the filler, and the polymer matrix, respectively, φ_f is the filler volume loading fraction, ζ is the shape factor, and s is the aspect ratio of the reinforcing fillers. From the measured Young's moduli of various composites incorporated with different CNC concentrations, the E_f value can be fitted to minimize the absolute residual error between the experimental values and the Halpin-Tsai model fitting values.

4.2.7 Polarized Light Microscopy

The dispersibility of the CNCs in the polymer matrix was analyzed by polarized light with an optical microscope (BX51, Olympus, Waltham, MA, USA) equipped with two cross polarizers. For this study, CNC incorporated polymer resins were printed by DLP into thin films with a thickness of 300 μm. All images were taken with a fixed exposure time of 100 ms, and the observed brightness intensity qualitatively corresponded to the relative distribution of CNCs within the polymer matrix.[130-131, 163-165] All samples were taken under transmission mode at full extinction.

4.2.8 Thermal Gravimetric Analysis

The percent weight loss as a function of temperature and the corresponding first derivative curve were determined by a thermal gravimetric analyzer (TGA STA 6000, PerkinElmer, MA, USA). The DLP processed composites' thermal degradation onset temperature (T_{onset}) and temperature at maximum rate of thermal degradation ($T_{max\ degradation}$) were measured and analyzed by the software of the tester. A sample weight of about 20 mg was equilibrated at 30 °C and then heated to 600 °C at a rate of 20 °C per min under N_2 atmosphere. Two samples were tested for each formulation, and averages and standard deviations for T_{onset} and $T_{max\ degradation}$ were reported.

4.2.9 Attenuated Total Reflectance-Fourier Transform Infrared Spectroscopy (ATR-FTIR)

FTIR spectra for 1 wt % CNC composite thin films with different curing layer thickness were obtained by ATR-FTIR (Nicolet iS50, ThermoFisher Scientific, Waltham, MA, USA) spectrometer under ambient conditions from averages of 32 scans with a scan resolution of 1 cm^{-1} in the range of 600 cm^{-1} to 4000 cm^{-1}. The FTIR instrument was equipped with an ATR accessory that is capable of analyzing both liquid and solid specimens. Spectra from the un-polymerized resin were analyzed by placing a droplet of the liquid resin onto the sampling lens. To better illustrate the disappearance of the C=C double bond peak, a wavenumber range between 1500 cm^{-1} and 1900 cm^{-1} is also presented. The C=O vibrational peak at 1725 cm^{-1} was used for spectra normalization, and then the conversion of the C=C double bond was tracked by the peak around 1625 cm^{-1}. After the front side (the side facing the DLP's projector) of the thin film was characterized, the thin film was flipped over to the back side before FTIR measurements were performed again.

4.2.10 Swelling Behavior of CNC Composites

Before water immersion, the mass of DLP 3D printed thin films was measured by a gravimetric balance. After immersing in water for a specified time, the samples were removed from water and then blotted to remove excess water remaining on surfaces. The mass of the swelled samples was then measured again in order to determine the swelling ratio. The evolution of these swelling ratios was recorded as a function of time for composites with different CNC concentrations. After one day of water immersion, the mass of the water infused CNC composites was again recorded based on different CNC concentrations and curing layer thicknesses. Five samples were tested for each CNC concentration and curing layer thickness, and averages with standard deviations were reported.

4.2.11 Dye Diffusion Kinetics of CNC Composites

The dye release-diffusion kinetics of the CNC composites were also determined through UV-Vis spectrophotometer analysis. DLP 3D printed CNC composite thin films with a fixed size (length, width, and thickness of approximately 8 by 8 by 0.3 mm, respectively) were first immersed in a 0.25 wt % toluidine blue O dye in water solution for one day, then removed from solution and rinsed with water to eliminate residue dye on their surfaces. The initial content of toluidine blue O loaded into the composite was determined from gravimetric measurements, as well as, the known toluidine blue O concentration used during the dye infiltration. Then, the dye infiltrated composite was place in a standard UV-Vis cuvette with 4 mL of DI-water (water to composite mass ratio of approximately 180), and the diffusion experiment was conducted at room temperature of about 22 °C with pH of around 7. By tracking the toluidine blue O dye dominant absorbance peak, the dye release-diffusion behaviors from the composites were studied as a function of time.

4.3 Results and Discussion

To understand the reinforcing capability of CNCs in PEGDA-based polymer matrices, dogbone-shaped structures of 1 wt % CNC in neat PEGDA were printed by DLP 3D printing. However, the resultant mechanical properties showed decrease in Young's modulus, strain at break, and ultimate strength (Figure 4.2).

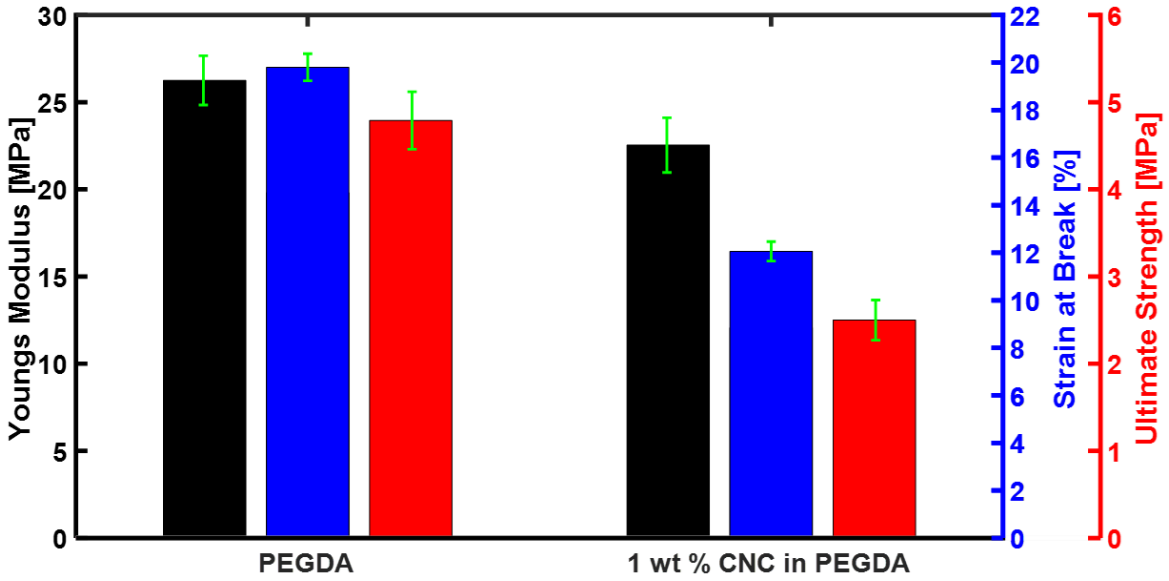

Figure 4.2: Comparison of mechanical properties between the neat PEGDA and the corresponding 1 wt % CNC in neat PEGDA. Dogbone-shaped structures with a dimension of about 30 by 5 by 0.3 mm were printed with DLP. The curing layer thickness was set at 100 µm. Three samples were tested to provide averages and standard deviations. Black bar: Young's modulus; Blue bar: Strain at break, and red bar: Ultimate strength.

The decrease in mechanical properties was attributed to poor CNC dispersibility and compatibility with neat PEGDA. PEGDA and DiGlyDA have very similar chemical structures except the latter contains hydroxyl groups in its macromolecular backbone (Figure 4.3).

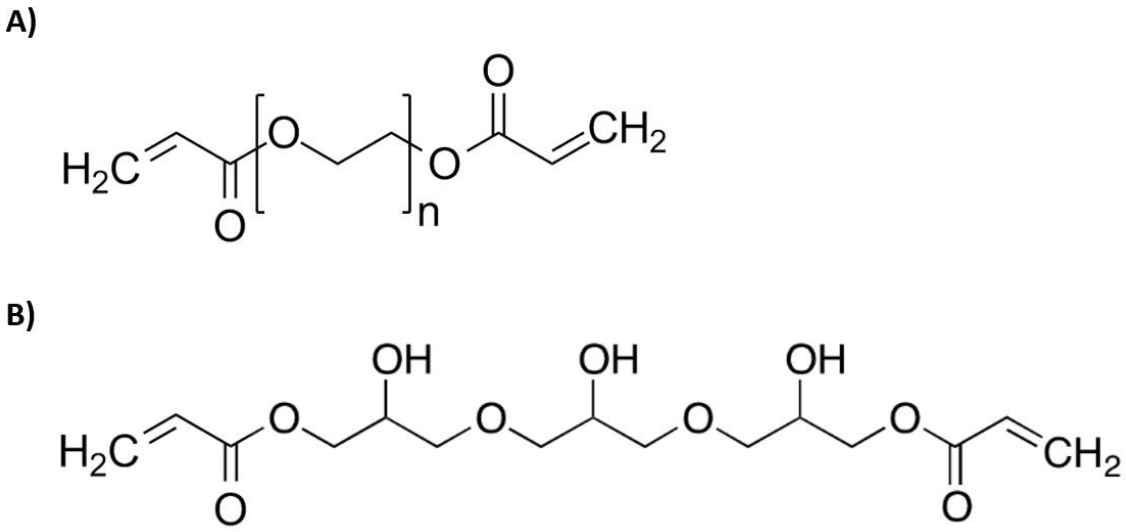

Figure 4.3: Chemical molecular structure of (A) PEGDA and (B) DiGlyDA.

Therefore, introducing DiGlyDA as a secondary polymer to PEGDA for co-polymerization should increase CNC compatibility. A 1:1 PEGDA to DiGlyDA ratio was chosen to provide maximum CNC compatibility while maintaining a low viscosity resin for DLP 3D printing. From the modified matrix resin formulation (1:1 PEGDA to DiGlyDA), different concentrations of CNCs were introduced and printed into composite thin films through DLP. Improvement in CNC dispersibility with the modified resin could be observed based on visual inspection (Figure 4.4A). The 1 wt % CNC in neat PEGDA had a slight hazy white hue despite application of high speed homogenization and sonication. On the other hand, the same CNC concentration in the modified matrix resin displayed a significantly reduced hazy white hue. This suggested that the co-polymerized matrix has successfully increased CNC dispersibility by decreasing self-interactions through competitive hydrogen bonding between CNCs and the modified polymer matrix. To demonstrate the hazy white hue was originating from CNCs, a 5 wt % CNC in 1:1 PEGDA to DiGlyDA thin film was also illustrated. As the concentration of CNCs increased, it was apparent that the hazy white hue increased. The composite thin films were also evaluated by UV-Vis Spectrophotometer under the transmittance mode (Figure 4.4B).

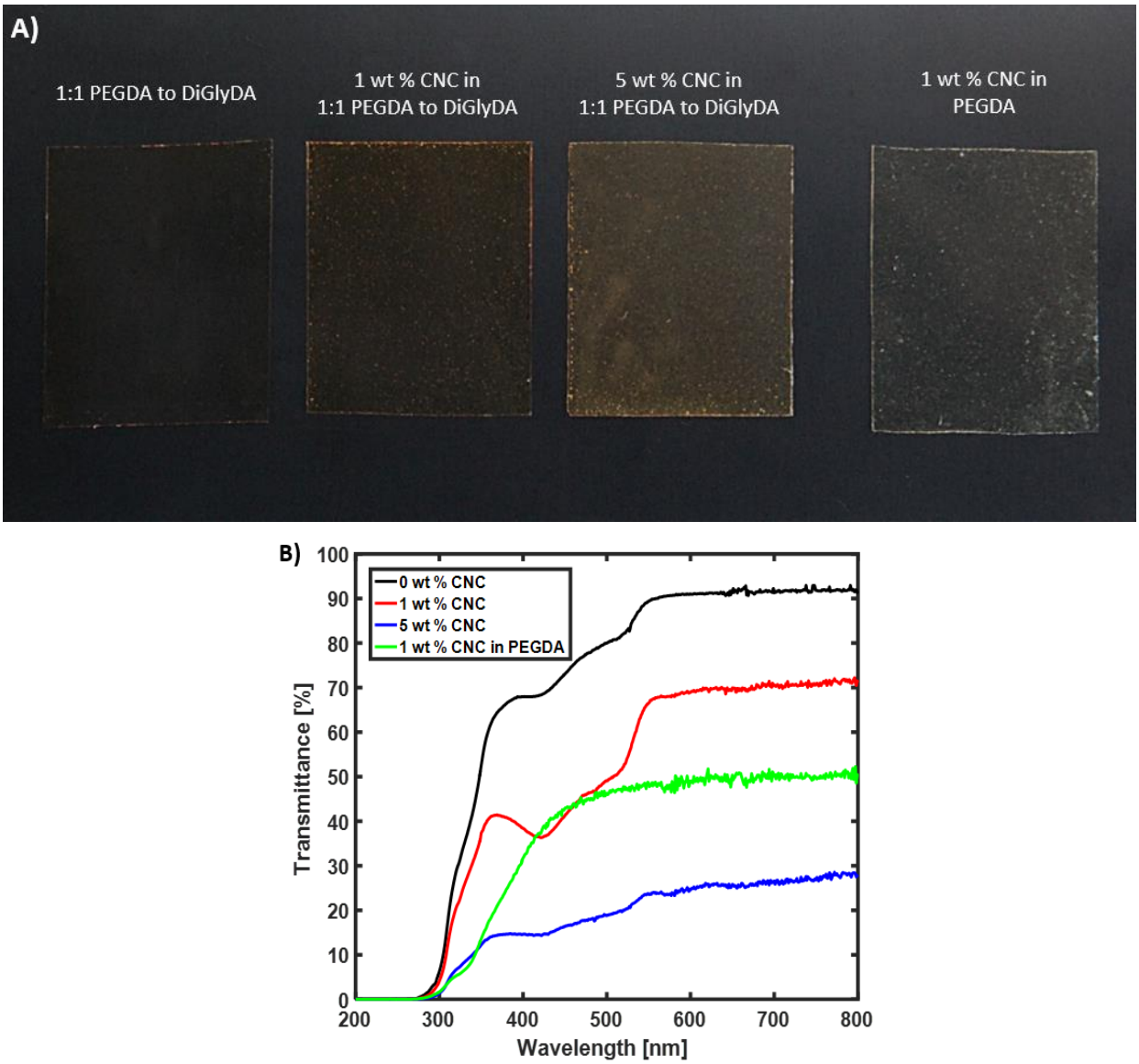

Figure 4.4: (A) Photographic images of thin film printed from 1:1 PEGDA to DiGlyDA, 1 wt % CNC in 1:1 PEGDA to DiGlyDA, 5 wt % CNC in 1:1 PEGDA to DiGlyDA, and 1 wt % CNC in neat PEGDA (Left to Right). All thin films had a total thickness of 300 µm. (B) UV-Vis transmittance spectra of the corresponding composite thin films made from 1:1 PEGDA to DiGlyDA (black), 1 wt % CNC in 1:1 PEGDA to DiGlyDA (red), 5 wt % CNC in 1:1 PEGDA to DiGlyDA (blue), and 1 wt % CNC in neat PEGDA (green).

The thin film printed from the modified matrix resin had a maximum UV-Vis transmittance of nearly 92 %. When 1 wt % CNC was incorporated into the modified matrix resin, a maximum UV-Vis transmittance of nearly 70 % was observed. On the other hand, 1 wt % CNC in neat PEGDA had a maximum UV-Vis transmittance of only 50 %. Due to the decrease in transmittance,

CNC agglomeration in neat PEGDA was more severe than in the modified matrix resin. Overall, both qualitative visual inspection and UV-Vis transmittance analysis supported that competitive hydrogen bonding can reduce CNC-CNC interaction, which can improve CNC dispersibility within the matrix.

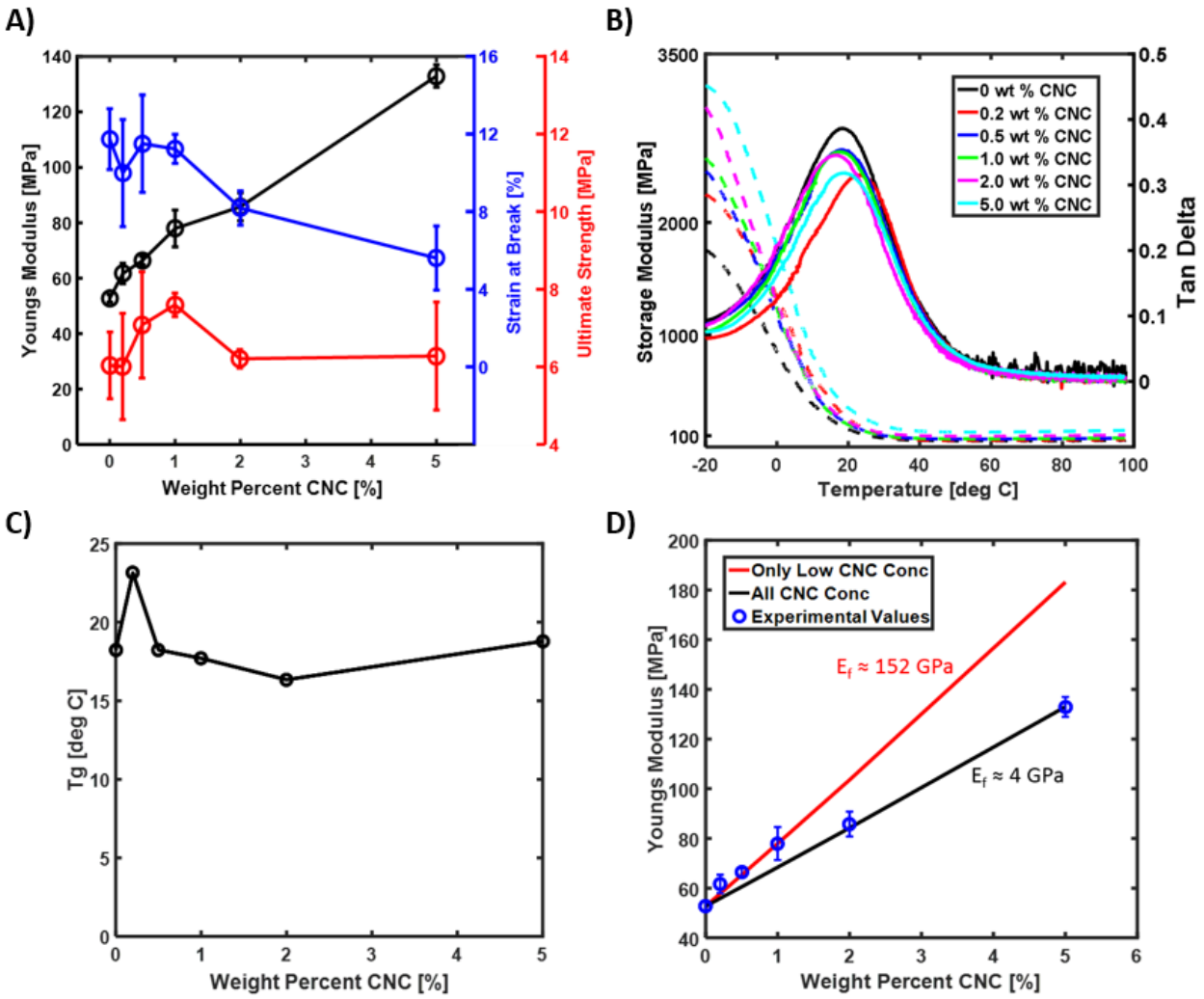

Figure 4.5: (A) DMA tensile mechanical properties of DLP printed dogbone-shaped composites with different CNC concentrations in the modified matrix ink. Black: Young's modulus; Blue: Strain at break, and Red: Ultimate strength. (B) Storage modulus (dashed lines) and tan delta (solid lines) for different CNC concentrations in the modified matrix ink as a function of temperature. (C) Resultant T_g of the composites as a function of incorporated CNC concentration. (D) Halpin-Tsai model fitting on obtained experimental tensile Young's moduli. Fitting was done for composites with all concentration of CNCs (black) and only low concentration of CNCs (red), and the fitted CNCs' Young's moduli that minimized the sum of the absolute residual errors are also shown.

To evaluate the potential mechanical enhancement from CNCs, tensile tests were performed on dogbone-shaped composites printed with different CNC concentrations (Figure 4.5A). The results show a continuous increase in average Young's modulus as the concentration of CNCs increased. The average strain at break was also maintained nearly constant around 10 % until the CNC concentration increased above 1 wt %. Meanwhile, the average ultimate strength displayed a peak value of 7.6 ± 0.3 MPa at 1 wt % CNC concentration, and then decreased slightly as CNC concentration increased. Overall, the addition of CNCs did not result in the decrease in ultimate strength when compared to the modified polymer matrix. Considering the significant increase in average modulus from 52.8 ± 1.4 MPa to 133.0 ± 4.0 MPa, without loss of ultimate strength, the addition of CNCs in PEGDA and DiGlyDA led to improved mechanical properties. Representative tensile stress-strain curves from dogbone-shaped composites with different CNC concentrations are also illustrated (Figure 4.6A).

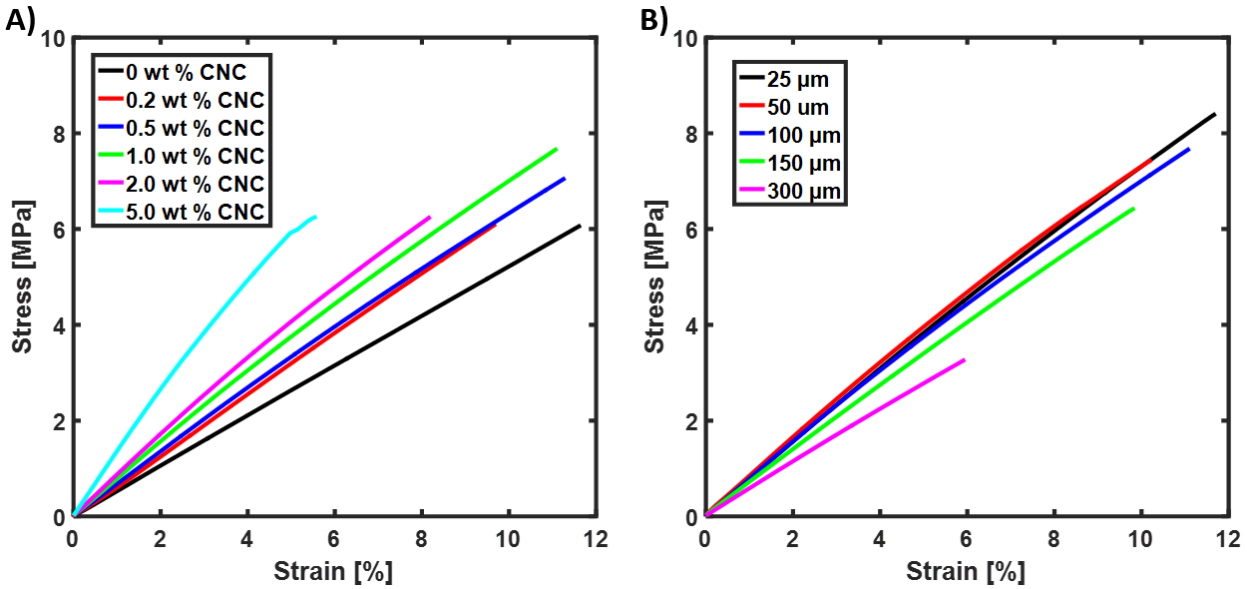

Figure 4.6: (A) Representative tensile stress-strain curves for DLP printed dogbone-shaped composites with different CNC concentrations in the modified matrix ink. Curing layer thickness for all samples was set at 100 µm. (B) Representative tensile stress-strain curves for DLP printed dogbone-shaped composites with different curing layer thickness. The concentration of CNCs incorporated in the modified matrix ink for all samples was set at 1 wt %.

Thermal-mechanical properties, such as glassy storage modulus, rubbery storage modulus, and tan delta of the composite, were also evaluated (Figure 4.5B). Storage moduli were plotted on a semi-log plot represented by the left axis, and the tan deltas were represented by the right axis. The glassy and the rubbery storage moduli also increased with increasing CNC concentration, which demonstrated the reinforcing effects of CNCs in composite in both the glassy and rubbery regimes (Figure 4.7).

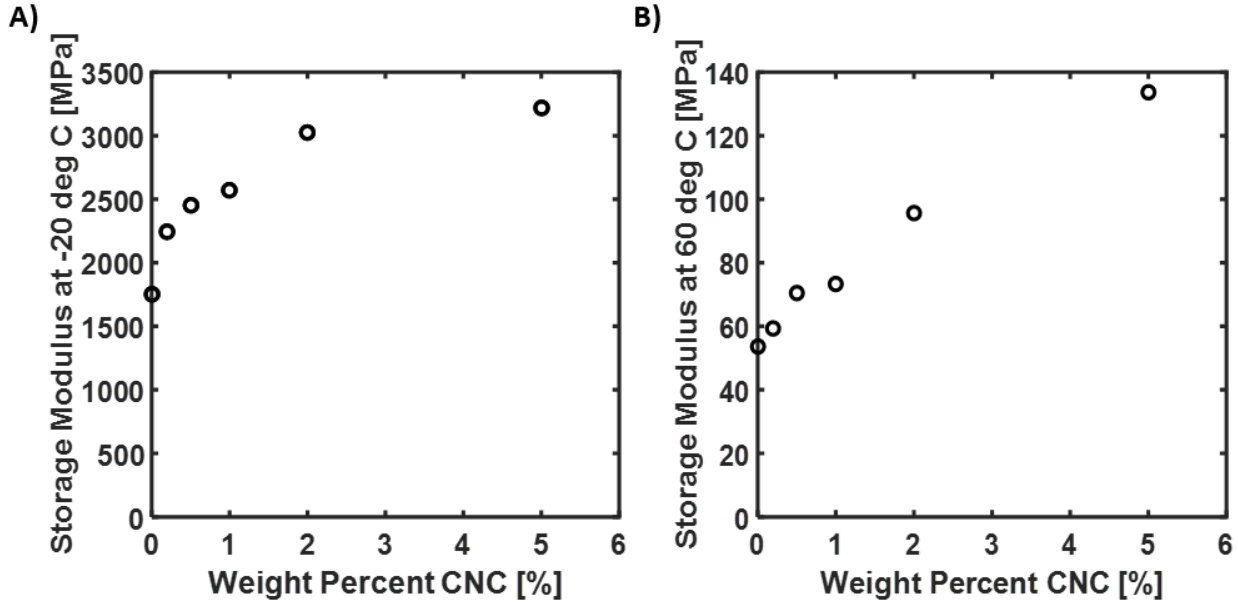

Figure 4.7: (A) Glassy state storage modulus evaluated at -20 °C as a function of CNC concentrations in the modified polymer matrix. (B) Rubbery state storage modulus evaluated at 60 °C as a function of CNC concentrations in the modified polymer matrix.

The resultant glass transition temperature (T_g) of the composites as a function of CNC concentration is illustrated (Figure 4.5C), which indicated that T_g remained relatively constant as the CNC concentration increased. To further evaluate the efficiency of CNC dispersion and mechanical property reinforcement, Young's moduli of the CNC composites were investigated and fitted by the Halpin-Tsai model (Figure 4.5D). When the fitting was conducted to all concentrations, the CNC's Young's modulus was estimated to be 4 GPa, which was much smaller than the established CNC modulus of 110 to 220 GPa in literature.[4] This was likely due to the

imperfect dispersion of CNCs within the 2 and 5 wt % CNC composites. Since the Halpin-Tsai model assumes a perfect dispersion of filler particles with no filler agglomeration, fitting only the low CNC concentration portion (≤ 1 wt %) of the curve resulted in a CNC Young's modulus of 152 GPa, which was within the literature established CNC Young's modulus. This is also consistent with the experimental observation in Figure 4.5A, where the strain at break decreased as the CNC concentration in the composite was in the range of 2 to 5 wt %. Therefore, the Halpin-Tsai fitting model demonstrated that sufficient CNC dispersion in the modified matrix was only achieved when the CNC loading was approximately 1 wt % or less.

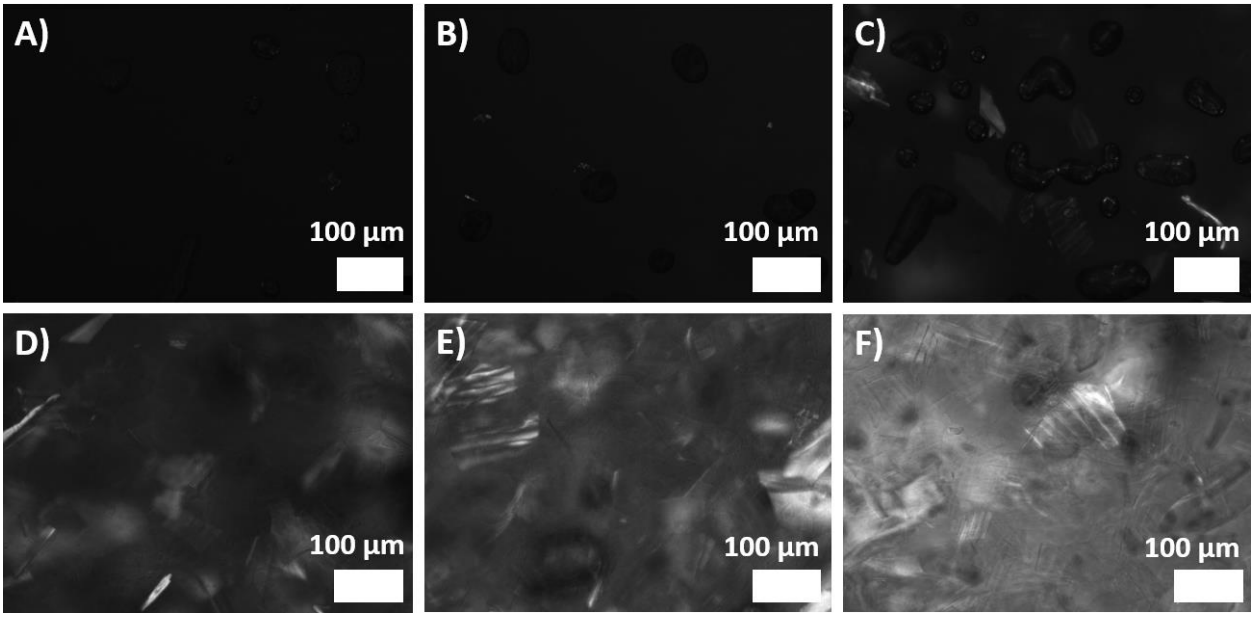

Figure 4.8: Polarized light microscopy images of composites with (A) 0 wt % CNC, (B) 0.2 wt % CNC, (C) 0.5 wt % CNC, (D) 1.0 wt % CNC, (E) 2.0 wt % CNC, and (F) 5.0 wt % CNC in 1:1 PEGDA to DiGlyDA.

To further confirm the relative distribution of CNCs within the modified polymer matrices, polarized light microscopy was performed on composites incorporated with different CNC concentrations. The superposition of the brightness intensity from the 3D thin film was then represented as 2D images (Figure 4.8). For the modified matrix polymer without CNCs, there was no areas of illumination due to all the polarized light being dampened out by the second cross

polarizer. As the CNC content increased, regions with agglomerated CNCs phase shifted the polarized light. As a result, the phase shifted polarized light was not completely dampened out by the second cross polarizer, and it indicated areas where CNCs agglomerated. Below 1 wt % CNC, there were only small regions of nanoscopic CNC aggregation. At 1 wt % CNC, regions of microscopic CNC aggregation began to appear in addition to nanoscopic CNC aggregation. Above 1 wt % CNC, regions with nanoscopic CNC aggregation, as well as, regions with severe microscopic aggregation of CNCs were observed. Overall, these results coincided well with the mechanical testing analysis.

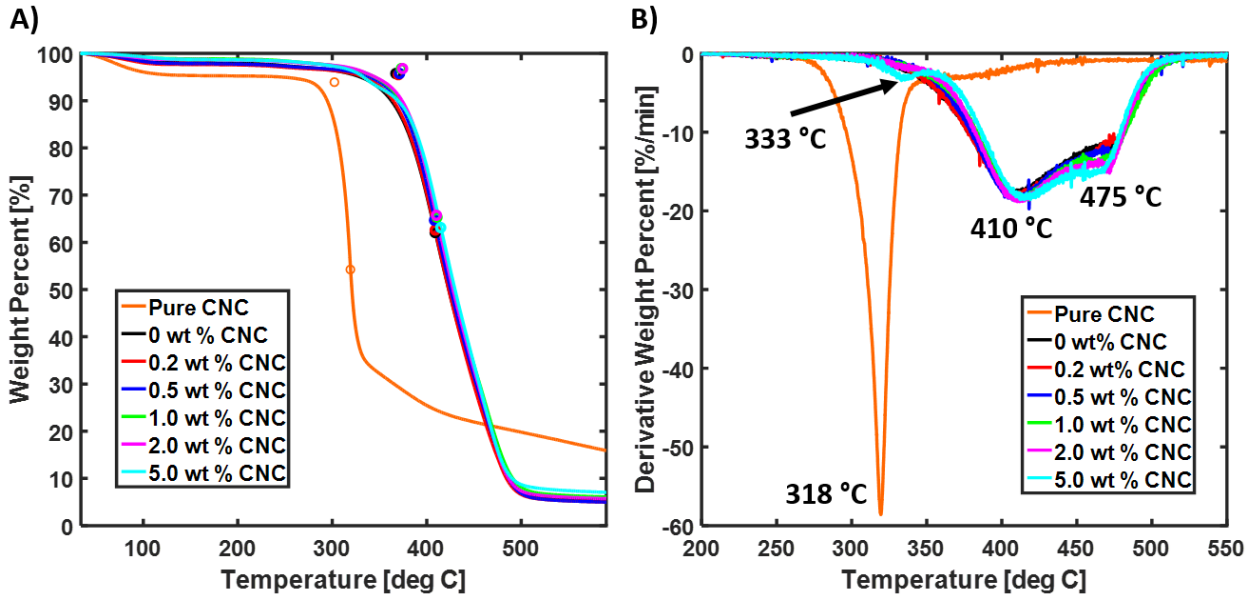

Figure 4.9: (A) Resultant TGA weight percent loss as a function of temperature for pure CNCs, the modified base polymer matrix, and composites from various CNC concentrations in the modified base polymer matrix. (B) Corresponding TGA first derivative curve for pure CNCs, the modified base polymer matrix, and composites from various CNC concentrations in the modified base polymer matrix.

Thermal decomposition behavior and stability of the CNC composites were also evaluated by TGA, and the resultant weight percent loss as a function of temperature curves (Figure 4.9A) and their corresponding first derivative curves (Figure 4.9B) are illustrated. Table 4.1 also shows the T_{onset} and the $T_{max\ degradation}$. From the first derivative curve of pure CNCs, there is a dominant

peak at 318 °C. This has been associated with the thermal decomposition of unsulfated crystals within the interior of CNCs, which includes depolymerization, dehydration, destabilization of glycosyl units, and decomposition of residual cellulosic solids. Overall, the thermal decomposition behavior of pure CNCs used in this study is consistent with previous literature reports.[130, 166-168] From the first derivative curve of the modified base resin, there is also one peak around 410 °C and a secondary peak around 475 °C. From literature reports, the first peak could be associated with the combined decomposition of PEGDA and DiGlyDA through bond dissociations. Meanwhile, the second peak could be attributed to the further degradation of polymer chains through multiple bond dissociation.[69, 169] The thermal decomposition behavior of the modified base resin is also similar to that observed by Palaganas et al.[69] For the 2 and 5 wt % CNC composites, there appeared to be an additional small peak around 333 °C. This is likely due to the aggregation of CNCs, as this peak is relatively close to the dominant peak of pure CNCs. For the CNC composites, both T_{onset} and $T_{max\ degradation}$ slightly increased when compared to the modified base polymer matrix, and the degree of increase appeared to be dependent on the concentration of CNCs incorporated into the matrix. Overall, these results suggested adding CNCs did not adversely affect the thermal stability of the composites, where temperature as high as 370 °C can be reached before degradation began to occur.

Table 4.1: T_{onset} and $T_{max\ degradation}$ values from TGA curves for pure CNCs, the neat modified base polymer matrix, and composites with various CNC concentrations in the modified base polymer matrix.

Sample	T_{onset} (°C)	$T_{max\ degradation}$ (°C)
Pure CNCs	305 ± 4	318 ± 2
0 wt % CNC	367 ± 1	410 ± 1
0.2 wt % CNC	371 ± 2	410 ± 1
0.5 wt % CNC	372 ± 2	410 ± 3
1.0 wt % CNC	374 ± 2	411 ± 1
2.0 wt % CNC	376 ± 2	413 ± 4
5.0 wt % CNC	377 ± 1	414 ± 1

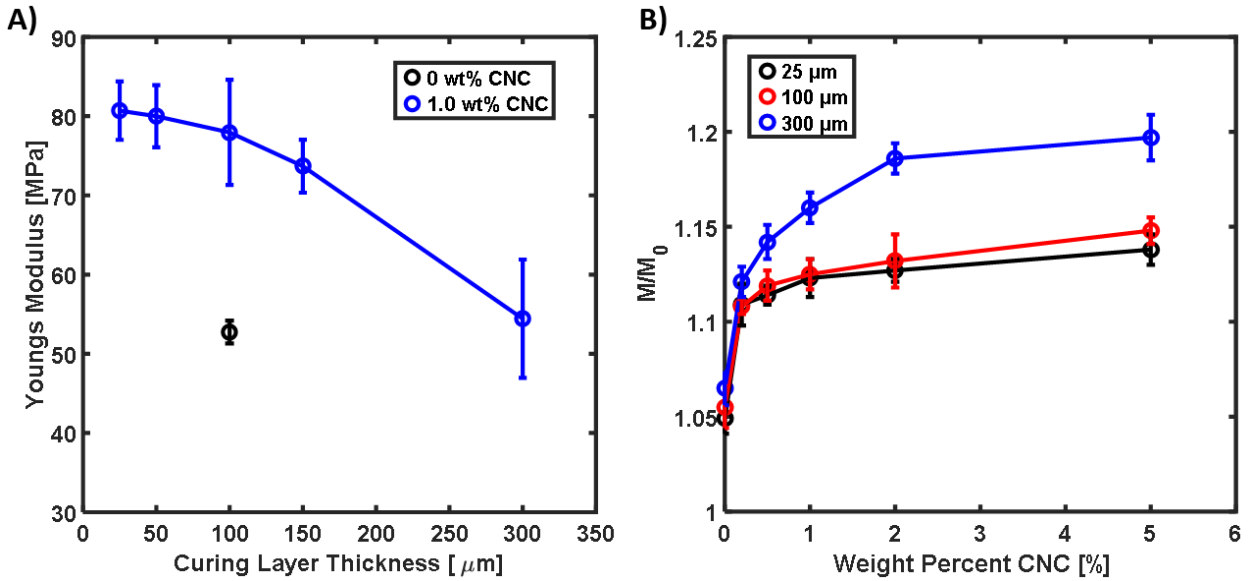

Figure 4.10: (A) The Young's moduli of DLP printed dogbone-shaped composites printed with different curing layer thickness are presented. The blue curve represents the modified polymer matrix reinforced with 1 wt % CNC, and the black data point represents the modified polymer matrix with no CNC reinforcement. The DLP projector's light intensity and layer exposure time were held constant at about 18 mW/cm^2 and 4 seconds, respectively. (B) After immersing in water for one day, the final mass swelling ratio of thin film composites printed with difference CNC concentrations and curing layer thickness are illustrated.

It is also possible to tune the composites' mechanical properties based on processing parameter from the DLP printing. Here, the curing layer thickness during DLP printing was varied between 25 µm and 300 µm, and the resultant Young's moduli from dogbone-shaped composites with 1 wt % CNC incorporation are illustrated (Figure 4.10A).The tensile testing results indicated that the Young modulus can be tuned from 80.7 ± 3.7 MPa to 54.4 ± 7.5 MPa as the curing layer thickness increase from 25 µm to 300 µm. The representative tensile stress-strain curves are also illustrated in Figure 4.6B. The decrease in Young's modulus is likely a result of light attenuation effect along the layer's thickness, which has been described in other literature reports.[170-172] Since light intensity decays exponentially, there can be a decrease in cross-linking density along the layer's z-direction. As a result, the layer's front side can have a higher degree of cure compared to the layer's back side. This is supported by FTIR analysis, where the C=C double bond peak around

1625 cm^{-1} diminished identically for the layer's front side regardless of curing layer thickness. On the other hand, the C=C double bond peak for the layer's back side diminished less and less with increasing curing layer thickness (Figure 4.11).

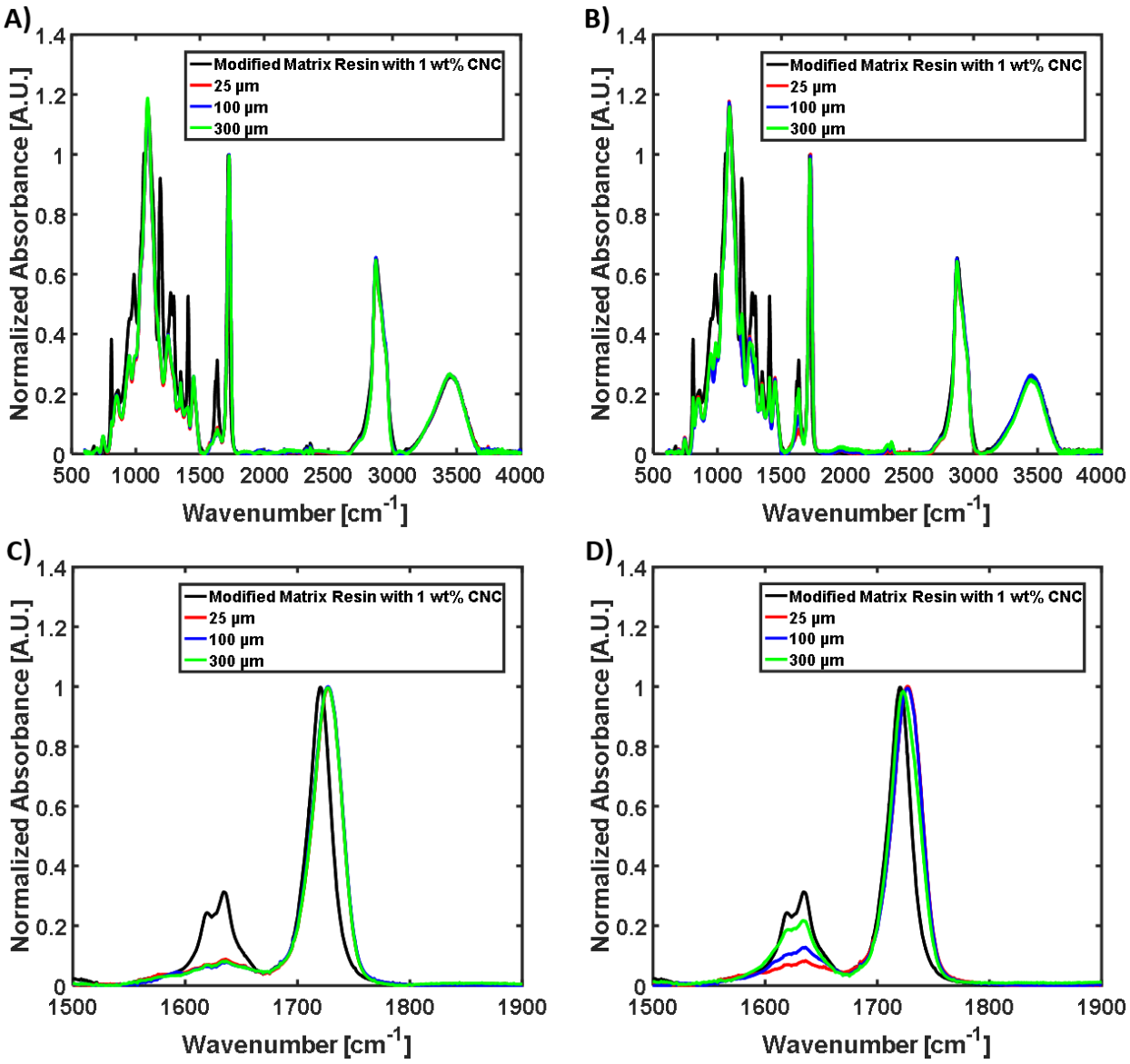

Figure 4.11: (A) The full FTIR spectra for the un-polymerized resin and the front side of the 1 wt % CNC composite thin films printed with different curing layer thicknesses. (B) The full FTIR spectra for the un-polymerized resin and the back side of the 1 wt % CNC composite thin films printed with different curing layer thicknesses. (C) The zoomed-in FTIR spectra for the un-polymerized resin and the front side of the 1 wt % CNC composite thin films printed with different curing layer thicknesses. (D) The zoomed-in FTIR spectra for the un-polymerized resin and the back side of the 1 wt % CNC composite thin films printed with different curing layer thicknesses.

Thus, confirming that light attenuation can result in a gradient of curing degree throughout the layer's thickness. In fact, FTIR analysis suggested that larger curing layer thickness actually led to a larger curing gradient across the layer. This can lead to weaker mechanical properties, as printed parts with larger curing thickness were comprised of weaker individual layers. Nevertheless, the effect of light attenuation did not seem significant when the curing layer thickness was 100 µm or less, which was reflected by the relatively constant average Young's modulus of around 80 MPa. However, the light attenuation effect became increasingly significant when the curing layer thickness increased beyond 100 µm, as the average Young's modulus decreased to 54.4 ± 7.5 MPa when the curing layer thickness was increased to 300 µm. Similar behavior was also observed in the corresponding strain at break and ultimate strength (Figure 4.12).

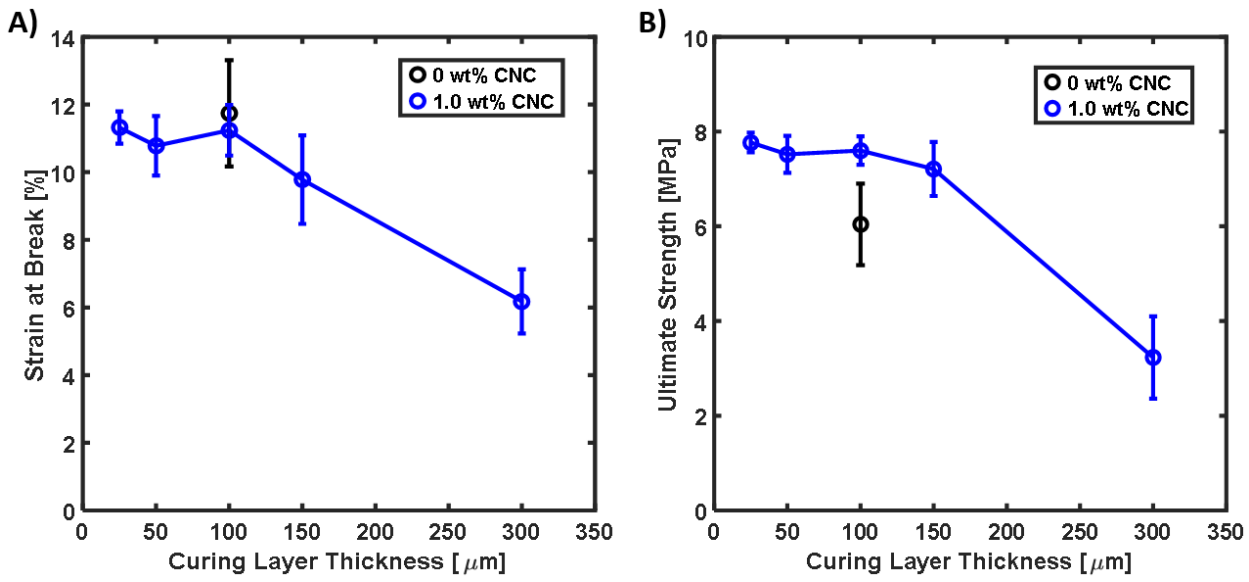

Figure 4.12: (A) The strain at break and (B) ultimate strength of dogbone-shaped composites printed with different curing layer thicknesses during DLP. The blue curve represents polymer matrix reinforced with 1 wt % CNC, and the black data point represents the polymer matrix with no CNC reinforcement. The DLP projector's light intensity and layer exposure time were held constant at about 18 mW/cm^2 and 4 seconds, respectively.

Overall, it was demonstrated that it is also possible to tune the mechanical properties of the composites based on curing layer thickness, which suggested that different DLP processing parameters can further influence the final 3D printed part's properties. Although light attenuation also occurs in neat resin, it is suspected that the light attenuation effects will be even stronger with the addition of higher CNC concentration in the resin. Furthermore, the water swelling behavior of the composites was also found to be tunable based on CNC concentration and curing layer thickness. After immersing the composites in water for one day, the final swelling ratios were recorded based on different incorporated CNC concentrations and curing layer thickness (Figure 4.10B). As CNC concentration in the polymer matrix increased, the mass swelling ratio increased regardless of the curing layer thickness. This was attributed to the highly hydrophilic nature of CNCs, which increased the polymer matrix's affinity for water absorption. As more water is absorbed into the polymer matrix, water absorption onto surfaces and interstitial sites of CNCs is also possible. It is also interesting to note that the increase in mass swelling ratio started to level off as CNC concentration increased above 1 wt %, which could be due to the inability of agglomerated CNCs to further increase the polymer matrix's affinity towards water absorption. When the composites were printed with a curing layer thickness of 25 µm, the final water mass infiltration was tunable from 5 % to 15 % of the initial composite's dry mass when the CNC concentration increased from 0 wt % to 5 wt %. It was also observed that the final water mass infiltration behavior for thin films printed with 100 µm curing layer thickness was similar to that printed with 25 µm. This was likely due to the fact that light attenuation effects were not significant for curing layer thickness of 100 µm or less. On the other hand, the final water mass infiltration of different CNC composite thin films increased from 7 % to 20 % of the initial composite's dry mass when the curing layer thickness was 300 µm. As a result, a lower degree of cure within the layer's

thickness can also enhance water infiltration due to the increase in the polymer matrix's free volume. Overall, these results indicated that both the hydrophilicity of CNCs and the light attenuation effects from curing layer thickness can be utilized to control the final swelling behavior of the composites.

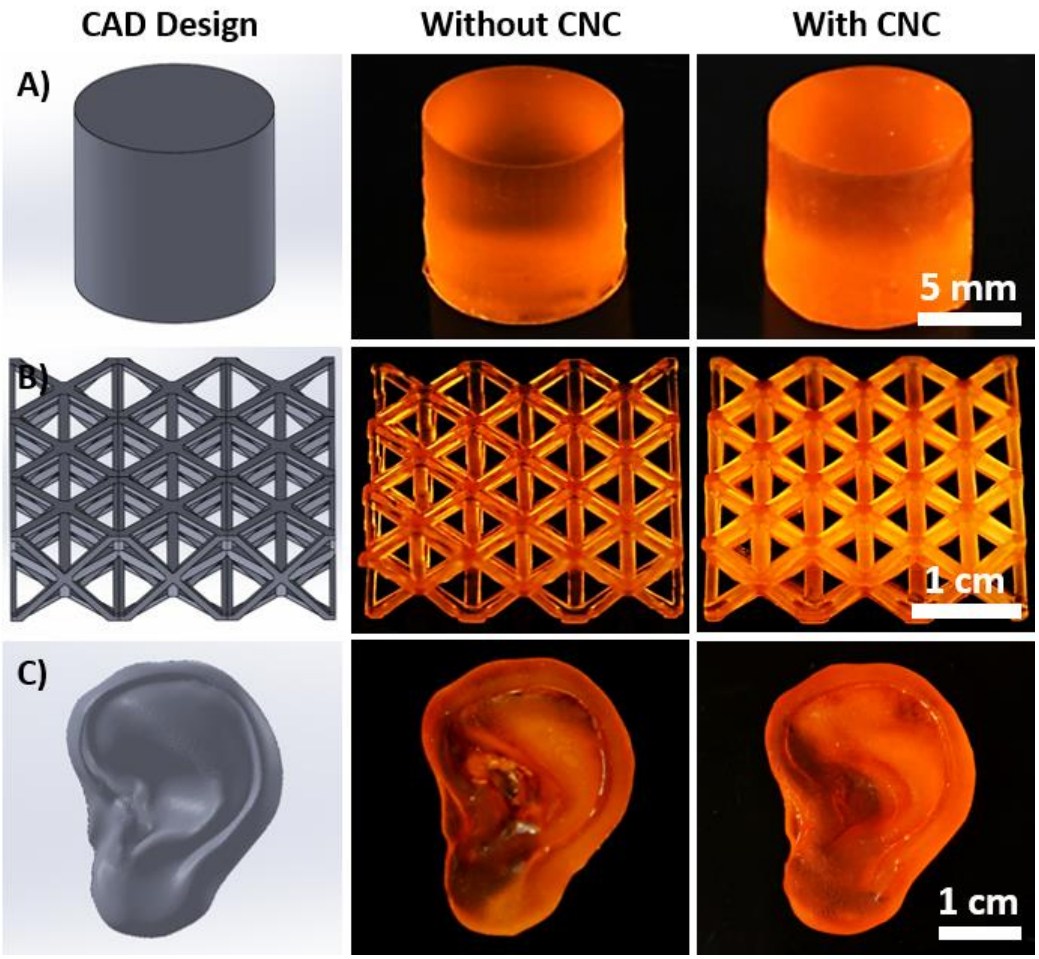

Figure 4.13: (A) A disk structure, (B) an octet-truss lattice structure, and (C) an ear model were printed by the DLP printer into 3D structures. The first column is the SolidWorks designs, second column is DLP 3D printed structures that are printed from the modified matrix resin without any CNC addition, and third column is the corresponding 3D structures that are printed from 1 wt % CNC incorporated into the modified matrix resin. The curing layer thickness was set at 100 µm.

CNC incorporated polymer resin was successfully printed by DLP into a standard disk (Figure 4.13A). A complicated octet-truss lattice structure with complex channels and strut interconnectivity was also printed (Figure 4.13B). To demonstrate the potential to use CNC

incorporated composites in biomedical related applications, an ear model was also printed with DLP (Figure 4.13C). Highly defined features, such as curves, contours, hills, and valleys, were also successfully translated from the ear's CAD design to the final printed structure with great fidelity. The various DLP 3D printed CNC composites are also illustrated from different perspectives (Figure 4.14). Even though the polymer resin contained CNCs, the resultant 3D composite structures not only closely matched to their SolidWorks designs, but they also similarly matched to the DLP 3D printed structures printed from the resin that did not contain any CNCs. This clearly indicates that CNC addition to the modified matrix resin did not interfere with the DLP 3D printing process.

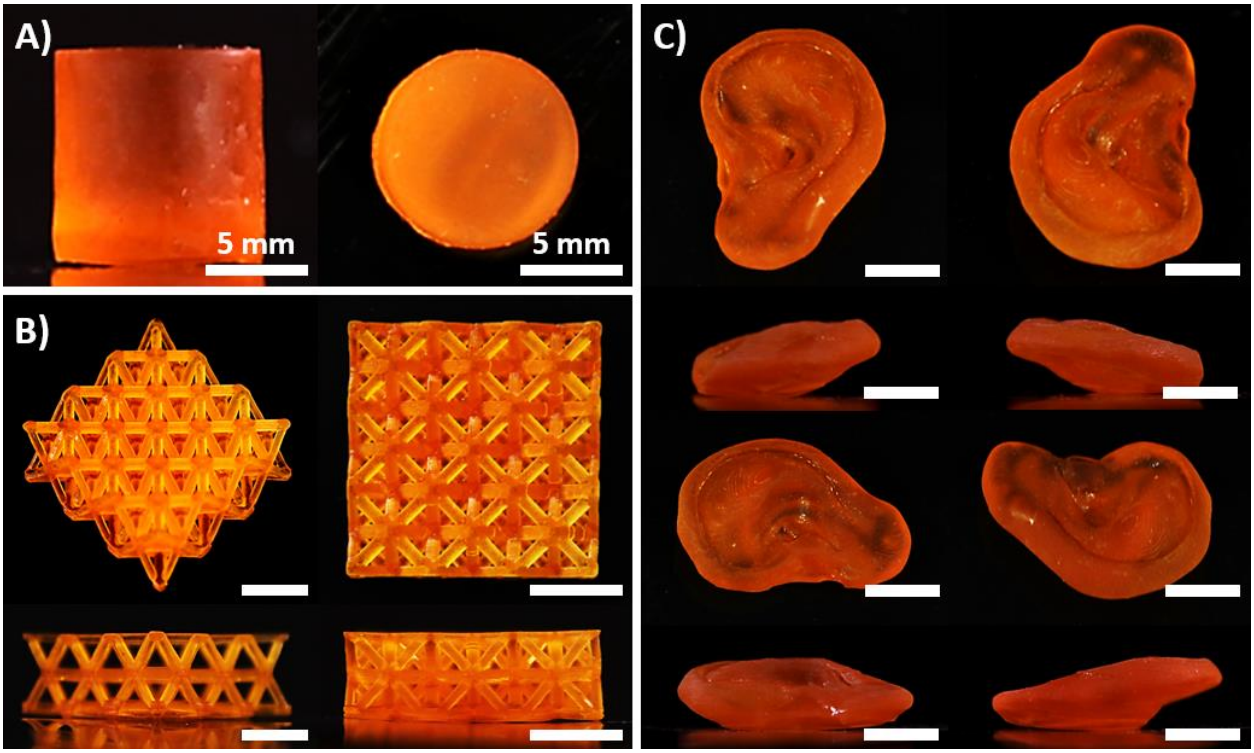

Figure 4.14: The resultant DLP printed (A) disk, (B) octet-truss lattice, and (C) ear model composite structures at 1 wt % CNC are illustrated from different perspectives. Unless specified, displayed scale bars are 1 cm.

To further assess the composites' potential for potential drug delivery or biomedical related applications, 3D printed composites were immersed in water to evaluate the swelling behavior as

a function of time (Figure 4.15A). After immersing the composites for one day, the final swelling ratios were also recorded based on different incorporated CNC concentrations (Figure 4.15B).

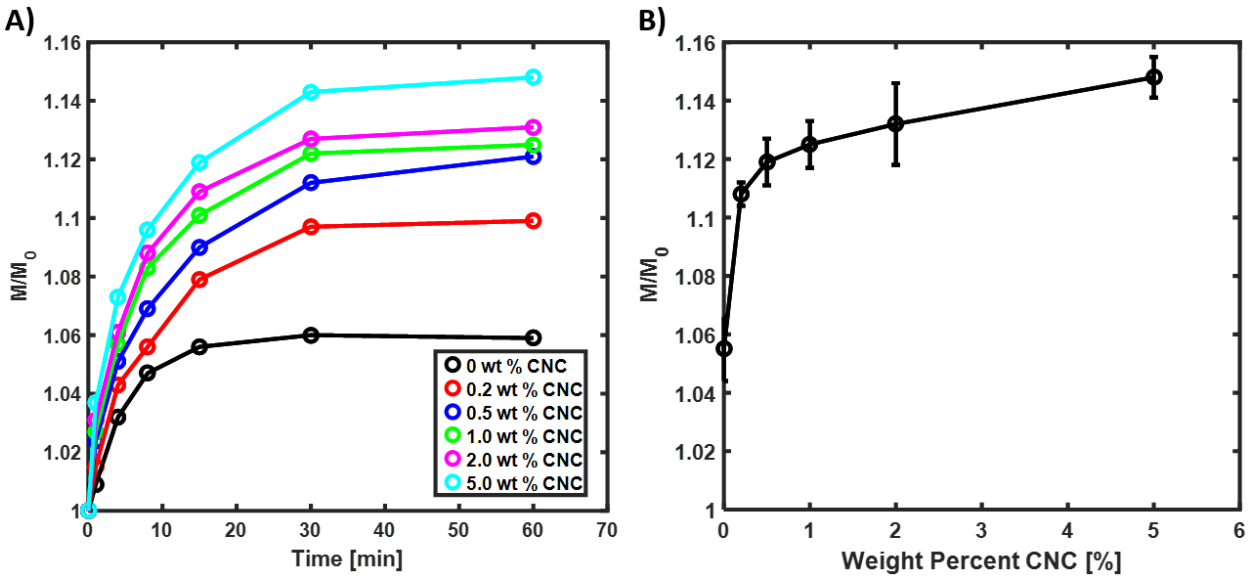

Figure 4.15: (A) The mass swelling ratios of composites incorporated with different CNC concentrations were recorded as a function of time. (B) The corresponding final mass swelling ratios of the composites after immersing them in water for one day. The curing layer thickness for all samples was set at 100 µm.

With no CNC incorporation, the final water mass infiltration was equilibrated at about 6 % of the polymer matrix's initial dry mass. For 5 wt % CNC composites, the final water mass infiltration was equilibrated at about 15 % of the initial composite's dry mass. These results indicated that both the final equilibrium swelling ratios and the initial swelling rate increased as CNC concentration in the polymer matrix increased. As water molecules were absorbed into the composite's matrix, it is likely that hydrogen bonding interactions between CNCs, PEGDA, and DiGlyDA were disrupted. This essentially led to an increase in free volume as the polymer matrix was loosened, and so additional water uptake was possible. With an increase in water uptake due to increase in CNC concentration, hydrogen bonding disruptions were also likely correspondingly accelerated. Thus, further speeding up the water uptake, and ultimately led to an increase in the initial swelling rate as well. Interestingly, the final equilibrium swelling ratio was also reached

within 30 minutes of water immersion regardless of incorporated CNC concentration. Even after one day of water immersion, the final equilibrium swelling ratio still remained relatively unchanged.

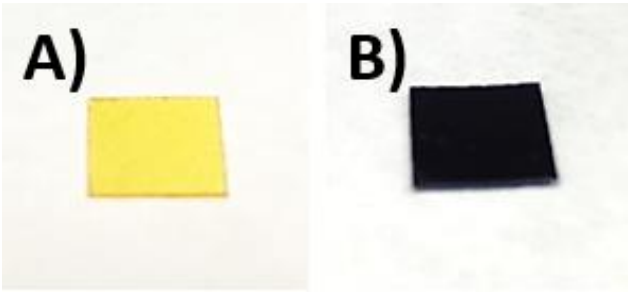

Figure 4.16: The color of the DLP processed thin film changed from (A) orange to (B) blue after it was infiltrated with 0.25 wt % Toluidine Blue O in water solution.

Furthermore, the release-diffusion kinetics of CNC reinforced composites were also studied, where toluidine blue O dye was used as a model compound for potential drug molecules. The main advantage of using toluidine blue O is that its hydrophilic nature will ensure efficient uptake into the CNC composites, and will also allow the dye's release-diffusion kinetics to be tracked with UV-Vis spectrophotometric methods. The dye infiltration into the CNC composites was confirmed, as the composites changed from an orange color that is indicative of the polymer resin to a blue color that is indicative of the dye solution (Figure 4.16). The dye infused composites were then placed in standard cuvettes filled with DI water, and the evolution of the toluidine blue O's dominant absorbance peak (~620 nm) with time were tracked using UV-Vis spectrophotometry (Figure 4.17A). The absorbance values were also converted to concentration values based on an obtained concentration calibration curve of the toluidine blue O dye (Figure 4.17B). Once the concentration of toluidine blue O was determined, the cumulative mass of diffused Toluidine Blue O can be obtained as a function of time (Figure 4.17C and 4.17D).

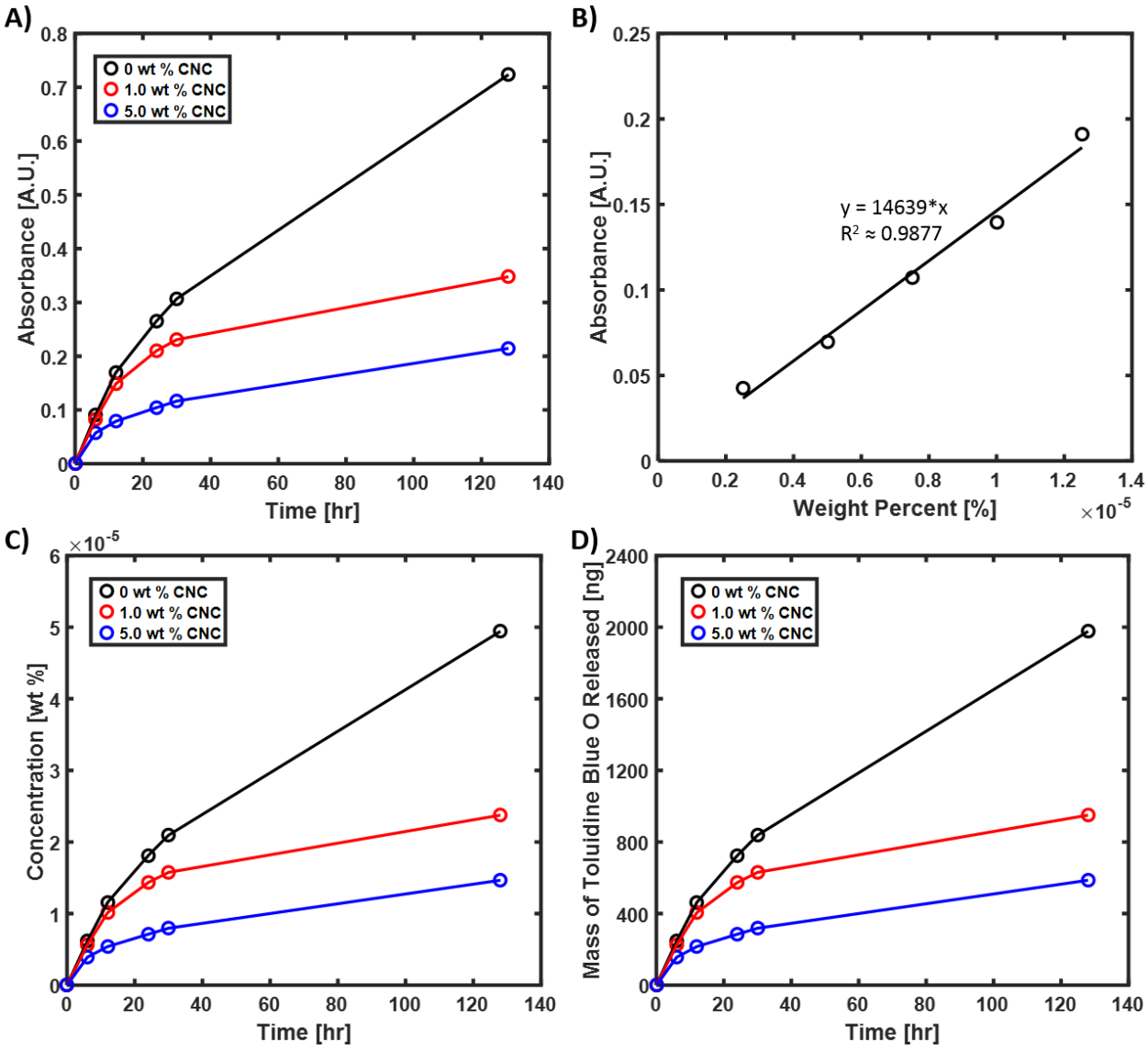

Figure 4.17: (A) The absorbance evolution of the toluidine blue O's dominant absorbance peak as a function of time. (B) The obtained concentration calibration curve of the toluidine blue O dye. (C) From the calibration curve, the concentration of toluidine blue O as a function of time was determined. (D) The cumulative mass of diffused toluidine blue O is then also determined and illustration as a function of time.

Based on the initial loaded dye content and the cumulative mass of diffused toluidine blue O, the percentage of cumulative toluidine blue O released was determined as a function of time (Figure 4.18A). From the cumulative mass of diffused toluidine blue O measurements, the

backward slope at each time point can also be calculated to estimate the release-diffusion rate of toluidine blue O as a function of time (Figure 4.18B).

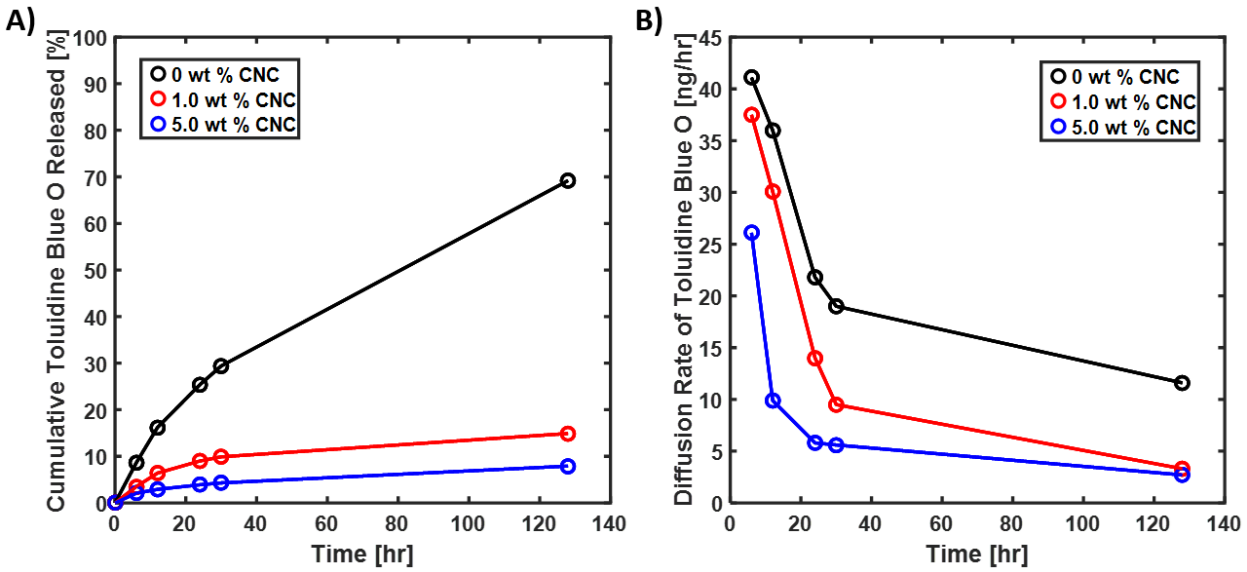

Figure 4.18: The diffusion kinetics from composites with various CNC concentrations as determined through UV-Vis spectrophotometric technique. (A) The cumulative percentage of toluidine blue O diffused out of the composites, and (B) the corresponding diffusion rates at different time are illustrated.

After nearly 5 days of dye release in water, about 70 % of the initial infiltrated toluidine blue O was released into the water for the sample without any CNC incorporation. On the other hand, only about 15 % and 8 % of the initial infiltrated toluidine blue O were released into the water for composites incorporated with 1 wt % and 5 wt % CNC, respectively. The toluidine blue O dye diffusion profiles suggested that increasing CNC incorporation led to decreasing diffusion rates, as the initial dye release rate also changed from about 40 ng/hr to 25 ng/hr as the concentration of incorporated CNCs increased from 1 wt % to 5 wt %. This observation was counter-intuitive because the increase in CNC concentration should lead to the increase in swellability of the polymer matrix, which should increase the ability for the toluidine blue O to diffuse out of the composite. It is possible that electrostatic interactions between the positively charged toluidine blue O dye and the negatively charged surfaces of CNCs can slow the dye's

desorption from CNCs' surfaces; however, further investigation is necessary. Nevertheless, these results suggested that it is also possible to tune the composite's diffusion profile and kinetics based on incorporated CNC concentrations. As a result, CNC concentrations could be controlled to modify the composite's Young's modulus, swelling, and diffusion characteristics depending on application requirements. Combining with DLP, 3D printed CNC composites could potentially satisfy the structural customizability and property tailorability as required in various biomedical related applications.

4.4 Conclusion

In this study, we prepared CNC incorporated photo-curable polymer resin that was suitable for DLP 3D printing. CNCs can be utilized as reinforcing fillers during composite processing to improve the mechanical properties of polymers. However, CNC dispersibility and compatibility with the polymer matrix are critically important as interfacial compatibility has a significant effect on the properties of 3D printed components. Utilizing competitive hydrogen bonding interactions from 1,3-diglycerolate diacrylate, CNC concentrations up to 1 wt % were compatibilized with PEGDA polymer matrices. Ultimately, mechanically enhanced and structurally complex CNC composite structures were successfully printed with DLP 3D printing, where CNC addition to the modified polymer matrix did not interfere with the 3D printing process. Furthermore, DLP parameters, such as curing layer thickness, can also be used to tune the mechanical properties and swelling behavior of the 3D printed CNC composites. The viability of using CNCs and DLP 3D printing to fabricate property-tunable and structurally customizable composites was confirmed, which encourages further utilization of sustainable nanocellulosic materials for potential biomedical related applications.

CHAPTER V: DIRECT INK WRITE (DIW) 3D PRINTED CELLULOSE NANOCRYSTAL AEROGEL STRUCTURES

5.1 Introduction[2]

3D printing or additive manufacturing can reduce the time needed to fabricate a highly customized object with complex geometry. The reduced fabrication time will also be highly beneficial due to the ever increasing demands for customized products. Currently, 3D printers are reaching the ability to fabricate structures with micrometers or higher resolution, and they have already impacted manufacturing processes within different industrial sectors.[23] While there are many 3D printing techniques for processing diverse materials, commonly used 3D printing materials, such as polyamide or acrylonitrile-butadiene-styrene,[12, 173-174] are petroleum-based. Given the wide usage and declining supply of petrochemical resources, there is a high incentive for using more sustainable and renewable alternatives.[1]

Cellulose nanocrystals (CNCs) have recently received significant attention due to their sustainability, availability, and unique nanoscale properties.[1, 4, 37, 40] As a result, it is conceivable and advantageous to substitute traditional 3D printing thermoplastics with nanocellulosic materials such as CNCs. Within the biomedical, cosmetics, pharmaceutical, and even packaging fields, there is also a need for more biocompatible and biodegradable aerogels.[175-178] Therefore, there is an increasing focus on processing purely cellulosic aerogels using MFCs,[179-180] CNFs,[181-184] or CNCs.[185] More commonly, the facile freeze-drying approach is adopted because low density and high porosity aerogels can be obtained. Yang et al.[185] fabricated chemically cross-linked CNC

[2] This chapter is modified from the following publication: **Li, V.**, Dunn, K. C., Zhang, Z., Deng, Y., Qi, H. J. (2017). Direct Ink Write (DIW) 3D Printed Cellulose Nanocrystals Aerogel Structures. *Scientific Reports*, 7, 8018. Permission for re-use is granted under the Creative Commons Attribution 4.0 International License.

aerogels using aldehyde modified CNCs and hydrazide modified CNCs, which resulted in aerogels with uniform pore structures with minimal structural collapse during drying. The cross-linked aerogel's low density also led to superabsorbent and oil/water separation properties. Zhang et al.[180] successfully fabricated crosslinked CNFs/MFCs aerogels with fast shape recovery properties in water. The resultant aerogels were robust enough to withstand a harsh solvent environment and mechanical agitation. Heath et al.[186] fabricated high porosity aerogels through solvent exchange with alcohol followed by supercritical carbon dioxide drying, and the resultant aerogels can lead to potential applications such as supports for catalysis, filters, or storage materials.

While there are still numerous other cellulosic aerogel fabrication approaches, one limitation is the inability to obtain aerogel 3D structures in a customizable manner to enable rapid fabrication of objects with complicated shapes. This has especially limited the aerogels' applicability, as they cannot adopt to specific needs as required by various applications. As a result, there have been increasing interests in utilizing 3D printing and wood-based materials for the fabrication of cellulosic structures with complex shapes. For example, Gatenholm et. al. reported 3D bioprinting of dissolve cellulose and functional nanofibril hydrogels with the potential for conductive electronic and other industrial applications.[55, 113] Hart et. al. also reported 3D printing of cellulose acetate-based structures that may be suited for medical or surgical use.[187] Pattinson et. al. have also reported CNC architectures printed via the DIW approach, where CNC alignments were achieved during 3D printing.[188]

In this study, DIW will be used to 3D print pure CNC aerogels with complex structures and customizable inner pore architectures. The unique dual pore CNC aerogels structures can also potentially have efficient cell integration capability as needed in tissue engineering applications. To ensure that the ink can be extruded efficiently during deposition but also maintain overall 3D

structures after deposition, various high concentration CNC gels with shear thinning behavior were prepared to test their 3D processability. To further enable inner pore architecture and overall structural customization, it was necessary to carefully control the aerogel's Computer Aided Designs (CAD), gel formulations, DIW processing specifications, and nozzle tip size. Ultimately, this study provided a unique solution for fabricating dual pore CNC aerogel 3D structures with controllable overall shape, resolution, porosity, and inner pore architecture.

5.2 Experimental Section

5.2.1 Materials

Freeze-dried CNCs derived from wood pulp and 11.8 wt % CNC in water suspension were purchased from University of Maine Process Development Center (Orono, ME, USA). Both the freeze-dried CNCs and the 11.8 wt % CNC suspension were used as received. Wet-strength additive cross-linker, polyamide-epichlorohydrin (Kymene), was kindly donated by Solenis LLC (Wilmington, DE, USA). De-ionized water was used in all experiments.

5.2.2 CNC Gel Formulation and Processing

Freeze-dried CNC-based on targeted weight percent was measured by a gravimetric balance, and then mixed with water. The mixture was further homogenized by a high shear probe homogenizer (T18 basic, Ultra Turrax, IKA Works Inc., USA) at 10,000 rpm until a homogeneous gel was obtained. The homogenized CNC gel mixture was then loaded into a syringe equipped with a tapered type nozzle. Next, 3D structures designed from SoildWorks design software (Dassault Systems, SolidWorks Inc., Waltham, MA, USA) were exported into STL formats, which were then interfaced with the Repetier software (Hot-World GmbH & Co. KG, Willich in North Rhine-Westphalia, Germany) to generate G-codes for each layer in the 3D structures. The G-code

designated the nozzle (x, z motion) and stage movement (y motion) for 3D structure construction through a layer-by-layer fashion. Compressed air was generated by a 135 psi Pancake Compressor (PCFP02003, Porter-Cable, Jackson, TN, USA) and directed to an air pressure controller (Ultimus V, Nordson EFD, East Providence, RI, USA), where a specified pressure was used to deposit the CNC gel through the nozzle. With a nozzle movement speed of 2 mm/s, 3D CNC gel structures were printed and then placed in a -20 °C freezer overnight. A lyophilizer (VirTis Freezemobile 25EL Sentry 2.0, USA) operating under 20 mTorr vacuum was then used to sublimate the frozen ice crystals for a duration of 2 days before 3D aerogel structures were obtained. For cross-linkable CNC aerogel, a trace amount of Kymene (2 wt % based on dry cellulose mass) was added to the CNC gel and then homogenized by a high shear probe homogenizer. After DIW and freeze-drying, the aerogel was cross-linked in an oven at 120 °C for 3 hours. Then, the cross-linked CNC aerogel was immersed into a 2.5 wt % Kymene in water solution for 3 hours before the Kymene infused CNC aerogel was removed from solution for another freeze-drying and oven treatment cycle.

5.2.3 Density Measurement and Porosity Calculation

A 1 cm^3 cubic structure was printed from the CNC gel mixture. After freeze-dry processing, the mass and volume of the aerogel were measured by a gravimetric balance and a caliper, respectively. After the density of the aerogel was measured, the porosity of the aerogel (Φ) was determined by Eq. 5.1,[182]

$$\Phi = \left(1 - \frac{\rho_{aerogel}}{\rho_s}\right) * 100\ \% \qquad (5.1)$$

where $\rho_{aerogel}$ is the calculated density of the aerogel sample, and ρ_s is the bulk density of the aerogel. The bulk density of the aerogel was set as the density of cellulose, which is 1600 mg cm^{-3} based on previous literature reports.[4, 130]

5.2.4 Field Emission-Scanning Electron Microscopy (FE-SEM) Characterization

To prepare the sample for SEM analysis, a drop of diluted CNCs in water was deposited onto a thin glass slide. Then, the glass slide was attached to the SEM sample holder with conductive double sided tape. After the water was evaporated under ambient air, the sample was sputter coated with gold for 60 seconds at 20 mA current with a Quorum Q-150T ES Sputter to help prevent charging. Planar cross-sections from CNC aerogel structures were also obtained through cryofracture using liquid N_2; then cross-sections were again attached to SEM sample holders with conductive double sided tape and sputter coated with gold before SEM was performed at 10 kV accelerating voltage.

5.2.5 Print Quality Evaluation

The quality of the DIW printed structures was determined by analyzing the edge of a 1 cm^3 cubic structure. First, optical images were converted into black and white images using a customized Matlab script. Then, the edge profiles from the right side of the cubes were traced into curves. From these curves, the mean absolute deviations and the mean smoothness deviations were determined according to Eq. 5.2 and 5.3,

$$Mean\ absolute\ deviation = \frac{1}{n}\left(\sum_{i=1}^{n} abs(L_i - L_{avg})\right) \tag{5.2}$$

$$Mean\ smoothness\ deviation = \frac{1}{n}\left(\sum_{i=1}^{n} abs(L_i - L_{i,best\ fit\ line})\right) \tag{5.3}$$

where *n* is the number of measured lengths, and *L* is the length determined from the Matlab script. Mean absolute deviation determines how the curve deviates from a perfectly straight line, where a lower deviation value indicates a straighter edge. On the other hand, mean smoothness deviation determines how the curve deviates from the best fitted line through the curve, where a lower deviation value indicates a smoother edge. After Matlab processing, mean absolute deviation and

mean smoothness deviation in units of pixel dimensions were converted into units of millimeters. The conversion was done based on a pixel to length conversion factor, which was determined through imageJ analysis.

5.2.6 CNC Aerogels' Compression Mechanical Property Evaluation via MTS Analysis

1 cm^3 cubic CNC aerogel structures processed by DIW were tested by a Mechanical Testing System (MTS Model 312.21 with a 2.3 ton load frame) loaded at a compression rate of 1 mm per min under ambient air and water environment. The initial Young's modulus was determined by the slope of the elastic region of the stress-strain curve. The stress and strain before break were determined at the point of first crack formation. Strain before densification was determined from the root of the best fitted line through the aerogel's densification region with an R^2 value of at least 0.98, and the corresponding stress was set as stress before densification.

5.3 Results and Discussion

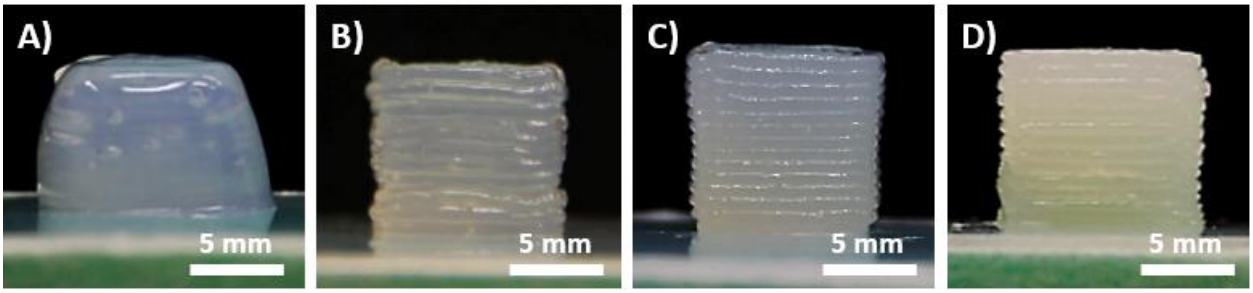

Figure 5.1: From 500 µm nozzle tip size, 1 cm^3 cubic CNC gel structures at (A) 11.8, (B) 15, (C) 20, and (D) 30 wt % are illustrated.

CNC gels at 11.8, 15, 20, and 30 wt % in water were prepared and 3D printed into a simple 1 cm^3 cubic structure through the DIW approach (Figure 5.1A to 5.1D). After freeze-drying, the aerogels' density and porosity were measured from their weight and volume. CNC gels with weight percent between 11.8 and 30 % resulted in an aerogel density range of 127 to 399 mg/cm^3,

while porosity ranged from 92.1 to 75.0 %. As the weight percent of CNCs increased, the density increased while the porosity decreased linearly. Both density and porosity can be extrapolated to the theoretical bulk cellulose's density and porosity of 1600 mg/cm^3 and 0 %, respectively (Table 5.1 and Figure 5.2).

Table 5.1: The measured density and porosity of various aerogels processed from gels with different weight percent of CNCs. The theoretical porosity and density for bulk cellulose are also provided.

Weight percent of CNCs (%)	Porosity (%)	Density (g/cm^3)
11.8	92.1	0.127
15	88.7	0.181
20	81.8	0.291
30	75.0	0.399
100	0.0	1.600

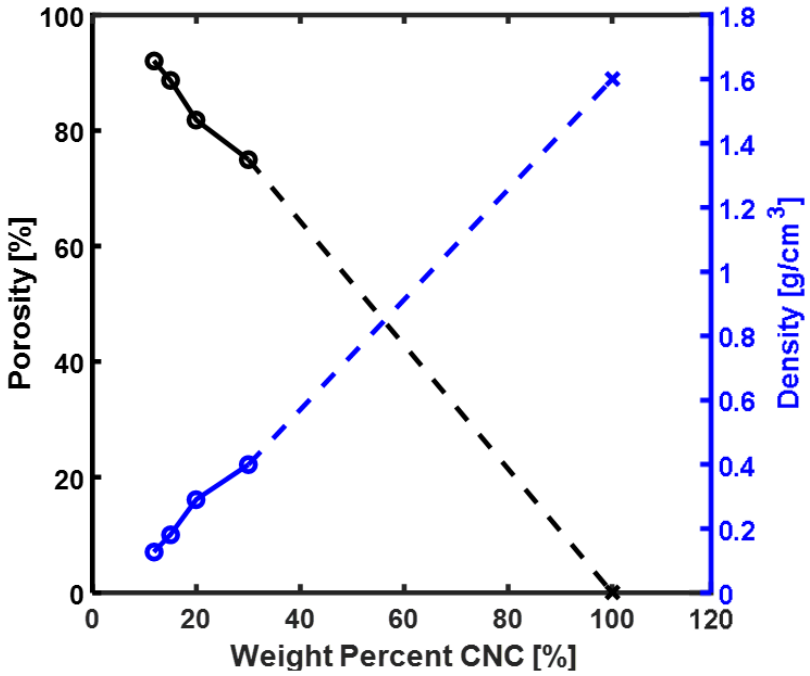

Figure 5.2: Density and porosity of the resultant 1 cm^3 cubic aerogels at different CNC weight percents (Symbol O). The theoretical porosity and density for bulk cellulose are also provided (Symbol X).

The linear decrease in porosity can be explained by decreasing pore sizes within the aerogel. During freeze-drying, smaller ice crystals were generated in structures with higher CNC concentrations due to decreasing water content in the gel. This is supported by SEM analysis of cross-sections from aerogels with different CNC concentrations, where decreasing macropore size was observed as the concentration of CNCs increased (Figure 5.3).

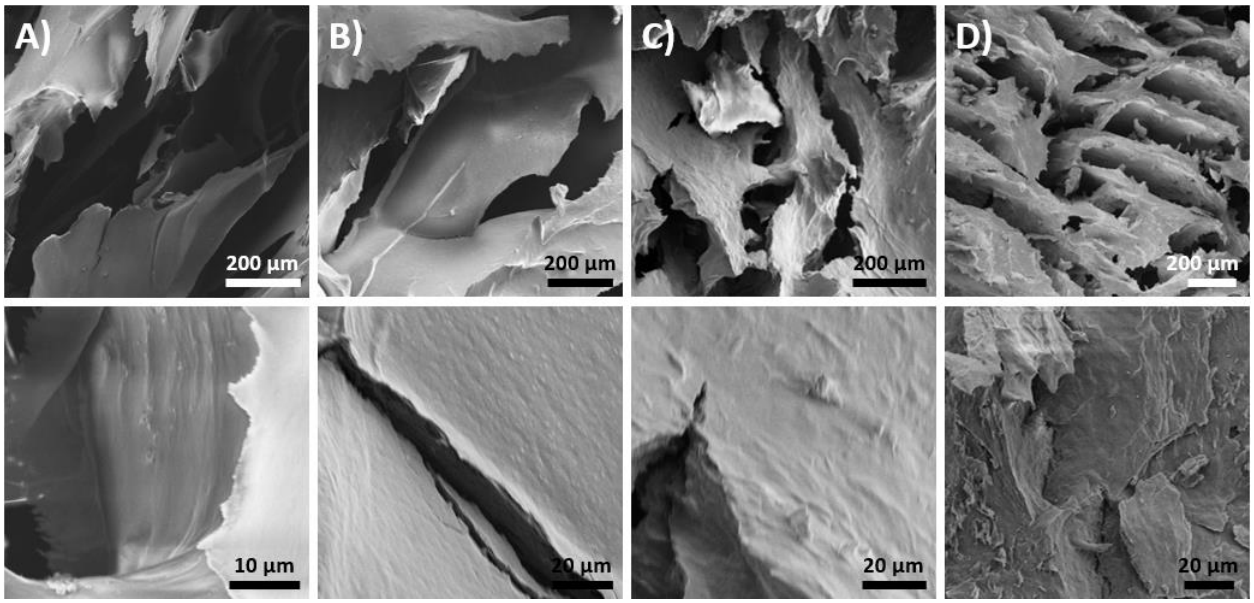

Figure 5.3: Planar cross sectional SEM images of freeze-dried 1 cm^3 cubic CNC aerogel structures using (A) 11.8 wt %, (B) 15 wt %, (C) 20 wt %, and (D) 30 wt % CNC gel are illustrated. Cross sections were obtained from cryofracture of DIW printed structures. Top is images taken at lower magnification, and bottom is corresponding images taken at higher magnification.

The formation of macroporous structures was consistent with other literature reports on water-based freeze-drying of cellulosic aerogels.[82, 189] At low freezing rates, ice crystal growth was much more dominant than ice crystal nucleation. As ice crystals grew, they further expanded and forced CNCs to aggregate in addition to CNCs' original tendency to form strong hydrogen bonds with themselves. The viscosities of CNCs gel at different concentrations were also evaluated through cone and plate viscometer measurements, and the viscosity was found to increase with CNC concentration (Figure 5.4A).

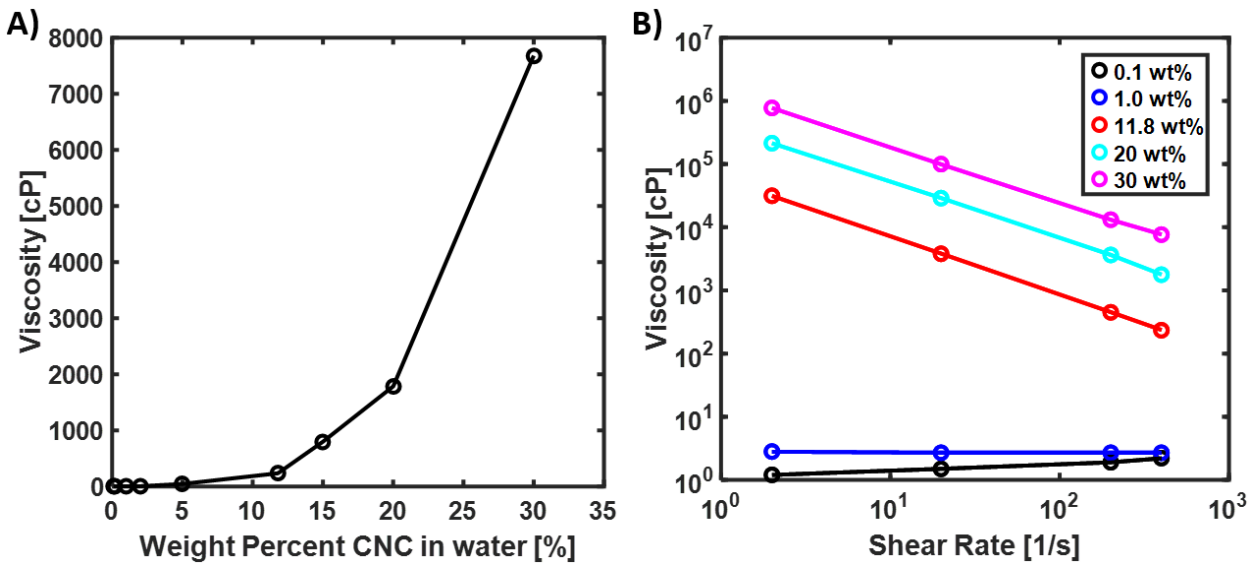

Figure 5.4: (A) The viscosity of CNC gels as a function of weight percent of CNCs. Viscosity displayed corresponds to the measured viscosity tested at the highest tested shear rate. (B) Viscosity versus shear rate curves at room temperature for different concentrations of CNC suspended in water. Both the x and y axes are in log base 10 scale.

Furthermore, the CNC gel changed from slightly shear thickening to highly shear thinning as CNC weight percent increased. This was confirmed when the slopes of the viscosity versus shear rate curves under the log-log scale were changed from positive to negative as the CNC weight percent increased (Figure 5.4B). This suggested that high shear and extensional flow within the nozzle can induce some degree of CNC alignment, as shear rate and CNC concentration increased. In effect, the shear thinning effect for efficient gel deposition during DIW was demonstrated. During gel extrusion, the shear thinning behavior favored efficient gel flow. After deposition, the high viscosity of the gel allowed the printed features to be maintained. Based on the viscosity of the gel, different pressures were required for gel deposition. For each CNC gel concentration and nozzle tip size combination, the width and height of the gel filament during printing can be controlled by optimizing the deposition pressure, printing speed, G-code extrusion width, and G-code layer height. By optimizing these processing parameters, targeted gel filament dimensions and CNC gel structures with high structural and dimensional accuracy can be reproducibly printed.

The viscosity, pressure needed for deposition, the mean absolute deviation, and the mean smoothness deviation from gel structures with different CNC concentrations are summarized in Figure 5.5 and Table 5.2.

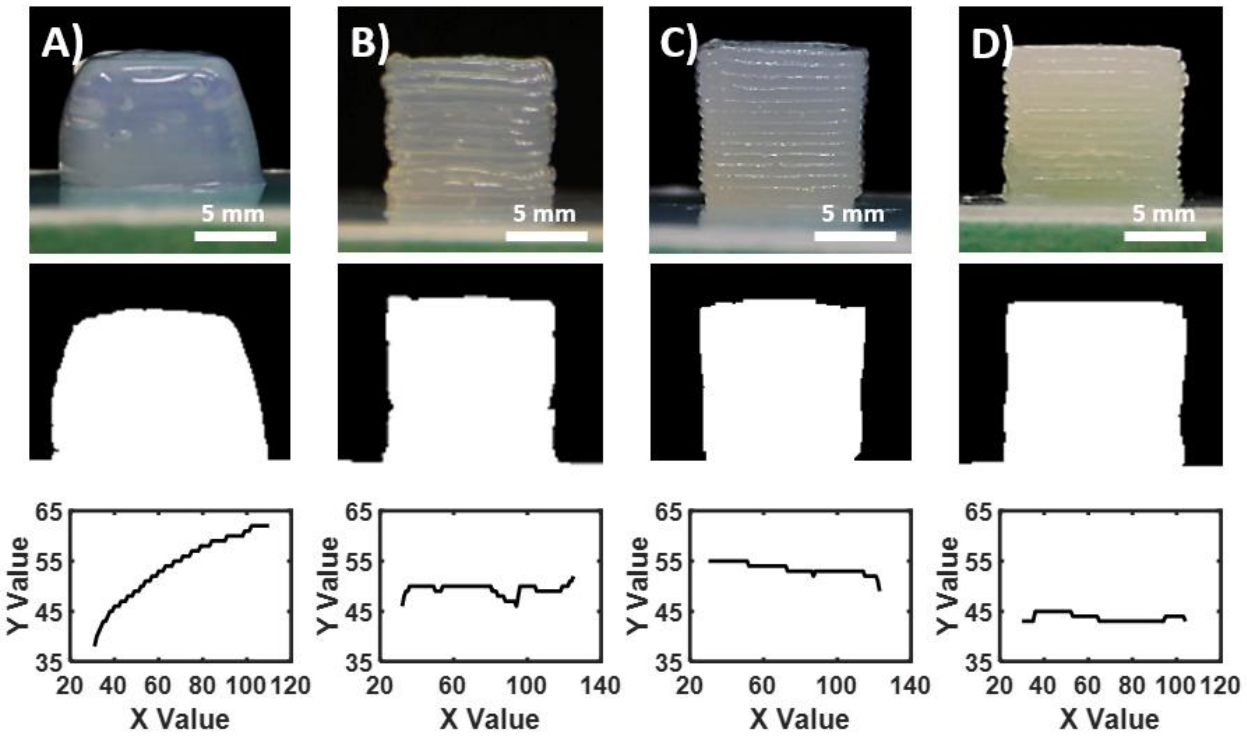

Figure 5.5: Optical images (first row), converted black and white images (second row), and traced curves from the right edge of the cube (third row) for CNC gels at weight percent of (A) 11.8, (B) 15, (C) 20, and (D) 30 % are illustrated. Structures were formed from a nozzle tip size of 500 µm.

Table 5.2: The viscosity (at the highest tested shear rate), pressure applied for deposition, mean absolute deviation, and mean smoothness deviation values for different weight percent of CNC gels are presented. G-code extrusion width of 0.9 mm, a G-code layer height of 0.7 mm, and a nozzle tip size of 500 µm were used.

Weight percent of CNCs (%)	Viscosity (cP)	Pressure Applied (psi)	Mean Absolute Deviation (mm)	Mean Smoothness Deviation (mm)
11.8	236.3	1	0.669	0.141
15	798.9	5	0.086	0.085
20	1785.3	20	0.083	0.040
30	7680.0	40	0.081	0.079

CNC concentrations higher than 30 wt % were not printed, as the power of the probe homogenizer to adequately homogenize the CNC gel was limited, and the pressure required for deposition was higher than the maximum pressure that could be controlled by the available air pressure controller. Based on edges from printed structures, the mean absolute deviations and mean smoothness deviation were also provided to evaluate the printed structure's shape fidelity and edge smoothness, respectively. Mean absolute deviation determines how the edge deviates from a straight line, and mean smoothness deviation determines how the edge deviates from a best fitted line through the edge. A lower mean absolute deviation represents structures with higher shape fidelity as these structures produce straighter edges, and a lower mean smoothness deviation represents structures with smoother edges.

Due to the increase in viscosity, the pressure needed to deposit the gel increased as the weight percent of CNCs increased. The mean absolute deviation also decreased as CNC weight percent increased, which suggested that higher viscosity gel can better maintain the printed edges and overall structure. The mean smoothness deviations were maintained at low values across all CNC concentrations, which suggested that there was good continuity along the edge even though the edge was composed of individually deposited layers. Printed structures from 11.8 wt % CNC could retain overall shape right after printing, but the relatively low viscosity gel usually resulted in structural sagging within 5 to 10 minutes (Figure 5.5A). As a result, the mean absolute deviation from 11.8 wt % CNC gel was significantly higher than the other CNC concentrations. Yet, the sagged structure still had a highly smoothed edge, owing to the CNC gel's liquid gel-like feature at 11.8 wt %. This led to a relatively low mean smoothness deviation, as the edge was highly smooth. Ultimately, the print quality was improved as the viscosity and CNC concentration of the gel increased.

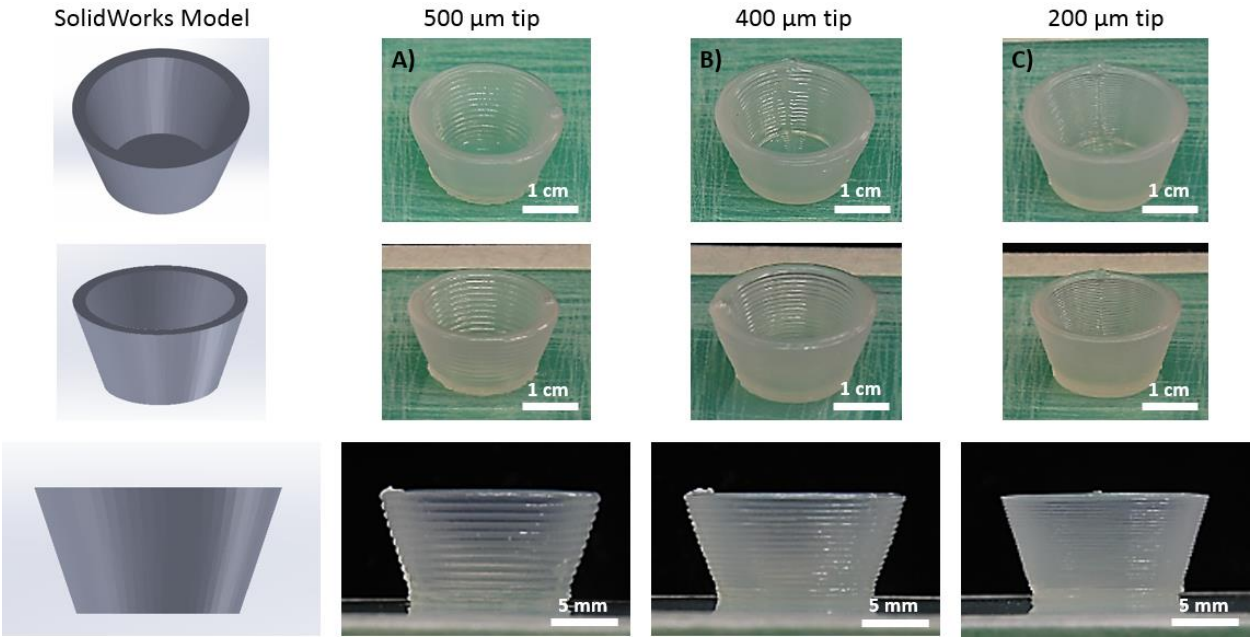

Figure 5.6: DIW 3D printed bowl gel structures from nozzle tip size of (A) 500 µm, (B) 400 µm, and (C) 200 µm. Structures were formed from 20 wt % CNC gel. The corresponding SolidWorks model and the DIW printed bowl gel structures are illustrated from different perspectives. Unless specified, displayed scale bars are 1 cm.

To further improve the printing quality, the 500 µm nozzle tip was replaced with nozzle tip sizes of 400 µm and 200 µm. Using 20 wt % CNC gel, bowl structures were printed from different nozzle tip sizes (Figure 5.6). To quantitatively assess the effect of nozzle tip sizes on print quality, 1 cm^3 cubic-shaped gel structures were again printed using nozzle tips of different sizes (500, 400 and 200 µm). Then, the mean absolute deviation and the mean smoothness deviation were evaluated. The results are summarized in Figure 5.7 and Table 5.3.

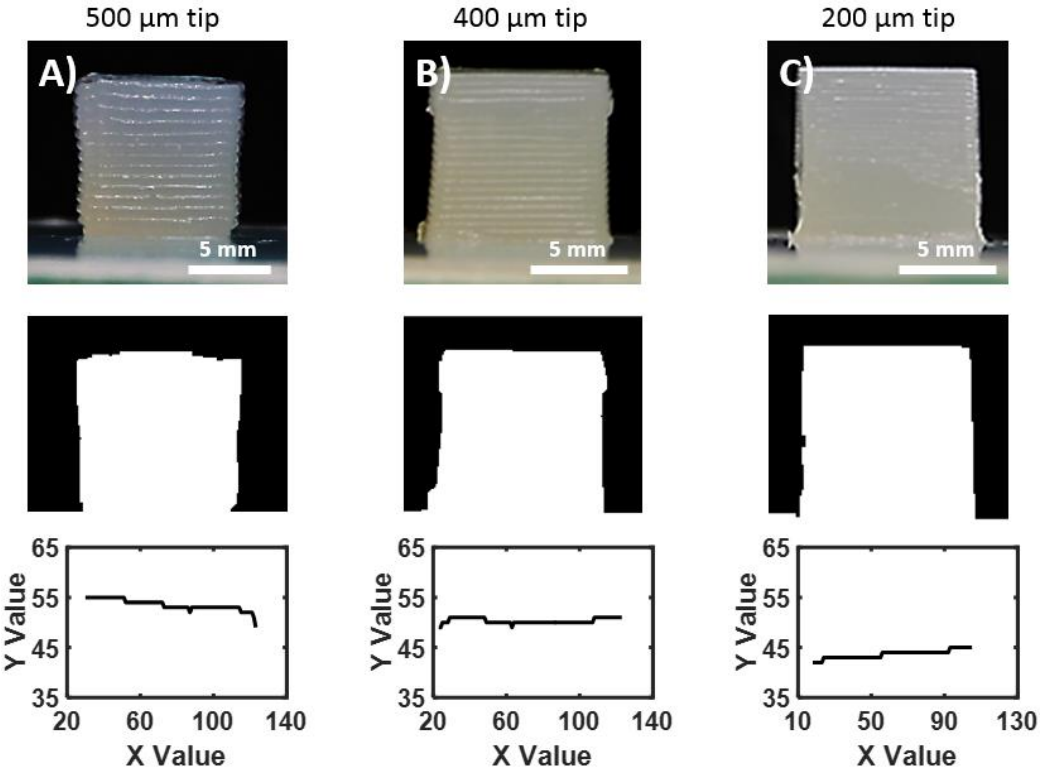

Figure 5.7: DIW 3D printed 1 cm^3 cubic gel structures from nozzle tip size of (A) 500 µm, (B) 400 µm, and (C) 200 µm. Optical images (first row), converted black and white images (second row), and traced curves from the right edge of the cube (third row) for different nozzle tip sizes are illustrated. Structures were formed from 20 wt % CNC gel.

Table 5.3: The G-code extrusion width, G-code layer height, pressure applied for deposition, mean absolute deviation, and mean smoothness deviation values for different nozzle tip sizes are presented. 20 wt % CNC gel ink was used.

Nozzle Tip Size (µm)	Width (mm)	Height (mm)	Pressure Applied (psi)	Mean Absolute Deviation (mm)	Mean Smoothness Deviation (mm)
500	0.9	0.7	20	0.083	0.040
400	0.5	0.5	40	0.038	0.033
200	0.3	0.3	60	0.079	0.030

Overall, the pressure required for deposition increased as the nozzle tip size decreased. The straightness and smoothness of various prints were also found to be similar across a variety of nozzle sizes. This suggests that the deposition pressure, printing speed, G-code extrusion width, and G-code layer height can be optimized for each nozzle tip size in a way that achieves prints

with similar edge quality. Nevertheless, even though the overall edge straightness and smoothness were similar for all nozzle tip sizes, the 200 µm resolution print still had the best printing quality and surface smoothness based on qualitative visual inspection. As the nozzle tip size decreased, the interconnectivity of each layer from the z-directional surface became more continuously smoothed. Overall, the print quality and surface smoothness improved as the printing resolution increased. However, the time required to complete the print also increased exponentially as the nozzle tip resolution increased. In fact, the estimated printing completion time increased from 20 mins/cm^3 to 130 mins/cm^3 of ink when the printing resolution increased from 500 µm to 200 µm. As a result, there was an inherent tradeoff between the printing resolution and the time required to complete the print.

To demonstrate the flexibility that can be realized by controlling the aerogel's 3D structures, 20 wt % CNC gel was printed into various structures, such as octet cube, pyramid, hexagonally twisting vase, nose model, ear model, and honeycomb with a nozzle tip size of 500 µm. The resultant gel and freeze-dried aerogel structures are illustrated (Figure 5.8).

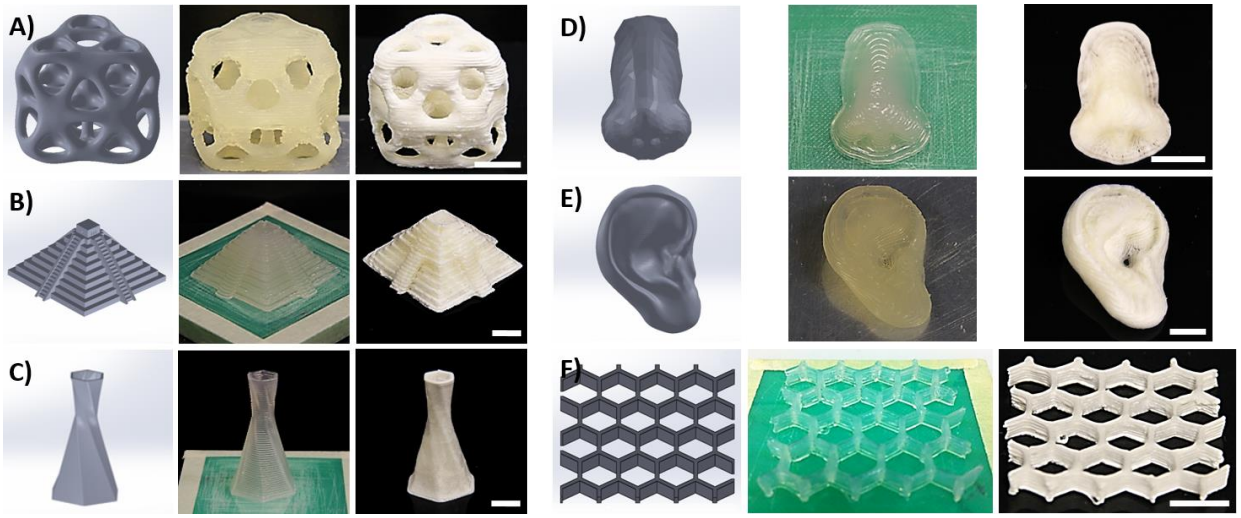

Figure 5.8: DIW 3D printed (A) octet cube, (B) pyramid, (C) hexagonally twisting vase, (D) nose model, (E) ear model, (F) and honeycomb from 20 wt % CNC gel and 500 µm nozzle tip are illustrated. First column is SolidWorks model, second column is DIW 3D printed gel structures, and third column is resultant structures after freeze-drying. Displayed scale bars are 1 cm.

It is evident from Figure 5.8 that the printed gel structures closely resemble the computer aided designs' (CAD) structures, thus demonstrating the ability to print CNC gel structures directly from CAD. Furthermore, there was no observable aerogel shrinkage or damage after freeze-drying. The high Young's modulus and strong hydrogen bonding potential provided by CNCs ended up limiting structural collapse or shrinkage during the ice crystal sublimation process. It should also be noted that gel structures were successfully printed without any support materials, which significantly reduced waste material. This was likely due to the CNCs' inherent light weight, and high viscosity at 20 wt % CNC.

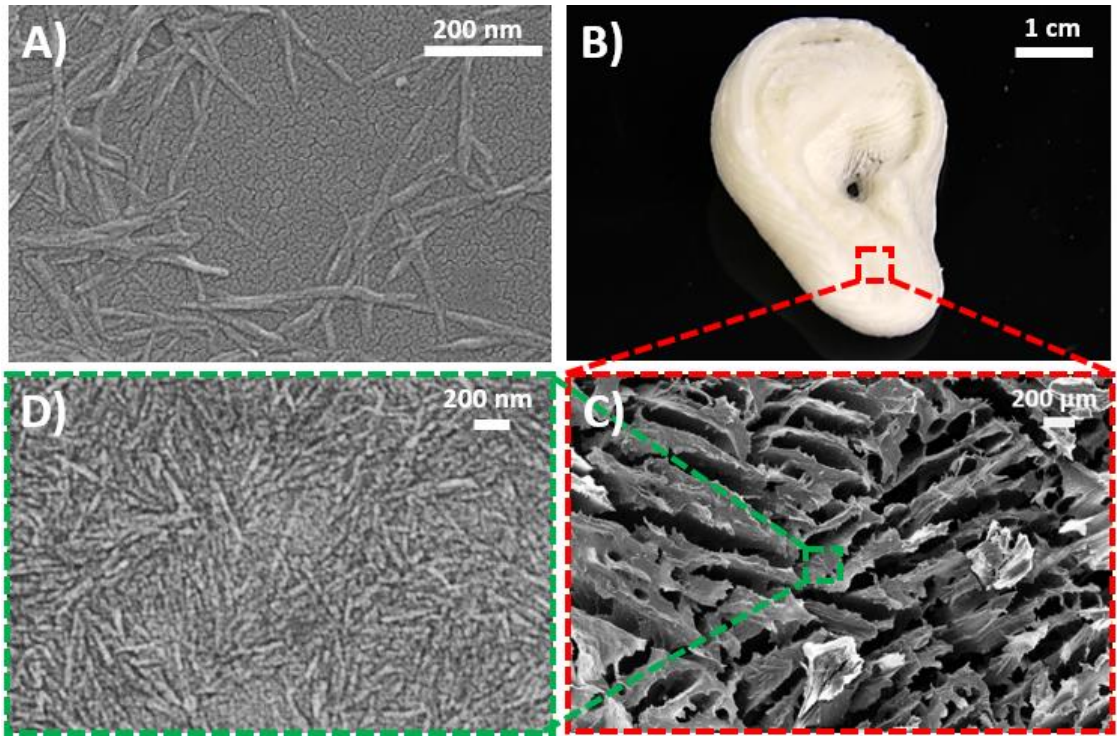

Figure 5.9: (A) SEM images of CNCs used during gel generation for DIW processing. (B) After DIW 3D printing followed by freeze-drying, an ear model without needing support material was successfully fabricated using 20 wt % CNC gel and 500 µm nozzle tip. (C) Macroporous structure of the aerogel was confirmed by SEM analysis. (D) CNCs, in a highly closed packed manner, that constituted the aerogel structure are also illustrated.

The CNCs used in this study were characterized by SEM (Figure 5.9A), which illustrated a CNC length and width of approximately 200 nm and 10 nm, respectively. After DIW 3D printing

and freeze-drying, the free-standing ear model aerogel structure (Figure 5.9B) was used to characterize the internal surface morphology through SEM. As seen in the aerogel's SEM image (Figure 5.9C), the porous nature of the CNC aerogel was confirmed. A distribution of macropore sizes, between 20 µm and 800 µm, was also observed (Figure 5.10). Upon higher magnification, the high concentration CNCs that constituted the aerogel structure were also observable (Figure 5.9D).

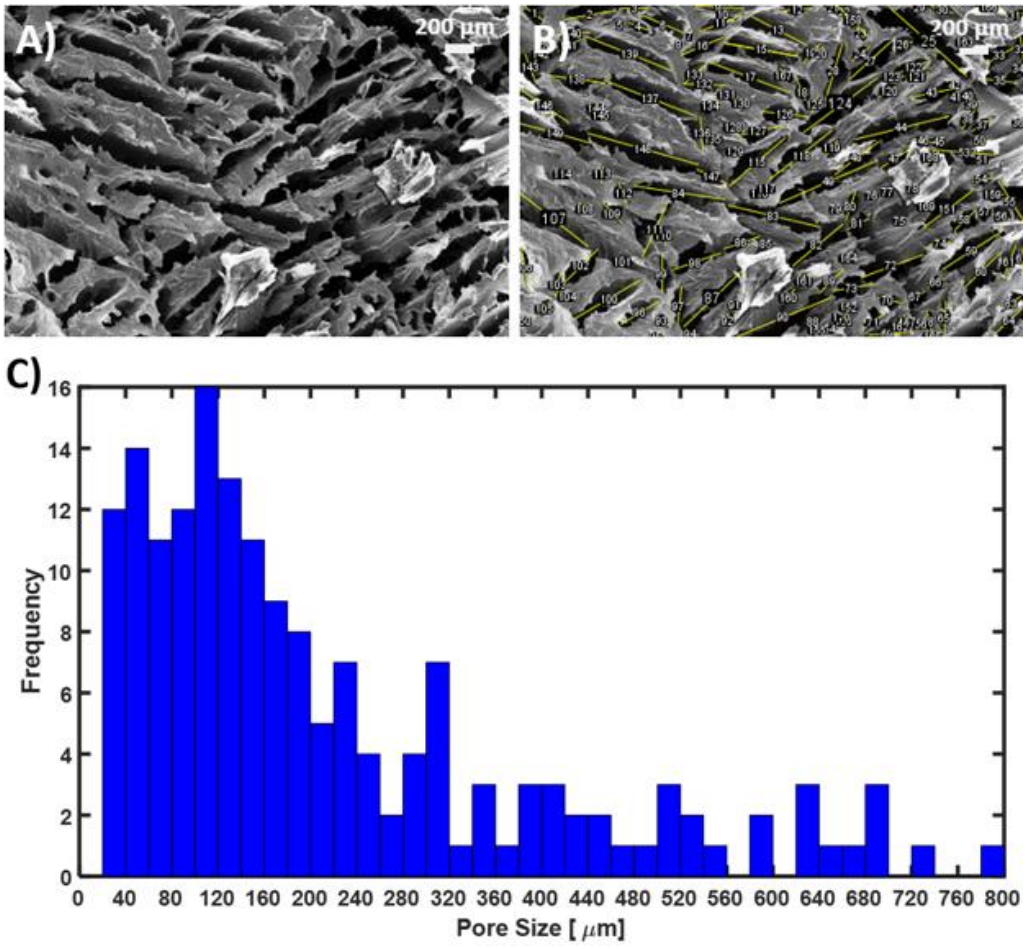

Figure 5.10: (A) Resultant SEM analysis of macroporous structure in aerogel that was freeze-dried from 20 wt% CNC gel. (B) Corresponding imageJ analysis for estimation of pore size distribution with a total pore size count of 170, and (C) the resultant pore size distribution plotted as a histogram with a bin size of 20 µm.

It was observed that CNCs were in highly close packed manner when compared to Figure 5.9A, which illustrated the strong self-hydrogen bonding potential of CNCs after freeze-drying.

Interestingly, the actual pore morphology in Figure 5.9C appeared to be elongated into platelet like shapes. Furthermore, nearby pores seemed to align in parallel with one another. This type of pore morphology is typically observed in aerogel processed at steady and slow freezing rate,[82, 179] which was the condition used in this study. More specifically, the physics of water freezing seem to favor an anisotropic ice crystal growth that is parallel to the movement of the ice-water freezing front. After sublimation, the resultant lamellar microstructures resembled the shape of platelets that are aligned parallel to one another. Depending on water content, freezing approach, and cooling speed, the freezing front could be controlled to tailor the thickness of the platelets.[190-191] Overall, this analysis demonstrated that it was possible to obtain porous aerogels with well controlled shapes from purely nanocellulosic materials by using the DIW technique followed by freeze-drying. These structurally complex CNC aerogels with controllable porosity promise great potential for tissue engineering applications due to their open cell type porous structures. This can allow solvent absorption, cell seeding medium infusion, oxygen permeation, nutrient transport, cell growth, or metabolic waste removal to occur within the aerogel. A macropore size distribution of 20 to 800 μm may also allow effective cell growth due to the comparable cell spreading length and pore sizes.[192-193] In an ideal scenario, cell growth can migrate through the aerogel using the smaller to medium pore sizes. Meanwhile, the larger pore sizes in the distribution can enable nutrient and metabolic waste diffusion to occur simultaneously until complete cell migration is achieved.[194] In fact, the compatibility between cellulose-based materials and bone or cartilage tissue has already been demonstrated by various reports,[9, 195-197] where cell integration and growth onto cellulose-based aerogels was successful. Our previous works have also tested cellulosic aerogels as culturing scaffolds, where 3T3 NIH cells were compatibilized with the cellulosic-scaffolds.[198]

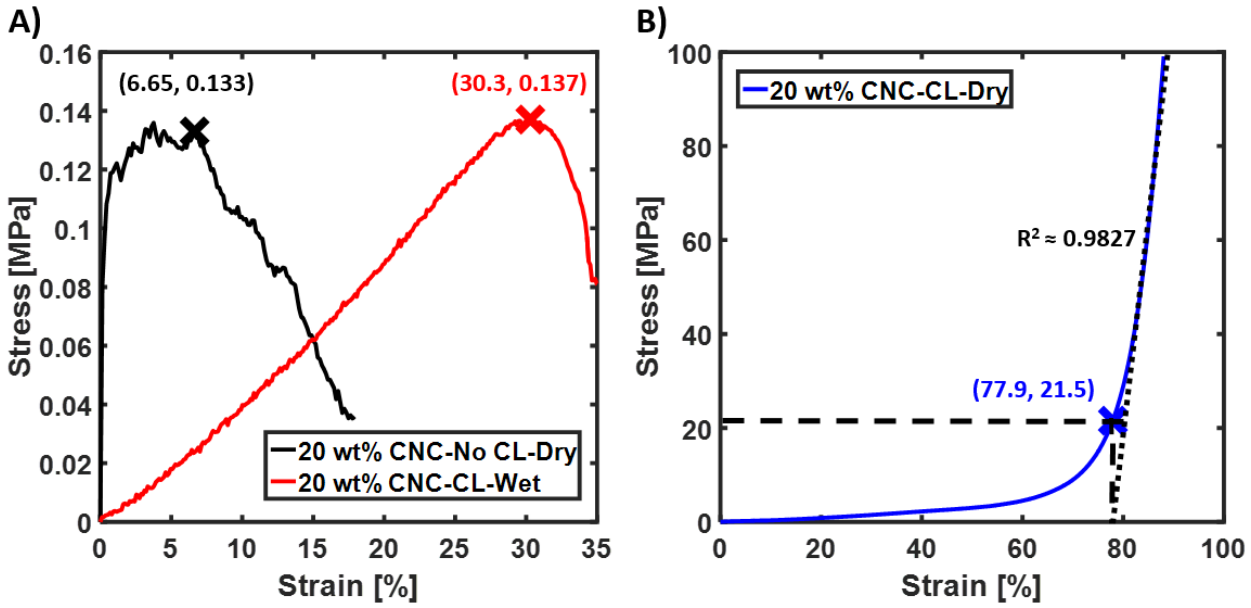

Figure 5.11: (A) Resultant MTS compression curve for CNC aerogel freeze-dried from 20 wt% CNC gel. The black curve represents the dry state stress-strain curve for CNC aerogel without any cross-linking (CL), and the red curve represents the wet state stress-strain curve for CNC aerogel cross-linked with 2.5 wt% Kymene. (B) The blue curve represents the dry state stress-strain curve for CNC aerogel cross-linked with 2.5 wt% Kymene. The best fitted line through the aerogel's densification region had an R^2 value of approximately 0.9827.

The mechanical properties of the CNC aerogels were also characterized by MTS compression analysis (Figure 5.11). The initial Young's modulus was determined to be approximately 7 MPa. The stress and strain before the first crack formation were 0.133 MPa and 6.65 %, respectively. The CNC aerogel's high stiffness but brittle nature was evident, which could lead to structure collapse during cell incorporation and growth. Since the CNC aerogel structures were not cross-linked, structural dissolution upon immersion into water or other organic solvents was also possible. Nevertheless, cross-linking of CNC aerogels structures was achievable by incorporation of a wet-strength additive known as, polyamide-epichlorohydrin (Kymene). Even through a small amount of Kymene addition to the CNC aerogel (2.5 wt % Kymene), the mechanical properties of the CNC aerogel were improved in both air and water environment. After cross-linking, Young's modulus increased from 7 MPa to 8.94 MPa. The CNC aerogel also became

less brittle, which led to a stress-strain curve with a densification region. The stress and strain before densification were determined to be 21.5 MPa and 77.9 %, respectively. While the CNC aerogel was immersed in water, the corresponding wet state mechanical properties were similarly evaluated. The resultant Young's modulus was determined to be approximately 380 kPa, while the stress and strain before the first crack formation were 0.137 MPa and 30.3 %, respectively. It appeared that water absorption had significantly soften the aerogel due to hydrogen bond disruption, but the compressibility of the water saturated CNC aerogel still improved from 6.65 % to 30.3 % through Kymene cross-linking. By cross-linking the CNC aerogel, cell growth without structural collapse may be possible.

To enable more efficient tissue regeneration onto scaffolds, recent efforts have been focused on fabricating dual pore structures with both structural pores and random pores. Dual pore scaffold systems had an advantage over traditional fully random porous structures for facilitating cell growth because the larger structural pores could enhance nutrient and oxygen transport, and this promoted homogeneous cell proliferation throughout the entire scaffold. Meanwhile, the smaller random pores provided the large surface areas necessary for high density cell growth. In fact, several cell-scaffold integration studies have already confirmed that the dual pore scaffold system led to improvements in cell count, metabolic activity, and uniformity of cell distribution when compared to fully random porous structures.[199-201] To further demonstrate the potential to utilize DIW-based 3D printing to fabricate biocompatible CNC aerogel scaffolds for tissue engineering applications, various dual pore CNC aerogel scaffolds were fabricated. More specifically, filaments were fabricated with orientation configurations of 0-45 °, 0-90 °, and 0-45-90-135 ° throughout each z-directional layer in the 3D gel structures (Figure 5.12). After freeze-

drying, porosity measurements indicated that the porosity can be tuned from about 80 % to 90 % purely from the filaments' orientational designs when using 20 wt % CNC gel.

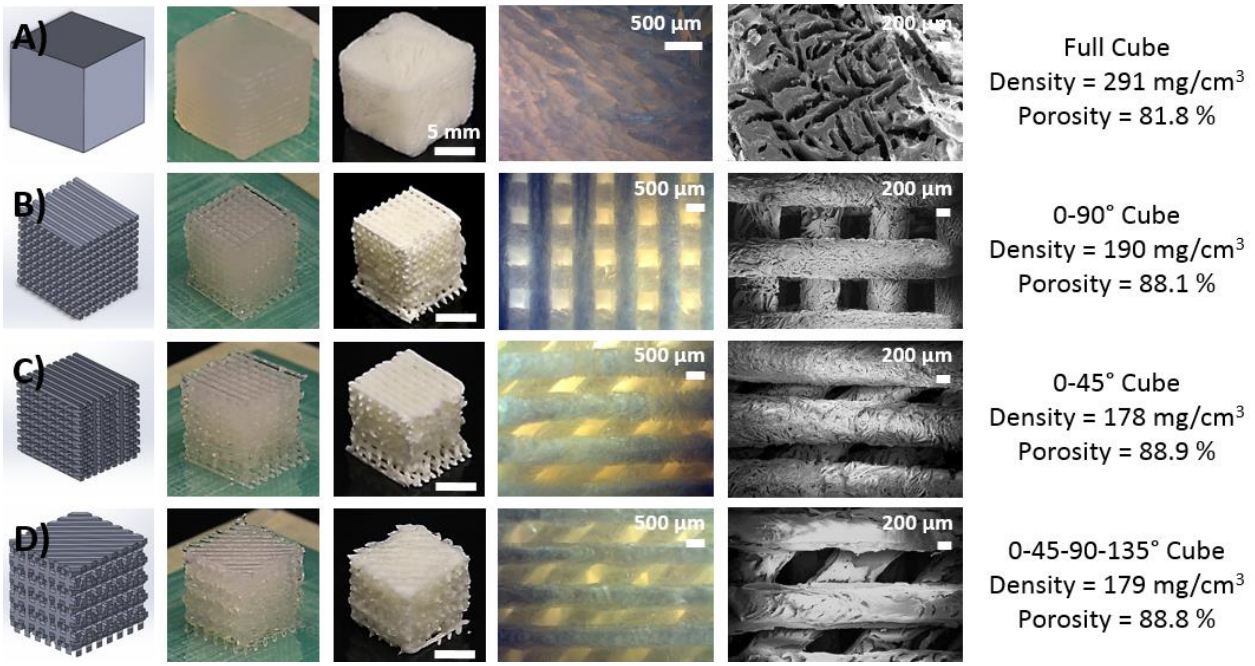

Figure 5.12: (A) Fully random porous CNC aerogel scaffold and various dual pore CNC aerogel scaffolds with filaments oriented in a (B) 0-90 °, (C) 0-45 °, and (D) 0-45-90-135 ° configuration throughout each z-directional layer. The SolidWorks models, gel structures, resultant aerogel structures after freeze-drying, optical microscope images, SEM images, and the measured density and porosity are displayed. Unless specified, displayed scale bars are 1 cm.

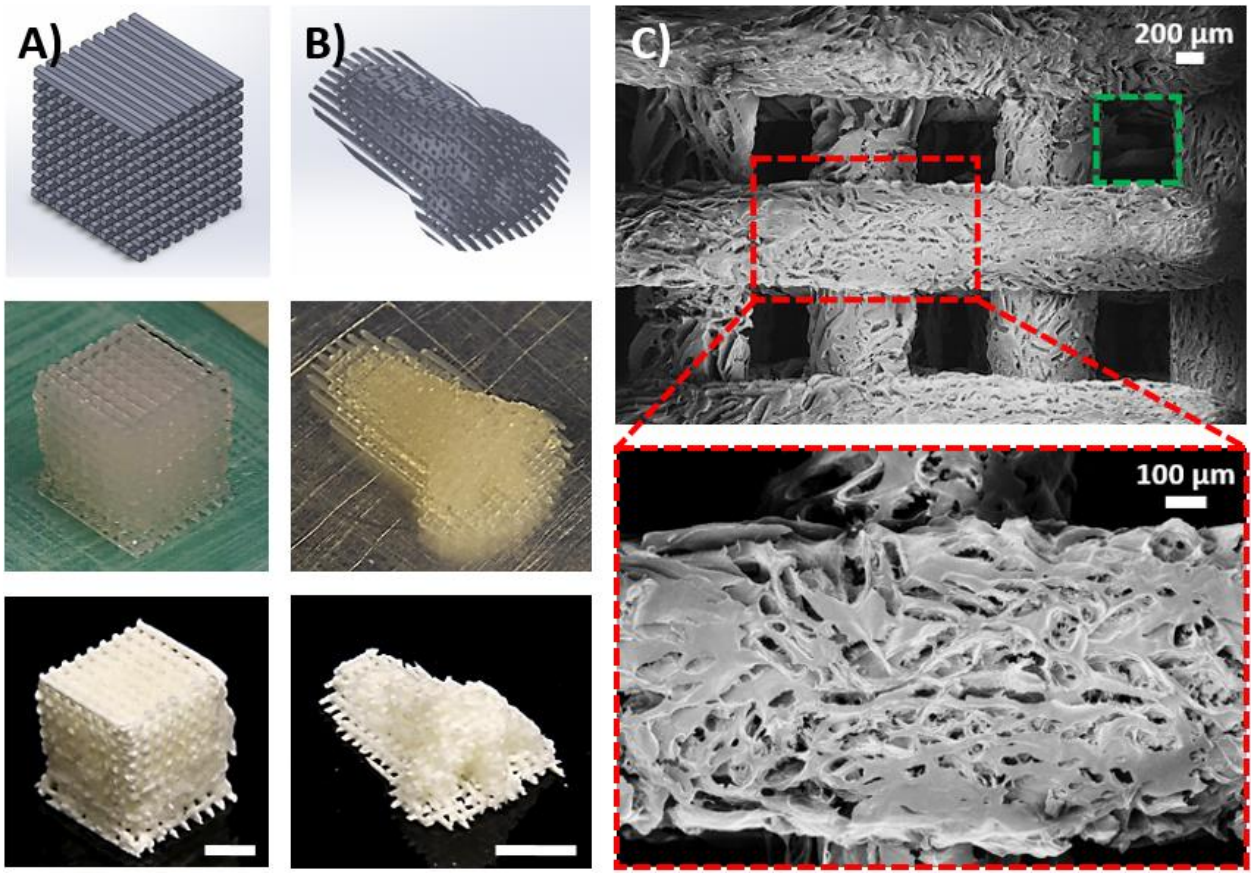

Figure 5.13: DIW 3D printed dual pore scaffold aerogel in a 0-90 ° configuration for (A) a cube and (B) a nose model. (C) The corresponding SEM images illustrate an average structural pore size of about 600 µm (green box) and a random pore size distribution of 20 to 800 µm (red box). 20 wt % CNC gel and 500 µm nozzle tip was used. Unless specified, displayed scale bars are 1 cm.

As demonstrations, a 1 cm^3 cubic structure and a nose model was also fabricated in a 0-90 ° structural configuration (Figure 5.13A and 5.13B). The G-code extrusion width and height was 700 µm, while the filament spacing was specified to be also 700 µm. From SEM analysis, the filaments had an average width of about 750 µm (Figure 5.13C). The increase in filament width could be attributed to a small degree of gel spreading after the deposition. Due to the slight increase in filament width, an average structural pore size of about 600 µm (green box) was observed. Moreover, a distribution of macropores (red box) was again observable on individual CNC filaments. Overall, the ability to utilize the DIW and freeze-drying technique to fabricate pure

CNC dual pore aerogel 3D structures was demonstrated. Based on the type of cells and their environmental growth requirements, the necessary structural and inner pore architectures can be controlled by tailoring the aerogel's CAD architectural designs, DIW processing specifications, gel formulations, and nozzle tip size. Overall, highly customizable CNC aerogel structures were successfully printed. Cell integration onto these aerogels and further improvements on their wet state mechanical properties will be a focus of future investigations.

5.4 Conclusion

A method that can 3D print pure CNC aerogels with well controlled overall structures and dual porous structures was developed. Gels at different weight percent of CNCs were prepared and printed into complex 3D structures through the DIW approach. After freeze-dry processing, an aerogel density range of 127 to 399 mg/cm^3 and a porosity range of 92.1 to 75.0 % were achievable with CNC gel concentrations of 11.8 to 30 wt %. Print quality assessments suggested that increasing weight percent of CNCs could provide straighter and smoother edges, while the surface smoothness could be improved by using a smaller nozzle tip size albeit at the cost of longer printing time. DIW 3D printed structures were also maintained with minimal shrinkage or damage even after freeze-drying. Various dual pore CNC aerogel scaffolds were also successfully processed, which promised great potential for a high degree of structural and inner pore architecture customization for different tissue engineering applications. These results demonstrated the highly capable DIW 3D printing and freeze-drying approach for creating complex and customizable CNC aerogel structures suited for target application requirements.

CHAPTER VI: DIRECT INK WRITE (DIW) 3D PRINTED CELLULOSE NANOFIBER AEROGEL STRUCTURES WITH HIGHLY DEFORMABLE, SHAPE RECOVERABLE AND FUNCTIONALIZABLE PROPERTIES

6.1 Introduction[3]

Processing materials into structures with great customizability has been pivotal to the development of 3D printed structures with practical applications instead of simply as ornamental displays. In fact, 3D printing has emerged in many fields with great potential, including aerospace,[138] automotive,[139] medical,[140] dental,[141] architecture,[94] sensor engineering,[142] advertisements,[202] packaging,[203] and food production.[143] 3D printing is also capable of processing a wide range of materials at great speed, resolution, and accuracy, which has opened up the possibility of building objects with a myriad of different functionalities.[204] Furthermore, cellulosic nanomaterials also exist as an interesting and new class of materials for 3D processing because of increasing focus towards a more sustainable society.[205]

Cellulosic nanomaterials, such as cellulose nanofibers (CNFs) or cellulose nanocrystals (CNCs), can be extracted from trees, plants, or even agricultural residues.[4, 39, 206] These materials are highly green and recyclable, and one particular area where nanocellulose has made significant impact is in the area of nanocellulose-based aerogel systems. Where these aerogels have shown astonishing applicability towards thermal insulation, catalyst supports, shock/vibration dampener, tissue engineering, sensing, solvent absorbents, filtering, and templating related applications.[207-

[3] This chapter is modified from the following publication: **Li, V.**, Mulyadi, A., Dunn, K. C., Deng, Y., Qi, H. J. (2018). Direct Ink Write 3D Printed Cellulose Nanofiber Aerogel Structures with Highly Deformable, Shape Recoverable and Functionalizable Properties. *ACS Sustainable Chemistry & Engineering*, 6, 2, 2011-2022.

[215] Yang et al. successfully fabricated chemically crosslinked CNC aerogels that demonstrated impressive shape recovery and superabsorbent properties.[185] Aulin et al. formed CNF aerogels with tunable oleophobicity through freeze-drying and chemical vapor deposition with 1H,1H,2H,2H-perfluorooctyl-trichlorosilane (PFOTS), where a hexadecane contact angle as high as 144 ° was reported.[216] Wu et al. fabricated ultralight, flexible, and fire-resistant carbon nanofiber aerogels from pyrolysis of bacterial cellulose aerogels. These aerogels displayed nearly complete shape recovery after a compressive strain of 90 % was applied.[217]

Although there are still numerous literature reports on functionalization of cellulosic aerogels, they typically lack overall shape and structural control. Based on literature reviews, there are still limited work on the functionalization and characterization of 3D printed cellulosic aerogels. Siqueira et al. reported direct-ink-write (DIW) of CNC textured cellular 3D architectures, where CNC alignment within the polymer filaments resulted in enhanced stiffness of the final processed parts.[188] Si et al. have successfully created superelastic nanofibrous 3D aerogel structures via injection molding and freeze-drying, and the resultant super lightweight aerogels displayed emulsion separation and compression dependent electrical properties.[218] Pattinson et al. used an extrusion-based 3D printing and vacuum drying technique to fabricate 3D cellulosic aerogel structures with robust mechanical properties and antimicrobial properties. The cellulosic gel can be printed into miniature forceps that may have surgical applications.[187] Håkansson et al. also fabricated 3D nanofibril hydrogels via DIW 3D printing techniques. A highly charged carboxymethylated CNF gel was utilized to assist with the DIW 3D printing process, and then cellulosic structures can be further modified to be electrically conductive via the addition of carbon nanotubes into the CNF gel.[55]

In this study, CNFs were used as the main component for aerogel fabrication, and DIW and freeze-drying was utilized to fabricate customizable and deformable 3D aerogel structures. As was already demonstrated in the previous study,[219] it is possible to DIW and freeze-dry CNC gel into 3D aerogel structures with a high level of controllability and customizability. However, the resultant pure CNC aerogels, similar to the traditional silica aerogels,[220] are brittle and are not easily deformable without structural damage. On the other hand, CNFs' long and soft nanoscale properties make it possible to form deformable networks through both physical entanglements and hydrogen bonding. However, the non-uniformity of network entanglements in CNF gel made them highly difficult to process by the DIW approach, as erratic pressure is required for deposition. As a result, DIW processing of purely CNF gel typically results in poor shape control. To enhance the homogeneity and printability of CNF-based gel, increasing the uniformity and dispersibility of CNFs in the gel should be beneficial for DIW printing. Herein, 2,2,6,6-Tetramethyl-1-piperidinyloxy (TEMPO) modification and high pressure homogenization were performed to create a defibrillated and TEMPO oxidized cellulose nanofiber (T-CNFs) gel that can be reproducibly processed by DIW. The resultant T-CNF gels have excellent DIW processability, and can be controllably and accurately 3D printed into purely T-CNF aerogel 3D structures with great customizability. The resultant T-CNF aerogels can also serve as templates for the facile addition of functionality.

6.2 Experimental Section

6.2.1 Materials

CNF suspension at 3.4 wt % in water was purchased from University of Maine Process Development Center (Orono, ME, USA). Polyamide-epichlorohydrin crosslinker resin (Kymene)

was kindly donated by Solenis LLC (Wilmington, DE, USA). Reagent grade sodium hypochlorite (NaClO) aqueous solution was purchased from Alfa Aesar (Tewksbury, MA, USA). Sodium bromide (NaBr) was purchased from EM Industries Inc (Hawthrone, NY, USA). 2,2,6,6-Tetramethyl-1-piperidinyloxy (TEMPO) was purchased from Chem-Impex Int'l Inc. (Wood Dale, IL, USA). Sodium hydroxide (NaOH) solution at 50 % in water was purchased from Sigma Aldrich (St. Louis, MO, USA). Polydimethyl diallyl ammonium chloride (Polydadmac) and polyvinyl sulfuric acid potassium salt (PVSK) were purchased from BTG Americas Inc. (Norcross, GA, USA). 1H,1H,2H,2H-perfluorooctyl-trichlorosilane (PFOTS) at 97 % purity and n-Decane at 99 % purity were purchased from Alfa Aesar. Epson 60 magenta dye was purchased from Epson Inc. (Suwa, Japan). Oil Blue N at 70 % dye content, 1.3 wt % poly(3,4-ethylenedioxythiophene)-poly(styrenesulfonate) (PEDOT:PSS) suspension in water, and 99.8 % Ethylene glycol (EG) anhydrous were purchased from Sigma Aldrich. All chemicals were purchased and used as received. De-ionized water was used in all experiments.

6.2.2 High Pressure Homogenized TEMPO Modified CNF (T-CNFs) Gel Generation

Adopted from Saito et al.,[221] 100 g of 3.4 wt % CNF suspension was first diluted with water to form a 1 wt % CNF suspension. To remove possible salt impurities in the CNF suspension, centrifugal processing was performed at 8000 rpm for 10 minutes. The clear supernatant was decanted and then re-suspended with water to re-form a 1 wt % washed CNF suspension without significant fibers lost during decantation. The washed suspension was then placed in a three-necked flask equipped with a pH sensor probe, and stirred at 400 rpm. The TEMPO oxidation reaction began with adding TEMPO (0.06 g, 1.1 mM) and NaBr (0.3 g, 8.7 mM) to the stirring suspension, and then NaClO (9.8 g, 0.4 M) was added to the suspension. Throughout the entire

oxidation reaction, the pH was maintained at approximately 10.5 by adding 0.5 M NaOH solution. After 2 hours of reaction, the TEMPO oxidized CNF suspension was purified by removing any remaining unreacted reactants through repeating centrifugal processing cycles until a pH of nearly 7 was obtained. Without significant fibers lost during centrifugal purification, the purified TEMPO oxidized CNF suspension was homogenized at about 22,000 psi with a high pressure homogenizer (NanoDeBEE, BEE International, South Easton, MA, USA). The high pressure homogenization process was repeated for 8 passes to obtain a nearly transparent TEMPO oxidized CNF suspension. To concentrate the high pressure homogenized suspension, water removal was done through vacuum filtration with Grade 42 ashless Whatman filter paper (purchased from Sigma Aldrich and used as received). The final weight percent of the resultant high pressure homogenized and TEMPO oxidized CNF (T-CNFs) gel from vacuum filtration was determined by oven evaporation. The final T-CNF gel was stored at 2 °C until further use.

6.2.3 T-CNF Gel Preparation for DIW, DIW Processing, and Aerogel Fabrication

The targeted weight of T-CNF gel was measured by a gravimetric balance, and mixed with Kymene and water. The mixture was then probe homogenized at 10,000 rpm to produce a DIW processable gel (Gel formulations: 2.8 wt % T-CNFs, 0.06 wt % Kymene in water). The T-CNF gel mixture was loaded into a syringe equipped with a tapered nozzle. 3D structures were designed by SolidWorks and were formatted as STL files, which interfaced with the Repetier software to generate the corresponding G-codes. The nozzle (x, z motion) and stage movement (y motion) were dictated by the generated G-code, so that layer-by-layer construction could occur. The perimeter method was used to form each layer, which permitted a reasonable degree of free-standing structures in the absence of support materials. A compressor was used to generate

compressed air for gel deposition, and an air pressure controller (Ultimus V, Nordson EFD, East Providence, RI, USA) was used to control the deposition pressure. With controllable deposition pressure, nozzle movement speed, G-code filament specifications, and nozzle size, it was possible to accurately construct different T-CNF 3D structures. After DIW processing, the 3D gel structures were placed in a -20 °C freezer overnight and freeze-dried for 2 days by a lyophilizer (VirTis Freezemobile 25EL Sentry 2.0, USA). To cross link the T-CNF aerogels, oven treatment at 120 °C for 3 hours was conducted. The crosslinked aerogels were stored under ambient environment until further use.

6.2.4 Density Measurement and Porosity Calculation

A 1 cm^3 cubic structure was DIW printed from the T-CNF gel mixture. After freeze-dry processing, the mass and volume of the aerogel were measured by a gravimetric balance and a caliper, respectively. The porosity of the aerogel (Φ) was determined by Eq. 6.1,

$$\Phi = \left(1 - \frac{\rho_{aerogel}}{\rho_{bulk}}\right) * 100\ \% \tag{6.1}$$

where $\rho_{aerogel}$ is the calculated density of the aerogel sample, and ρ_{bulk} is the bulk density of the aerogel. The bulk density of the aerogel was estimated from the gel's composition through Eq. 6.2,[182]

$$\rho_{bulk} = \frac{1}{\frac{x_{TCNF}}{\rho_{cellulose}} + \frac{x_{Kymene}}{\rho_{Kymene}}} \tag{6.2}$$

where x_{TCNF}, and x_{Kymene} are the respective weight fraction of T-CNFs and Kymene in the aerogel. According to previous literature reports,[4, 182] the density of cellulose is set as 1600 mg/cm^3 and the density of Kymene is set as 1150 mg/cm^3.

6.2.5 Qualitative Assessment of Fiber Length Distribution via Fiber Quality Analyzer (FQA)

CNF and T-CNF suspensions from different homogenization conditions were diluted with de-ionized water and then tested by the Fiber Quality Analyzer (FQA-360, OpTest Equipment Inc., Hawkesbury, Ontario, Canada). It should be noted that the FQA has a fiber length detection limit between 70 and 15,000 μm. Since fibers having lengths lower than 70 μm are not accurately captured by the digital camera and image-processing software, the obtained results only serve as an estimated qualitative representation of the suspension's actual fiber length distribution.

6.2.6 Surface Specific Charge Density Evaluation of CNCs, T-CNFs, and Kymene via Polyelectrolyte Charge Titration

10 g of polydadmac was first titrated with PVSK using the Particle Charge Detector (PCD) titrator and monitor (MüTek, BTG Americas Inc., Norcross, GA, USA) until a charge potential of zero mV was reached, and the volume of PVSK (V_b) used was recorded. Then, 0.1 wt % CNF and T-CNF suspensions in polydadmac were made and placed under magnetic stirring for 2 hours. 10 g of the resultant suspensions was titrated similarly as above, and the volume of PVSK (V_p) titrant used was recorded. The surface specific charge density of the corresponding cellulosic materials was calculated according to Eq. 6.3,[222]

$$q = \frac{(V_p - V_b) * c * 1000}{w} \tag{6.3}$$

where q is the surface specific charge density in mmol/kg, c is the concentration of titrant, and w is the solid mass content of pulp. q_{Kymene} was determined similarly with the exception of 0.01 wt % Kymene was mixed in PVSK before being titrated by polydadmac, and the position of V_p and V_b was switched in Eq. 6.3 for q determination of cationic species.

Assuming $q_{DIwater}$ is zero mmol/kg, the surface specific charge density of T-CNF gel was estimated according to Eq. 6.4,

$$q_{gel\ formulation} \approx y_{TCNF} * q_{TCNF} + y_{Kymene} * q_{Kymene} \quad (6.4)$$

where y_{TCNF} and y_{Kymene} are the respective weight fraction of T-CNFs and Kymene in the gel formulation.

6.2.7 Viscosity Characterization with Cone and Plate Viscometer

The viscosity of T-CNF suspensions and gel mixtures was analyzed by the DV3THV cone and plate viscometer (Brookfield Engineering Labs Inc., Middleboro, MA, USA). All measurements were done at room temperature of around 22 °C, and a cone spindle of CPA-52Z was used. The corresponding plate used was CPA-44PSYZ. Viscosity was measured as a function of shear rate, where the shear rate ranged from 0.2 s^{-1} to 500 s^{-1}. A minimum of 10 measurements were collected for each sample at each corresponding shear rate, and the averaged value was reported. The CPA-52Z cone spindle has a cone angle of 3 ° and a radius of 1.2 cm. For all viscosity characterizations, the gap separation between the spindle and the plate was set at 0.013 mm. To minimize potential wall slip effects, about 3 grams of gel mixture was distributed evenly across the entire plate surface before each characterization was performed. All reported viscosity values corresponded to the viscosity obtained at the highest tested shear rate of 500 s^{-1}.

6.2.8 Attenuated Total Reflectance-Fourier Transform Infrared Spectroscopy (ATR-FTIR) Characterization

FTIR spectra of uncross-linked CNF aerogel and Kymene cross-linked T-CNF aerogel were obtained with an ATR-FTIR (RAM II Vertex 80v, Bruker, MA, USA) under ambient

conditions from 64 scans with a scan resolution of 4 cm^{-1} in the range of 600 cm^{-1} to 4000 cm^{-1}. The FTIR instrument was equipped with a PLATINUM ATR single reflection diamond ATR accessory that is capable of analyzing both solid and liquid specimens. Spectra were analyzed from cryofractured aerogel cross sections with length, width, and thickness of approximately 1 cm by 1 cm by 2 mm, respectively. To better illustrate the evolution of the carboxylate C=O peak and ester C=O peak, only the wavenumber range between 600 cm^{-1} and 2000 cm^{-1} was presented.

6.2.9 Field Emission-Scanning Electron Microscopy (FE-SEM) and SEM-Energy Dispersive Spectroscopy (SEM-EDS)

Planar cross sections from freeze-dried T-CNF aerogel 3D structures were obtained through cryofracture using liquid N_2, then cross sections were attached to SEM sample holders with conductive double sided tape. The samples were then sputter coated with gold for 45 seconds at 20 mA current to help prevent charging, and they were then imaged by a Hitachi SU8010 FE-SEM (Hitachi America, Ltd., Tarrytown, NY, USA) at 5 kV accelerating voltage. To qualitatively analyze the homogeneity of PFOTS deposition throughout the T-CNF aerogel, SEM-Energy Dispersive Spectroscopy (EDS) was done to track the fluorine, carbon, and oxygen mapping distribution in the aerogel's cross-section. The cross-section was obtained by cryofracture with liquid N_2, and then sputter coated with gold for 15 seconds to help prevent charging. Then, the SEM-EDS analysis was done by a Zeiss LEO 1530 FE-SEM at 5 kV accelerating voltage.

6.2.10 Mechanical Testing System (MTS)

Adopted from ASTM D1621-16, crosslinked 1 cm^3 cubic T-CNF aerogel 3D structures were tested in the z-direction by a universal material testing machine (Criterion Model 41, MTS,

Eden Prairie, MN, USA) at a compression rate of 1 mm per min under ambient air or water environment. Initial compression Young's modulus was determined from the slope of the elastic region of the stress-strain curve. The strain before densification was set as the root of a linear fitted line through the densification regime with an R^2 value of at least 0.98. The corresponding stress was set as stress before densification. A total of three T-CNF aerogel samples were tested for each aerogel under various conditions, and averages with standard deviations for the aerogel's initial Young's modulus, strain before densification, and stress before densification were reported.

6.2.11 Water Absorption Capacity

The crosslinked 1 cm^3 cubic aerogel's initial weight (w_0) was measured by a gravimetric balance before it was immersed in water for 3 hours. The water saturated aerogel was then removed from the water, and excess water on the aerogel's surface was blotted before the final weight of the water saturated aerogel was measured (w). The water absorption capacity was evaluated according to Eq. 6.5.

$$Absorption\ Capacity = \frac{w - w_0}{w_0} \tag{6.5}$$

Two samples were tested, and the average was reported. The theoretical absorption capacity can also be determined by the porosity (Φ) and density (ρ) of the aerogel through Eq. 6.6.[182]

$$Theoretical\ Absorption\ Capacity = \frac{\Phi}{100} * \frac{\rho_{water}}{\rho_{aerogel}} \tag{6.6}$$

6.2.12 Wet State Shape Recovery and Recovery Repeatability Analysis

A crosslinked 1 cm^3 cubic T-CNF aerogel 3D structure was cryofractured into cubes with dimensions of 0.5 cm, and then immersed in water for 3 hours. The water saturated aerogel was placed onto a dynamic mechanical analyzer (DMA, model Q800, TA Instruments, New Castle,

DE, USA) equipped with a compression clamp set up, and then samples were tested in the z-direction under controlled force mode. A total of two T-CNF aerogel samples were tested for each compression amount, and average shape recovery percentages with standard deviations are reported. The force was ramped at 1N per min until a specified strain was reached. The force was then kept constant for 1 min before the force was released at 2N per min until zero. A relatively slow force ramp rate was chosen to ensure the specified strain can be reached without significant overshoot. The zero force condition was held constant for another minute before one full compression and releasing cycle was completed. The percentage of aerogel recovered at the i^{th} cycle (R_i) can be obtained from the strain history with Eq. 6.7,

$$R_i = \left(1 - \frac{\varepsilon_{lost,i}}{100}\right) * 100\ \% \tag{6.7}$$

where $\varepsilon_{lost,i}$ is the tracked strain in % at the end of the i^{th} compression and release cycle.

6.2.13 PFOTS Modified T-CNF Aerogel 3D Structure, Contact Angle Measurements, and Oil/Water Separation

Hydrophobic T-CNF aerogel was prepared by chemical vapor deposition (CVD) of PFOTS. Specifically, an uncovered glass vial containing 0.5 mL of PFOTS was placed inside a glass bottle. The crosslinked 1 cm^3 cube of T-CNF aerogel was also inserted into the glass bottle and remained in non-contact with the liquid. The glass bottle was then tightly sealed and placed in an oven at 75 °C for 4 h. Upon reaction completion, the aerogel was removed from the glass bottle and kept under vacuum to remove unreacted vapor. The resultant PFOTS modified T-CNF aerogel was then kept in ambient condition until further characterization. The static sessile drop method was employed to capture the water and decane contact angle on the PFOTS modified T-CNF aerogel, where a FTÅ200 contact angle analyzer (First Ten Ångstroms, Portsmouth, VA, USA)

equipped with an optical video camera was utilized. Approximately 5 µL of water or decane was deposited onto the aerogel during each measurement, and averages from contact angles at different locations of the aerogel were reported. For water and decane contact angle measurements, nine and two different locations were tested, respectively. To illustrate the hydrophilic T-CNF aerogel and the PFOTS modified T-CNF aerogel's ability to perform oil/water separation, water was dyed red by Epson magenta 60. On the other hand, decane was dyed blue by Oil Blue N. Hydrophilic T-CNF aerogel was able to remove water droplets from decane, and the hydrophobic PFOTS modified T-CNF aerogel was able to remove decane droplets from water.

6.2.14 Functionalization and Characterization of PEDOT:PSS Templated T-CNF Aerogel 3D Structure

A mixture of EG and PEDOT:PSS in water was first prepared to generate a 5 wt % EG in PEDOT:PSS-water suspension. The crosslinked 1 cm^3 cubic T-CNF aerogel was then immersed into the suspension for 3 hours. Afterward, the aerogel was removed from the suspension and dried under ambient environment. Before characterizing the aerogel's electromechanical properties, the aerogel was immersed in water for 3 hours. The sample was then placed onto the DMA under compression configuration, and the strain history during compression-release cycles was tracked. A compression amount of 50 % was tested, and a total of 5 compression-release cycles were again performed. A total of three PEDOT:PSS templated T-CNF aerogel samples were tested, and average shape recovery percentages with standard deviations are reported. To record the resistance change during cyclic compression and release, two copper electrodes were connected to the top and bottom surfaces of the PEDOT:PSS templated T-CNF aerogel (Figure 6.1). The electrodes were also connected to a multimeter (model Keithley2100, Keithley Instruments, Cleveland, OH,

USA), which was controlled by a LabVIEW data acquisition program. To illustrate the aerogel's electromechanical properties during compression-release cycles, a LED light bulb was connected to the electrical circuit. The multimeter was replaced by a power source, and the electromechanical response of the PEDOT:PSS templated T-CNF aerogel was confirmed by the LED light bulb's illumination fluctuations during compression-release cycles.

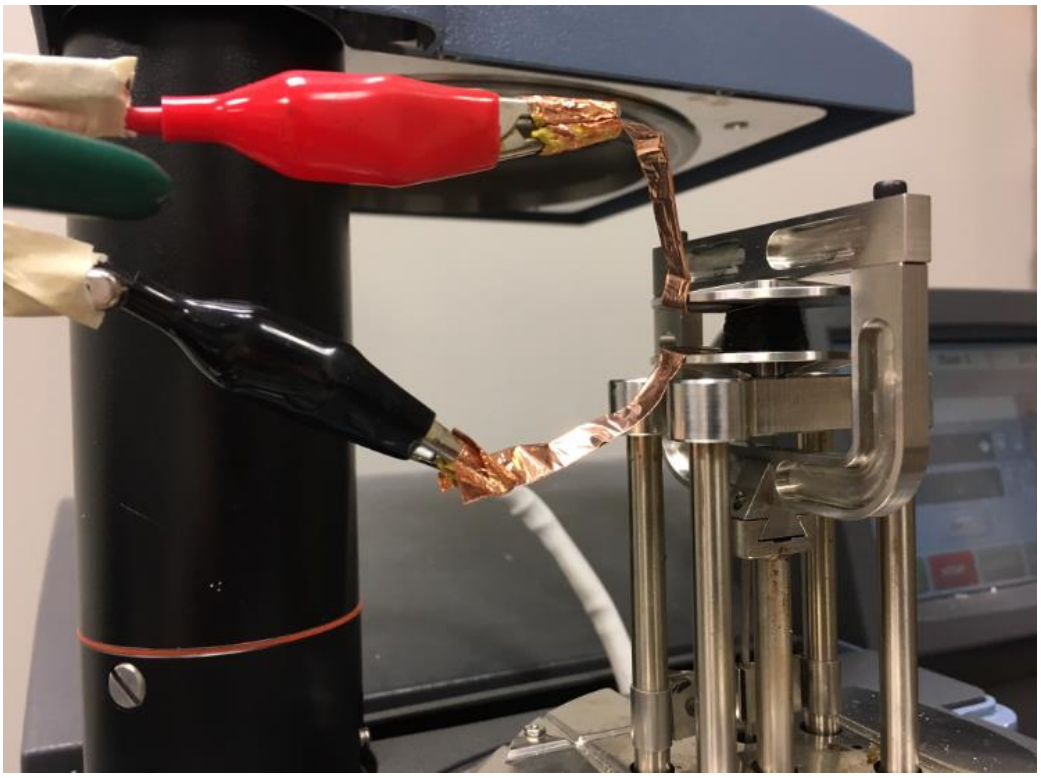

Figure 6.1: The DMA experimental setup for measuring the PEDOT:PSS templated T-CNF aerogel's electromechanical properties during compression-release cycles is illustrated. The two copper electrodes were placed onto the top and bottom surfaces of the aerogel, and then connected to a multimeter to track the resistance change during mechanical testing.

6.3 Results and Discussion

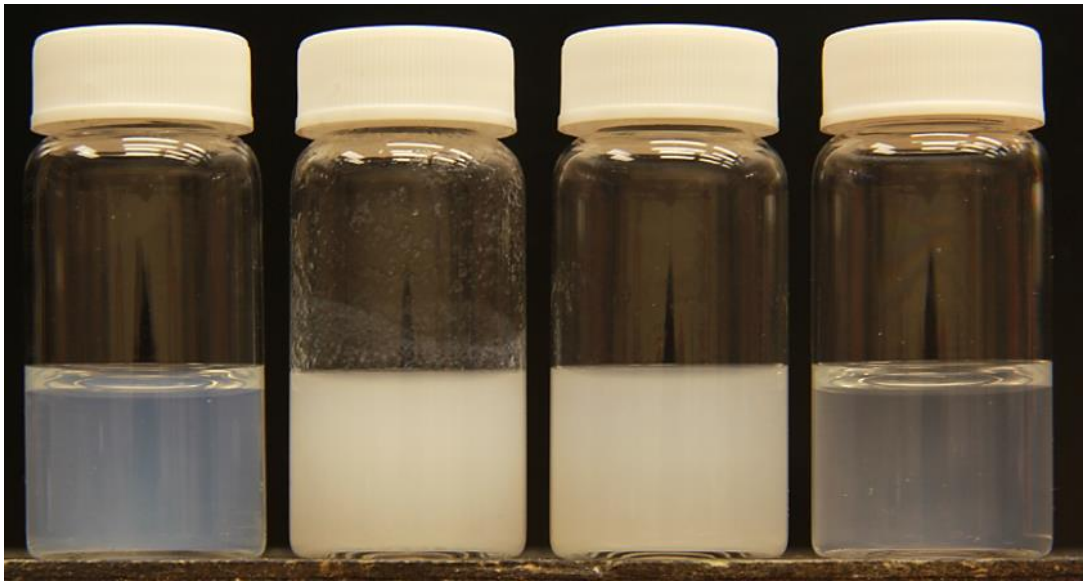

Figure 6.2: From left to right, suspensions of CNCs, CNFs, TEMPO oxidized CNFs, and T-CNFs in water are illustrated, respectively. All suspensions are at approximately 1 wt % concentration.

To DIW print purely CNF gels, it is crucial to make a stable and uniform CNF suspension with the desired viscosity and fluid dynamic properties. To increase the dispersibility of CNFs in water, reducing the CNFs' length distribution and introducing high charge density on the CNFs' surfaces are two important factors. It has been known that TEMPO oxidation of CNFs can increase the negative repulsive charge between individual fibers.[221, 223-226] Combined with high pressure homogenization, a highly defibrillated and highly charged TEMPO CNF suspension can be formed (Figure 6.2). After concentrating the suspension through vacuum filtration, the resultant T-CNF gel can be DIW processed into various 3D structures. The overall processing scheme is summarized in Figure 6.3.

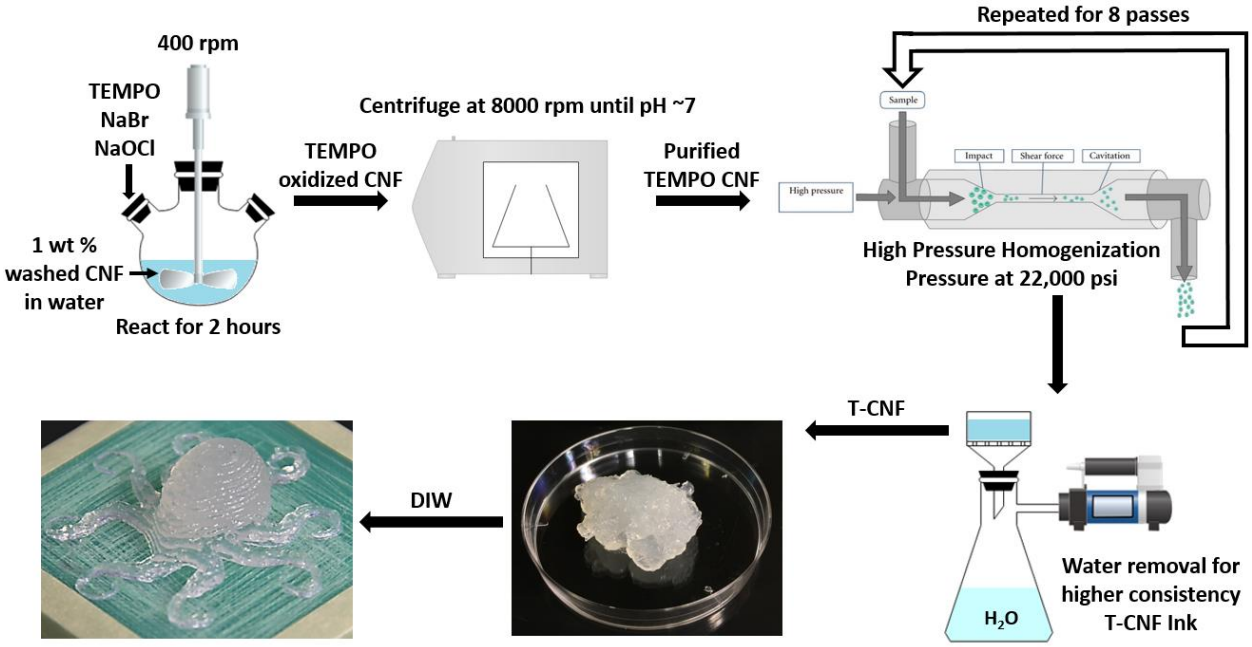

Figure 6.3: Overall processing scheme for the generation of DIW processable T-CNF gel from the original CNFs in water suspension as obtained from the University of Maine Process Development Center.

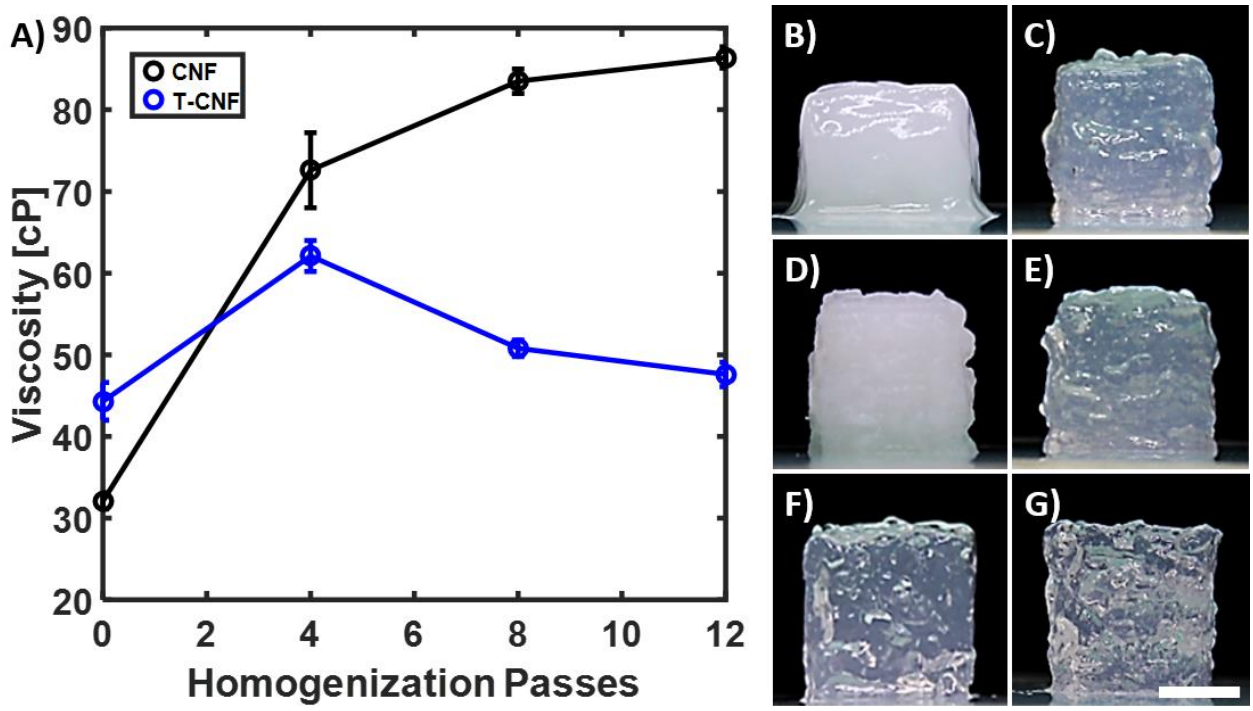

Figure 6.4: (A) Prior to T-CNF gel concentrating for DIW processing, viscosity of CNF and T-CNF suspensions as a function of homogenization passes are illustrated. All suspensions were at approximately 1 wt %. (B-G) After T-CNF gel concentrating, the gels were DIW processed into 1 cm^3 cubic structures. When the T-CNF gels were concentrated to 2.8 wt %, gels with (B) 0, (C) 4, (F) 8, and (G) 12 homogenization passes yielded viscosities of 368, 488, 515, and 505 cP, respectively. When the T-CNF gels were concentrated to approximately 515 cP, gels with (D) 0, (E) 4, (F) 8, and (G) 12 homogenization passes had T-CNF concentration of 3.6, 3.0, 2.8, and 2.8 wt %, respectively. The displayed scale bar represents 5 mm.

As the number of repeating homogenization passes was varied, the viscosity of CNF and T-CNF suspensions at approximately 1 wt % was studied to evaluate the effect of homogenization on DIW processability (Figure 6.4A). The viscosity of the CNF suspensions increased as the number of homogenization passes increased, which could be explained by the increase in fiber-fiber interactions as CNFs became increasingly defibrillated. On the other hand, increasing passes of homogenization led the viscosity of T-CNF suspensions to first increase and then decrease. After 4 homogenization passes, it appeared that repulsive interactions from the carboxyl groups' functionalization dominated over the attractive interactions between individual fibers. Due to the decrease in fiber-fiber interactions, the viscosity of the suspensions correspondingly decreased. T-

CNF suspensions homogenized with 8 and 12 passes also displayed similar viscosity, which suggested that 8 homogenization passes were enough to yield a suspension with stabilized and uniform fiber length distribution. The fiber length distributions of CNF and T-CNF suspensions processed from different homogenization conditions are also qualitatively illustrated in Figure 6.5.

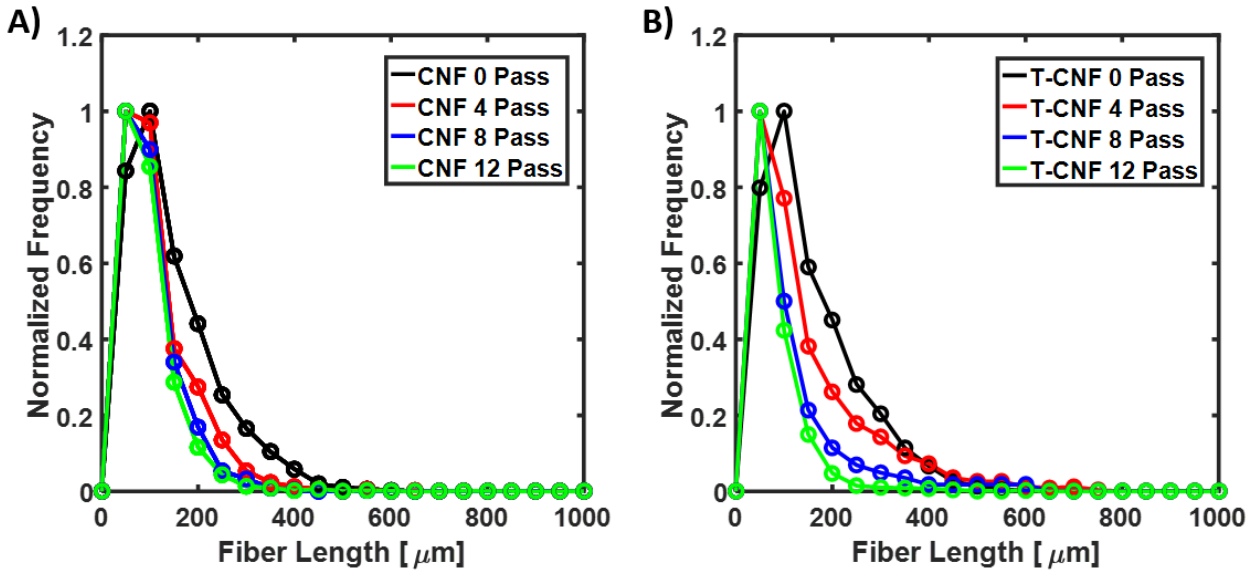

Figure 6.5: (A) Qualitative estimation of CNFs' fiber length distribution after the suspension was homogenized for 0 (black), 4 (red), 8 (blue), and 12 (green) repeated homogenization passes. (B) The corresponding qualitative estimation of T-CNFs' fiber length distribution from different homogenization conditions.

T-CNF suspensions with different numbers of homogenization passes were also concentrated through vacuum filtration, and then DIW processed into 1 cm^3 cubic structures (Figure 6.5B to 6.5G). T-CNF gel at 2.8 wt % and without any homogenization yielded a cubic structure, but structural sagging occurred within 5 minutes after DIW printing because the viscosity of 368 cP was too low to maintain the structure (Figure 6.5B). On the other hand, 2.8 wt % T-CNF gel with 4 homogenization passes had a viscosity of 488 cP, which allowed the overall shape to be maintained. However, the gel deposition was still slightly inhomogeneous, which led to various defects within the printed structure (Figure 6.5C). Though there are many factors that can contribute to structural sagging, the gel's viscosity appeared to be the dominant contributing

factor to the 3D printed gel's ability to hold its shape after DIW processing. When T-CNF suspensions with different numbers of homogenization passes were all concentrated such that they had similar viscosities of around 515 cP, the resultant DIW processed cubic structures were able to maintain their shape for long periods of time (Figure 6.5D to 6.5G). Nevertheless, due to irregular gel deposition during DIW processing, gels with 4 passes or less still resulted in some defects in the 3D printed structure (Figure 6.5D and 6.5E). Meanwhile, gels homogenized with 8 and 12 passes yielded structures with very few defects in the 3D printed cubic structures (Figure 6.5F and 6.5G). From qualitative visual inspection, the straightness of cube's edges from Figure 6.5F and 6.5G is superior to that from Figure 6.5D and 6.5E. Moreover, the fidelity of cube's corners is also better in comparison, as the corners are more succinct and regular. These results suggested that 8 homogenization passes were required to fully defibrillate the carboxylated CNFs, and produce gels that can be DIW processed into structures with sufficient quality. Since 12 homogenization passes did not yield any significant improvement in the fiber length distribution uniformity or in the final printed cubic structural quality, 8 homogenization passes were used to develop DIW processable T-CNF gel for the rest of this study.

Table 6.1: The surface specific charge densities of CNFs, T-CNFs, and Kymene as determined by polyelectrolyte charge titration.

Materials	w **(g)**	V_b **(mL)**	V_p **(mL)**	**c (M)**	**Estimated Surface Specific Charge Density (mmol/kg)**
CNFs	0.01	10.969	10.514	0.001	-46
T-CNFs	0.01	10.969	2.605	0.001	-826
Kymene	0.001	8.307	2.516	0.001	5356

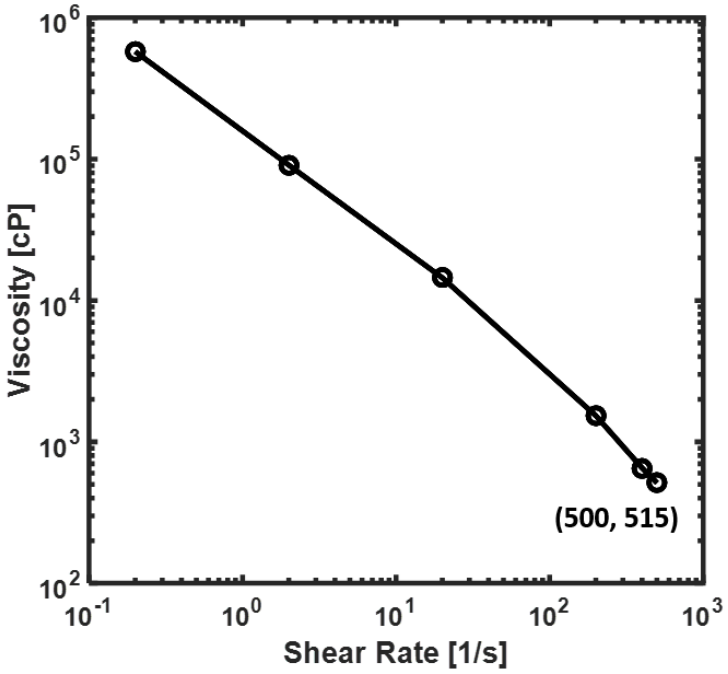

Figure 6.6: While under a room temperature of 22 °C, viscosity versus shear rate curve for 2.8 wt % T-CNF gel obtained from 8 homogenization passes is illustrated.

Polyelectrolyte charge titration was also performed to determine the surface specific charge densities of CNFs, T-CNFs, and Kymene, which were found to be about -50, -830, and 5360 mmol/kg, respectively (Table 6.1). CNFs' tendency to agglomerate and form non-uniform network entanglements is attributed to the low surface specific charge density of only -50 mmol/kg. With TEMPO oxidation and high pressure homogenization, the resultant T-CNFs' surface specific charge density decreased significantly to -830 mmol/kg. When comparing the estimated surface specific charge density of the original 3.4 wt % CNF gel (-1.6 mmol/kg) to the 2.8 wt % T-CNF gel (-19.8 mmol/kg), this nearly 10 fold decrease in surface specific charge density allowed the T-CNF gel to be deposited with a consistent pressure during DIW processing. The 2.8 wt % T-CNF gel also displayed shear thinning behavior with a viscosity of 515 ± 6 cP at the highest tested shear rate (Figure 6.6), which allowed the gel to be processed by DIW into different complicated structures while still maintaining the processed shapes. Due to the relatively high viscosity of the

T-CNF gel, no support material was needed during DIW processing, which also reduced the cost and generation of waste materials.

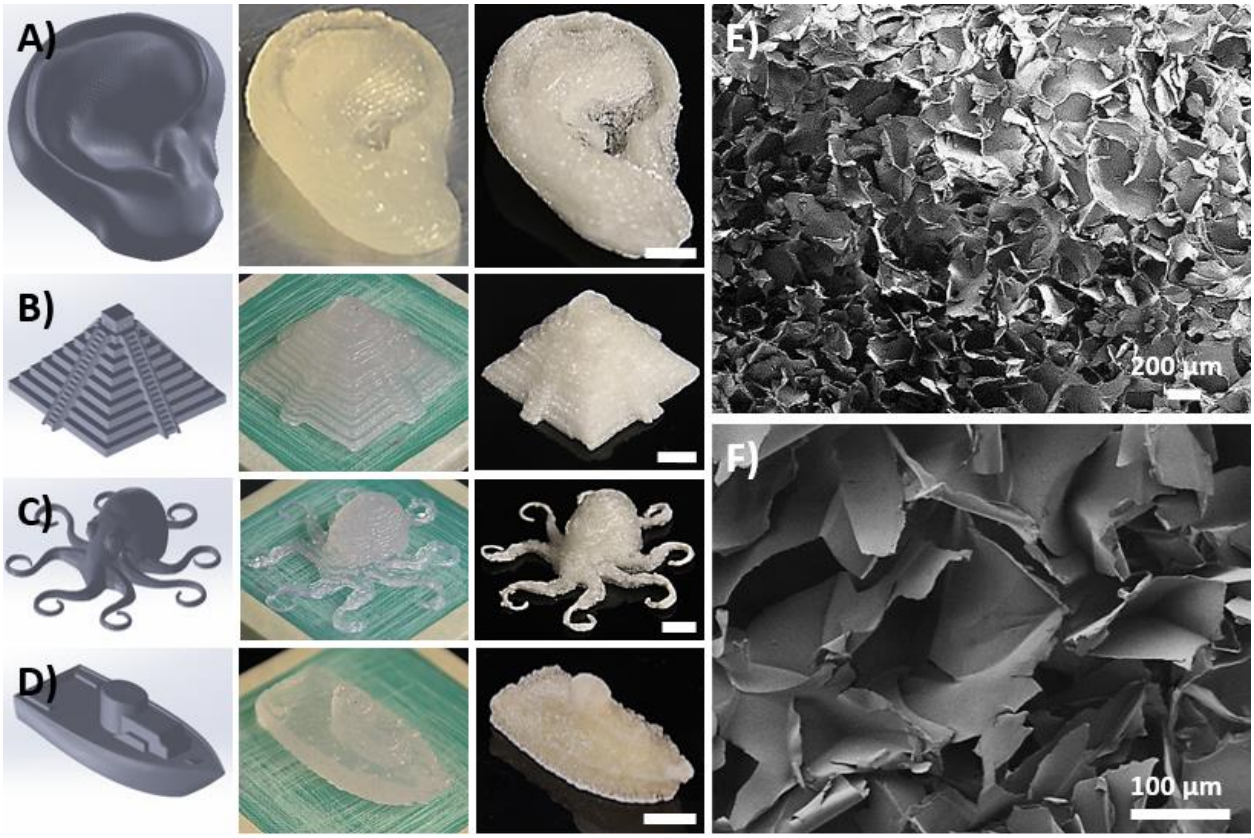

Figure 6.7: DIW 3D printed (A) ear model, (B) pyramid, (C) octopus, and (D) boat structures from 2.8 wt % T-CNF gel and 800 µm nozzle tip. The first column is SolidWorks model, the second column is DIW 3D printed gel structures, and the third column is resultant structures after freeze-drying. Displayed scale bars are 1 cm. (E) SEM characterization of the internal surface and pore morphology from cross sections of 3D printed cubic T-CNF aerogel. (F) Polyhedron like pores in the micro-size regime were observed at higher magnification.

The SolidWorks CAD models, the DIW processed gel structures, and the freeze-dried aerogel structures are correspondingly illustrated in Figure 6.7. With a deposition pressure of 2.5 psi, nozzle movement speed of 10 mm/s, G-code width and height of 0.8 cm, and nozzle size of 800 µm, 3D T-CNF gel structures were reproducibly printed that closely resembled the CAD designs. There was also minimal shrinkage or damage to the aerogel structures after the ice crystals were sublimated during freeze-drying. 1 cm^3 cubic T-CNF aerogel was also processed by DIW

and freeze-drying, and the resultant density and porosity of the aerogel were determined to be approximately 26 mg/cm^3 and 98 %, respectively. The internal surface and pore morphology were characterized by FE-SEM (Figure 6.7E). The inner pore morphologies displayed 2D sheet-like skeleton structures with polyhedron-like pores. During freeze-drying, T-CNFs likely agglomerated along the longitudinal direction due to their high aspect ratio. The overall internal surface and pore morphology of 3D printed T-CNF aerogels were consistent with other literature reports.[209-210, 212] SEM analysis also revealed that the 3D printed T-CNF aerogel exhibited pore sizes in the macroporous regime, which was likely because slow freezing rate favored ice crystal growth much more than ice crystal nucleation (Figure 6.7F).

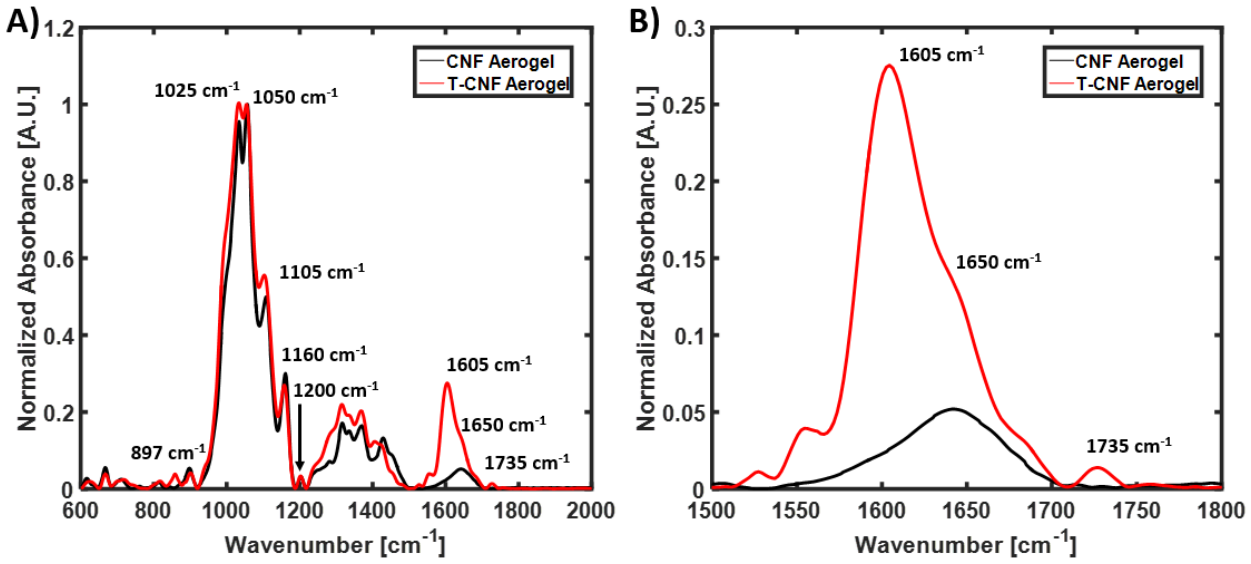

Figure 6.8: (A) Resultant ATR-FTIR spectra from CNF aerogel without cross-linking (black), and ATR-FTIR spectra from 3D printed T-CNF aerogel with cross-linking (red). The spectra were normalized to the peak of the C-O-C vibration in the cellulose pyranose rings (1050 cm^{-1}). (B) The spectra were further zoomed into a wavenumber range between 1500 and 1800 cm^{-1} to better illustrate the peak emergence of C=O stretching in carboxylate groups (1605 cm^{-1}), and C=O stretching in ester bonds (1735 cm^{-1}).

To crosslink the T-CNF aerogel, oven treatment at 120 °C for 3 hours was performed. FTIR spectra of CNF aerogel without crosslinking and Kymene crosslinked T-CNF aerogel were obtained and are illustrated in Figure 6.8. The crosslinking mechanism can be explained by the

self-polymerization of Kymene through amide linkages between carboxylic acid groups and amino groups via condensation reactions, while also covalently forming ester linkages between the carboxylic groups on the cellulosic surfaces and the azetidinium groups on Kymene (Figure 6.9).[227]

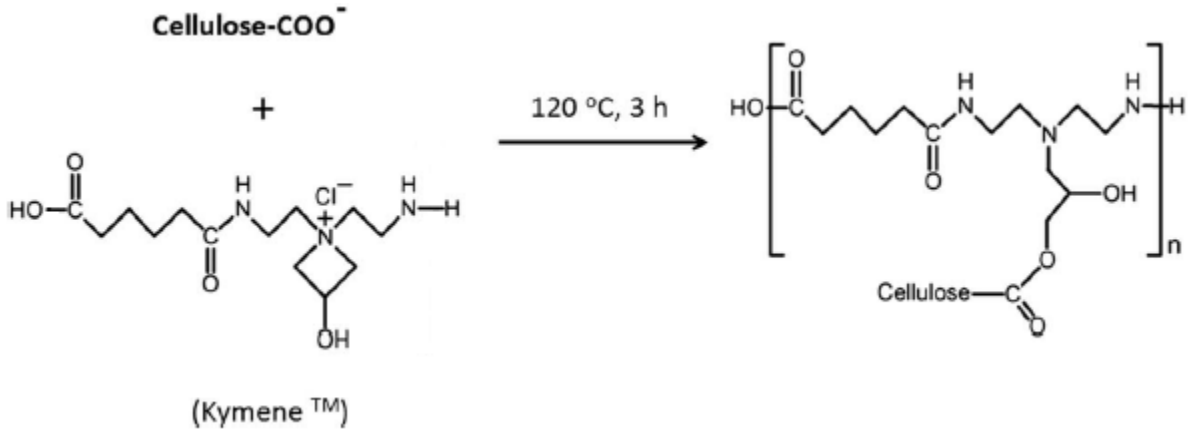

Figure 6.9: Cross-linking mechanism of Kymene and T-CNFs. Kymene self-polymerizes through amide linkages via condensation reactions, while also forming ester bonds between the carboxyl groups on T-CNFs and the azetidinium groups on Kymene.[227]

As a result, the degree of crosslinking was determined by the amount of available carboxylic groups for ester bond formations, and the amount of Kymene added to the gel formulation. The wavenumbers at 897 cm^{-1}, 1025 cm^{-1}, 1050 cm^{-1}, 1605 cm^{-1}, and 1735 cm^{-1} are associated with C-O-C deformation of the β 1-4 glycosidic linkage, C-O-H vibration in the cellulose pyranose rings, C-O-C vibration in the cellulose pyranose rings, C=O stretching of carboxylate groups, and C=O stretching of ester bonds, respectively. The wavenumbers at 1105 cm^{-1}, 1160 cm^{-1}, and 1200 cm^{-1} are related to the C-O/C-C stretching, C-O-C asymmetric stretching of the β 1-4 glycosidic linkage, and C-O-H in plane deformation. Additional peaks at 1316 cm^{-1}, 1335 cm^{-1}, 1370 cm^{-1}, 1425 cm^{-1}, and 1650 cm^{-1} have been associated with CH_2 wagging, OH bending, CH deformation vibration, CH_2/O-C-H in-plane deformation, and OH stretching of adsorbed water, respectively (Figure 6.8A). Major peaks at 2900 cm^{-1} and 3340 cm^{-1} were also observed in both spectra; these have been assigned to C-H stretching and OH stretching,

respectively.[227-231] Once the spectra were normalized to the peak at 1050 cm^{-1}, the largest difference between the two spectra occurred at 1605 cm^{-1}, and 1735 cm^{-1} (Figure 6.8B). It was evident that not only was the TEMPO oxidation confirmed by the presence of carboxylate groups at 1605 cm^{-1}, but an excess of carboxylate groups was actually observed even after crosslinking. As a result, Kymene at a higher concentration can be added to the gel formulation to further increase the aerogel's crosslinking degree. The C=O ester bond at 1735 cm^{-1} also confirmed the presence of crosslinking through ester bond formations. Overall, the TEMPO oxidation of CNFs and the subsequent Kymene crosslinking was confirmed by FTIR, which resembled the results described by Saito et al. and other literature reports.[221, 225, 232] Furthermore, the resultant crosslinked T-CNF aerogel's structural integrity was also maintained under water and applied force. Interestingly, the T-CNF aerogel's density did not significantly change after the aerogel was crosslinked, which was likely due to only a small amount of cross-linker was added to the gel formulation (2 wt % by dry cellulose mass).

The mechanical properties of the T-CNF aerogels were tested by the MTS machine in compression under the dry or wet state, and the initial Young's modulus, strain before densification, and the corresponding stress were determined. The initial compression Young's modulus was determined from the slope of the elastic region of the stress-strain curve, which was typically less than 0.5 % strain. The average initial Young's modulus of the uncrosslinked T-CNF aerogels was approximately 2.1 ± 0.1 MPa (Figure 6.10A).

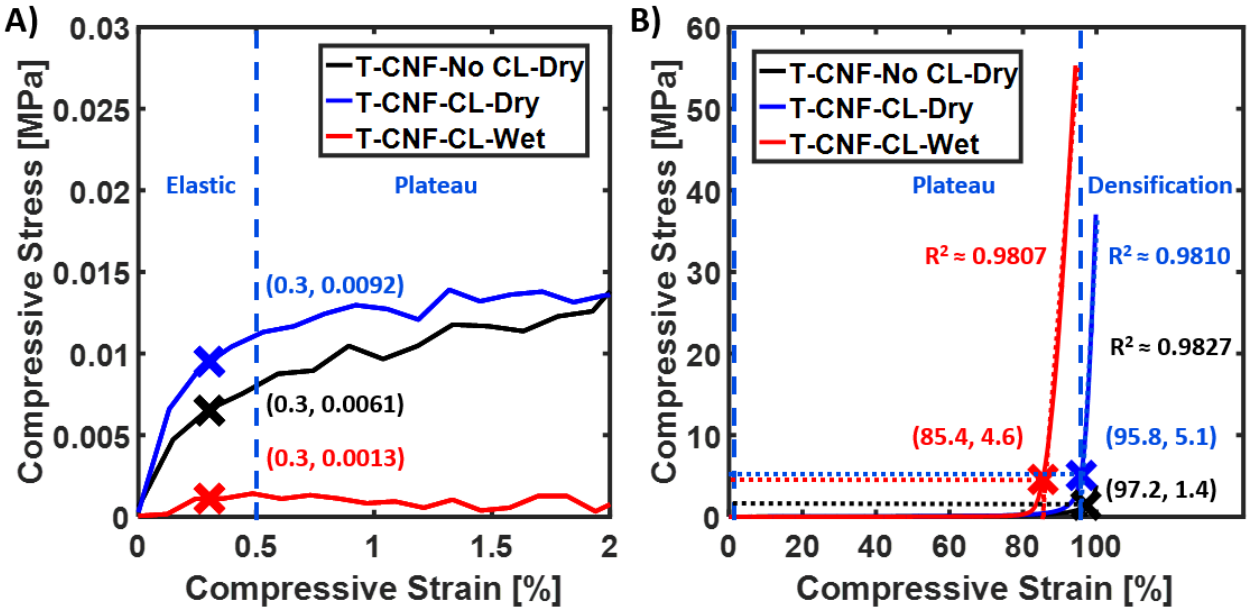

Figure 6.10: (A) Representative mechanical compression curves for uncrosslinked (No CL) T-CNF aerogel under the dry state (black), cross-linked (CL) T-CNF aerogel under the dry state (blue), and cross-linked T-CNF aerogel under the wet state (red). The elastic, plateau, and densification regimes in the compressive stress-strain curve are also illustrated. The mechanical compression curves were zoomed into a compressive strain range between 0 and 2 % to illustrate the slope of the elastic region, which was typically less than 0.5 % strain. (B) The corresponding full mechanical compression curves, and their respective strain and stress before densification are also illustrated. The corresponding strain and stress before densification for each curves are represented by the symbol X.

After crosslinking, the average initial Young's modulus of the dry state T-CNF aerogels increased to 3.2 ± 0.2 MPa. This indicates that crosslinking actually stiffened the dry state aerogels due to covalent linkages between T-CNFs and the polymerized Kymene network. Once the aerogel was crosslinked, the water saturated aerogels were able to withstand applied force without structural collapse. This was likely due to CNFs' ability to form a physically entangled network, which was then crosslinked with the polymerized Kymene through ester linkages and ultimately formed a double interpenetrating network. However, crosslinked T-CNF aerogel under the wet state was significantly softened when compared to the dry state, as an average wet state Young's modulus of 470 ± 30 kPa was determined. This was attributed to water molecules disrupting the

hydrogen bonding interactions in T-CNFs. Overall, T-CNF aerogel was highly deformable, as the compressive stress-strain curve exhibited elastic, plateau, and densification regimes (Figure 6.10A and 6.10B). The strain before densification represented the extent to which aerogels can be reversibly compressed without significant loss in shape recovery, whereas the densification regime signified irreversible pore collapse, pore wall contact, and sudden hardening of the aerogel.

For uncrosslinked T-CNF aerogel under the dry state, an impressive average compressive strain before densification of 96.8 ± 1.1 % was achievable (Figure 6.10B). After crosslinking, the dry state T-CNF aerogel still had an average compressive strain of 96.3 ± 0.5 % before densification occurred. The dry state aerogel's strain before densification was similar regardless of crosslinking. This was likely because crosslinking had little effect on the pore sizes (pore wall to pore wall separation distances) of the dry state aerogel, so practically equivalent deformability was achieved before densification occurred. Under the wet state, an average compressible strain as high as 84.6 ± 0.9 % was possible before the aerogel began to densify. During compression, wet state aerogels are likely able to better resist deformation because the pores are contained with water instead of air. As a result, the decrease in strain before densification for aerogels under the wet state could be attributed to entrapped water within the pores of the aerogels. Overall, the highly deformable nature of T-CNF aerogel was confirmed. Finally, the determined average stress before densification was 1.4 ± 0.1 MPa, 5.7 ± 0.5 MPa, and 4.9 ± 0.3 MPa for uncrosslinked T-CNF aerogel in the dry state, crosslinked T-CNF aerogel in the dry state, and crosslinked T-CNF aerogel in the wet state, respectively. These results revealed that Kymene served as an efficient strength additive for T-CNF aerogel. This was attributed to Kymene's ability to strengthen the connectivity between T-CNFs, as additional carboxylic groups were functionalized onto CNFs during TEMPO oxidation. Once the aerogels were saturated with water, the formation of a double interpenetrating

network also counteracted the hydrogen bond disruption between T-CNFs to produce an average final stress of 4.9 MPa before densification occurred. For the remaining of this study, only the properties of crosslinked T-CNF aerogels are discussed.

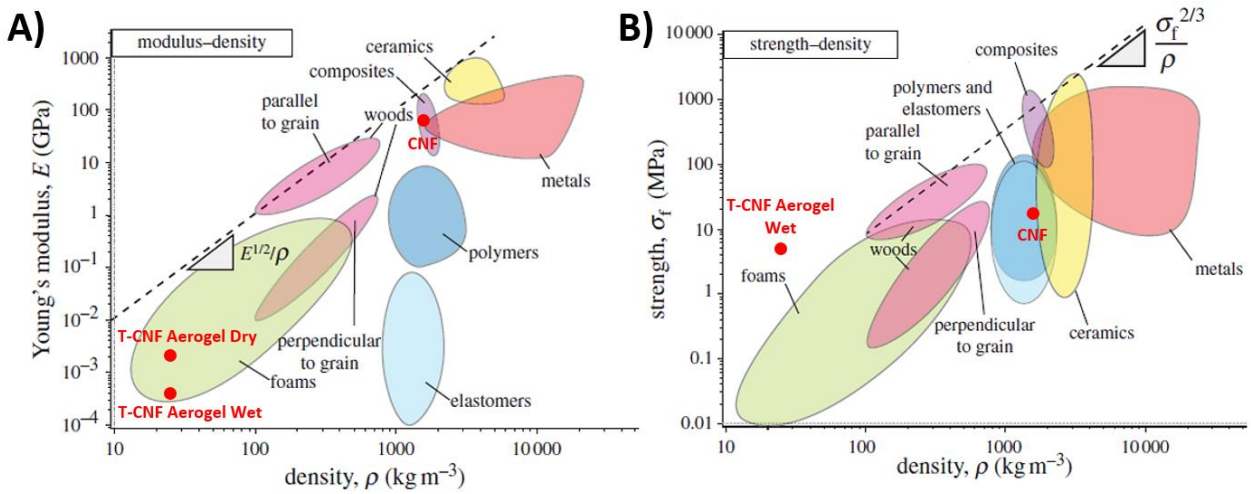

Figure 6.11: (A) Young's modulus-density Ashby plot for different engineering materials; the specific Young's modulus of 3D printed T-CNF aerogels under the dry and wet state and the literature established mechanical properties of CNFs are also included. (B) The corresponding strength-density Ashby plot, and the specific strength before densification of 3D printed T-CNF aerogels under the wet state are illustrated. The performance index of $\sigma^{2/3}/\rho$ illustrates the material's ability to resist bending stresses. Each point along the dashed line have the same performance index value.[47]

From modulus-density and strength-density Ashby plots as described by Gibson et al.,[47] the specific Young's modulus and specific strength of T-CNF aerogels are also illustrated (Figure 6.11). These results indicated that the 3D printed T-CNF aerogels under the dry and wet state both have specific Young's moduli that are similar to those of other foam like materials (Figure 6.11A). Though the corresponding aerogel's specific yield strengths are also comparable to other foam like materials, the wet state T-CNF aerogels displayed specific strength before densification (the maximum strength that can reversibly obtained during compression) that not only exceeds that of other foam-based materials, but also approaches the strength performance index of other high performance materials (Figure 6.11B). The shape recoverability and recovery repeatability of

water saturated T-CNF aerogels with different amounts of compression (15 %, 50 %, and 80 % compression) were also characterized by DMA (Figure 6.12A). For T-CNF aerogel under the wet state, the average recovery percentages were determined to be around 99.7 ± 0.3 %, 98.0 ± 0.2 %, and 95.5 ± 1.4 % for compression amounts of 15, 50, and 80 %, respectively. Because the strain before densification for T-CNF aerogel under the wet state was approximately 85 %, it appeared that shape recovery of nearly 95 % was possible as long as the amount of compression did not exceed the strain before densification. The average percentages of aerogel recovered after 5 cycles of compression and release were 98.8 ± 0.5 %, 96.9 ± 0.1 %, and 92.6 ± 0.4 % for compression amounts of 15, 50, and 80 %, respectively. The decrease in shape recovery percentage with the number of compression-release cycles suggested that the compressions were slightly irreversible, but the percentage of aerogel recovered still remained higher than 90 % with a compression amount of 80 %. The water saturated T-CNF aerogel was also compressed and released in successively increasing compressive strain increments of 20 %, and the stress-strain behavior of the aerogel during loading and unloading is provided (Figure 6.12B).

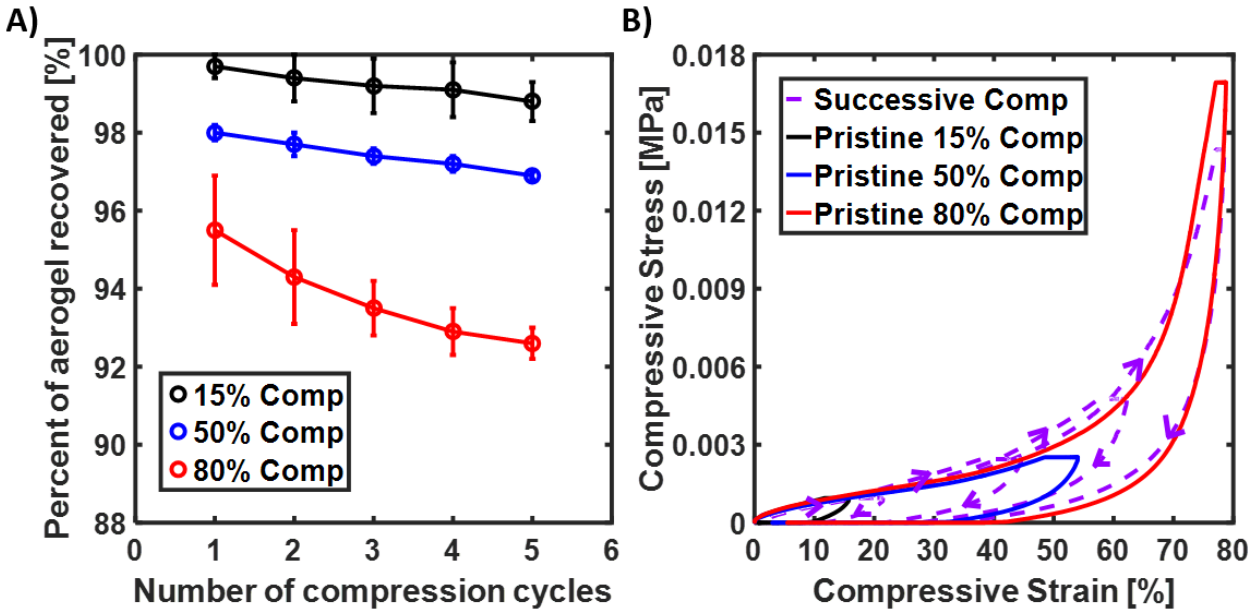

Figure 6.12: (A) DMA characterization of the shape recovery and the compression-release cyclic recovery repeatability of water saturated T-CNF aerogels with 15 % (black), 50 % (blue), and 80 % (red) compressions. (B) Stress-strain curve of water saturated T-CNF aerogel during loading and unloading cycle of successively increasing compression strain amount (purple, dashed line) is illustrated. Stress-strain curves of three pristine water saturated T-CNF aerogels during loading and unloading cycles of different compression amounts are also illustrated.

The resultant stress-strain curve suggested that the compressibility of T-CNF aerogel is highly reversible, as the loading curves at successively increasing compression amounts were practically overlapping with each other. Nonetheless, hysteresis was present between the loading and unloading curves, which suggested that there was dissipative energy lost during compression and release. The stress-strain behavior is also different from the well-known Mullins effect,[233-234] which describes the stress softening behavior of rubber-like materials. The main difference occurs in the subsequent reloading cycles, where the reloading curves follow the original primary loading path instead of following the previous cycle's unloading path. It appears that hydrogen bond reformations throughout the aerogel can be fully re-established during the one minute of stress-free interval between each compression and release cycle, which produced the highly reversible and reproducible compressive behavior of the aerogel. The stress-strain curves from three pristine

T-CNF aerogels compressed and released at different compression amounts are also provided; they displayed compressive behavior similar to that of the aerogel compressed at successively increasing amounts of compression. The stress-strain curves of T-CNF aerogels during the 5 cycles of compression and release further support the aerogel's compressive reversibility and reproducibility, as the stress-strain curves nearly overlapped with one another during each compression and release cycle (Figure 6.13). Overall, the deformability of the water saturated T-CNF aerogel and the repeatability of its nearly full shape recovery was demonstrated.

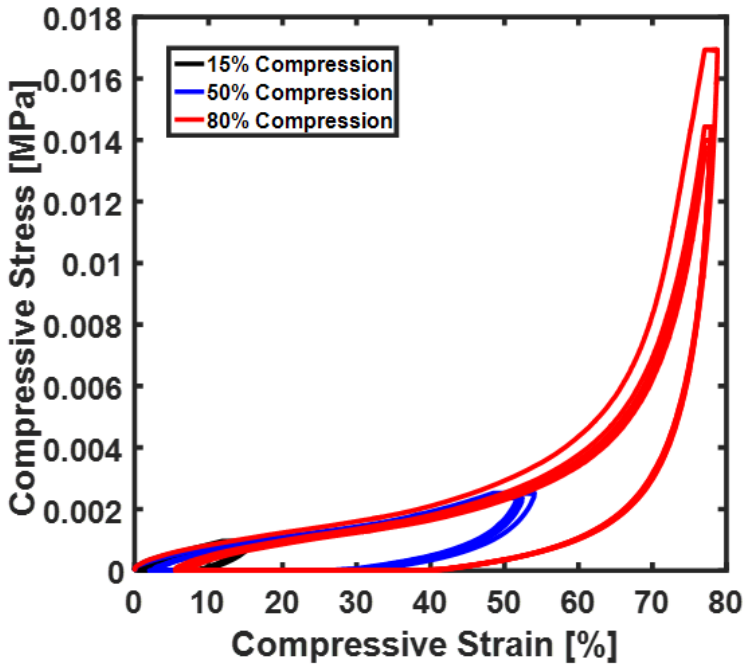

Figure 6.13: Loading and unloading stress-strain curve of water saturated T-CNF aerogels during the 5 compression-release cycles at different compression amount.

The water absorption capacity of T-CNF aerogel was also characterized by gravimetric methods. The average water absorption capacity of the T-CNF aerogels was determined to be 35 ± 1 g/g. It is apparent that T-CNF aerogels can absorb a large amount of water-based on the original dry aerogel weight. The reason for efficient water uptake for T-CNF aerogel is likely due to the swelling of amorphous regions in T-CNFs and water retention in the aerogel's pores. The

theoretical water absorption capacity was calculated to be 38 g/g. This suggests that approximately 8 % of the pore volumes were inaccessible by water, as only 92 % of the theoretical water absorption capacity was measured experimentally. This could be due to slight defects within the 3D printed aerogels or to potential air entrapment within the aerogels.

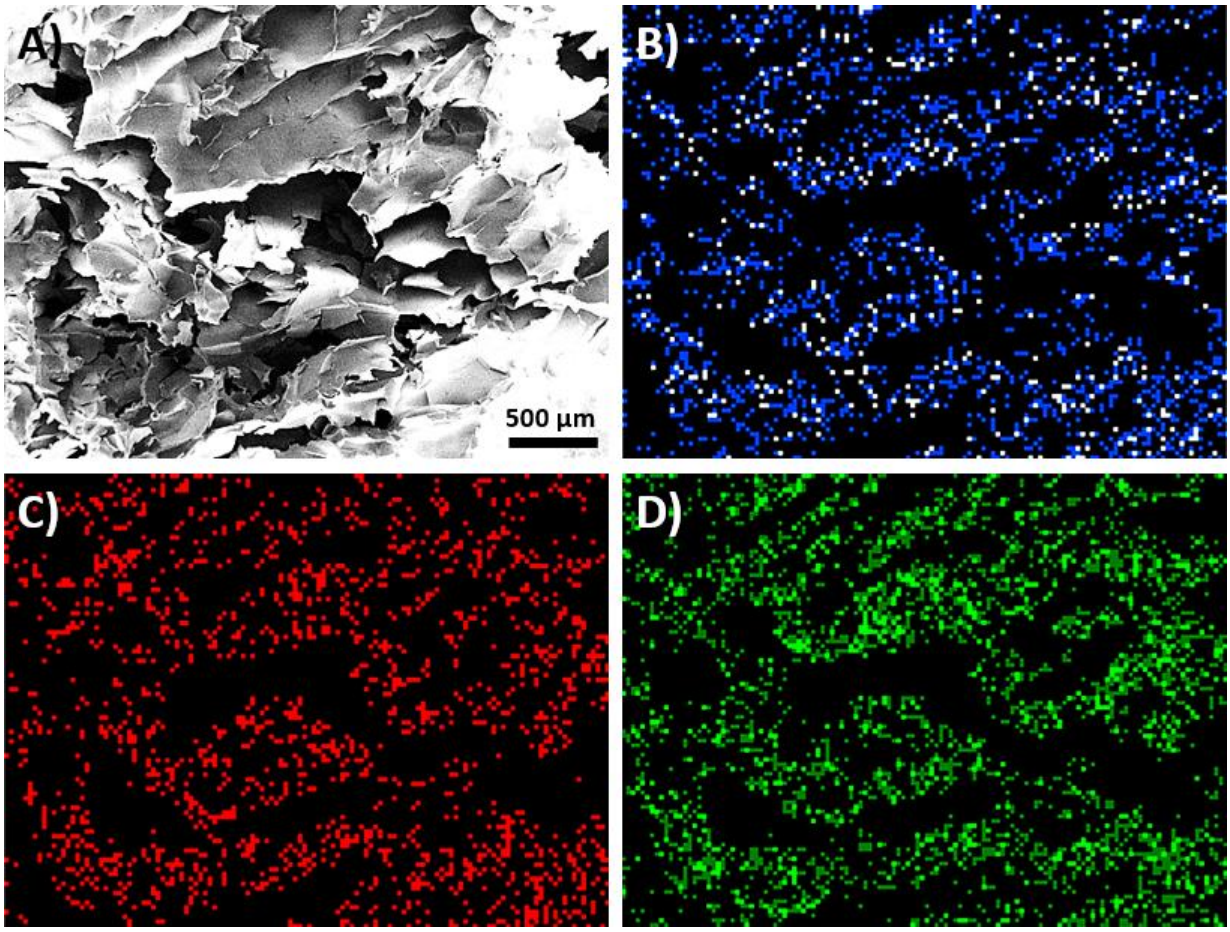

Figure 6.14: (A) SEM image of the PFOTS modified T-CNF aerogel's cross section that was utilized during SEM-EDS imaging. (B) The carbon mapping distribution across the aerogel's cross section was labeled in blue. (C) The oxygen mapping distribution across the aerogel's cross section was labeled in red. (D) The fluorine mapping distribution across the aerogel's cross section was labeled in green.

3D printed T-CNF aerogels can be used as templates for facile addition of functionality by various modification approaches. For example, the hydrophilic T-CNF aerogel can be made hydrophobic through chemical vapor deposition (CVD) with PFOTS. Before CVD, water and

decane absorption capacities of the hydrophilic aerogel were about 35 g/g and 8 g/g, respectively. After CVD, water and decane absorption capacities of the hydrophobic aerogel were about 1.01 g/g and 4 g/g, respectively. As a result, it was confirmed that CVD with PFOTS had rendered the T-CNF aerogel hydrophobic. The homogeneity of the deposited PFOTS was also qualitatively confirmed by SEM-EDS imaging (Figure 6.14), where the fluorine distribution (unique to PFOTS) was observed to coincide with the carbon and oxygen distribution (dominantly contributed by cellulose) throughout the entire T-CNF aerogel's cross section. In fact, water contact angle assessment of 9 different locations revealed an average contact angle of 141 ± 7 °, where the largest measured contact angle was 150 ° (Figure 6.15A). Though the hydrophilic T-CNF aerogel remained below the water meniscus after 3 hours of water immersion (Figure 6.15B), the nearly super hydrophobic T-CNF aerogel rose back to the top of the water meniscus after forcibly immersing the aerogel under water for 3 hours (Figure 6.15C).

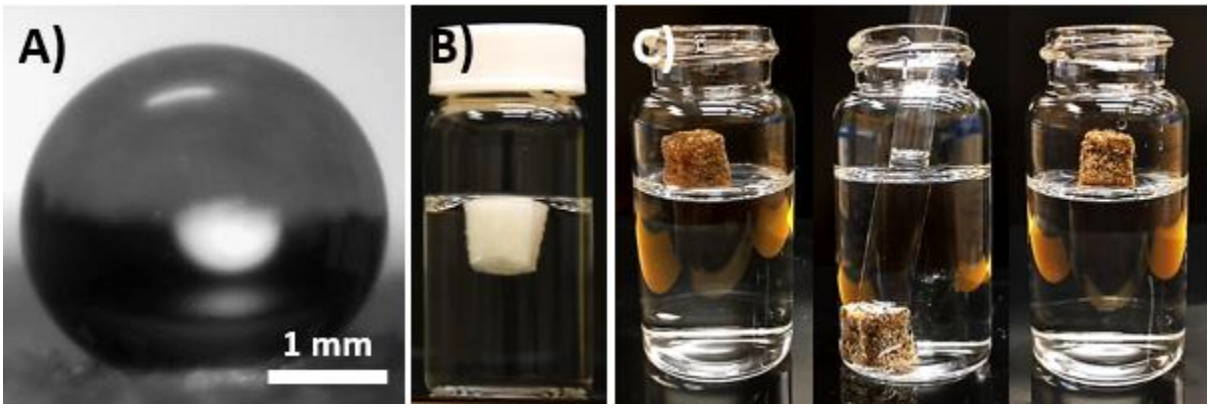

Figure 6.15: (A) Static sessile drop water contact angle measurement on the PFOTS modified T-CNF aerogel. (B) Photographic image of the hydrophilic T-CNF aerogel that is floating below the water meniscus after it was immersed in water for 3 hours. (C) Photographic images of the PFOTS modified T-CNF aerogel that floated on top of the water meniscus before immersing in water (Left), the PFOTS modified T-CNF aerogel that was forcibly immersed in water (Middle), and the PFOTS modified T-CNF aerogel that rose back to the top of the water meniscus after forcibly immersing under water for 3 hours (Right) are illustrated.

Water droplets can also easily roll off the surface of nearly super hydrophobic T-CNF aerogel, as air pockets on the surfaces of the aerogel likely created a Cassie-Baxter wetting state

that further enhanced the hydrophobic effect (Figure 6.16A and 6.16B). Although the contact angle hysteresis (CAH, which defines the difference between advancing and receding angles) was not rigorously characterized, it was estimated that the PFOTS modified T-CNF aerogel should have an extremely low water CAH (approximately 1 °). This was because even the slightest tilt of the aerogel will result in the water droplet rolling off the aerogel's surface. As a result, it is possible to modify the 3D printed T-CNF aerogels into a highly water non-wettable and water non-absorbing aerogel through a CVD process with PFOTS.

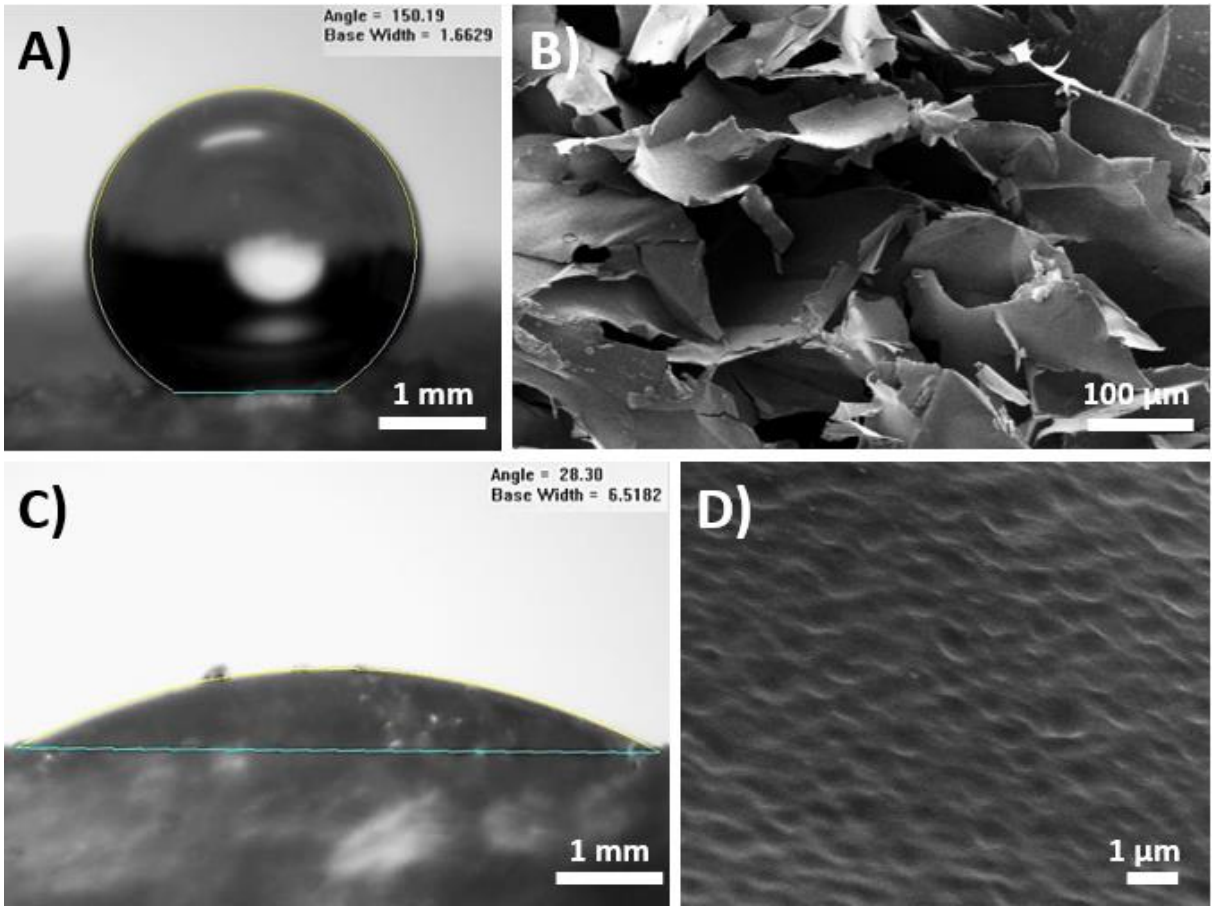

Figure 6.16: (A) Representative optical video camera image of water contact angle assessment on the PFTOS modified T-CNF aerogel. (B) SEM characterization of PFOTS modified T-CNF aerogel's surface, which revealed an aerogel surface with air pockets that can enhance hydrophobicity. (C) Representative optical video camera image of decane contact angle assessment on the PFTOS modified T-CNF aerogel. (D) Similar SEM characterization at higher magnification, which illustrated the surface roughness characteristics of the PFOTS modified T-CNF aerogel.

The PFOTS modified T-CNF aerogel also displayed increased oil repellency, as the decane absorption capacity decreased nearly 2 fold after the modification. However, the aerogel was still oleophilic because decane contact angle assessment of 2 different locations revealed an average contact angle of 28 ± 1 ° (Figure 6.16C). Interestingly, PFOTS modification did not result in the superoleophobic properties as described by Aulin et al.[216] It is postulated that the superoleophobic property is highly dependent on surface roughness, so it is possible that the surface roughness of the PFOTS modified T-CNF aerogel (Figure 6.16D) is simply not high enough to support a decane contact angle greater than 90 ° even though the aerogel has a Cassie-Baxter like surface. Utilizing the average water contact angle, decane contact angle, Young's equation, and Fowkes' method, the surface energy of the PFOTS modified T-CNF aerogel was estimated to be around 24.6 mN/m, which was only slightly higher than the surface tension of decane. The estimated surface energy of the PFOTS modified T-CNFs also helped explain the difference in water and decane absorption reduction degree (35 fold versus 2 fold decrease), as the relative difference between the aerogel's estimated surface energy (24.6 mN/m) and water's surface tension (72.8 mN/m) was much larger than the difference with decane's surface tension (23.8 mN/m). Overall, the ability to modify the hydrophobicity of the 3D printed T-CNF aerogels with a simple CVD process was confirmed, and this can have potential applications in oil-in-water separation. To demonstrate the potential for oil/water separation, Epson 60 magenta and Oil Blue N were used to dye the water and decane phase, respectively. As a demonstration, water droplets (dyed red) in decane was successfully removed by the 3D printed hydrophilic T-CNF aerogels (Figure 6.17A and 6.17B). Conversely, decane droplets (dyed blue) in water was successfully removed by the PFOTS modified T-CNF aerogels (Figure 6.17C and 6.17D).

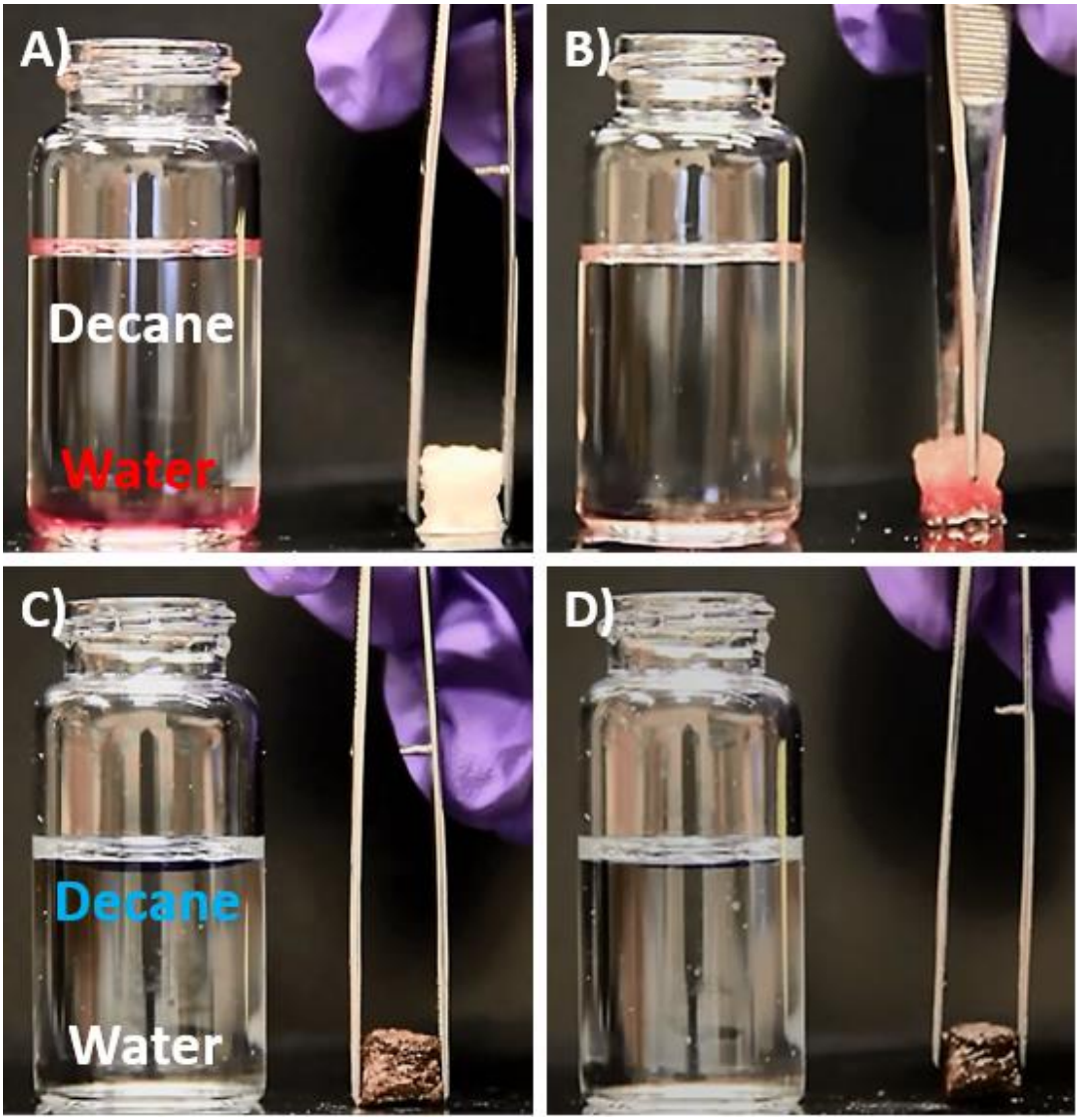

Figure 6.17: (A) Before preforming water-oil separation, the hydrophilic T-CNF aerogel structure and the solution of water droplets (dyed red) in decane are illustrated. (B) After performing water-oil separation, the hydrophilic T-CNF aerogel structure was able to successfully remove the water droplets from decane. (C) Before performing oil-water separation, the hydrophobic T-CNF aerogel structure and the solution of decane droplets (dyed blue) in water are illustrated. (D) After preforming oil-water separation, the hydrophobic T-CNF aerogel structure was able to successfully remove the decane droplets from water.

The 3D printed T-CNF aerogel could also be rendered electrically conductive by the incorporation of PEDOT:PSS, which is commonly used in preparing conductive polymer surfaces. Surprisingly, even though PEDOT:PSS was water soluble, it remained associated with the CNF network after the PEDOT:PSS templated T-CNF aerogel was immersed in water for 3 hours. The

amount of compression tested during electromechanical characterization was about 50 %, and the compressive strain with the normalized resistance during the 5 compression-release cycles are illustrated (Figure 6.18A).

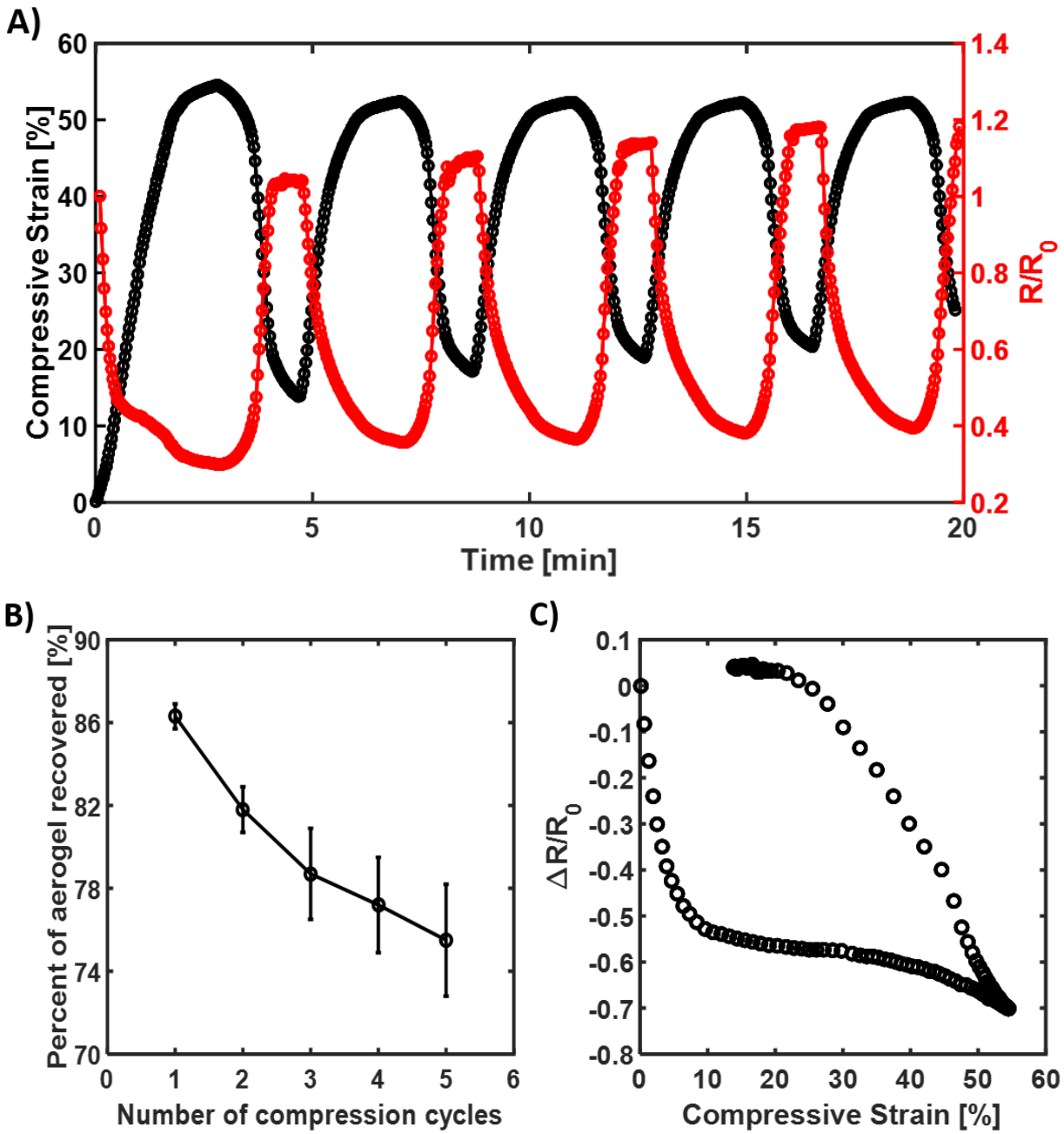

Figure 6.18: (A) The compressive strain history of the PEDOT:PSS templated T-CNF aerogel (black), and the corresponding normalized resistance (red) during the 5 compression-release cycles. (B) The shape recovery percentage of PEDOT:PSS templated T-CNF aerogel during the 5 compression-release cycles. (C) From the first compression-release cycle, the normalized resistance change in relations with the compressive strain is illustrated.

The initial measured resistance was approximately 5,890 Ω, and the final measured resistance at the end of the 5 compression-release cycle was approximately 6,970 Ω. The lowest measured resistance was approximately 1,760 Ω, which was obtained at the most compressed state of 54.5 % during the first compression-release cycle. The resistance reduced with aerogel compression because additional contacts between the fibers were created during compression, which temporarily increased the number of electrical contacts in the conductive network when compared to the uncompressed aerogel. However, even though the aerogel was recovering less and less, the resistance of the aerogel increased with successive compression-release cycles (nearly 20 % increase after 5 cycles of compression and release). The increase in aerogel resistance was likely attributed to irreversible damage to the PEDOT:PSS conductive network during compression and release, which reflected the inherently brittle nature of PEDOT:PSS. Materials with stronger conductive stability during strain deformable can potentially be used to improve the electrical properties and repeatability of the 3D printed T-CNF aerogel. Furthermore, the average percent recovery of the T-CNF aerogel decreased from 98.0 ± 0.2 % to 86.3 ± 0.6 % when it was templated with PEDOT:PSS. As the recoverability of the aerogel is highly dependent on the re-establishment of hydrogen bonding in the aerogel network, the decrease in aerogel recoverability could be due to the incorporated PEDOT:PSS inhibiting hydrogen bond reformations between T-CNFs. It is also possible that irreversible damage to the PEDOT:PSS network ended up restricting the T-CNF network recovery. With 5 repeated compression-release cycles, the average percent recovery of PEDOT:PSS templated T-CNF aerogel further reduced to 75.5 ± 2.7 % (Figure 6.18B). The normalized resistance change during the first compression-release cycle was also plotted as a function of compressive strain (Figure 6.18C). It revealed that the largest resistance change actually occurred during the first 10 % of compression. The normalized resistance change then

slowly leveled out as the compressive stain increased to 54.5 %. On the other hand, the largest resistance change during release occurred when the strain decreased from 54.5 to about 20 % before the normalized resistance change leveled out. As a result, the resistance change was most sensitive during the first 10 % of compression. Meanwhile, resistance change increased in a more regular fashion during the first 35 % of release. For subsequent compression-release cycles, the behavior of the normalized resistance change was similar, except the resistance change occurred in a regular fashion during both the compression and release steps (Figure 6.19).

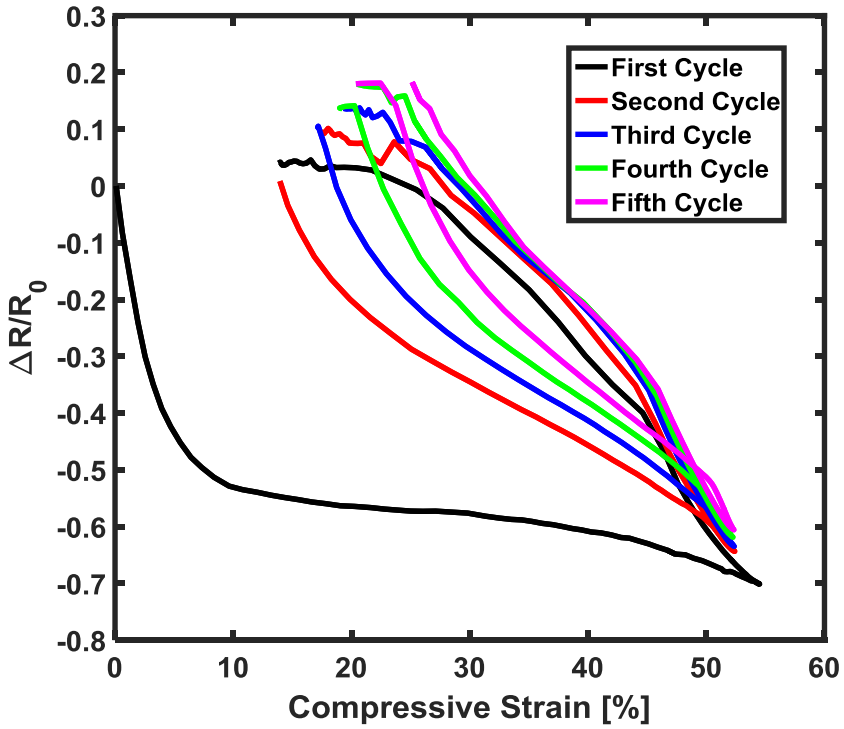

Figure 6.19: The behavior of the normalized resistance change in relation to the compressive strain during the 5 compression-release cycles is illustrated.

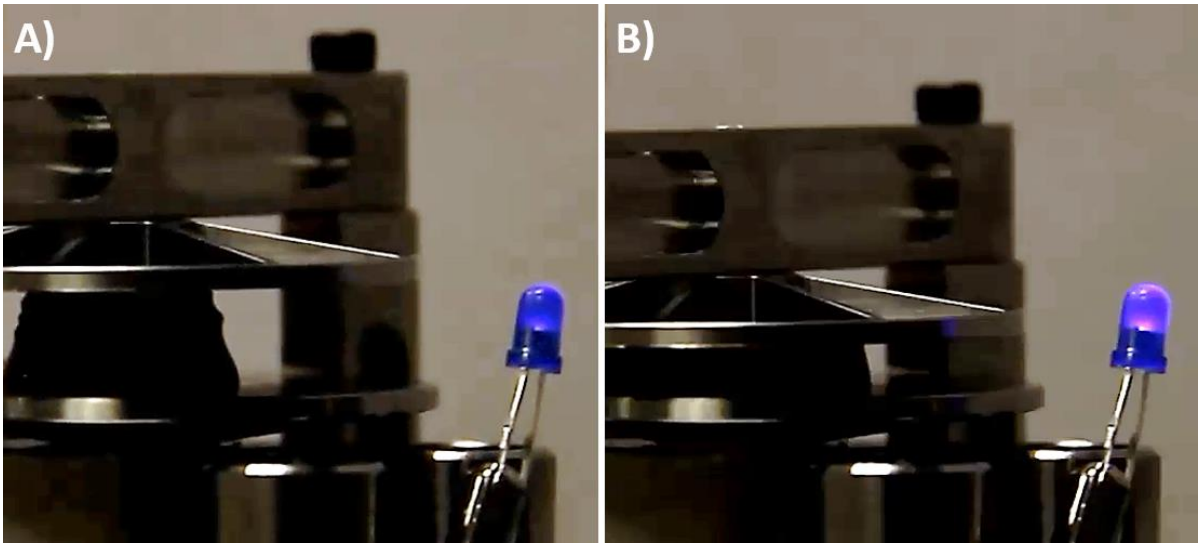

Figure 6.20: (A) The LED bulb's light intensity that was emitted during the PEDOT:PSS templated T-CNF aerogel's stress-free state is illustrated. (B) The corresponding LED bulb's light intensity that was emitted when the aerogel was compressed by about 50 % is also illustrated.

This suggests that irreversible damage to the PEDOT:PSS conductive pathway occurred most prominently during the first compression cycle, but further damage was more incremental and continuous during the subsequent compression-release cycles. Lastly, an LED light bulb was connected to the PEDOT:PSS templated T-CNF aerogel, where the electrical circuit was completed with a power source. During the 5 compression-release cycles, the emitted light intensity of the LED bulb fluctuated in correspondence with the normalized resistance of the aerogel (Figure 6.20A and 6.20B). Overall, the ability to modify the 3D printed T-CNF aerogel with electrical conductivity was demonstrated, where shape customizable aerogels with both deformability and conductivity can be realized for various electronic related applications.

6.4 Conclusion

In conclusion, TEMPO mediated oxidation of CNFs increased the surface repulsive charge of individual fibers. Combined with high pressure homogenization, the surface specific charge density of T-CNFs decreased significantly beyond that of the original CNFs. The network

entanglement homogeneity of T-CNF gel also improved, which allowed purely T-CNF 3D structures to be accurately and reproducibly printed via the DIW approach. After freeze-drying, a purely T-CNF aerogel with density and porosity of approximately 26 mg/cm^3 and 98 % was respectively obtained. The addition of carboxylate groups onto the surface of CNFs also facilitated Kymene crosslinking, which allowed the T-CNF aerogel to maintain structural integrity even under water and applied force. The crosslinked double interpenetrating network of T-CNFs and polymerized Kymene provided a T-CNF aerogel with an impressive deformability of greater than 96 % before densification occurred. While the aerogel was saturated with water, more than 80 % of the aerogel could still be compressed before aerogel densification. The shape recovery repeatability was also evaluated, and more than 90 % shape recovery was maintained after 5 compression-release cycles, even though the aerogel was compressed nearly 80 %. The resultant 3D printed T-CNF aerogel structures can easily serve as templates for facile addition of functionality. As examples, functionalizations by PFOTS and PEDOT:PSS were performed, which provided deformable T-CNF aerogel 3D structures that were nearly super hydrophobic and electromechanically responsive. These aerogels may have potential for oil/water separation or electronic related applications. With the customizability of the overall 3D structure, impressive deformability, repeatable shape recoverability, and possibility for addition of many different functionalities, the adoptability of T-CNF aerogels has been greatly extended for various potential applications.

CHAPTER VII: CELLULOSE NANOCRYSTAL SUPPORT MATERIAL FOR 3D PRINTING COMPLEXLY SHAPED STRUCTURES VIA MULTI-MATERIALS-MULTI-METHODS PRINTING

7.1 Introduction[4]

3D printing technologies have seen significant development in the past decade, in part due to many different varieties of 3D printers becoming available.[26, 235-239] According to ASTM classification standards, the seven main types of 3D printing techniques are material extrusion, material jetting, vat photo-polymerization, powder bed fusion, reactive binder jetting, directed energy deposition, and stacked sheet lamination.[53] Depending on the type of 3D printer used, materials with different properties are required for proper 3D processing. For example, direct-ink-write (DIW) 3D printing, a form of material extrusion, requires high viscosity ink with appreciable shear thinning behavior for material deposition and shape holding during 3D printing. In contrast, inkjet-based 3D printing requires low viscosity ink with strict control on physical properties such as stable surface tension. As a result, different materials have their own unique processing requirement needs, while also providing different properties and functionalities to the final printed part.

The concept of hybrid 3D printing has also been steadily gaining popularity, as it combines multiple 3D printing methods and different processing tools like robotic arm pick-and-place (P+P) or spray coating technologies into an integrated fabrication platform.[240-244] Hybrid 3D printing is also able to take advantage of the unique processing capability of each 3D printing techniques to

[4] This chapter is modified from a submitted publication: **Li, V.**, Kuang, X., Hamel, M. C., Roach, D., Deng, Y., Qi, H. J. (2018). Cellulose Nanocrystals Support Material for 3D Printing Complexly Shaped Structures via Multi-Materials-Multi-Methods Printing. S*ubmitted to Additive Manufacturing.*

print different materials, and produce intricately shaped and multi-functional structures that are made of heterogeneous materials. For example, Valentine et. al. utilized DIW 3D printing to print conductive and dielectric elastomer, and then used robotic arm P+P to insert electronic components within the target structure during 3D printing.[245] The resultant structures demonstrated potential application in wearable electronics, soft robotics, and biomedical devices. Tong et. al. also utilized a DIW-based extrusion technique and a robotic arm P+P system to fabricate nerve cuffs with locking mechanisms that are suited for neural interfacing related applications.[246] Yoon et. al. combined inkjet printing and spray coating techniques to fabricate 3D hydrogel structures suitable for potential tissue engineering applications.[247] Raza et. al. was able to combine both DIW and inkjet 3D printing methods together in order to process a multi-materials 3D part that is composed of metal, rubber, and plastics, and demonstrated the highly extended manufacturing capability of hybrid 3D printing technology.[248] Other works have also demonstrated the possibility to utilize different hybrid 3D printing strategies, such as dual FDM 3D printing,[249] multi-materials-multi-technology stereolithographic 3D printing,[250] and stereolithographic-DIW 3D printing,[251] to fabricate highly complex and functional structures that are composed of multiple materials. Overall, with increasing needs and demands for more complex and intricate 3D structures, it is conceivable that combining different 3D printing techniques into a single multi-materials-multi-methods (M^4) 3D printing platform can be highly beneficial.

During 3D printing, a sacrificial support material is usually a critical component for the successful fabrication of highly complex objects. This is because overhanging or bridge like features in 3D structures can only be fabricated when the depositing target material are laid on top of a sacrificial support structure. Otherwise, the depositing target materials would simply deform from the intended printing shape due to viscous thread instability or gravitational forces.

Depending on the 3D printing methods and the complexity of structures, support materials can be more than 50% of the total materials used in a 3D printing job. However, traditional support materials are un-sustainable and non-recyclable because they are typically polymerized or solidified along with the target structure. During post processing, this makes it difficult to remove the support material. In some cases, caustic solvent, such as sodium hydroxide or alkaline bath, is needed in order to efficiently remove the support material.[252] This can generate excess waste due to a large quantity of solvents have to be used, which creates the issue of environmental pollution and is non-sustainable. Therefore, there is a strong need to develop environmentally friendly and sustainable inks that can serve as support materials. Cellulosic nanomaterials, such as cellulose nanocrystals (CNCs) and cellulose nanofibers (CNFs), can be derived from trees, plants, and even agricultural residues.[2, 4, 39] These cellulosic resources are abundantly available, recyclable, and sustainable, which can make 3D printing more sustainable and environmentally friendly.[42, 45, 77, 91]

In previous studies, the ability of using DIW 3D printing to print CNC and CNF gels into highly customizable 3D structures with controllable properties, quality, and shape was demonstrated.[219, 253] These DIW 3D printable gels are entirely cellulosic in nature and water-based. For example, CNCs were mixed directly with water in order to produce a CNC gel that can be easily processed by DIW 3D printing. Compared with tradition petroleum-based polymeric support materials used in 3D printing, CNCs suspended in water are in nanoparticles form and are also non-UV light sensitive. As a result, CNC gel is less absorbable onto other polymer matrices that are cured by UV light, which allows them to be completely washed away with water during post processing of 3D printing.

In this study, the feasibility of using CNC gel as supporting material in dual DIW and DIW-inkjet hybrid 3D printing in order to fabricate various complexly shaped structures was explored.

After 3D printing, the CNC gel was removed quickly and efficiently using water in order to produce the final target structure. The potential of using CNC gel as support material and M^4 hybrid 3D printing to fabricate highly complex structures was also demonstrated. Since CNC gel is derived from forestry products and is entirely water-based, using CNC gel as support materials can make the 3D printing process more environmentally friendly, sustainable, and potentially recyclable.

7.2 Experimental Section

7.2.1 Materials

Freeze-dried CNCs were purchased from University of Maine Process Development Center (Orono, ME, USA) and used as received. Butyl acrylate, polycaprolactone (Mn of 70,000 to 90,000), fumed silica powder (0.2 to 0.3 μm particles), and phenylbis(2,4,6-trimethylbenzoyl)phosphine oxide (Irgacure 819) photoinitiator powder were purchased from Sigma-Aldrich (St. Louis, MO, USA) and used as received. An UV curable aliphatic urethane diacrylate-based oligomer (EBECRYL 8413) was kindly donated by Allnex Inc. (Alpharetta, GA, USA) and used as received. UV curable inkjet ink (ETIJET ULX5832 CYAN) were purchased from SunJet DIC Inkjet Solutions (Parsippany, NJ, USA) and used as received. De-ionized water was used in all experiments.

7.2.2 3D Printing Ink Preparation

CNC aqueous gel (20 wt %) was prepared as according to our previous study.[219] Briefly, CNC gel was prepared by mixing an appropriate amount of freeze-dried CNCs and water together through probe homogenization at 10,000 rpm. Also adopted from our previous work with minor

modifications,[254] an elastomeric resin that is UV curable was prepared by first mixing polycaprolactone with butyl acrylate, and then stirred with a magnetic stir bar at 70 °C until the polycaprolactone was fully dissolved. While keeping the resin around 70 °C to improve mixing, a 1:1 mass ratio of EBECRYL 8413 was added to the dissolved polycaprolactone-butyl acrylate solution, and mixed by hand until a homogeneous resin was obtained. Irgacure 819 and fumed silica were subsequently added and mixed by hand until a homogeneous elastomeric resin was obtained (Formulation: 46.5 wt % butyl acrylate, 0.7 wt % polycaprolactone, 46.5 wt % EBECRYL 8413, 1.5 wt % Irgacure 819, and 4.8 wt % fumed silica). The final elastomeric resin's container was wrapped in aluminum foil, and stored at room temperature until further use. Before DIW 3D printing, the CNC gel and the elastomeric resin were placed in separate syringes. To ensure all air bubbles were removed from the syringes, centrifugation processing was performed at 5000 rpm for 10 mins.

7.2.3 Multi-Material-Multi-Method (M^4) Printing

The multi-materials-multi-methods (M^4) printer is comprised of a printing stage that is controlled by the Aerotech Inc. motion system. (Pittsburgh, PA, USA), where the stage can travel between different printing modules. In this study, a DIW system with dual material deposition capability, and a piezoelectrically driven drop-on-demand inkjet print-head (Xaar, Cambridge, United Kingdom) with UV lamp attachment (FE300UV LED lamps, Phoseon Technology, Hillsboro, OR, USA) were used.

The DIW system utilizes a pneumatic dispenser (Ultimus V, Nordson EFD, East Providence, RI, USA) to controllably extrude printing materials from syringes using specified compressed air pressures. The movement of the syringe was programmed to follow the g-code

generated by the in-house developed software, which uses STL file obtained from SolidWorks as the input. By controlling the pneumatic deposition and the syringe movement, one layer of the 3D structure can be formed line-by-line. Ultimately, the entire 3D structure can be fabricated in a layer-by-layer manner. In order to print two materials using the same DIW system, a switching unit was developed to direct compressed air between two separate syringes. The generated g-code can also instruct the switching unit to direct the compressed air to the syringe holding the elastomeric resin when printing the target structure, or re-direct the air to the syringe holding the CNC gel when printing the support structure. A printing pause was inserted in between each switching action, which allowed the deposition pressure to be adjusted depending on which material was to be deposited next. In this manner, a single layer comprised of both the elastomeric resin and the CNC gel can be printed. After each layer of the structure was deposited, the built stage was moved under the UV lamp for polymerization. The movement speed of the elastomeric syringe was 10 mm/s, whereas the movement speed of the CNC syringe was 40 mm/s. Meanwhile, the extrusion pressure for the elastomeric resin and the CNC gel were around 10 psi and 8.5 psi, respectively. The inner diameter of the tapered type nozzle attached to each syringe was 400 μm.

The inkjet system utilizes an inkjet supply system (Hydra, Xaar, Cambridge, United Kingdom) to achieve proper meniscus pressure and temperature control for consistent inkjet resin deposition from the Xaar print-head. The SolidWorks design of the inkjet structure was first formatted as a STL file, and then processed with the in-house developed software into grayscale images. These images were loaded to the Xaar print-head, and controlled the shape of each deposited inkjet layer. After each inkjet layer was deposited, it passed over the UV lamp in order to polymerize the layer. The corresponding support structure was processed similarly as before

using the in-house developed software, and was integrated together with the inkjet processing instructions to produce the final g-code script for 3D object fabrication via DIW-inkjet.

7.2.4 Rheological Characterization via Cone and Plate Viscometry

While under a room temperature of about 22 °C, the viscosity of the elastomeric resin, the CNC gel, and the inkjet ink were analyzed by the DV2TLV and DV3THV cone and plate viscometers (Brookfield Engineering Labs Inc., Middleboro, MA, USA). Cone spindles of CPA-40Z, CPA-41Z, and CPA-52Z were used. Cone plates of CPA-44YZ and CPA-44PSYZ were also used during the viscosity characterization. Viscosity was measured as a function of shear rate, where the shear rate ranged between 0.2 s^{-1} and 500 s^{-1}. A minimum of 10 measurements were collected for each sample at each corresponding shear rate, and averaged values were reported. The gap separation between the spindle and the plate was set at 0.013 mm. To minimize potential wall slip effects, about 3 grams of resin or gel were distributed across the entire plate surface before each characterization was performed.

7.2.5 Attenuated Total Reflectance-Fourier Transform Infrared Spectroscopy (ATR-FTIR) Analysis

Elastomeric and inkjet layers that were sandwiched between two CNC gel layers were fabricated through dual DIW or DIW-inkjet 3D printing. After the CNC gel support was removed with water, both the topside and the underside of the dried elastomeric and inkjet layers were analyzed by ATR-FTIR (Nicolet iS50, ThermoFisher Scientific, Waltham, MA, USA) spectrometer under ambient conditions from an averages of 32 scans with a scan resolution of 1 cm^{-1} in the range of 600 cm^{-1} to 4000 cm^{-1}. After the topside of the layer was characterized, FTIR

analysis was preformed again after the layer was flipped over to the underside. Spectra for pure CNCs was analyzed by placing freeze-dried CNC powder onto the sampling lens.

7.2.6 Surface Morphology Analysis with Field Emission-Scanning Electron Microscopy (FE-SEM)

The washed and dried elastomeric and inkjet layers were first attached to the SEM sample holders with conductive double sided tape, and then sputter coated (Q-150T ES Sputter, Quorum Technologies, Laughton, East Sussex, London) with gold for 30 seconds at 20 mA current. Then, SEM imaging (LEO 1530, Zeiss, Jena, Germany) was performed at 20 kV accelerating voltage.

7.2.7 Thickness Tester Evaluated Inkjet Layer Thickness as a Function of Number of Passes Over the Inkjet Print-head

Inkjet layers were fabricated based on the number of passes over the inkjet print-head, and their resultant thicknesses were evaluated using a Thickness Tester (89-100, Thwing-Albert Instr. Co., Philadelphia, PA, USA). Each inkjet layer was tested five times, and average values were presented. The best fitted line through the data points was done to evaluate the final average thickness of the inkjet layer per each pass over the print-head.

7.3 Results and Discussion

The dual DIW and the DIW-inkjet 3D printing process were used to construct various complexly shaped structures. During dual DIW 3D printing, both the elastomeric resin and the CNC gel were deposited onto the printing stage. Then, the printing stage moved over to the UV lamp unit, where the elastomeric resin was polymerized. Since the CNC gel is not photocurable,

the gel remained as a gel structure that served as the support structure for the next deposition layer. Similarly, the DIW-inkjet printing process worked by depositing the CNC gel with the pneumatic dispenser, while the UV curable inkjet ink was deposited by the Xaar print-head. The shape of the inkjet layer was controlled by the grayscale image that was loaded to the print-head, and then the deposited inkjet layer was polymerized by UV light irradiation. As a result, a 3D structure consisting of either elastomeric resin and CNC gel, or inkjet ink and CNC gel was printed through a layer-by-layer manner. A schematic for both the dual DIW and the DIW-inkjet 3D printing process is provided (Figure 7.1A), and the actual multi-materials-multi-methods (M^4) printer used during hybrid 3D printing is also illustrated (Figure 7.1B). After 3D printing, the overall concept is to use water to efficiently remove the sustainable CNC gel support material, and then produce the final target structure (Figure 7.1C).

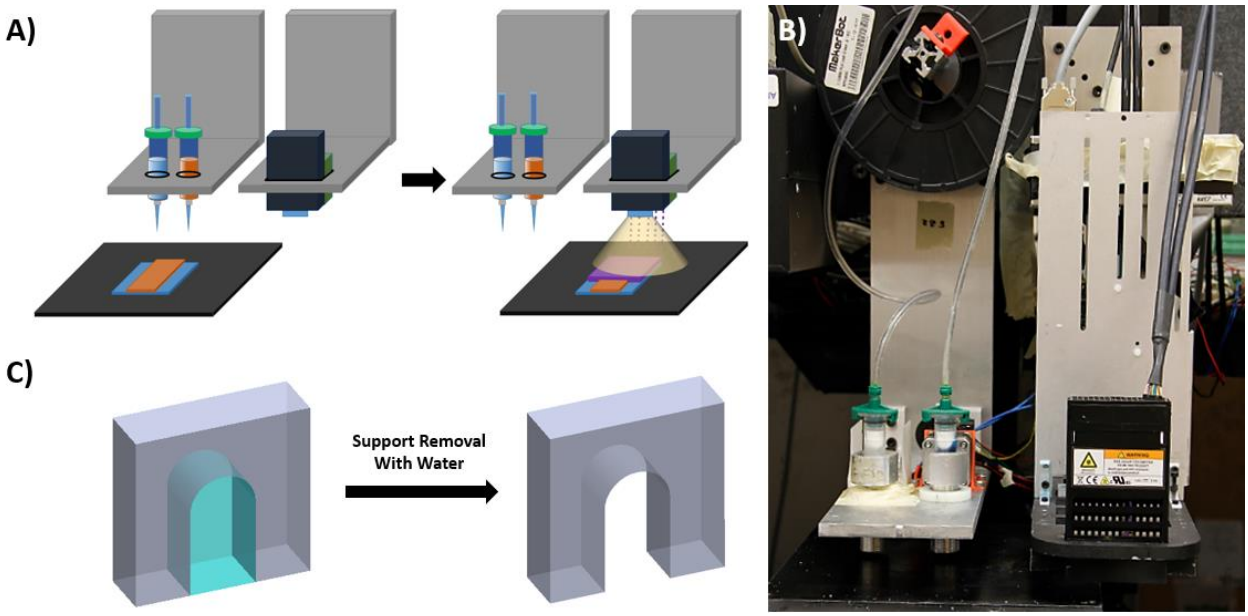

Figure 7.1: (A) Schematic illustration of the dual DIW and DIW-inkjet 3D printing process. (B) The actual multi-material-multi-method hybrid printer used during 3D printing. (C) Schematic illustration of using water to remove the CNC support material in order to produce the final target structure.

During dual DIW and DIW-inkjet 3D printing, the rheology of the resin, gel, and ink is an important criterion to consider. The DIW processable material must have a high viscosity such that the printed shape can be maintained, and it must also be shear thinning so that extrusion through the nozzle is possible during deposition. The rheological behavior of both the elastomeric resin and the CNC gel were characterized, and it was clear that both the resin and the gel displayed appreciable shear thinning effect. In fact, their viscosities decreased by over three orders of magnitude in the shear rate range between 0.2 and 500 s^{-1}. This supports that both the elastomeric resin and the CNC gel are able to flow efficiently during DIW 3D printing because high shear is applied across the nozzle as the inks are deposited. Once they were deposited, their high viscosities ensured that the printed shapes were maintained without any structural sagging. On the other hand, the inkjet ink displayed the required Newtonian behavior, where the viscosity was kept relatively low at around 42 ± 1 cP regardless of shear rate (Figure 7.2A).

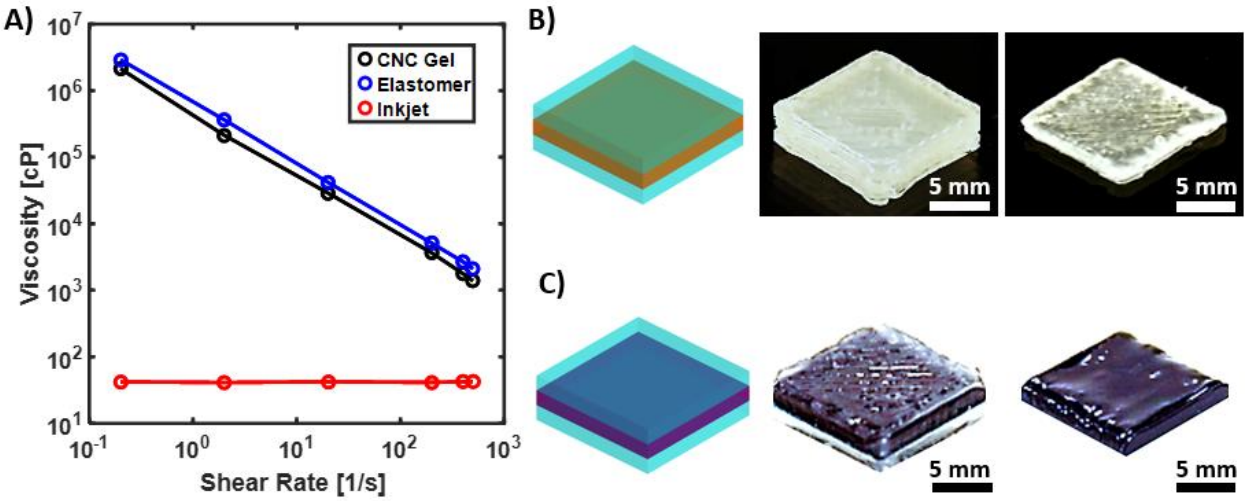

Figure 7.2: (A) The viscosity versus shear rate curves at room temperature for the elastomeric resin, CNC gel, and inkjet ink are illustrated. (B) Left: The SolidWorks model of an elastomeric layer sandwiched between two CNC layers is presented. Middle: The as-printed structure after dual DIW 3D processing. Right: The final obtained target structure after washing away the CNC support material with water. (C) Similarly, the corresponding model and structures from DIW-inkjet 3D processing of an inkjet layer sandwiched between two CNC layers are presented.

Both the dual DIW and DIW-inkjet 3D printing process began by first designing the target structure and the corresponding support structure using SolidWorks. For dual DIW 3D printing, the SolidWorks models for both the target and the support structure were processed by the in-house developed software into a finalized g-code script. Depending on which material was to be deposited, the g-code script can also control the nozzle deposition to switch between the syringes holding the elastomeric resin and the CNC gel. As an initial demonstration, a structure with an elastomeric layer (colored orange) sandwiched between two CNC gel layers (colored light blue) was fabricated through dual DIW 3D printing. The SolidWorks model, the as-printed structure, and the final obtained structure after CNC support removal with water are correspondingly illustrated from left to right (Figure 7.2B). For DIW-inkjet 3D printing, the target structure's SolidWorks model was first sliced into greyscale images before they were transformed into inkjet processing instructions. The support structure's SolidWorks model was processed by the in-house developed software, and then integrated with the inkjet processing instructions to produce the finalized g-code script for 3D structure fabrication. Similarly, a structure with an inkjet layer (colored purple) that was sandwiched between two CNC gel layers was also fabricated through DIW-inkjet 3D printing. The resultant as-printed structure and the final obtained structure after water washing are also illustrated (Figure 7.2C).

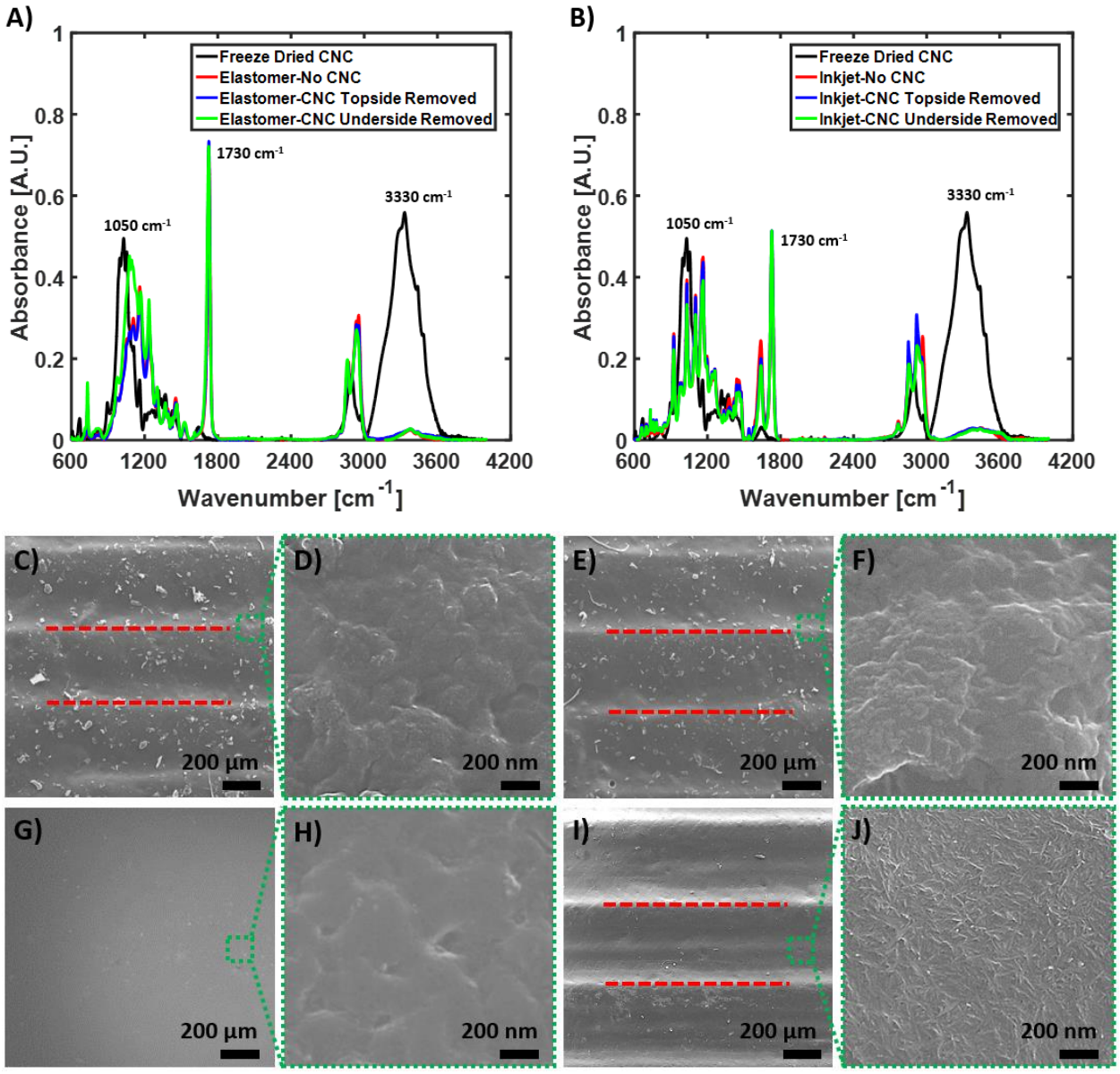

Figure 7.3: (A) The FTIR spectra for the freeze-dried CNCs (black), the dual DIW 3D printed elastomeric layer without any CNC deposition (red), the topside of the dual DIW 3D printed elastomeric layer that was sandwiched between two CNC gel layers (blue), and the corresponding underside of the elastomeric layer (green) are illustrated. (B) The corresponding FTIR spectra for the analysis of the inkjet layer processed with DIW-inkjet 3D printing. (C) Low magnification SEM images of the dual DIW 3D printed elastomeric layer's topside. The red dash lines in the low magnification images showcase the width of the filament like features. (D) The corresponding SEM image was taken at high magnification, where the filaments' interfacial bonding is illustrated. (E) Low magnification SEM images of the dual DIW 3D printed elastomeric layer's underside. (F) The corresponding SEM image was taken at high magnification, where the filaments' interfacial bonding is again illustrated. (G) Low magnification SEM images of the DIW-inkjet 3D printed inkjet layer's topside. (H) The corresponding SEM image was taken at high magnification. (I) Low magnification SEM images of the DIW-inkjet 3D printed inkjet layer's underside. (J) The corresponding SEM image was taken at high magnification.

To study the effectiveness of using water to remove CNC gel from both the elastomeric and the inkjet surfaces, the previously fabricated sandwiched elastomeric and inkjet layers were analyzed using FTIR methods (Figure 7.3A and 7.3B). For comparative purposes, an elastomeric layer and an inkjet layer without any CNC gel layer sandwiching were also fabricated with the M^4 printer. The FTIR spectra for pure CNCs was first obtained in order to evaluate if there are any CNCs debris on the washed elastomeric or inkjet layers. CNCs exhibited a FTIR spectrum with peaks at wavenumbers of 895 cm^{-1}, 1030 cm^{-1}, and 1050 cm^{-1}, which are cellulose's characteristic peaks for C-O-C deformations of the β 1-4 glycosidic bond, C-O-H stretching in the pyranose rings, and C-O-C vibrations in the cellulose pyranose rings. Other peaks between 1110 cm^{-1} and 1430 cm^{-1} are also characteristics peaks for cellulose's C-O, C-C, C-H, and C-O-H related vibrations. Most importantly, the major peaks at 2900 cm^{-1} and 3330 cm^{-1} were also present, which are attributed to C-H stretching and O-H stretching in absorbed water and in cellulose.[255-260] Comparing the spectra from CNCs and that for a DIW 3D printed elastomeric layer without any CNC sandwiching, the most drastic differences were the peak emergence at 1730 cm^{-1} and the peak disappearance at 3330 cm^{-1} (Figure 7.3A). The peak at 1730 cm^{-1} can be attributed to the C=O ester vibrations in acrylate related functional groups.[261] At the same time, the absence of cellulosic material also led to the major O-H vibrational peak (3330 cm^{-1}) related to absorbed water on cellulosic surfaces and hydroxyl functional groups within cellulosic structures to significantly reduce. The same phenomena were observed in the spectra for both the topside and the underside of the washed elastomeric layers that were sandwiched between CNC gel layers, which suggested that water was also able to effectively remove CNCs from the elastomeric surfaces. In fact, spectra for elastomeric layer without and with CNC sandwiching were practically identical. As a result, FTIR analysis supported that water can effectively remove the CNC gel from both the topside and

the underside of the elastomeric material. Similar observations were also seen for the FTIR analysis for the inkjet layers, where the significantly reduced peak intensity at 3330 cm^{-1} suggested that practically all CNCs were removed on both the topside and the underside of the inkjet layer after water washing (Figure 7.3B).

The xy-directional surface morphology of the elastomeric and inkjet layers was also studied through SEM characterization. Both the topside and the underside of the elastomeric and inkjet layers that were sandwiched between CNC gel layers were analyzed (Figure 7.3C to 7.3J). The topside of the elastomeric layer shows that the surface has filament like features (Figure 7.3C). In fact, ImageJ analysis confirmed that the filament like features (red dash lines) had a width of about 400 µm, which matched closely with the inner diameter of the nozzle tips that was used during DIW processing. The DIW printed elastomer filaments are also well bonded together (Figure 7.3D), as higher magnification SEM images show that the elastomeric filaments are well attached together without significant separations or defects. Similarly, lower magnification image of the elastomeric layer's underside also illustrates filament like features (Figure 7.3E), and the corresponding higher magnification image showcases that the filaments are also well attached to one another (Figure 7.3F). On the other hand, the topside of the inkjet layer displays a morphology of an extremely smooth surface at both low and high magnification (Figure 7.3G and 7.3H). Meanwhile, the underside of the inkjet layer displayed filament like features (Figure 7.3I). ImageJ analysis again confirmed that the width of each filament features is approximately 400 µm (red dash lines). The difference between the inkjet's topside and underside surfaces could be explained by the low viscosity of the inkjet ink and the DIW-inkjet processing steps. As the first CNC gel layer in the sandwiched structured was formed, the layer likely also has filament like features because the CNC gel has similar rheological properties as the elastomeric resin. When the inkjet

layer was then deposited, the low viscosity inkjet ink was likely able to flow into the interfacial filament spaces left behind by the underlying CNC gel filaments. Afterwards, the layer was then polymerized with UV light to produce a negative image of the underlying filament like CNC gel layer. As more inkjet layers were deposited, the surface morphology became highly smooth because any further defects and features left on the surface were gradually filled by the low viscosity inkjet fluid and then UV polymerized. When the second CNC gel layer in the sandwiched structured was formed, the underlying inkjet layer was already UV polymerized into a solid layer, so subsequent CNC gel filament deposition no longer had any effect on the topside's smooth surface morphology. Interestingly, the higher magnification SEM image for the inkjet's underside displayed a surface morphology that resembled tightly packed CNCs (Figure 7.3J). Typically, a low SEM accelerating voltage of no greater than 10 kV is usually used when performing SEM imaging of cellulosic or biological materials in order to avoid burning effects.[262] Since a SEM accelerating voltage of 20 kV were used and there was no burning effect observed during SEM imaging, it supported that the observed tightly packed CNC surface morphology did not result from CNCs that were left on the underside surface of inkjet layer. Instead, it was more likely that the inkjet ink formed a negative image of the CNCs on the underlying CNC gel layer, as the low viscosity inkjet ink was able to adapt to even the nanoscale morphological features of CNCs before it was polymerized by the UV lamp. This was further supported by the FTIR analysis, where the CNC dominant peak at 3330 cm^{-1} is not prominent for the inkjet layer's underside. As a result, the low viscosity inkjet ink not only created a negative image of the underlying features at the macroscopic level (the filament like features), but also surface morphologies at the nanoscopic level (tightly packed CNCs like features).

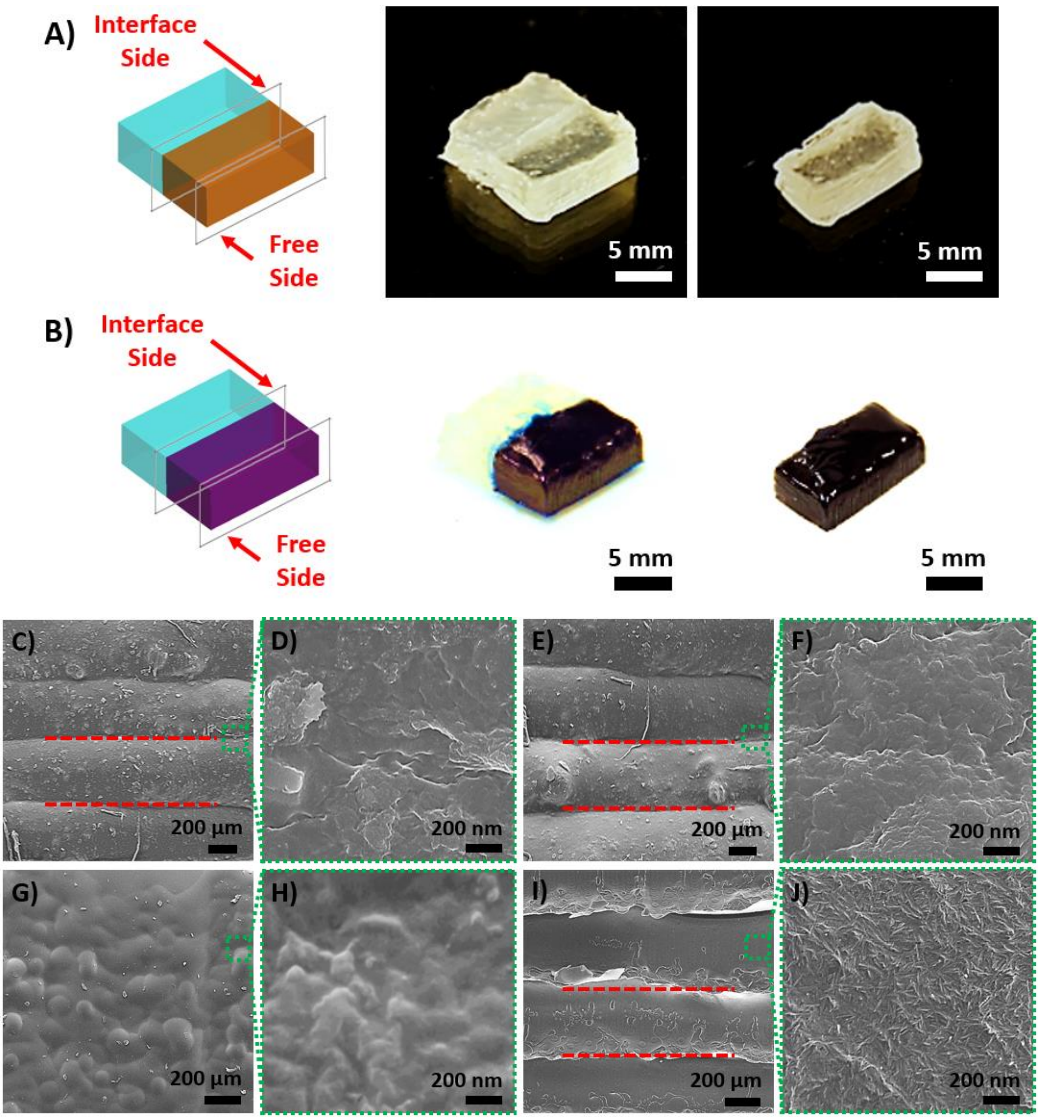

Figure 7.4: (A) Left: The SolidWorks model of an elastomeric structure with CNC support next to it is presented, where both the free side and the interface side are also illustrated. Middle: The as-printed structure after dual DIW 3D processing. Right: The final obtained target structure after washing away the CNC support material with water. (B) Similarly, the corresponding model and structures from DIW-inkjet 3D processing of an inkjet structure with CNC support next to it are illustrated. (C) Low magnification SEM images of the dual DIW 3D printed elastomeric structure's z-directional surface on the free side. The red dash lines in the low magnification image showcase the thickness of the filament like features. (D) The corresponding SEM image taken at high magnification, where the filaments' interfacial bonding in the z-direction is illustrated. (E) Low magnification SEM images of the dual DIW 3D printed elastomeric structure's z-directional surface on the interface side. (F) The corresponding SEM image taken at high magnification, where the filaments' interfacial bonding in the z-direction is again illustrated. (G) Low magnification SEM images of the DIW-inkjet 3D printed inkjet structure's z-directional surface on the free side. (H) The corresponding SEM image taken at high magnification. (I) Low magnification SEM images of the DIW-inkjet 3D printed inkjet layer's structure's z-directional surface on the interface side. (J) The corresponding SEM image taken at high magnification.

Furthermore, the z-directional morphological features of the elastomeric and inkjet structures were also characterized by SEM (Figure 7.4), where two different z-directional surfaces were analyzed. The first was the free side surface, which represented the z-directional surface that was fabricated without any CNC support next to it. The second was the interface side, which represented the z-directional surface that was fabricated with the CNC support structure next to it. It was again observed that the elastomeric z-directional surface was composed of filaments of about 400 μm thickness on both the free side and the interface side, where each filament appeared to be well bonded with one another. During inkjet printing, the resolution of each deposited inkjet layer was estimated to be 30.8 μm per pass over the print-head. The inkjet layer thicknesses as a function of number of passes over the print-head were analyzed using a Thickness Tester (Figure 7.5). On the other hand, the resolution of DIW printing is limited by the inner diameter of the nozzle tip. In this case, tapered nozzles with an inner diameter of 400 μm were used to deposit the CNC gel support material. During layer-by-layer formation in the 3D printing process, it then became necessary to match the layer thickness of both the inkjet and the CNC material within each sliced layer of the 3D structure. Since the Thickness Tester evaluated inkjet thickness for 13 passes was approximated to be about 405.9 ± 0.9 μm, a total of 13 inkjet deposition passes was performed to match with the layer resolution of each CNC gel layer deposition.

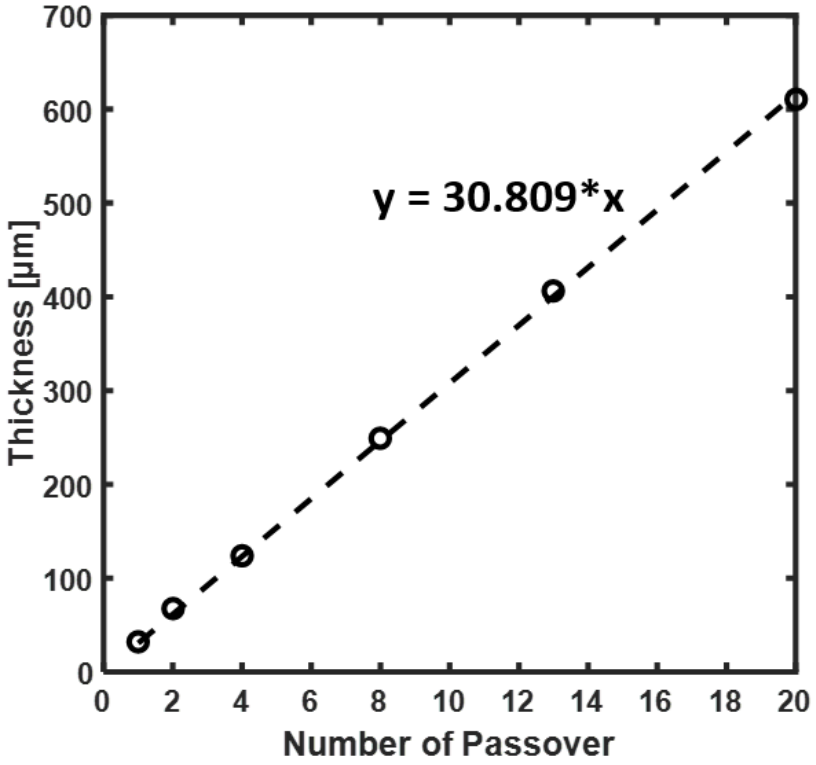

Figure 7.5: The thickness tester evaluated thickness of the inkjet layer printed with different number of passes over the inkjet print-head. The best fitted line illustrated that the thickness of each inkjet layer per pass was approximately 30.8 µm.

Through repeating cycles of 13 inkjet depositions to one CNC gel deposition to form each layer, structures made of polymerized inkjet material and CNC support material can be fabricated. During SEM analysis, the free side of the inkjet structure's z-directional surface did not exhibit filament like features, but instead displayed a relatively smooth surface with beads like surface roughness. The beads like features could be attributed to the low viscosity inkjet ink still had the ability to flow when the stage was moving to the UV lamp, so the ink slightly flowed pass the layer's outer boundary in the xy-direction and cascaded down the z-direction before it was polymerized. When the interface side of the inkjet structure was analyzed, filament like features that resulted from the negative image of the CNC gel layers were again observed. The filament features on the inkjet structure's z-directional interfacial surface also had a thickness of approximately 400 µm, which again supported that 13 inkjet passes were required to match the

filament thickness of each CNC gel layer. Upon higher magnification, a negative image of the CNCs resulting from the adjacent CNC gel layer was again observed. Overall, it was confirmed that water can effectively remove the CNC gel from both the elastomeric surfaces and the inkjet surfaces. Furthermore, unique surface morphologies can be left behind depending on the 3D printing strategy employed, and on whether or not the CNC gel was deposited next to the structure.

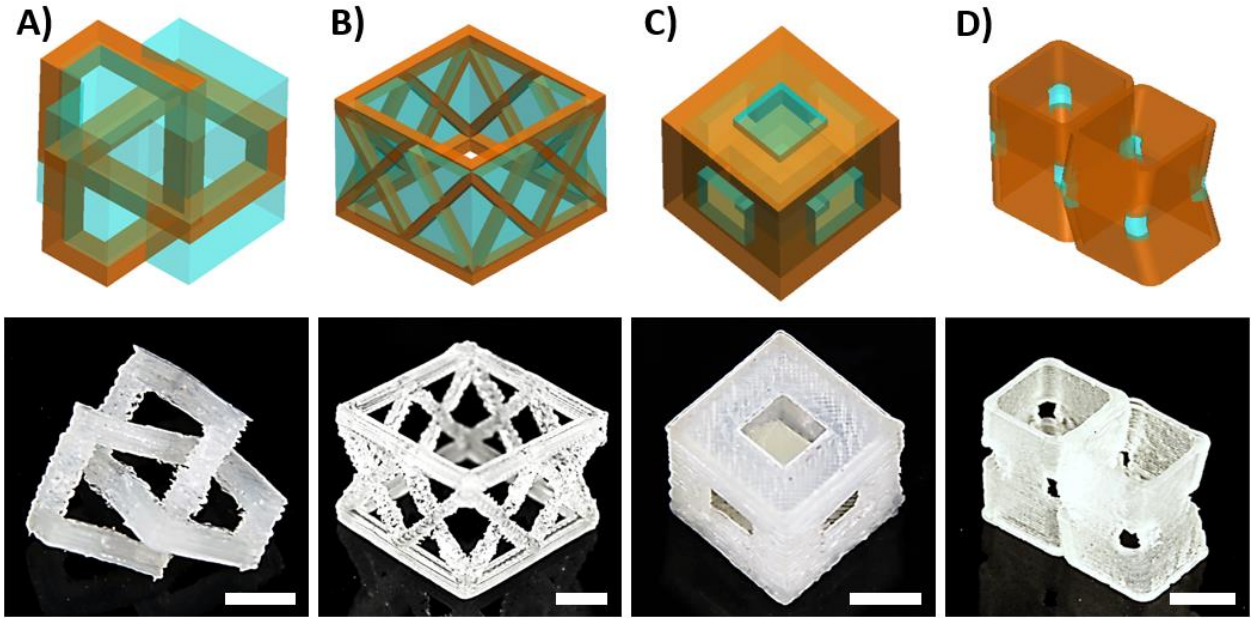

Figure 7.6: The SolidWorks models (top) and the resultant dual DIW 3D printed structures with support removed (bottom) are illustrated. Various structures include (A) cubic trefoil knot, (B) box with cross frame as boundary, (C) box frame containing a cube within its center, and (D) a zippered origami tube. Displayed scale bars are 1 cm.

Utilizing CNC gel as support materials, various complex structures such as a cubic trefoil knot, a box with cross frame as boundary, a box frame containing a cube within its center, and a zippered origami tube were 3D printed through the dual DIW printing approach (Figure 7.6). A cubic trefoil knot with beams that looped within itself was successfully printed, and this print was only made possible with support material because the separation between beam components was necessary during DIW 3D processing (Figure 7.6A). In this case, the CNC gel served as a sustainable, renewable, and green support material, which offered significant advantage compared

to traditional petroleum-based support materials. Support removal is also made significantly easier, as the CNC gel was quickly and efficiently removed using water because CNC nanoparticles have less bonding tendency with other UV curable polymeric surfaces. Since the CNC gel was originally made in water, the resultant CNC suspension generated during support removal can even be potentially re-processed back into a gel with the appropriate CNC concentration that is suitable for DIW 3D printing. In another instance, a box with cross frame as boundary was also successfully fabricated using CNC support material and dual DIW 3D printing (Figure 7.6B). Typically, DIW 3D printing of pillars in the z-direction without any support material is difficult because of pillars' location displacement with gravitational effect or other processing related factors. While using CNC gel as support, this phenomenon was significantly reduced because the CNC gel ended up limiting the movement of the pillars during DIW printing. This allowed each layer of the pillars to be accurately deposited on top of each other, which allowed a highly difficult structure such as a box with cross frame as boundary to be successfully fabricated. In another demonstration, it was also demonstrated that CNC gel can be printed between two different target structures in order to produce a box frame containing a cube within its center (Figure 7.6C). Once the CNC gel was removed, a contained cube can be rattled inside the box frame. To further demonstrate the ability to use CNC gel as support material to fabricate highly complex objects, a bi-directionally foldable zippered origami tube structure was fabricated (Figure 7.6D).

Figure 7.7: (A) The dual DIW 3D printed origami tube's overall shape was maintained when a static weight was applied in the tube's x-direction. (B) The dual DIW 3D printed origami tube was re-configured into a 2D shape when a static weight was applied in the tube's y-direction. (C) Similarly, the dual DIW 3D printed origami tube was re-configured into a relatively flat 2D shape when a static weight was applied in the tube's z-direction. The applied weight in all three cases was 200 grams, and the displayed scale bars are 1 cm.

Typically, two mirrored Miura-ori units are first stacked together in order to form an origami unit. Then, two origami units are attached together on their side via a zig-zag manner in order to form a zippered origami tube structure.[263-264] Here, the fabrication of the zippered origami tube structure was made significantly easier because the structure was directly 3D printed in a one-step processing approach instead of the traditional multi-steps fabrication and assembly approach. During 3D fabrication of origami tubes, it is also necessary to introduce holes near the hinge regions and at the apex of fold lines. Otherwise, the origami tube structure can be easily damaged or can be difficult to be folded during its 2D and 3D shape re-configuration.[265] In this case, CNC gel support material was utilized in the fabrication of the origami tube's hinge and apex regions. After support removal with water, the origami tube was able to repeatedly re-configure from a 3D shape into a 2D shape in the y- and z-axes, while the structure remained relatively stiff in the x-axis (Figure 7.7). This type of origami tube structure can have potential applications in solar arrays, robotics, deployable canopies, outer space architectures, and many others.[265-267]

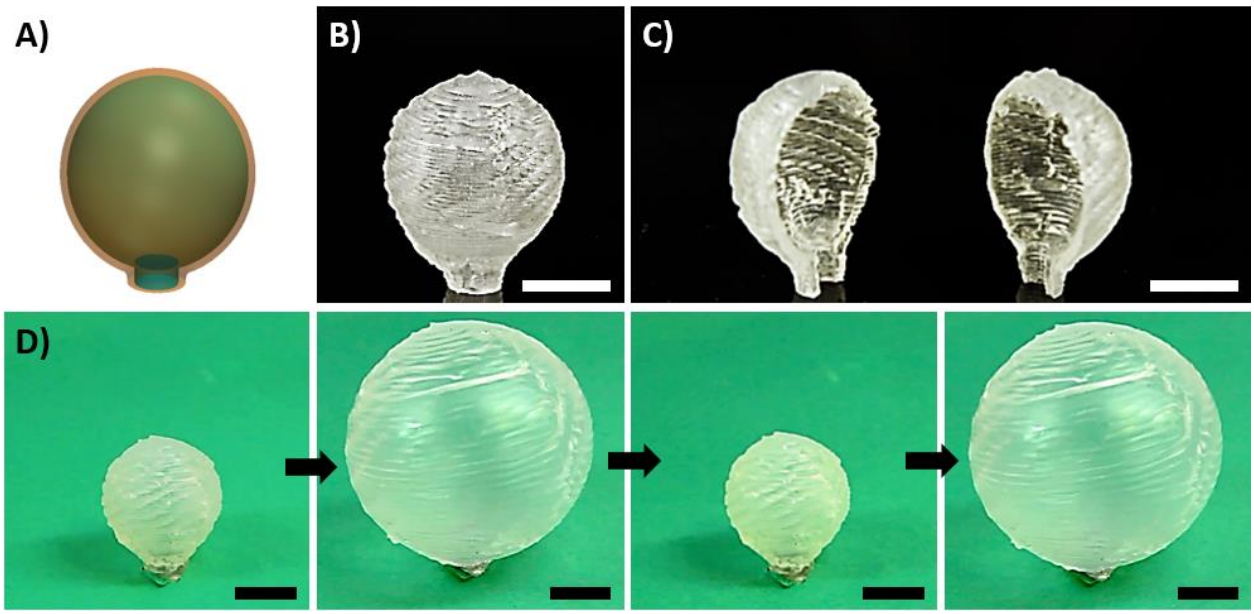

Figure 7.8: Using the dual DIW 3D printing approach, a balloon structure was fabricated while CNC gel served as the support material. (A) The SolidWorks model of the balloon structure. (B) After CNC support removal with water, the final balloon structure is illustrated. (C) The resultant balloon is cut in half to showcase the successful removal of the CNC support material even in a highly confined environment. (D) Another balloon was fabricated, and the balloon's reversible inflation process using air is illustrated from left to right. Displayed scale bars are 1 cm.

In addition, 3D printing a hollow sphere like structure in a layer-by-layer manner is usually difficult because the radius of each ring in the layer is constantly changing during the hollow sphere's fabrication. For example, as the radius of the ring increases, it becomes increasing difficult to use DIW to properly deposit the ink filament into the desired ring shape because of viscous thread instability effect. As a result, 3D printing technique like digital light processing is usually used to process hollow structures, where the need for support material is not necessary.[157] Nevertheless, it is still possible to use support material during DIW-based 3D printing in order to help with the fabrication of hollow structures. In this case, CNC gel can be used as the support material within a hollow balloon structure, which can help minimize viscous thread instability effect because the outer boundary of the deposited CNC layer can serve as an outline for the elastomeric filament to follow. In effect, the elastomeric ring layer will be contained between air

and the CNC gel instead of between air on both sides. In this regard, a balloon structure and its corresponding support structure were first fabricated with SolidWorks (Figure 7.8A). Afterwards, a balloon structure was successfully fabricated while using CNCs as support material (Figure 7.8B). Furthermore, it was demonstrated that even in a highly confined environment, such as the inside of a balloon, water was still able to easily remove the CNC support material. In fact, the balloon was cut in half, and qualitative visual inspection supported that all of the CNC gel was successfully removed from the inside of the balloon (Figure 7.8C). Additionally, the elastomeric rings were not only well bonded with one another, but our previous study had also shown that the polymerized elastomer has a strain before break of up to 600 %.[254] Since the polymerized elastomer is highly stretchable and the layer interfaces are well bonded together, it is possible to use air to reversibly inflate the 3D printed balloon. The 3D printed balloon was also able to expand to more than eight times its original volume without having air leakage or structural damage (Figure 7.8D). Overall, it was demonstrated that CNC gel can be used as support material in many different ways in order to print different variety of highly complex structures through the dual DIW 3D printing approach, and then water can be used to easily remove the support material during post processing.

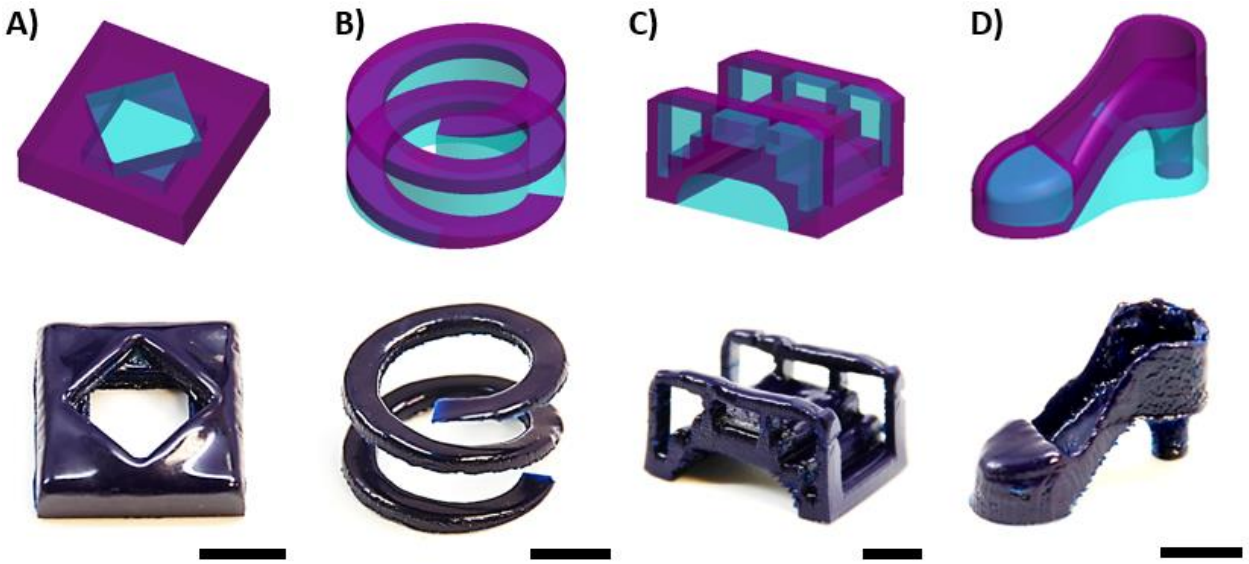

Figure 7.9: The SolidWorks models (top) and the resultant DIW-inkjet 3D printed structures with support removed (bottom) are illustrated. Various structures include (A) a box with square and diamond opening on each side, (B) a spiral, (C) a bridge, and (D) a high heel structure. Displayed scale bars are 1 cm.

CNC gel can serve as support material in not only DIW 3D printing, but also in other 3D printing techniques such as inkjet printing. Utilizing the DIW-inkjet printing approach while using CNC gel as support, a box with square and diamond opening on each side, a spiral, a bridge, and a high heel structure were successfully fabricated (Figure 7.9). During the 3D printing process, the inkjet ink was deposited onto the CNC support and then was polymerized by UV light irradiation. Similar to the dual DIW printing process, the inkjet material is UV sensitive while the CNC gel is not. As a result, water can again be use to quickly remove the support material once the printing is completed. As a simple demonstration, a box with square and diamond opening on each side was first printed (Figure 7.9A). In another instance, a spiral structure was also successfully printed (Figure 7.9B). Furthermore, a bridge structure was also targeted for DIW-inkjet processing. In this case, CNC support was not only needed in the bridge's underside, but was also needed on the topside during the fabrication of the bridge's suspensions and railings. After DIW-inkjet printing and subsequent CNC support removal, an intricately shaped bridge was successfully fabricated

(Figure 7.9C). Furthermore, an apparel related structure of a high heel was also successfully printed via the DIW-inkjet 3D printing approach (Figure 7.9D). For a high heel structure, CNC gel support was not only needed in the underside of the heel, but was also needed in the toe region of the heel. In the toe region, the inkjet material needed to form a protective canopy over the toes. This required the inkjet ink to surround the sacrificial CNC support material. As a result, even encapsulation-like feature were made possible during inkjet-based 3D printing while using CNC gel as support. Overall, it was demonstrated that CNC gel can also be used as support material in multiple different ways to form complex features within a structure during DIW-inkjet 3D printing.

7.4 Conclusion

In conclusion, CNC gel was used as a sustainable support material during the fabrication of complex structures with a multi-materials-multi-methods (M^4) printer that has dual DIW and DIW-inkjet hybrid 3D printing capability. While traditional petroleum-based support materials are un-sustainable, non-recyclable, and are difficult to remove, CNC gel support material is sustainable, potentially recyclable, and can be easily removed using water. Both FTIR and SEM characterization illustrated that CNC gel was effectively removed from both the elastomeric surfaces and the inkjet surfaces during post processing with water washing. Furthermore, unique surface morphologies were left behind depending on which side of the structure the CNC gel was deposited and on which hybrid 3D printing method was used. Utilizing dual DIW 3D printing strategies, various complexly shaped structures were successfully fabricated while using CNCs as support material. Even in a highly confined environment, such as the inside of a balloon, water was still able to easily remove the CNC support material during post processing. The interlayer adhesion of the elastomeric filaments was also demonstrated by the balloon's reversible inflation

process. Not only was air not able to leak from the balloon during inflation, but the balloon was able to expand to at least eight time its original volume. CNC gel was also able to serve as support material during DIW-inkjet 3D printing, and various complexly shaped structures with intricate features were also successfully fabricated. Overall, these complexly shaped structures fabricated by CNC gel support material and the M^4 hybrid 3D printer demonstrated potential for prototyping or other more advance applications.

CHAPTER VIII: OVERALL CONCLUSIONS AND FUTURE DIRECTIONS

8.1 Overall Conclusions

In this dissertation, nanocelluloses were utilized in different 3D printing techniques, such as digital light processing and direct ink write, in order to produce high performance composites or cellulosic structures. By adjusting the surface chemistries of CNCs and CNFs, their interactions between each other and with the surrounding matrix environment were optimized in a way such that they are compatible with the polymer matrix or with the processing requirements of the 3D printing techniques. The rheological properties of various CNC and CNF-based formulations and gels were also tailored such that they are reproducibly processable by the targeted 3D printing methods. This enabled the ability to take advantage of 3D printing's agile and customizable processing characteristics, and led to the successful fabrication of a number of nanocellulose related 3D structures with high shape complexity. Furthermore, processing parameters from the 3D printing technique itself can also provide additional means to tailor the final products' quality, inner architectural features, shape fidelity, and properties. Thus, this dissertation was able to verify the ability to use nanocellulose during 3D printing, and was able to create nanocellulosic composites and nanocellulosic structures that demonstrated high performance capability, enhanced mechanical property, and tailorable functionality. As structural and property tailorability of nanocellulose 3D structure was greatly enhanced, it definitely increased their applicability and usage in a multitude of different potential engineering applications.

From the first study, CNCs were incorporated into a PEGDA-based photocurable polymer, and then DLP processed into 3D composite structures. To improve the interfacial compatibility between CNCs and the polymer matrix, DiGlyDA was added to the base PEGDA matrix. The

competitive hydrogen bonding from DiGlyDA co-polymerization had successfully increased the compatibility and dispersibility of CNCs. After DLP 3D processing, the composite's mechanical property and water absorption capability were not only improved by CNC incorporation, but was also tunable based the incorporated CNC concentrations. Furthermore, curing layer thickness during DLP 3D printing was able to be adjusted to tune the composite's final properties due to light attenuation effects. Lastly, the ability to use DLP to process CNC-based photocurable resin into complexly shaped CNC composites was demonstrated. Thus, greatly enabling CNC-based composite 3D structures for potential biomedical related applications.

In the second study, a purely water-based CNC gel was generated for DIW 3D printing. While the concentration of CNCs in the gel was found to have a significant impact on the gel's printability and final printed part's shape fidelity, high concentration CNC gel demonstrated the necessary shear thinning behavior for proper DIW processing. Once the CNC gel was processed into 3D gel structures, a freeze-drying process was applied to remove the water without causing shape deformation or collapse. Based on the CNC concentration and DIW processing parameters, the density, porosity, resolution, print quality, and inner pore architecture were all found to be tunable. It was demonstrated that not only a number of different CNC aerogel 3D structures were successfully fabricated, but dual pore CNC aerogel structures were also successfully fabricated. Ultimately, this study has opened up many different CNC aerogel customization possibilities, and has demonstrated the 3D printed aerogels' potential for tissue engineering applications.

From the third study, TEMPO surface oxidation and high pressure homogenization were able to significantly improve the network entanglement homogeneity of CNF-based gel, which allowed the gel to be reproducibly and reliably processed by DIW 3D printing. After printing and freeze-drying, the resultant T-CNF aerogels were extremely light weight and highly porous.

Kymene was also added to the gel formulation, so subsequent aerogel cross-linking is possible. After cross-linking, the aerogel's shape and structure was maintained even under water and applied force, which has been attributed to the formation of double interpenetrating network from ester linkages between the T-CNFs' entangled network and the Kymeme's polymerized network. As a result, the aerogel had excellent shape recoverability and compressibility. In fact, the aerogel displayed a wet state specific strength before densification that not only exceeded that of other foam-based materials, but also approached the strength performance index of other high performance materials. In addition, incorporation of additional functionality to the aerogel was done. For example, PFOTS was added to the T-CNF aerogel through chemical vapor deposition, which rendered the aerogel nearly super-hydrophobic for potential oil/water separation applications. In another instance, PEDOT:PSS was templated to the T-CNF aerogel through simple physical interactions, and it added mechanically responsive electrical conductivity to the aerogel such that it has potential electronic related applications.

In the fourth study, CNC gel was used as a sustainable and potentially recyclable support material for fabricating complexly shaped structures using a M^4 hybrid 3D printer. While traditional support materials are non-renewable, non-recyclable, and difficult to remove, CNC gel-based support is sustainable, potentially recyclable, and can be easily removed with a simple water washing process. While using CNC gel and the M^4 hybrid 3D printer, an elastomeric resin and an inkjet ink were processed into different kinds of intricately shaped structures using dual DIW and DIW-inkjet hybrid 3D printing, respectively. FTIR and FE-SEM analysis also demonstrated that simple water washing was able to effectively remove the CNC gel, and produced the final target structure. Depending on which side of the structure the CNC gel was deposited and on which hybrid 3D printing method was used, unique surface morphologies were also left behind on the

surfaces of the target structure. The interfacial adhesion between the elastomeric layers was also found to be excellent, as a balloon structure was fabricated such that it can be reversibly inflated without having any air leakage or structural damage. Overall, using CNCs as a sustainable support material to fabricate complexly shaped structures with hybrid 3D printing was verified, and these structures demonstrated potential for prototyping and many other advance applications.

8.2 Future Directions

Overall, the scientific objectives outlined in this dissertation were explored, and the targeted research studies also demonstrated the strength of 3D printing in processing nanocellulose into highly shape customizable composites and structures with tunable properties. Nevertheless, there is still a lot of room for future scientific exploration. As seen in the first study, the main goal was to utilize the CNC composites for biomedical related applications. However, actual cell culturing on these 3D printed composite structures has not been fully studied yet, which suggests an important area of future investigation. In the second study, highly customizable CNC aerogel structures were successfully printed. However, cell integration onto the CNC aerogel scaffold structure was also not demonstrated. In addition, the wet state mechanical properties of CNC aerogel were still relatively poor. Therefore, it may be of interest to further improve the CNC aerogel's wet state mechanical property. In the third study, mechanically responsive electrical conductivity was successfully templated to the T-CNF aerogels. However, the brittle nature of the PEDOT:PSS polymer led to decreasing responsivity with increasing compression-release cycle. As a result, exploration of other materials with stronger conductive stability during strain deformable can potentially improve the electrical properties of the templated T-CNF aerogel 3D structures. In the fourth study, it is also desirable to utilize T-CNF gel as a secondary DIW material

during hybrid 3D printing. In this case, instead of simply washing away the T-CNF gel during post processing, a freeze-drying process can be done to potentially generate aerogel-elastomer or aerogel-inkjet hybrid composite structures. Further work can also be done to demonstrate the hybrid composite structures' potential for energy dampening applications or soft robotic related applications.

Another interesting research direction is studying the pyrolysis of 3D printed nanocellulosic structures in order to produce electrically conductive 3D structures that are derived from cellulose. The processing condition of the pyrolysis process still remains to be a highly interesting area of research, as it is desirable to produce structurally stable but electrically conductive objects after performing pyrolysis. These studies can lead to advancements in 3D printed cellulose-based electronic applications, such as batteries, supercapacitors, sensors, smart packaging, etc. Another future study area with potentially high impact is finding an energy efficient process for removing water from nanocellulosic 3D structures. Currently, freeze-drying is done to sublimate the frozen ice crystals within the DIW 3D printed structure, but this process can be energy and time intensive. As a result, there is a need to develop an innovative air drying or energy efficient evaporative technique for removing water from 3D printed structures without causing significant shape distortion or collapse. Lastly, there are also many opportunities in utilizing nanocellulosic materials within the field of 4D printing. In this case, a 3D printed nanocellulosic structure could potentially experience a shape change when an external stimulus such as light, heat or moisture is applied. Overall, there are still numerous opportunities for innovative discovery in the field of nanocellulose and 3D printing, and the emergence of different commercializable 3D products and technologies that are based on nanocellulose may be expected in the near future.

REFERENCES

(1) Faruk, O.; Bledzki, A. K.; Fink, H.-P.; Sain, M. Progress Report on Natural Fiber Reinforced Composites. *Macromol Mater Eng* **2014,** *299* (1), 9-26, DOI: 10.1002/mame.201300008.

(2) Moon, R. J.; Schueneman, G. T.; Simonsen, J. Overview of Cellulose Nanomaterials, Their Capabilities and Applications. *Jom-Us* **2016,** *68* (9), 2383-2394, DOI: 10.1007/s11837-016-2018-7.

(3) Klemm, D.; Heublein, B.; Fink, H. P.; Bohn, A. Cellulose: fascinating biopolymer and sustainable raw material. *Angewandte Chemie* **2005,** *44* (22), 3358-93, DOI: 10.1002/anie.200460587.

(4) Moon, R. J.; Martini, A.; Nairn, J.; Simonsen, J.; Youngblood, J. Cellulose nanomaterials review: structure, properties and nanocomposites. *Chemical Society reviews* **2011,** *40* (7), 3941-94, DOI: 10.1039/c0cs00108b.

(5) Thaysen, A. C.; Bunker, H. J. Studies on the bacterial decomposition of textile fibers. IV. Note on the action of B. subtilis and B. mesentericus on cellulose. *Biochem J* **1926,** *20*, 692-694, DOI: 10.1042/bj0200692.

(6) Turbak, A. F.; Snyder, F. W.; Sandberg, K. R. Microfibrillated cellulose, a new cellulose product: properties, uses, and commercial potential. *Journal of Applied Polymer Science: Applied Polymer Symposium* **1983,** *37* (Proc. Cellul. Conf., 9th, 1982, Part 2), 815-827.

(7) Turbak, A. F.; Snyder, F. W.; Sandberg, K. R. Suspensions containing microfibrillated cellulose. 1984.

(8) Peter Zamiska , J. C., Haohui Lu, and Wheeler Weise. Literature Review of 3D Printer. Master of Science Southern Illinois University, Illinois, 2013.

(9) Markstedt, K.; Mantas, A.; Tournier, I.; Martinez Avila, H.; Hagg, D.; Gatenholm, P. 3D Bioprinting Human Chondrocytes with Nanocellulose-Alginate Bioink for Cartilage Tissue Engineering Applications. *Biomacromolecules* **2015,** *16* (5), 1489-96, DOI: 10.1021/acs.biomac.5b00188.

(10) Cooperstein, I.; Layani, M.; Magdassi, S. 3D printing of porous structures by UV-curable O/W emulsion for fabrication of conductive objects. *J. Mater. Chem. C* **2015,** *3* (9), 2040-2044, DOI: 10.1039/c4tc02215g.

(11) Joseph Muskin, a. M. R. Three-Dimensional Printing Using a Photoinitiated Polymer. *Journal of Chemical Education* **2010,** *87* (5), 3, DOI: 10.1021/ed800170t.

(12) Justin Beroz, M. B., and A. John Hart. Direct_write_Self Assembly of 3D Colloidial Microstructures. **2012**, 4, DOI: 9780964002494/HH2012.

(13) Korpela, J.; Kokkari, A.; Korhonen, H.; Malin, M.; Narhi, T.; Seppala, J. Biodegradable and bioactive porous scaffold structures prepared using fused deposition modeling. *Journal of biomedical materials research. Part B, Applied biomaterials* **2013,** *101* (4), 610-9, DOI: 10.1002/jbm.b.32863.

(14) Lee, H.; Fang, N. X. Micro 3D printing using a digital projector and its application in the study of soft materials mechanics. *Journal of visualized experiments : JoVE* **2012,** (69), e4457, DOI: 10.3791/4457.

(15) Li, X.; Cui, R.; Sun, L.; Aifantis, K. E.; Fan, Y.; Feng, Q.; Cui, F.; Watari, F. 3D-Printed Biopolymers for Tissue Engineering Application. *International Journal of Polymer Science* **2014,** *2014*, 1-13, DOI: 10.1155/2014/829145.

(16) Ma, R. R.; Belter, J. T.; Dollar, A. M. Hybrid Deposition Manufacturing: Design Strategies for Multimaterial Mechanisms Via Three-Dimensional Printing and Material Deposition. *Journal of Mechanisms and Robotics* **2015,** *7* (2), 021002, DOI: 10.1115/1.4029400.

(17) Sun, C.; Fang, N.; Wu, D. M.; Zhang, X. Projection micro-stereolithography using digital micro-mirror dynamic mask. *Sensors and Actuators A: Physical* **2005,** *121* (1), 113-120, DOI: 10.1016/j.sna.2004.12.011.

(18) Wendel, B.; Rietzel, D.; Kühnlein, F.; Feulner, R.; Hülder, G.; Schmachtenberg, E. Additive Processing of Polymers. *Macromol Mater Eng* **2008,** *293* (10), 799-809, DOI: 10.1002/mame.200800121.

(19) Choi, J. Y.; Das, S.; Theodore, N. D.; Kim, I.; Honsberg, C.; Choi, H. W.; Alford, T. L. Advances in 2D/3D Printing of Functional Nanomaterials and Their Applications. *Ecs Journal of Solid State Science and Technology* **2015,** *4* (4), P3001-P3009, DOI: 10.1149/2.0011504jss.

(20) Espalin, D.; Muse, D. W.; MacDonald, E.; Wicker, R. B. 3D Printing multifunctionality: structures with electronics. *The International Journal of Advanced Manufacturing Technology* **2014,** *72* (5-8), 963-978, DOI: 10.1007/s00170-014-5717-7.

(21) Ren, X. Y.; Shao, H. P.; Lin, T.; Zheng, H. 3D gel-printing-An additive manufacturing method for producing complex shape parts. *Mater Design* **2016,** *101*, 80-87, DOI: 10.1016/j.matdes.2016.03.152.

(22) Chimene, D.; Lennox, K. K.; Kaunas, R. R.; Gaharwar, A. K. Advanced Bioinks for 3D Printing: A Materials Science Perspective. *Ann Biomed Eng* **2016,** *44* (6), 2090-2102, DOI: 10.1007/s10439-016-1638-y.

(23) Gross, B. C.; Erkal, J. L.; Lockwood, S. Y.; Chen, C.; Spence, D. M. Evaluation of 3D printing and its potential impact on biotechnology and the chemical sciences. *Anal Chem* **2014,** *86* (7), 3240-53, DOI: 10.1021/ac403397r.

(24) Hull, C. W. US 4575330A - Apparatus For Production Of Three-Dimensional Objects By Stereolithography. 1984-08-08.

(25) Associates, W. *Wohlers Report 2017 Annual Worldwide Progress Report*; 2017.

(26) Wang, Q.; Sun, J.; Yao, Q.; Ji, C.; Liu, J.; Zhu, Q. 3D printing with cellulose materials. *Cellulose* **2018,** *25* (8), 4275-4301, DOI: 10.1007/s10570-018-1888-y.

(27) Kalsoom, U.; Nesterenko, P. N.; Paull, B. Recent developments in 3D printable composite materials. *Rsc Adv* **2016,** *6* (65), 60355-60371, DOI: 10.1039/c6ra11334f.

(28) Kirchmajer, D. M.; Gorkin Iii, R.; in het Panhuis, M. An overview of the suitability of hydrogel-forming polymers for extrusion-based 3D-printing. *J Mater Chem B* **2015,** *3* (20), 4105-4117, DOI: 10.1039/c5tb00393h.

(29) Jungst, T.; Smolan, W.; Schacht, K.; Scheibel, T.; Groll, J. Strategies and Molecular Design Criteria for 3D Printable Hydrogels. *Chem Rev* **2016,** *116* (3), 1496-539, DOI: 10.1021/acs.chemrev.5b00303.

(30) Nguyen, D. T.; Meyers, C.; Yee, T. D.; Dudukovic, N. A.; Destino, J. F.; Zhu, C.; Duoss, E. B.; Baumann, T. F.; Suratwala, T.; Smay, J. E.; Dylla-Spears, R. 3D-Printed Transparent Glass. *Adv Mater* **2017,** *29* (26), DOI: 10.1002/adma.201701181.

(31) Yu, Y.; Liu, F.; Zhang, R.; Liu, J. Suspension 3D Printing of Liquid Metal into Self-Healing Hydrogel. *Advanced Materials Technologies* **2017,** *2* (11), 1700173, DOI: 10.1002/admt.201700173.

(32) Muth, J. T.; Dixon, P. G.; Woish, L.; Gibson, L. J.; Lewis, J. A. Architected cellular ceramics with tailored stiffness via direct foam writing. *PNAS* **2017,** *114* (8), 1832-1837, DOI: 10.1073/pnas.1616769114.

(33) Pierre, A.; Weger, D.; Perrot, A.; Lowke, D. Penetration of cement pastes into sand packings during 3D printing: analytical and experimental study. *Mater Struct* **2018,** *51* (1), DOI: 10.1617/s11527-018-1148-5.

(34) Lee, K. G.; Park, K. J.; Seok, S.; Shin, S.; Kim, D. H.; Park, J. Y.; Heo, Y. S.; Lee, S. J.; Lee, T. J. 3D printed modules for integrated microfluidic devices. *RSC Adv.* **2014,** *4* (62), 32876-32880, DOI: 10.1039/c4ra05072j.

(35) Eichhorn, S. J.; Dufresne, A.; Aranguren, M.; Marcovich, N. E.; Capadona, J. R.; Rowan, S. J.; Weder, C.; Thielemans, W.; Roman, M.; Renneckar, S.; Gindl, W.; Veigel, S.; Keckes, J.; Yano, H.; Abe, K.; Nogi, M.; Nakagaito, A. N.; Mangalam, A.; Simonsen, J.; Benight, A. S.; Bismarck,

A.; Berglund, L. A.; Peijs, T. Review: current international research into cellulose nanofibres and nanocomposites. *J Mater Sci* **2009,** *45* (1), 1-33, DOI: 10.1007/s10853-009-3874-0.

(36) Youssef Habibi, L. A. L., and Orlando J. Rojas. Cellulose Nanocrystals_Chemistry, Self Assembly, and Applications. *Chemical Society reviews* **2010,** *110*, 22, DOI: 10.1021/cr900339w.

(37) Siró, I.; Plackett, D. Microfibrillated cellulose and new nanocomposite materials: a review. *Cellulose* **2010,** *17* (3), 459-494, DOI: 10.1007/s10570-010-9405-y.

(38) Gardner, D. J.; Oporto, G. S.; Mills, R.; Samir, M. A. S. A. Adhesion and Surface Issues in Cellulose and Nanocellulose. *J Adhes Sci Technol* **2008,** *22* (5-6), 545-567, DOI: 10.1163/156856108x295509.

(39) Peng, B. L.; Dhar, N.; Liu, H. L.; Tam, K. C. Chemistry and applications of nanocrystalline cellulose and its derivatives: A nanotechnology perspective. *The Canadian Journal of Chemical Engineering* **2011,** *89* (5), 1191-1206, DOI: 10.1002/cjce.20554.

(40) Youssef Habibi, L. A. L., and Orlando J. Rojas†. Cellulose Nanocrystals_Chemistry, Self Assembly, and Applications. *Chemical Review* **2010,** *110*, 22, DOI: 10.1021/cr900339w.

(41) Mohammadkazemi, F.; Azin, M.; Ashori, A. Production of bacterial cellulose using different carbon sources and culture media. *Carbohydrate polymers* **2015,** *117*, 518-23, DOI: 10.1016/j.carbpol.2014.10.008.

(42) Li, T.; Aspler, J.; Kingsland, A.; Cormier, L. M.; Zou, X. 3D Printing – A Review of Technologies, Markets, and Opportunities For the Forest Industry. *Journal of Science & Technology for Forest Products and Processes* **2016,** *5* (2), 30 - 37.

(43) Hausmann, M. K.; Ruhs, P. A.; Siqueira, G.; Lauger, J.; Libanori, R.; Zimmermann, T.; Studart, A. R. Dynamics of Cellulose Nanocrystal Alignment during 3D Printing. *ACS nano* **2018,** *12* (7), 6926-6937, DOI: 10.1021/acsnano.8b02366.

(44) Stephanie Beck-Candanedo, M. R., and Derek G. Gray. Effect of Reaction Conditions on the Properties and Behavior of Wood Cellulose Nanocrystals Suspensions. *Biomacromolecules* **2005,** *6*, 7, DOI: 10.1021/bm049300p.

(45) Habibi, Y.; Lucia, L. A.; Rojas, O. J. Cellulose Nanocrystals-Chemistry, Self Assembly, and Applications. *Chemical Review* **2010,** *110*, 22, DOI: 10.1021/cr900339w.

(46) Faruk, O.; Bledzki, A. K.; Fink, H.-P.; Sain, M. Biocomposites reinforced with natural fibers: 2000–2010. *Progress in Polymer Science* **2012,** *37* (11), 1552-1596, DOI: 10.1016/j.progpolymsci.2012.04.003.

(47) Gibson, L. J. The hierarchical structure and mechanics of plant materials. *Journal of the Royal Society, Interface / the Royal Society* **2012,** *9* (76), 2749-66, DOI: 10.1098/rsif.2012.0341.

(48) Kafy, A.; Kim, H. C.; Zhai, L.; Kim, J. W.; Hai, L. V.; Kang, T. J.; Kim, J. Cellulose long fibers fabricated from cellulose nanofibers and its strong and tough characteristics. *Sci Rep* **2017,** *7* (1), 17683, DOI: 10.1038/s41598-017-17713-3.

(49) Stelte, W.; Sanadi, A. R. Preparation and Characterization of Cellulose Nanofibers from Two Commercial Hardwood and Softwood Pulps. *Industrial & Engineering Chemistry Research* **2009,** *48* (24), 11211-11219.

(50) Guhados, G.; Wan, W.; Hutter, J. L. Measurement of the Elastic Modulus of Single Bacterial Cellulose Fibers Using Atomic Force Microscopy. *Langmuir* **2005,** *21* (14), 6642-6646, DOI: 10.1021/la0504311.

(51) Iwamoto, S.; Kai, W.; Isogai, A.; Iwata, T. Elastic Modulus of Single Cellulose Microfibrils from Tunicate Measured by Atomic Force Microscopy. *Biomacromolecules* **2009,** *10*, 2271-2276, DOI: 10.1021/bm900520n.

(52) Nogi, M.; Komoda, N.; Otsuka, K.; Suganuma, K. Foldable nanopaper antennas for origami electronics. *Nanoscale* **2013,** *5* (10), 4395-9, DOI: 10.1039/c3nr00231d.

(53) ASTM, ASTM 52900-2015-E-Standard Terminology for Additive Manufacturing Technologies-General Principles Terminology. ASTM: ISO/ASTM International, 2016; p 9.

(54) Martínez Ávila, H.; Schwarz, S.; Rotter, N.; Gatenholm, P. 3D bioprinting of human chondrocyte-laden nanocellulose hydrogels for patient-specific auricular cartilage regeneration. *Bioprinting* **2016,** *1-2*, 22-35, DOI: 10.1016/j.bprint.2016.08.003.

(55) Håkansson, K. M. O.; Henriksson, I. C.; de la Peña Vázquez, C.; Kuzmenko, V.; Markstedt, K.; Enoksson, P.; Gatenholm, P. Solidification of 3D Printed Nanofibril Hydrogels into Functional 3D Cellulose Structures. *Advanced Materials Technologies* **2016,** *1* (7), 1600096, DOI: 10.1002/admt.201600096.

(56) Henriksson, I.; Gatenholm, P.; Hagg, D. A. Increased lipid accumulation and adipogenic gene expression of adipocytes in 3D bioprinted nanocellulose scaffolds. *Biofabrication* **2017,** *9* (1), 015022, DOI: 10.1088/1758-5090/aa5c1c.

(57) Muller, M.; Ozturk, E.; Arlov, O.; Gatenholm, P.; Zenobi-Wong, M. Alginate Sulfate-Nanocellulose Bioinks for Cartilage Bioprinting Applications. *Ann Biomed Eng* **2017,** *45* (1), 210-223, DOI: 10.1007/s10439-016-1704-5.

(58) Markstedt, K.; Escalante, A.; Toriz, G.; Gatenholm, P. Biomimetic Inks Based on Cellulose Nanofibrils and Cross-Linkable Xylans for 3D Printing. *Acs Appl Mater Inter* **2017,** *9* (46), 40878-40886, DOI: 10.1021/acsami.7b13400.

(59) Nguyen, D.; Hagg, D. A.; Forsman, A.; Ekholm, J.; Nimkingratana, P.; Brantsing, C.; Kalogeropoulos, T.; Zaunz, S.; Concaro, S.; Brittberg, M.; Lindahl, A.; Gatenholm, P.; Enejder,

A.; Simonsson, S. Cartilage Tissue Engineering by the 3D Bioprinting of iPS Cells in a Nanocellulose/Alginate Bioink. *Sci Rep* **2017,** *7* (1), 658, DOI: 10.1038/s41598-017-00690-y.

(60) Farahani, R. D.; Chizari, K.; Therriault, D. Three-dimensional printing of freeform helical microstructures: a review. *Nanoscale* **2014,** *6* (18), 10470-85, DOI: 10.1039/c4nr02041c.

(61) Murphy, S. V.; Atala, A. 3D bioprinting of tissues and organs. *Nat Biotechnol* **2014,** *32* (8), 773-85, DOI: 10.1038/nbt.2958.

(62) Lundahl, M. J.; Klar, V.; Wang, L.; Ago, M.; Rojas, O. J. Spinning of Cellulose Nanofibrils into Filaments: A Review. *Industrial & Engineering Chemistry Research* **2016,** *56* (1), 8-19, DOI: 10.1021/acs.iecr.6b04010.

(63) Atila, D.; Keskin, D.; Tezcaner, A. Cellulose acetate based 3-dimensional electrospun scaffolds for skin tissue engineering applications. *Carbohydrate polymers* **2015,** *133*, 251-61, DOI: 10.1016/j.carbpol.2015.06.109.

(64) Malda, J.; Visser, J.; Melchels, F. P.; Jungst, T.; Hennink, W. E.; Dhert, W. J.; Groll, J.; Hutmacher, D. W. 25th anniversary article: Engineering hydrogels for biofabrication. *Adv Mater* **2013,** *25* (36), 5011-28, DOI: 10.1002/adma.201302042.

(65) Kim, S. 3D Model Data Generation and Conversion for 3D Printers. *J Electron Mater* **2015,** *44* (3), 815-822, DOI: 10.1007/s11664-014-3584-5.

(66) Chung, P.; Heller, J. A.; Etemadi, M.; Ottoson, P. E.; Liu, J. A.; Rand, L.; Roy, S. Rapid and Low-cost Prototyping of Medical Devices Using 3D Printed Molds for Liquid Injection Molding. *Jove-J Vis Exp* **2014,** (88), DOI: ARTN e5174510.3791/51745.

(67) Feng, X. H.; Yang, Z. Z.; Chmely, S.; Wang, Q. W.; Wang, S. Q.; Xie, Y. J. Lignin-coated cellulose nanocrystal filled methacrylate composites prepared via 3D stereolithography printing: Mechanical reinforcement and thermal stabilization. *Carbohydrate polymers* **2017,** *169*, 272-281, DOI: 10.1016/j.carbpol.2017.04.001.

(68) Kumar, S.; Hofmann, M.; Steinmann, B.; Foster, E. J.; Weder, C. Reinforcement of Stereolithographic Resins for Rapid Prototyping with Cellulose Nanocrystals. *Acs Appl Mater Inter* **2012,** *4* (10), 5399-5407, DOI: 10.1021/am301321v.

(69) Palaganas, N. B.; Mangadlao, J. D.; de Leon, A. C.; Palaganas, J. O.; Pangilinan, K. D.; Lee, Y. J.; Advincula, R. C. 3D Printing of Photocurable Cellulose Nanocrystal Composite for Fabrication of Complex Architectures via Stereolithography. *Acs Appl Mater Inter* **2017,** *9* (39), 34314-34324, DOI: 10.1021/acsami.7b09223.

(70) Wolfberger, A.; Petritz, A.; Fian, A.; Herka, J.; Schmidt, V.; Stadlober, B.; Kargl, R.; Spirk, S.; Griesser, T. Photolithographic patterning of cellulose: a versatile dual-tone photoresist for

advanced applications. *Cellulose (Lond)* **2015,** *22* (1), 717-727, DOI: 10.1007/s10570-014-0471-4.

(71) Lin, X.; Kavalakkatt, J.; Lux-Steiner, M. C.; Ennaoui, A. Inkjet-Printed Cu2ZnSn(S, Se)4 Solar Cells. *Adv Sci (Weinh)* **2015,** *2* (6), 1500028, DOI: 10.1002/advs.201500028.

(72) Cho, D.-W.; Lee, J.-S.; Jang, J.; Jung, J. W.; Park, J. H.; Pati, F.; Lee, J.-S. Inkjet-based 3D printing. *IOP Concise Physics* **2017**, 1-7, DOI: 10.1088/978-1-6817-4079-9ch3.

(73) Derby, B. Additive Manufacture of Ceramics Components by Inkjet Printing. *Engineering-London* **2015,** *1* (1), 113-123, DOI: 10.15302/j-eng-2015014.

(74) Derby, B. Inkjet Printing of Functional and Structural Materials: Fluid Property Requirements, Feature Stability, and Resolution. *Ann Rev Mater Res* **2010,** *40* (1), 395-414, DOI: 10.1146/annurev-matsci-070909-104502.

(75) Singh, S.; Sharma, V. S.; Sachdeva, A. Progress in selective laser sintering using metallic powders: a review. *Mater Sci Tech-Lond* **2016**, 1-13, DOI: 10.1179/1743284715y.0000000136.

(76) Gunasekera, D. H. A. T.; Kuek, S.; Hasanaj, D.; He, Y. F.; Tuck, C.; Croft, A. K.; Wildman, R. D. Three dimensional ink-jet printing of biomaterials using ionic liquids and co-solvents. *Faraday Discuss* **2016,** *190*, 509-523, DOI: 10.1039/c5fd00219b.

(77) Xu, W.; Wang, X.; Sandler, N.; Willfor, S.; Xu, C. Three-Dimensional Printing of Wood-Derived Biopolymers: A Review Focused on Biomedical Applications. *Acs Sustain Chem Eng* **2018,** *6* (5), 5663-5680, DOI: 10.1021/acssuschemeng.7b03924.

(78) Kim, M.; Kim, G. 3D multi-layered fibrous cellulose structure using an electrohydrodynamic process for tissue engineering. *J Colloid Interface Sci* **2015,** *457*, 180-7, DOI: 10.1016/j.jcis.2015.07.007.

(79) Holzl, K.; Lin, S.; Tytgat, L.; Van Vlierberghe, S.; Gu, L.; Ovsianikov, A. Bioink properties before, during and after 3D bioprinting. *Biofabrication* **2016,** *8* (3), 032002, DOI: 10.1088/1758-5090/8/3/032002.

(80) Gao, X.; Shi, Z.; Kusmierczyk, P.; Liu, C.; Yang, G.; Sevostianov, I.; Silberschmidt, V. V. Time-dependent rheological behaviour of bacterial cellulose hydrogel. *Materials science & engineering. C, Materials for biological applications* **2016,** *58*, 153-9, DOI: 10.1016/j.msec.2015.08.019.

(81) Hubbe, M. A.; Tayeb, P.; Joyce, M.; Tyagi, P.; Kehoe, M.; Dimic-Misic, K.; Pal, L. Rheology of nanocellulose-rich aqueous suspensions: A Review. *Bioresources* **2017,** *12* (4), 9556-9661.

(82) Dash, R.; Li, Y.; Ragauskas, A. J. Cellulose nanowhisker foams by freeze casting. *Carbohydrate polymers* **2012,** *88* (2), 789-792, DOI: 10.1016/j.carbpol.2011.12.035.

(83) Correa, D.; Papadopoulou, A.; Guberan, C.; Jhaveri, N.; Reichert, S.; Menges, A.; Tibbits, S. 3D-Printed Wood: Programming Hygroscopic Material Transformations. *3d Print Addit Manuf* **2015,** *2* (3), 106-116, DOI: 10.1089/3dp.2015.0022.

(84) Tenhunen, T.-M.; Moslemian, O.; Kammiovirta, K.; Harlin, A.; Kääriäinen, P.; Österberg, M.; Tammelin, T.; Orelma, H. Surface tailoring and design-driven prototyping of fabrics with 3D-printing: An all-cellulose approach. *Mater Design* **2018,** *140*, 409-419, DOI: 10.1016/j.matdes.2017.12.012.

(85) Jiang, Y.; Zhou, J.; Yang, Z.; Liu, D.; Xv, X.; Zhao, G.; Shi, H.; Zhang, Q. Dialdehyde cellulose nanocrystal/gelatin hydrogel optimized for 3D printing applications. *J Mater Sci* **2018,** *53* (16), 11883-11900, DOI: 10.1007/s10853-018-2407-0.

(86) Shao, Y.; Chaussy, D.; Grosseau, P.; Beneventi, D. Use of Microfibrillated Cellulose/Lignosulfonate Blends as Carbon Precursors: Impact of Hydrogel Rheology on 3D Printing. *Industrial & Engineering Chemistry Research* **2015,** *54* (43), 10575-10582, DOI: 10.1021/acs.iecr.5b02763.

(87) Habib, A.; Sathish, V.; Mallik, S.; Khoda, B. 3D Printability of Alginate-Carboxymethyl Cellulose Hydrogel. *Materials (Basel)* **2018,** *11* (3), DOI: 10.3390/ma11030454.

(88) Wang, Z.; Xu, J.; Lu, Y.; Hu, L.; Fan, Y.; Ma, J.; Zhou, X. Preparation of 3D printable micro/nanocellulose-polylactic acid (MNC/PLA) composite wire rods with high MNC constitution. *Ind Crop Prod* **2017,** *109*, 889-896, DOI: 10.1016/j.indcrop.2017.09.061.

(89) Cataldi, A.; Rigotti, D.; Nguyen, V. D. H.; Pegoretti, A. Polyvinyl alcohol reinforced with crystalline nanocellulose for 3D printing application. *Mater Today Commun* **2018,** *15*, 236-244, DOI: 10.1016/j.mtcomm.2018.02.007.

(90) Tao, Y.; Wang, H.; Li, Z.; Li, P.; Shi, S. Q. Development and Application of Wood Flour-Filled Polylactic Acid Composite Filament for 3D Printing. *Materials (Basel)* **2017,** *10* (4), DOI: 10.3390/ma10040339.

(91) Xu, W.; Pranovich, A.; Uppstu, P.; Wang, X.; Kronlund, D.; Hemming, J.; Oblom, H.; Moritz, N.; Preis, M.; Sandler, N.; Willfor, S.; Xu, C. Novel biorenewable composite of wood polysaccharide and polylactic acid for three dimensional printing. *Carbohydrate polymers* **2018,** *187*, 51-58, DOI: 10.1016/j.carbpol.2018.01.069.

(92) Winter, A.; Mundigler, N.; Holzweber, J.; Veigel, S.; Muller, U.; Kovalcik, A.; Gindl-Altmutter, W. Residual wood polymers facilitate compounding of microfibrillated cellulose with poly(lactic acid) for 3D printer filaments. *Philosophical transactions. Series A, Mathematical, physical, and engineering sciences* **2018,** *376* (2112), DOI: 10.1098/rsta.2017.0046.

(93) Pitt, K.; Lopez-Botello, O.; Lafferty, A. D.; Todd, I.; Mumtaz, K. Investigation into the material properties of wooden composite structures with in-situ fibre reinforcement using additive manufacturing. *Compos Sci Technol* **2017,** *138*, 32-39, DOI: 10.1016/j.compscitech.2016.11.008.

(94) Henke, K.; Treml, S. Wood based bulk material in 3D printing processes for applications in construction. *Eur J Wood Wood Prod* **2013,** *71* (1), 139-141, DOI: 10.1007/s00107-012-0658-z.

(95) Gardan, J.; Roucoules, L. 3D printing device for numerical control machine and wood deposition. *Journal of Engineering Research and Applications* **2014,** *4* (12), 123-131.

(96) Kariz, M.; Sernek, M.; Kuzman, M. K. Use of wood powder and adhesive as a mixture for 3D printing. *Eur J Wood Wood Prod* **2015,** *74* (1), 123-126, DOI: 10.1007/s00107-015-0987-9.

(97) Oksman, K.; Aitomäki, Y.; Mathew, A. P.; Siqueira, G.; Zhou, Q.; Butylina, S.; Tanpichai, S.; Zhou, X.; Hooshmand, S. Review of the recent developments in cellulose nanocomposite processing. *Composites Part A: Applied Science and Manufacturing* **2016,** *83*, 2-18, DOI: 10.1016/j.compositesa.2015.10.041.

(98) Jonoobi, M.; Mathew, A. P.; Abdi, M. M.; Makinejad, M. D.; Oksman, K. A Comparison of Modified and Unmodified Cellulose Nanofiber Reinforced Polylactic Acid (PLA) Prepared by Twin Screw Extrusion. *Journal of Polymers and the Environment* **2012,** *20* (4), 991-997, DOI: 10.1007/s10924-012-0503-9.

(99) Robles, E.; Urruzola, I.; Labidi, J.; Serrano, L. Surface-modified nano-cellulose as reinforcement in poly(lactic acid) to conform new composites. *Ind Crop Prod* **2015,** *71*, 44-53, DOI: 10.1016/j.indcrop.2015.03.075.

(100) Pei, A.; Zhou, Q.; Berglund, L. A. Functionalized cellulose nanocrystals as biobased nucleation agents in poly(l-lactide) (PLLA) – Crystallization and mechanical property effects. *Compos Sci Technol* **2010,** *70* (5), 815-821, DOI: 10.1016/j.compscitech.2010.01.018.

(101) Murphy, C. A.; Collins, M. N. Microcrystalline cellulose reinforced polylactic acid biocomposite filaments for 3D printing. *Polym Composite* **2018,** *39* (4), 1311-1320, DOI: 10.1002/pc.24069.

(102) Dong, J.; Li, M.; Zhou, L.; Lee, S.; Mei, C.; Xu, X.; Wu, Q. The influence of grafted cellulose nanofibers and postextrusion annealing treatment on selected properties of poly(lactic acid) filaments for 3D printing. *Journal of Polymer Science Part B: Polymer Physics* **2017,** *55* (11), 847-855, DOI: 10.1002/polb.24333.

(103) Wang, J.; Chiappone, A.; Roppolo, I.; Shao, F.; Fantino, E.; Lorusso, M.; Rentsch, D.; Dietliker, K.; Pirri, C. F.; Grgtzmacher, H. All-in-One Cellulose Nanocrystals for 3D Printing of Nanocomposite Hydrogels. *Angew Chem Int Ed* **2018,** *57* (9), 2353 –2356, DOI: 10.1002/anie.201710951.

(104) De France, K. J.; Hoare, T.; Cranston, E. D. Review of Hydrogels and Aerogels Containing Nanocellulose. *Chem Mater* **2017,** *29* (11), 4609-4631, DOI: 10.1021/acs.chemmater.7b00531.

(105) Montalvo Navarrete, J. I.; Hidalgo-Salazar, M. A.; Escobar Nunez, E.; Rojas Arciniegas, A. J. Thermal and mechanical behavior of biocomposites using additive manufacturing. *International*

Journal on Interactive Design and Manufacturing (IJIDeM) **2017,** *12* (2), 449-458, DOI: 10.1007/s12008-017-0411-2.

(106) Tran, T. N.; Bayer, I. S.; Heredia-Guerrero, J. A.; Frugone, M.; Lagomarsino, M.; Maggio, F.; Athanassiou, A. Cocoa Shell Waste Biofilaments for 3D Printing Applications. *Macromol Mater Eng* **2017,** *302* (11), 1700219, DOI: 10.1002/mame.201700219.

(107) Le Duigou, A.; Castro, M.; Bevan, R.; Martin, N. 3D printing of wood fibre biocomposites: From mechanical to actuation functionality. *Mater Design* **2016,** *96*, 106-114, DOI: 10.1016/j.matdes.2016.02.018.

(108) Parandoush, P.; Lin, D. A review on additive manufacturing of polymer-fiber composites. *Compos Struct* **2017,** *182*, 36-53, DOI: 10.1016/j.compstruct.2017.08.088.

(109) Yang, Y.; Wang, H.; Li, H.; Ou, Z.; Yang, G. 3D printed tablets with internal scaffold structure using ethyl cellulose to achieve sustained ibuprofen release. *Eur J Pharm Sci* **2018,** *115*, 11-18, DOI: 10.1016/j.ejps.2018.01.005.

(110) Haverhalsa, L. M.; Brown, E. K.; Foley, M. P.; De Long, H. C.; Trulove, P. C. Formation of Surface Structures on Biopolymer Substrates Through the Inkjet Printing of Ionic Liquids. *Ecs Transactions* **2012,** *50* (11), 615-621, DOI: 10.1149/05011.0615ecst.

(111) Li, L.; Zhu, Y.; Yang, J. 3D bioprinting of cellulose with controlled porous structures from NMMO. *Mater Lett* **2018,** *210*, 136-138, DOI: 10.1016/j.matlet.2017.09.015.

(112) Sweely, K. D.; Fox, E. T.; Brown, E. K.; Haverhals, L. M.; De Long, H. C.; Trulove, P. C. Inkjet Printing Ionic Liquids for the Formation of Surface Structures on Biopolymer Substrates. *Ecs Transactions* **2014,** *64* (4), 575-582, DOI: 10.1149/06404.0575ecst.

(113) Markstedt, K.; Sundberg, J.; Gatenholm, P. 3D Bioprinting of Cellulose Structures from an Ionic Liquid. *3d Print Addit Manuf* **2014,** *1* (3), 115-121, DOI: 10.1089/3dp.2014.0004.

(114) Holland, S.; Tuck, C.; Foster, T. Selective recrystallization of cellulose composite powders and microstructure creation through 3D binder jetting. *Carbohydrate polymers* **2018,** *200*, 229-238, DOI: 10.1016/j.carbpol.2018.07.064.

(115) Lanaro, M.; Forrestal, D. P.; Scheurer, S.; Slinger, D. J.; Liao, S.; Powell, S. K.; Woodruff, M. A. 3D printing complex chocolate objects: Platform design, optimization and evaluation. *Journal of Food Engineering* **2017,** *215*, 13-22, DOI: 10.1016/j.jfoodeng.2017.06.029.

(116) Derossi, A.; Caporizzi, R.; Azzollini, D.; Severini, C. Application of 3D printing for customized food. A case on the development of a fruit-based snack for children. *Journal of Food Engineering* **2018,** *220*, 65-75, DOI: 10.1016/j.jfoodeng.2017.05.015.

(117) Vancauwenberghe, V.; Katalagarianakis, L.; Wang, Z.; Meerts, M.; Hertog, M.; Verboven, P.; Moldenaers, P.; Hendrickx, M. E.; Lammertyn, J.; Nicolaï, B. Pectin based food-ink

formulations for 3-D printing of customizable porous food simulants. *Innov Food Sci Emerg* **2017,** *42*, 138-150, DOI: 10.1016/j.ifset.2017.06.011.

(118) Lille, M.; Nurmela, A.; Nordlund, E.; Metsä-Kortelainen, S.; Sozer, N. Applicability of protein and fiber-rich food materials in extrusion-based 3D printing. *Journal of Food Engineering* **2018,** *220*, 20-27, DOI: 10.1016/j.jfoodeng.2017.04.034.

(119) Sun, J.; Zhou, W.; Yan, L.; Huang, D.; Lin, L.-y. Extrusion-based food printing for digitalized food design and nutrition control. *Journal of Food Engineering* **2018,** *220*, 1-11, DOI: 10.1016/j.jfoodeng.2017.02.028.

(120) Huber, T.; Clucas, D.; Vilmay, M.; Pupkes, B.; Stuart, J.; Dimartino, S.; Fee, C. 3D Printing Cellulose Hydrogels Using LASER Induced Thermal Gelation. *Journal of Manufacturing and Materials Processing* **2018,** *2* (3), 42, DOI: 10.3390/jmmp2030042.

(121) Salmoria, G. V.; Klauss, P.; Paggi, R. A.; Kanis, L. A.; Lago, A. Structure and mechanical properties of cellulose-based scaffolds fabricated by selective laser sintering. *Polym Test* **2009,** *28* (6), 648-652, DOI: 10.1016/j.polymertesting.2009.05.008.

(122) Feygin, M. Apparatus and method for forming an integral object from laminations. 1986-06-06, 1986.

(123) Wimpenny, D. I.; Bryden, B.; Pashby, I. R. Rapid laminated tooling. *J Mater Process Tech* **2003,** *138* (1-3), 214-218, DOI: 10.1016/s0924-0136(03)00074-8.

(124) Zhang, J.; Fu, J.; Song, X.; Jiang, G.; Zarrin, H.; Xu, P.; Li, K.; Yu, A.; Chen, Z. Laminated Cross-Linked Nanocellulose/Graphene Oxide Electrolyte for Flexible Rechargeable Zinc-Air Batteries. *Adv Energy Mater* **2016,** *6* (14), 1600476, DOI: 10.1002/aenm.201600476.

(125) Song, J.; Chen, C.; Zhu, S.; Zhu, M.; Dai, J.; Ray, U.; Li, Y.; Kuang, Y.; Li, Y.; Quispe, N.; Yao, Y.; Gong, A.; Leiste, U. H.; Bruck, H. A.; Zhu, J. Y.; Vellore, A.; Li, H.; Minus, M. L.; Jia, Z.; Martini, A.; Li, T.; Hu, L. Processing bulk natural wood into a high-performance structural material. *Nature* **2018,** *554* (7691), 224-228, DOI: 10.1038/nature25476.

(126) Fu, Q.; Yan, M.; Jungstedt, E.; Yang, X.; Li, Y.; Berglund, L. A. Transparent plywood as a load-bearing and luminescent biocomposite. *Compos Sci Technol* **2018,** *164*, 296-303, DOI: 10.1016/j.compscitech.2018.06.001.

(127) Abdelmouleh, M.; Boufi, S.; Belgacem, M. N.; Dufresne, A.; Gandini, A. Modification of cellulose fibers with functionalized silanes: Effect of the fiber treatment on the mechanical performances of cellulose-thermoset composites. *Journal of Applied Polymer Science* **2005,** *98* (3), 974-984, DOI: 10.1002/app.22133.

(128) Jin Gu, a. J. M. C. Polylactic acid composites incorporating casein functionalized cellulose nanowhiskers. *Journal of Biological Engineering* **2013,** *7* (31), 10, DOI: 10.1186/1754-1611-7-31.

(129) Girouard, N.; Schueneman, G. T.; Shofner, M. L.; Meredith, J. C. Exploiting colloidal interfaces to increase dispersion, performance, and pot-life in cellulose nanocrystal/waterborne epoxy composites. *Polymer* **2015,** *68*, 111-121, DOI: 10.1016/j.polymer.2015.05.009.

(130) Xu, S.; Girouard, N.; Schueneman, G.; Shofner, M. L.; Meredith, J. C. Mechanical and thermal properties of waterborne epoxy composites containing cellulose nanocrystals. *Polymer* **2013,** *54* (24), 6589-6598, DOI: 10.1016/j.polymer.2013.10.011.

(131) Chen, Q.; Liu, P.; Nan, F.; Zhou, L.; Zhang, J. Tuning the iridescence of chiral nematic cellulose nanocrystal films with a vacuum-assisted self-assembly technique. *Biomacromolecules* **2014,** *15* (11), 4343-50, DOI: 10.1021/bm501355x.

(132) Ben Mabrouk, A.; Ferraria, A. M.; Botelho do Rego, A. M.; Boufi, S. Highly transparent nancomposite films based on polybutylmethacrylate and functionalized cellulose nanocrystals. *Cellulose* **2013,** *20* (4), 1711-1723, DOI: 10.1007/s10570-013-9916-4.

(133) Tan, C. J.; Peng, J.; Lin, W. H.; Xing, Y. X.; Xu, K.; Wu, J. C.; Chen, M. C. Role of surface modification and mechanical orientation on property enhancement of cellulose nanocrystalsipolymer nanocomposites. *Eur Polym J* **2015,** *62*, 186-197, DOI: 10.1016/j.eurpolymj.2014.11.033.

(134) O'Brien, F. J. Biomaterials & scaffolds for tissue engineering. *Materials Today* **2011,** *14* (3), 88-95, DOI: 10.1016/s1369-7021(11)70058-x.

(135) Chan, B. P.; Leong, K. W. Scaffolding in tissue engineering: general approaches and tissue-specific considerations. *European spine journal : official publication of the European Spine Society, the European Spinal Deformity Society, and the European Section of the Cervical Spine Research Society* **2008,** *17 Suppl 4*, 467-79, DOI: 10.1007/s00586-008-0745-3.

(136) Jansen, E. J.; Sladek, R. E.; Bahar, H.; Yaffe, A.; Gijbels, M. J.; Kuijer, R.; Bulstra, S. K.; Guldemond, N. A.; Binderman, I.; Koole, L. H. Hydrophobicity as a design criterion for polymer scaffolds in bone tissue engineering. *Biomaterials* **2005,** *26* (21), 4423-31, DOI: 10.1016/j.biomaterials.2004.11.011.

(137) Kantaros, A.; Chatzidai, N.; Karalekas, D. 3D printing-assisted design of scaffold structures. *Int J Adv Manuf Tech* **2016,** *82* (1-4), 559-571, DOI: 10.1007/s00170-015-7386-6.

(138) Joshi, S. C.; Sheikh, A. A. 3D printing in aerospace and its long-term sustainability. *Virtual Phys Prototy* **2015,** *10* (4), 175-185, DOI: 10.1080/17452759.2015.1111519.

(139) Bikas, H.; Stavropoulos, P.; Chryssolouris, G. Additive manufacturing methods and modelling approaches: a critical review. *Int J Adv Manuf Tech* **2016,** *83* (1-4), 389-405, DOI: 10.1007/s00170-015-7576-2.

(140) Ventola, C. L. Medical Applications for 3D Printing-Current and Projected Uses. *Pharmacy and Therapeutics* **2014,** *39* (10), 704-711.

(141) Tunchel, S.; Blay, A.; Kolerman, R.; Mijiritsky, E.; Shibli, J. A. 3D Printing/Additive Manufacturing Single Titanium Dental Implants: A Prospective Multicenter Study with 3 Years of Follow-Up. *Int J Dent* **2016**, DOI: Artn 859097110.1155/2016/8590971.

(142) Singh, M.; Haverinen, H. M.; Dhagat, P.; Jabbour, G. E. Inkjet printing-process and its applications. *Adv Mater* **2010,** *22* (6), 673-85, DOI: 10.1002/adma.200901141.

(143) Yang, F.; Zhang, M.; Bhandari, B. Recent development in 3D food printing. *Crit Rev Food Sci* **2017,** *57* (14), 3145-3153, DOI: 10.1080/10408398.2015.1094732.

(144) de Leon, A. C.; Chen, Q.; Palaganas, N. B.; Palaganas, J. O.; Manapat, J.; Advincula, R. C. High performance polymer nanocomposites for additive manufacturing applications. *Reactive and Functional Polymers* **2016,** *103*, 141-155, DOI: 10.1016/j.reactfunctpolym.2016.04.010.

(145) Esmaeilian, B.; Behdad, S.; Wang, B. The evolution and future of manufacturing: A review. *J Manuf Syst* **2016,** *39*, 79-100, DOI: 10.1016/j.jmsy.2016.03.001.

(146) Li, Y.; Zhu, H.; Wang, Y.; Ray, U.; Zhu, S.; Dai, J.; Chen, C.; Fu, K.; Jang, S.-H.; Henderson, D.; Li, T.; Hu, L. Cellulose-Nanofiber-Enabled 3D Printing of a Carbon-Nanotube Microfiber Network. *Small Methods* **2017,** *1* (10), 1700222, DOI: 10.1002/smtd.201700222.

(147) Schubert, C.; van Langeveld, M. C.; Donoso, L. A. Innovations in 3D printing: a 3D overview from optics to organs. *The British journal of ophthalmology* **2014,** *98* (2), 159-61, DOI: 10.1136/bjophthalmol-2013-304446.

(148) Kuzmenko, V.; Karabulut, E.; Pernevik, E.; Enoksson, P.; Gatenholm, P. Tailor-made conductive inks from cellulose nanofibrils for 3D printing of neural guidelines. *Carbohydrate polymers* **2018,** *189*, 22-30, DOI: 10.1016/j.carbpol.2018.01.097.

(149) Sultan, S.; Mathew, A. P. 3D printed scaffolds with gradient porosity based on a cellulose nanocrystal hydrogel. *Nanoscale* **2018,** *10* (9), 4421-4431, DOI: 10.1039/c7nr08966j.

(150) Vardanyan, V.; Poaty, B.; Chauve, G.; Landry, V.; Galstian, T.; Riedl, B. Mechanical properties of UV-waterborne varnishes reinforced by cellulose nanocrystals. *J Coat Technol Res* **2014,** *11* (6), 841-852, DOI: 10.1007/s11998-014-9598-3.

(151) Johan Felix, P. G., and H. P. Schreiber. Plasma Modification of Cellulose Fibers-Effects on Some Polymer Composite Properties. *Journal of Applied Polymer Science* **1994,** *51*, 11.

(152) Eichhorn, S. J., Baillie, C.A., Zafeiropoulos, N., Mwaikambo, L.Y., Ansell, M.P., Dufresne, A., Entwistle, K.M., Herrera-Franco, P.J., Escamilla, G.C., Groom, Leslie H., Hughes, M., Hill, C., Rials, Timothy G., and Wild, P.M. Review Current international research into cellulosic fibers and composites. *J Mater Sci* **2001,** *36*, 25.

(153) Kim, J.; Montero, G.; Habibi, Y.; Hinestroza, J. P.; Genzer, J.; Argyropoulos, D. S.; Rojas, O. J. Dispersion of cellulose crystallites by nonionic surfactants in a hydrophobic polymer matrix. *Polymer Engineering & Science* **2009,** *49* (10), 2054-2061, DOI: 10.1002/pen.21417.

(154) Anuj Kumar, Y. S. N., N. K. Bhardwaj, V. Choudhary. Synthesis and characterization of cellulose nanocrystals-PVA based bionanocomposite. *Advanced Materials Letters* **2013,** *4* (8), 6, DOI: 10.5185/amlett.2012.12482.

(155) Liu, K.; Liang, H.; Nasrallah, J.; Chen, L.; Huang, L.; Ni, Y. Preparation of the CNC/Ag/beeswax composites for enhancing antibacterial and water resistance properties of paper. *Carbohydrate polymers* **2016,** *142*, 183-8, DOI: 10.1016/j.carbpol.2016.01.044.

(156) Yang, J.; Han, C. R.; Duan, J. F.; Xu, F.; Sun, R. C. Mechanical and viscoelastic properties of cellulose nanocrystals reinforced poly(ethylene glycol) nanocomposite hydrogels. *ACS Appl Mater Interfaces* **2013,** *5* (8), 3199-207, DOI: 10.1021/am4001997.

(157) Patel, D. K.; Sakhaei, A. H.; Layani, M.; Zhang, B.; Ge, Q.; Magdassi, S. Highly Stretchable and UV Curable Elastomers for Digital Light Processing Based 3D Printing. *Adv Mater* **2017,** *29* (15), DOI: Artn 160600010.1002/Adma.201606000.

(158) Yanez-Soto, B.; Liliensiek, S. J.; Murphy, C. J.; Nealey, P. F. Biochemically and topographically engineered poly(ethylene glycol) diacrylate hydrogels with biomimetic characteristics as substrates for human corneal epithelial cells. *J Biomed Mater Res A* **2013,** *101* (4), 1184-94, DOI: 10.1002/jbm.a.34412.

(159) Warner, J.; Soman, P.; Zhu, W.; Tom, M.; Chen, S. Design and 3D Printing of Hydrogel Scaffolds with Fractal Geometries. *Acs Biomater Sci Eng* **2016,** *2* (10), 1763-1770, DOI: 10.1021/acsbiomaterials.6b00140.

(160) Zhu, J.; Marchant, R. E. Design properties of hydrogel tissue-engineering scaffolds. *Expert review of medical devices* **2011,** *8* (5), 607-26, DOI: 10.1586/erd.11.27.

(161) Mazzoccoli, J. P.; Feke, D. L.; Baskaran, H.; Pintauro, P. N. Mechanical and cell viability properties of crosslinked low- and high-molecular weight poly(ethylene glycol) diacrylate blends. *J Biomed Mater Res A* **2010,** *93* (2), 558-66, DOI: 10.1002/jbm.a.32563.

(162) J.C. Halpin, a. J. L. K. The Halpin Tsai Equations: A Review. *Polymer Engineering & Science* **1976,** *16* (5), 9.

(163) L. Heux, G. C., and C. Bonini. Nonflocculating and Chiral-Nematic Self-ordering of Cellulose Microcrystals Suspensions in Nonpolar Solvents. *Langmuir* **2000,** *16*, 3, DOI: 10.1021/la9913957.

(164) Cheung, C. C. Y.; Giese, M.; Kelly, J. A.; Hamad, W. Y.; MacLachlan, M. J. Iridescent Chiral Nematic Cellulose Nanocrystal/Polymer Composites Assembled in Organic Solvents. *Acs Macro Letters* **2013,** *2* (11), 1016-1020, DOI: 10.1021/mz400464d.

(165) Querejeta-Fernandez, A.; Chauve, G.; Methot, M.; Bouchard, J.; Kumacheva, E. Chiral Plasmonic Films Formed by Gold Nanorods and Cellulose Nanocrystals. *J Am Chem Soc* **2014,** *136* (12), 4788-4793, DOI: 10.1021/ja501642p.

(166) Rämänen, P.; Penttilä, P. A.; Svedström, K.; Maunu, S. L.; Serimaa, R. The effect of drying method on the properties and nanoscale structure of cellulose whiskers. *Cellulose* **2012,** *19* (3), 901-912, DOI: 10.1007/s10570-012-9695-3.

(167) Roman, M.; Winter, W. T. Effect of Sulfate Groups from Sulfuric Acid Hydrolysis on the Thermal Degradation Behavior of Bacterial Cellulose. *Biomacromolecules* **2004,** *5* (5), 1671-1677, DOI: 10.1021/bm034519+.

(168) Wang, N.; Ding, E. Y.; Cheng, R. S. Thermal degradation behaviors of spherical cellulose nanocrystals with sulfate groups. *Polymer* **2007,** *48* (12), 3486-3493, DOI: 10.1016/j.polymer.2007.03.062.

(169) Nair, S. S.; Zhu, J. Y.; Deng, Y.; Ragauskas, A. J. Hydrogels Prepared from Cross-Linked Nanofibrillated Cellulose. *Acs Sustain Chem Eng* **2014,** *2* (4), 772-780, DOI: 10.1021/sc400445t.

(170) Vitale, A.; Cabral, J. T. Frontal Conversion and Uniformity in 3D Printing by Photopolymerisation. *Materials (Basel)* **2016,** *9* (9), DOI: 10.3390/ma9090760.

(171) Zhao, Z.; Wu, J.; Mu, X.; Chen, H.; Qi, H. J.; Fang, D. Desolvation Induced Origami of Photocurable Polymers by Digit Light Processing. *Macromol Rapid Commun* **2017,** *38* (13), DOI: 10.1002/marc.201600625.

(172) Wu, J.; Zhao, Z.; Hamel, C. M.; Mu, X.; Kuang, X.; Guo, Z.; Qi, H. J. Evolution of material properties during free radical photopolymerization. *J Mech Phys Solids* **2018,** *112*, 25-49, DOI: 10.1016/j.jmps.2017.11.018.

(173) Roberson, D.; Shemelya, C. M.; MacDonald, E.; Wicker, R. Expanding the applicability of FDM-type technologies through materials development. *Rapid Prototyping J* **2015,** *21* (2), 137-143, DOI: 10.1108/Rpj-12-2014-0165.

(174) Lewis, J. A. Direct Ink Writing of 3D Functional Materials. *Adv Funct Mater* **2006,** *16* (17), 2193-2204, DOI: 10.1002/adfm.200600434.

(175) Dhar, P.; Bhardwaj, U.; Kumar, A.; Katiyar, V. Cellulose Nanocrystals: A Potential Nanofiller for Food Packaging Applications. **2014,** *1162*, 197-239, DOI: 10.1021/bk-2014-1162.ch017.

(176) Maleki, H.; Duraes, L.; Garcia-Gonzalez, C. A.; Del Gaudio, P.; Portugal, A.; Mahmoudi, M. Synthesis and biomedical applications of aerogels: Possibilities and challenges. *Advances in colloid and interface science* **2016,** *236*, 1-27, DOI: 10.1016/j.cis.2016.05.011.

(177) Zhu, C.; Han, T. Y.; Duoss, E. B.; Golobic, A. M.; Kuntz, J. D.; Spadaccini, C. M.; Worsley, M. A. Highly compressible 3D periodic graphene aerogel microlattices. *Nature communications* **2015,** *6*, 6962, DOI: 10.1038/ncomms7962.

(178) Zhu, C.; Liu, T.; Qian, F.; Han, T. Y.; Duoss, E. B.; Kuntz, J. D.; Spadaccini, C. M.; Worsley, M. A.; Li, Y. Supercapacitors Based on Three-Dimensional Hierarchical Graphene Aerogels with Periodic Macropores. *Nano Lett* **2016,** *16* (6), 3448-56, DOI: 10.1021/acs.nanolett.5b04965.

(179) Lee, J.; Deng, Y. The morphology and mechanical properties of layer structured cellulose microfibril foams from ice-templating methods. *Soft Matter* **2011,** *7* (13), 6034, DOI: 10.1039/c1sm05388d.

(180) Zhang, W.; Zhang, Y.; Lu, C.; Deng, Y. Aerogels from crosslinked cellulose nano/micro-fibrils and their fast shape recovery property in water. *J Mater Chem* **2012,** *22* (23), 11642-11650, DOI: 10.1039/c2jm30688c.

(181) Sehaqui, H.; Zhou, Q.; Berglund, L. A. High-porosity aerogels of high specific surface area prepared from nanofibrillated cellulose (NFC). *Compos Sci Technol* **2011,** *71* (13), 1593-1599, DOI: 10.1016/j.compscitech.2011.07.003.

(182) Mulyadi, A.; Zhang, Z.; Deng, Y. Fluorine-Free Oil Absorbents Made from Cellulose Nanofibril Aerogels. *ACS Appl Mater Interfaces* **2016,** *8* (4), 2732-40, DOI: 10.1021/acsami.5b10985.

(183) Sehaqui, H.; Zhou, Q.; Ikkala, O.; Berglund, L. A. Strong and tough cellulose nanopaper with high specific surface area and porosity. *Biomacromolecules* **2011,** *12* (10), 3638-44, DOI: 10.1021/bm2008907.

(184) Olsson, R. T.; Azizi Samir, M. A.; Salazar-Alvarez, G.; Belova, L.; Strom, V.; Berglund, L. A.; Ikkala, O.; Nogues, J.; Gedde, U. W. Making flexible magnetic aerogels and stiff magnetic nanopaper using cellulose nanofibrils as templates. *Nat Nanotechnol* **2010,** *5* (8), 584-8, DOI: 10.1038/nnano.2010.155.

(185) Yang, X.; Cranston, E. D. Chemically Cross-Linked Cellulose Nanocrystal Aerogels with Shape Recovery and Superabsorbent Properties. *Chem Mater* **2014,** *26* (20), 6016-6025, DOI: 10.1021/cm502873c.

(186) Heath, L.; Thielemans, W. Cellulose nanowhisker aerogels. *Green Chem* **2010,** *12* (8), 1448, DOI: 10.1039/c0gc00035c.

(187) Pattinson, S. W.; Hart, A. J. Additive Manufacturing of Cellulosic Materials with Robust Mechanics and Antimicrobial Functionality. *Advanced Materials Technologies* **2017**, 1600084, DOI: 10.1002/admt.201600084.

(188) Siqueira, G.; Kokkinis, D.; Libanori, R.; Hausmann, M. K.; Gladman, A. S.; Neels, A.; Tingaut, P.; Zimmermann, T.; Lewis, J. A.; Studart, A. R. Cellulose Nanocrystal Inks for 3D Printing of Textured Cellular Architectures. *Adv Funct Mater* **2017,** *27* (12), 1604619, DOI: 10.1002/adfm.201604619.

(189) Salas, C.; Nypelö, T.; Rodriguez-Abreu, C.; Carrillo, C.; Rojas, O. J. Nanocellulose properties and applications in colloids and interfaces. *Curr Opin Colloid In* **2014,** *19* (5), 383-396, DOI: 10.1016/j.cocis.2014.10.003.

(190) Sylvain Deville, E. S., Ravi K. Nalla, Antoni P. Tomsia. Freezing as a Path to Build Complex Composites. *Science* **2006,** *311* (5760), 515-518, DOI: 10.1126/science.1120937.

(191) Deville, S.; Saiz, E.; Tomsia, A. P. Freeze casting of hydroxyapatite scaffolds for bone tissue engineering. *Biomaterials* **2006,** *27* (32), 5480-9, DOI: 10.1016/j.biomaterials.2006.06.028.

(192) Joly, P.; Duda, G. N.; Schone, M.; Welzel, P. B.; Freudenberg, U.; Werner, C.; Petersen, A. Geometry-driven cell organization determines tissue growths in scaffold pores: consequences for fibronectin organization. *Plos One* **2013,** *8* (9), e73545, DOI: 10.1371/journal.pone.0073545.

(193) Chiu, Y. C.; Cheng, M. H.; Engel, H.; Kao, S. W.; Larson, J. C.; Gupta, S.; Brey, E. M. The role of pore size on vascularization and tissue remodeling in PEG hydrogels. *Biomaterials* **2011,** *32* (26), 6045-51, DOI: 10.1016/j.biomaterials.2011.04.066.

(194) A. K. Salem, R. S., R. G. Pearson,1 M. C. Davies, S. J. B. Tendler, C. J. Roberts, P. M. Williams,; Shakesheff, K. M. Interactions of 3T3 fibroblasts and endothelial cells with defined pore features. *J Biomed Mater Res A* **2002,** *61* (2), 212-217, DOI: 10.1002/jbm.10195.

(195) Atila, D.; Keskin, D.; Tezcaner, A. Crosslinked pullulan/cellulose acetate fibrous scaffolds for bone tissue engineering. *Mat Sci Eng C-Mater* **2016,** *69*, 1103-1115, DOI: 10.1016/j.msec.2016.08.015.

(196) He, J. X.; Tan, W. L.; Han, Q. M.; Cui, S. Z.; Shao, W. L.; Sang, F. Fabrication of silk fibroin/cellulose whiskers-chitosan composite porous scaffolds by layer-by-layer assembly for application in bone tissue engineering. *J Mater Sci* **2016,** *51* (9), 4399-4410, DOI: 10.1007/s10853-016-9752-7.

(197) Muller, F. A.; Muller, L.; Hofmann, I.; Greil, P.; Wenzel, M. M.; Staudenmaier, R. Cellulose-based scaffold materials for cartilage tissue engineering. *Biomaterials* **2006,** *27* (21), 3955-3963, DOI: 10.1016/j.biomaterials.2006.02.031.

(198) Cai, H. L.; Sharma, S.; Liu, W. Y.; Mu, W.; Liu, W.; Zhang, X. D.; Deng, Y. L. Aerogel Microspheres from Natural Cellulose Nanofibrils and Their Application as Cell Culture Scaffold. *Biomacromolecules* **2014,** *15* (7), 2540-2547, DOI: 10.1021/bm5003976.

(199) Mohanty, S.; Sanger, K.; Heiskanen, A.; Trifol, J.; Szabo, P.; Dufva, M.; Emneus, J.; Wolff, A. Fabrication of scalable tissue engineering scaffolds with dual-pore microarchitecture by combining 3D printing and particle leaching. *Materials science & engineering. C, Materials for biological applications* **2016,** *61*, 180-9, DOI: 10.1016/j.msec.2015.12.032.

(200) Park, K.; Jung, H. J.; Son, J. S.; Park, K. D.; Kim, J.-J.; Ahn, K.-D.; Han, D. K. Preparation of Biodegradable Polymer Scaffolds with Dual Pore System for Tissue Regeneration. *Macromol Symp* **2007,** *249-250* (1), 145-150, DOI: 10.1002/masy.200750324.

(201) Jung, H. J.; Park, K.; Kim, J. J.; Lee, J. H.; Han, K. O.; Han, D. K. Effect of RGD-immobilized dual-pore poly(L-lactic acid) scaffolds on chondrocyte proliferation and extracellular matrix production. *Artificial organs* **2008,** *32* (12), 981-9, DOI: 10.1111/j.1525-1594.2008.00660.x.

(202) Huang, S. H.; Liu, P.; Mokasdar, A.; Hou, L. Additive manufacturing and its societal impact: a literature review. *Int J Adv Manuf Tech* **2013,** *67* (5-8), 1191-1203, DOI: 10.1007/s00170-012-4558-5.

(203) Krivec, M.; Roshanghias, A.; Abram, A.; Binder, A. Exploiting the combination of 3D polymer printing and inkjet Ag-nanoparticle printing for advanced packaging. *Microelectron Eng* **2017,** *176*, 1-5, DOI: 10.1016/j.mee.2016.12.021.

(204) Khoo, Z. X.; Teoh, J. E. M.; Liu, Y.; Chua, C. K.; Yang, S. F.; An, J.; Leong, K. F.; Yeong, W. Y. 3D printing of smart materials: A review on recent progresses in 4D printing. *Virtual Phys Prototy* **2015,** *10* (3), 103-122, DOI: 10.1080/17452759.2015.1097054.

(205) Isogai, A. Wood nanocelluloses: fundamentals and applications as new bio-based nanomaterials. *J Wood Sci* **2013,** *59* (6), 449-459, DOI: 10.1007/s10086-013-1365-z.

(206) Sehaqui, H.; Allais, M.; Zhou, Q.; Berglund, L. A. Wood cellulose biocomposites with fibrous structures at micro- and nanoscale. *Compos Sci Technol* **2011,** *71* (3), 382-387, DOI: 10.1016/j.compscitech.2010.12.007.

(207) Innerlohinger, J.; Weber, H. K.; Kraft, G. Aerocellulose: Aerogels and aerogel-like materials made from cellulose. *Macromol Symp* **2006,** *244*, 126-135, DOI: 10.1002/masy.200651212.

(208) Toivonen, M. S.; Kaskela, A.; Rojas, O. J.; Kauppinen, E. I.; Ikkala, O. Ambient-Dried Cellulose Nanofibril Aerogel Membranes with High Tensile Strength and Their Use for Aerosol Collection and Templates for Transparent, Flexible Devices. *Adv Funct Mater* **2015,** *25* (42), 6618-6626, DOI: 10.1002/adfm.201502566.

(209) Jiang, F.; Hsieh, Y.-L. Super water absorbing and shape memory nanocellulose aerogels from TEMPO-oxidized cellulose nanofibrils via cyclic freezing–thawing. *J. Mater. Chem. A* **2014,** *2* (2), 350-359, DOI: 10.1039/c3ta13629a.

(210) Chen, W.; Yu, H.; Li, Q.; Liu, Y.; Li, J. Ultralight and highly flexible aerogels with long cellulose I nanofibers. *Soft Matter* **2011,** *7* (21), 10360, DOI: 10.1039/c1sm06179h.

(211) Kim, C.; Youn, H.; Lee, H. Preparation of cross-linked cellulose nanofibril aerogel with water absorbency and shape recovery. *Cellulose* **2015,** *22* (6), 3715-3724, DOI: 10.1007/s10570-015-0745-5.

(212) Cervin, N. T.; Aulin, C.; Larsson, P. T.; Wågberg, L. Ultra porous nanocellulose aerogels as separation medium for mixtures of oil/water liquids. *Cellulose* **2011,** *19* (2), 401-410, DOI: 10.1007/s10570-011-9629-5.

(213) Wang, M.; Anoshkin, I. V.; Nasibulin, A. G.; Korhonen, J. T.; Seitsonen, J.; Pere, J.; Kauppinen, E. I.; Ras, R. H. A.; Ikkala, O. Modifying Native Nanocellulose Aerogels with Carbon Nanotubes for Mechanoresponsive Conductivity and Pressure Sensing. *Adv Mater* **2013,** *25* (17), 2428-2432, DOI: 10.1002/adma.201300256.

(214) Sabo, R.; Yermakov, A.; Law, C. T.; Elhajjar, R. Nanocellulose-Enabled Electronics, Energy Harvesting Devices, Smart Materials and Sensors: A Review. *J Renew Mater* **2016,** *4* (5), 297-312, DOI: 10.7569/jrm.2016.634114.

(215) Wicklein, B.; Kocjan, A.; Salazar-Alvarez, G.; Carosio, F.; Camino, G.; Antonietti, M.; Bergstrom, L. Thermally insulating and fire-retardant lightweight anisotropic foams based on nanocellulose and graphene oxide. *Nat Nanotechnol* **2015,** *10* (3), 277-83, DOI: 10.1038/nnano.2014.248.

(216) Aulin, C.; Netrval, J.; Wågberg, L.; Lindström, T. Aerogels from nanofibrillated cellulose with tunable oleophobicity. *Soft Matter* **2010,** *6* (14), 3298, DOI: 10.1039/c001939a.

(217) Wu, Z. Y.; Li, C.; Liang, H. W.; Chen, J. F.; Yu, S. H. Ultralight, flexible, and fire-resistant carbon nanofiber aerogels from bacterial cellulose. *Angewandte Chemie* **2013,** *52* (10), 2925-9, DOI: 10.1002/anie.201209676.

(218) Si, Y.; Yu, J.; Tang, X.; Ge, J.; Ding, B. Ultralight nanofibre-assembled cellular aerogels with superelasticity and multifunctionality. *Nature communications* **2014,** *5*, 5802, DOI: 10.1038/ncomms6802.

(219) Li, V. C.-F.; Dunn, C. K.; Zhang, Z.; Deng, Y.; Qi, H. J. Direct Ink Write (DIW) 3D Printed Cellulose Nanocrystal Aerogel Structures. *Sci Rep-Uk* **2017,** *7* (1), 8018, DOI: 10.1038/s41598-017-07771-y.

(220) Fu, J.; He, C.; Huang, J.; Chen, Z.; Wang, S. Cellulose nanofibril reinforced silica aerogels: optimization of the preparation process evaluated by a response surface methodology. *RSC Adv.* **2016,** *6* (102), 100326-100333, DOI: 10.1039/c6ra20986f.

(221) Saito, T.; Nishiyama, Y.; Putaux, J.-L.; Vignon, M.; Isogai, A. Homogeneous Suspensions of Individualized Microfibrils from TEMPO-Catalyzed Oxidation of Native Cellulose. *Biomacromolecules* **2006,** *7* (6), 1687–1691, DOI: 10.1021/bm060154s.

(222) Bhardwaj, N. K.; Hoang, V.; Nguyen, K. L. Effect of refining on pulp surface charge accessible to polydadmac and FTIR characteristic bands of high yield kraft fibres. *Bioresource Technol* **2007,** *98* (4), 962-6, DOI: 10.1016/j.biortech.2006.03.001.

(223) Saito, T.; Kimura, S.; Nishiyama, Y.; Isogai, A. Cellulose Nanofibers Prepared by TEMPO-Mediated Oxidation of Native Cellulose. *Biomacromolecules* **2007,** *8* (8), 2485–2491, DOI: 10.1021/bm0703970.

(224) Saito, T.; Shibata, I.; Isogai, A.; Suguri, N.; Sumikawa, N. Distribution of carboxylate groups introduced into cotton linters by the TEMPO-mediated oxidation. *Carbohydrate polymers* **2005,** *61* (4), 414-419, DOI: 10.1016/j.carbpol.2005.05.014.

(225) Masruchin, N.; Park, B.-D.; Causin, V.; Um, I. C. Characteristics of TEMPO-oxidized cellulose fibril-based hydrogels induced by cationic ions and their properties. *Cellulose* **2015,** *22* (3), 1993-2010, DOI: 10.1007/s10570-015-0624-0.

(226) Isogai, A.; Saito, T.; Fukuzumi, H. TEMPO-oxidized cellulose nanofibers. *Nanoscale* **2011,** *3* (1), 71-85, DOI: 10.1039/c0nr00583e.

(227) Obokata, T.; Isogai, A. The mechanism of wet-strength development of cellulose sheets prepared with polyamideamine-epichlorohydrin (PAE) resin. *Colloids and Surfaces A: Physicochemical and Engineering Aspects* **2007,** *302* (1-3), 525-531, DOI: 10.1016/j.colsurfa.2007.03.025.

(228) Jiang, F.; Hsieh, Y.-L. Self-assembling of TEMPO Oxidized Cellulose Nanofibrils As Affected by Protonation of Surface Carboxyls and Drying Methods. *Acs Sustain Chem Eng* **2016,** *4* (3), 1041-1049, DOI: 10.1021/acssuschemeng.5b01123.

(229) Karim, Z.; Hakalahti, M.; Tammelin, T.; Mathew, A. P. In situ TEMPO surface functionalization of nanocellulose membranes for enhanced adsorption of metal ions from aqueous medium. *RSC Adv.* **2017,** *7* (9), 5232-5241, DOI: 10.1039/c6ra25707k.

(230) Cintrón, M.; Hinchliffe, D. FT-IR Examination of the Development of Secondary Cell Wall in Cotton Fibers. *Fibers* **2015,** *3* (1), 30-40, DOI: 10.3390/fib3010030.

(231) Mohamed, M. A.; Salleh, W. N. W.; Jaafar, J.; Asri, S. E. A. M.; Ismail, A. F. Physicochemical properties of "green" nanocrystalline cellulose isolated from recycled newspaper. *RSC Adv.* **2015,** *5* (38), 29842-29849, DOI: 10.1039/c4ra17020b.

(232) Obokata, T.; Isogai, A. The mechanism of wet-strength development of cellulose sheets prepared with polyamideamine-epichlorohydrin (PAE) resin. *Colloid Surface A* **2007,** *302* (1-3), 525-531, DOI: 10.1016/j.colsurfa.2007.03.025.

(233) Qi, H.; Boyce, M. C. Constitutive model for stretch-induced softening of the stress-stretch behavior of elastomeric materials. *J Mech Phys Solids* **2004,** *52* (10), 2187-2205, DOI: 10.1016/j.jmps.2004.04.008.

(234) Cantournet, S.; Desmorat, R.; Besson, J. Mullins effect and cyclic stress softening of filled elastomers by internal sliding and friction thermodynamics model. *Int J Solids Struct* **2009,** *46* (11-12), 2255-2264, DOI: 10.1016/j.ijsolstr.2008.12.025.

(235) Placone, J. K.; Engler, A. J. Recent Advances in Extrusion-Based 3D Printing for Biomedical Applications. *Adv Healthc Mater* **2018,** *7* (8), e1701161, DOI: 10.1002/adhm.201701161.

(236) Layani, M.; Wang, X.; Magdassi, S. Novel Materials for 3D Printing by Photopolymerization. *Adv Mater* **2018,** *30* (41), e1706344, DOI: 10.1002/adma.201706344.

(237) Nadgorny, M.; Ameli, A. Functional Polymers and Nanocomposites for 3D Printing of Smart Structures and Devices. *ACS Appl Mater Interfaces* **2018,** *10* (21), 17489-17507, DOI: 10.1021/acsami.8b01786.

(238) Liu, Z.; Zhang, M.; Bhandari, B.; Wang, Y. 3D printing: Printing precision and application in food sector. *Trends in Food Science & Technology* **2017,** *69*, 83-94, DOI: 10.1016/j.tifs.2017.08.018.

(239) Ligon, S. C.; Liska, R.; Stampfl, J.; Gurr, M.; Mulhaupt, R. Polymers for 3D Printing and Customized Additive Manufacturing. *Chem Rev* **2017,** *117* (15), 10212-10290, DOI: 10.1021/acs.chemrev.7b00074.

(240) MacDonald, E.; Wicker, R. Multiprocess 3D printing for increasing component functionality. *Science* **2016,** *353* (6307), DOI: 10.1126/science.aaf2093.

(241) Macdonald, E.; Salas, R.; Espalin, D.; Perez, M.; Aguilera, E.; Muse, D.; Wicker, R. B. 3D Printing for the Rapid Prototyping of Structural Electronics. *Ieee Access* **2014,** *2*, 234-242, DOI: 10.1109/ACCESS.2014.2311810.

(242) Kataria, A.; Rosen, D. W. Building around inserts: methods for fabricating complex devices in stereolithography. *Rapid Prototyping J* **2001,** *7* (5), 253-262, DOI: 10.1108/13552540110410459.

(243) Yoon, H.-S.; Jang, K.-H.; Kim, E.; Lee, H.-T.; Ahn, S.-H. Hybrid 3D printing by bridging micro/nano processes. *J Micromech Microeng* **2017,** *27* (6), 065006, DOI: 10.1088/1361-6439/aa6758.

(244) Wang, L.; Liu, J. Compatible hybrid 3D printing of metal and nonmetal inks for direct manufacture of end functional devices. *Science China Technological Sciences* **2014,** *57* (11), 2089-2095, DOI: 10.1007/s11431-014-5657-3.

(245) Valentine, A. D.; Busbee, T. A.; Boley, J. W.; Raney, J. R.; Chortos, A.; Kotikian, A.; Berrigan, J. D.; Durstock, M. F.; Lewis, J. A. Hybrid 3D Printing of Soft Electronics. *Adv Mater* **2017,** *29* (40), DOI: 10.1002/adma.201703817.

(246) Tong, Y.; Murbach, J. M.; Subramanian, V.; Chhatre, S.; Delgado, F.; Martin, D. C.; Otto, K. J.; Romero-Ortega, M.; Johnson, B. N. A Hybrid 3D Printing and Robotic-assisted Embedding Approach for Design and Fabrication of Nerve Cuffs with Integrated Locking Mechanisms. *Mrs Adv* **2018,** *3* (40), 2365-2372, DOI: 10.1557/adv.2018.378.

(247) Yoon, S.; Park, J. A.; Lee, H. R.; Yoon, W. H.; Hwang, D. S.; Jung, S. Inkjet-Spray Hybrid Printing for 3D Freeform Fabrication of Multilayered Hydrogel Structures. *Adv Healthc Mater* **2018,** *7* (14), e1800050, DOI: 10.1002/adhm.201800050.

(248) Raza, I.; Iannucci, L.; Curtis, P. T. Introducing a Multimaterial Printer for the Deposition of Low Melting Point Alloys, Elastomer, and Ultraviolet Curable Resin. *3d Print Addit Manuf* **2017,** *4* (2), 83-89, DOI: 10.1089/3dp.2016.0053.

(249) Espalin, D.; Alberto Ramirez, J.; Medina, F.; Wicker, R. Multi-material, multi-technology FDM: exploring build process variations. *Rapid Prototyping J* **2014,** *20* (3), 236-244, DOI: 10.1108/rpj-12-2012-0112.

(250) Wicker, R. B.; MacDonald, E. W. Multi-material, multi-technology stereolithography. *Virtual Phys Prototy* **2012,** *7* (3), 181-194, DOI: 10.1080/17452759.2012.721119.

(251) Joe Lopes, A.; MacDonald, E.; Wicker, R. B. Integrating stereolithography and direct print technologies for 3D structural electronics fabrication. *Rapid Prototyping J* **2012,** *18* (2), 129-143, DOI: 10.1108/13552541211212113.

(252) Priedeman, W. R. J.; Brosch, A. L. Soluble material and process for three-dimensional modeling. 2004.

(253) Li, V. C. F.; Mulyadi, A.; Dunn, C. K.; Deng, Y.; Qi, H. J. Direct Ink Write 3D Printed Cellulose Nanofiber Aerogel Structures with Highly Deformable, Shape Recoverable, and Functionalizable Properties. *Acs Sustain Chem Eng* **2018,** *6* (2), 2011-2022, DOI: 10.1021/acssuschemeng.7b03439.

(254) Kuang, X.; Chen, K.; Dunn, C. K.; Wu, J.; Li, V. C. F.; Qi, H. J. 3D Printing of Highly Stretchable, Shape-Memory, and Self-Healing Elastomer toward Novel 4D Printing. *ACS Appl Mater Interfaces* **2018,** *10* (8), 7381-7388, DOI: 10.1021/acsami.7b18265.

(255) Mohamed, M. A.; WN, W. S.; Jaafar, J.; Ismail, A. F.; Abd Mutalib, M.; Mohamad, A. B.; MF, M. Z.; Awang, N. A.; Mohd Hir, Z. A. Physicochemical characterization of cellulose

nanocrystal and nanoporous self-assembled CNC membrane derived from Ceiba pentandra. *Carbohydrate polymers* **2017,** *157*, 1892-1902, DOI: 10.1016/j.carbpol.2016.11.078.

(256) Du, L.; Wang, J.; Zhang, Y.; Qi, C.; Wolcott, M. P.; Yu, Z. Preparation and Characterization of Cellulose Nanocrystals from the Bio-ethanol Residuals. *Nanomaterials (Basel)* **2017,** *7* (3), DOI: 10.3390/nano7030051.

(257) Sofla, M. R. K.; Brown, R. J.; Tsuzuki, T.; Rainey, T. J. A comparison of cellulose nanocrystals and cellulose nanofibres extracted from bagasse using acid and ball milling methods. *Advances in Natural Sciences: Nanoscience and Nanotechnology* **2016,** *7* (3), 035004, DOI: 10.1088/2043-6262/7/3/035004.

(258) Kumar, A.; Negi, Y. S.; Choudhary, V.; Bhardwaj, N. K. Characterization of Cellulose Nanocrystals Produced by Acid-Hydrolysis from Sugarcane Bagasse as Agro-Waste. *Journal of Materials Physics and Chemistry* **2014,** *2* (1), 1-8, DOI: 10.12691/jmpc-2-1-1.

(259) Li, J.; Wang, Y.; Wei, X.; Wang, F.; Han, D.; Wang, Q.; Kong, L. Homogeneous isolation of nanocelluloses by controlling the shearing force and pressure in microenvironment. *Carbohydrate polymers* **2014,** *113*, 388-93, DOI: 10.1016/j.carbpol.2014.06.085.

(260) Nacos, M.; Katapodis, P.; Pappas, C.; Daferera, D.; Tarantilis, P.; Christakopoulos, P.; Polissiou, M. Kenaf xylan – A source of biologically active acidic oligosaccharides. *Carbohydrate polymers* **2006,** *66* (1), 126-134, DOI: 10.1016/j.carbpol.2006.02.032.

(261) Luo, Q.; Shen, Y.; Li, P.; Wang, C.; Zhao, Z. Synthesis and characterization of crosslinking waterborne fluorinated polyurethane-acrylate with core-shell structure. *Journal of Applied Polymer Science* **2014,** *131* (21), DOI: 10.1002/app.40970.

(262) Park, J. B.; Kim, Y.-J.; Kim, S.-M.; Yoo, J. M.; Kim, Y.; Gorbachev, R.; Barbolina, I. I.; Kim, S. J.; Kang, S.; Yoon, M.-H.; Cho, S.-P.; Novoselov, K. S.; Hong, B. H. Non-destructive electron microscopy imaging and analysis of biological samples with graphene coating. *2d Mater* **2016,** *3* (4), 045004, DOI: 10.1088/2053-1583/3/4/045004.

(263) Filipov, E. T.; Tachi, T.; Paulino, G. H. Origami tubes assembled into stiff, yet reconfigurable structures and metamaterials. *Proc Natl Acad Sci U S A* **2015,** *112* (40), 12321-6, DOI: 10.1073/pnas.1509465112.

(264) Filipov, E. T.; Paulino, G. H.; Tachi, T. Origami tubes with reconfigurable polygonal cross-sections. *Proceedings. Mathematical, physical, and engineering sciences* **2016,** *472* (2185), 20150607, DOI: 10.1098/rspa.2015.0607.

(265) Zhao, Z.; Kuang, X.; Wu, J.; Zhang, Q.; Paulino, G. H.; Qi, H. J.; Fang, D. 3D printing of complex origami assemblages for reconfigurable structures. *Soft Matter* **2018,** *14* (39), 8051-8059, DOI: 10.1039/c8sm01341a.

(266) Liu, K.; Paulino, G. H. Nonlinear mechanics of non-rigid origami: an efficient computational approach. *Proceedings. Mathematical, physical, and engineering sciences* **2017,** *473* (2206), 20170348, DOI: 10.1098/rspa.2017.0348.

(267) Cheung, K. C.; Tachi, T.; Calisch, S.; Miura, K. Origami interleaved tube cellular materials. *Smart Mater Struct* **2014,** *23* (9), 094012, DOI: 10.1088/0964-1726/23/9/094012.